

Optimal and Robust Feedback Control of Quantum Systems

S. Z. Sayed Hassen

A thesis submitted in fulfilment
of the requirements of the degree of
Doctor of Philosophy



School of Engineering and Information Technology
University College
University of New South Wales
Australian Defence Force Academy

30 July 2010

COPYRIGHT STATEMENT

I hereby grant the University of New South Wales or its agents the right to archive and to make available my thesis or dissertation in whole or part in the University libraries in all forms of media, now or here after known, subject to the provisions of the Copyright Act 1968. I retain all proprietary rights, such as patent rights. I also retain the right to use in future works (such as articles or books) all or part of this thesis or dissertation. I also authorise University Microfilms to use the 350 word abstract of my thesis in Dissertation Abstract International (this is applicable to doctoral theses only). I have either used no substantial portions of copyright material in my thesis or I have obtained permission to use copyright material; where permission has not been granted I have applied/will apply for a partial restriction of the digital copy of my thesis or dissertation.

.....

S. Z. Sayed Hassen

30 July 2010

AUTHENTICITY STATEMENT

I certify that the Library deposit digital copy is a direct equivalent of the final officially approved version of my thesis. No emendation of content has occurred and if there are any minor variations in formatting, they are the result of the conversion to digital format.

.....

S. Z. Sayed Hassen

30 July 2010

Statement of Originality

I hereby declare that this submission is my own work and to the best of my knowledge it contains no materials previously published or written by another person, or substantial proportions of material which have been accepted for the award of any other degree or diploma at UNSW or any other educational institution, except where due acknowledgement is made in the thesis. Any contribution made to the research by others, with whom I have worked at UNSW or elsewhere, is explicitly acknowledged in the thesis. I also declare that the intellectual content of this thesis is the product of my own work, except to the extent that assistance from others in the project's design and conception or in style, presentation and linguistic expression is acknowledged.

.....
S. Z. Sayed Hassen

30 July 2010

Acknowledgements

This achievement would not have been possible without the encouragement and support of my wife, *Soraya*. When everything was pointing towards continuing a comfortable life under the tropical sun (including our back of the envelope calculation in attempting to quantify the pros/cons of such a venture), she happily accepted to give it all away – including her job – to accompany me. I am deeply indebted to you for keeping me unaware and taking care of the many things that needed my attention during my candidature.

I am grateful to my supervisor Prof Ian Petersen for the award of a generous scholarship during my time in Canberra. *“To know how to suggest is the great art of teaching”* – *H. F. Amiel*. Ian’s numerous suggestions during our weekly meetings, right from day one, have been the driving force towards the successful completion of this body of work. His guidance and influence will last for a lifetime and I only hope that I have been able to live up to his expectations as a PhD student.

I would like to thank Assoc. Prof. E. H. Huntington for taking the time to provide me with quick crash courses in quantum optics whenever I knocked on her door. She has also been instrumental towards the successful completion of experimental work in the laser laboratory during the early stages of my candidature. I would also like to thank my co-supervisor Prof. Matthew James from ANU. Auditing his courses on Quantum Control and attending the weekly reading sessions he organised at ANU has broadened my scope of the area.

My thanks and gratitude also goes to numerous people who have helped me to varying degrees during my candidature. These include Assoc. Prof. V. Ougrinovski, Assoc. Prof. H. Pota and Dr. M. Heurs. I would also like to acknowledge our team of control students in Room 208, where we had numerous discussions on a range of control and general “philosophical” topics. These include H. Harno,

O. Ur Rehman, A. Maalouf, X. Yang and H. Ouyang. Lately, Dr. A. Kallapur also joined in with his two pennies worth of “spices”. We managed to keep a sense of humour through it all.

On a more personal note, I would like to acknowledge my eldest brother, *Akhtar*, who has epitomised academic achievement and hard work for me since my younger years. More importantly, I would like to thank him for providing a “safety net” for myself and my family throughout our time in Australia. I would not be half the person I am without him. I also appreciate the understanding shown by my parents and in-laws, who unselfishly waved away their grandchildren during my candidature. My thanks also goes to my dear brother *Ibrahim* and his family for ensuring that I always feel at home every time I come back to Mauritius for holidays. Last but not least, I dedicate this PhD to my two angels, *Tariq* and *Saiif*, who have provided us with so much joy and happiness.

Abstract

Quantum systems have been traditionally subjected to ad hoc control approaches, which although effective, can be restrictive in terms of performance. In an effort to provide for a wider range of potential applications of the next generation of quantum technology, more sophisticated control schemes which can squeeze maximum performance from the closed-loop system are necessary. There is no doubt that the knowledge and use of quantum models in the controller design process, can lead to improved performance. In this thesis, we consider three topics of interest in the broad field of quantum control. The motivation for the first two topics arises out of a need to devise systematic control schemes to optimally control practical quantum systems. We show that for some important problems arising in quantum technology, the application of optimal control schemes can (in theory) achieve performance levels which are limited only by the quantum noises present in the system. The quantum systems we consider are of current interest to experimentalists and physicists working in the field of quantum optics. In the last topic of this thesis, we investigate a robust theoretical approach to the control of quantum systems. Quantum systems are very rarely known to a high degree of accuracy and in particular, they are afflicted by additional sources of uncertainty which are not present in classical systems. Here, we model uncertainty in the “observables” of the quantum systems and using the concept of relative entropy and the framework of Radon-Nikodym derivatives, we formulate and extend a quantum version of the classical risk-sensitive control result. The risk-sensitive control approach is known to possess inherent robust properties and we use a quantum version of this result to determine an upper bound on the cost of a risk-neutral problem, obtained using a nominal model of a simple quantum system. Next, we give an overview of each topic.

Overview

In the first part of the thesis, we investigate the frequency-locking problem of an optical resonant cavity. This nonlinear control problem forms an integral part of almost every quantum optics experiment and the resonant frequency has been traditionally controlled in the physics literature using ad hoc control approaches which work only in small local regions of operation. In the work presented here, we consider systematic optimal control approaches to frequency-lock an optical cavity. First, we direct our attention at the local problem where we identify a linear state-space model for the complete system using experimental frequency response data. A variant of the linear quadratic Gaussian (LQG) control approach is used to design a controller. This controller is implemented and successfully tested on an experimental test-bed. Then, we consider a more general frequency-locking problem. The cavity locking problem suffers from a strong inherent nonlinearity making it a particularly challenging control problem. An interesting feature of the system is that it possesses a repetitive characteristic at equal frequency intervals. Although this is not modelled in the system description, we propose an approach that takes advantage of this practical characteristic of the problem. We first model the nonlinearity by using a singular perturbation approach which allows for a separation of the different time-scales of the overall system. Then, we place realistic instantaneous bounds on the measurement noises and compute convex sets within which lies the frequency difference between the driving laser and the resonant frequency of the cavity. In this way, we reformulate the original nonlinear problem into one that is amenable to linear control design techniques and we construct a time-varying Kalman filter to estimate the states of the nonlinear system and regulate the system using an optimal control law. We confirm the viability of this novel approach through simulation results.

In the second part of the thesis, we consider the problem of regulating an

optical squeezer. Squeezed states of light have numerous potential applications ranging from gravitational wave detection, quantum teleportation, quantum cryptography and quantum communication. We model such a nonlinear device and analyse its steady-state behaviour. In particular, we show how the steady-state operating point of the squeezer determines the type of squeezed states of light generated. At different operating points, we design classical controllers for the linearised system and show that they cannot suppress inherent quantum noises. This result is as expected from the Heisenberg uncertainty principle. Our aim here is to optimise the level of squeezing observed by rejecting the various sources of classical noises acting on the system. A prerequisite to the generation of squeezed states of light however is that the optical squeezer needs to be frequency-locked. The control objective is therefore two-fold – there is a requirement to frequency lock the optical squeezer and also to minimise the effect of classical sources of noise on the system. First, we assume that the optical squeezer is frequency-locked and design a controller to suppress sources of classical noise. Depending on the type of squeezed states desired, we design an optimal controller at a specific operating point that minimises the effect of different sources of classical noises feeding into the optical squeezer. Then, we consider the more general case where we design a multivariable controller to frequency-lock the optical squeezer as well as suppress the effect of classical noises.

In the final part of the thesis, we extend the work of James and Petersen (see [1,2]) where a risk-sensitive control approach to a two-level quantum system is formulated. A controller for a system is usually designed on the basis of a nominal model which only approximates a true system. Quantum systems whose evolution in time are governed by stochastic master equations are no exception to this. A probabilistic approach to the measurement and feedback control of quantum systems is considered and based on classical control theory, we propose an approach in which the model uncertainties appear in the “observables” of a quantum system. Then, we formulate equivalent risk-neutral and risk-sensitive optimal control problems for the quantum systems. Our interest in the risk-sensitive control approach is due to its close connections with minimax games and its inherent robust properties. Using the concept of relative entropy and within the framework of Radon-Nikodym derivatives, we provide a measure of the “distance” between a nominal and true quantum system. In particular, we

derive an upper bound for a certain risk-neutral cost function for a class of true quantum system dynamics which differ from that of a nominal system. A two-level system is used to exemplify the concepts covered.

Contents

Statement of Originality	i
Acknowledgements	ii
Abstract	iv
Overview	v
I Frequency Locking of an Optical Resonant Cavity	1
1 Introduction	2
1.1 Side Locking	3
1.2 Dither Locking	5
1.3 Pound-Drever-Hall technique	6
1.4 Motivation	10
2 Background	12
2.1 Laser	12
2.2 Coherent States	13
2.3 Quantum Noise	14
2.4 Quadratures	14
2.5 Homodyne Detection	15
2.6 Fabry-Perot Cavity	16
3 Cavity Modelling and Identification of the Overall System	19
3.1 Schematic of Experimental Set-Up	20
3.2 Cavity Model	22
3.3 Subspace System Identification	24
3.4 Subspace Identification of the cavity system	27
4 Controller Design	32
4.1 Deterministic Linear Optimal Regulator Problem	32
4.2 Optimal Observer	35

4.3	Separation Principle	39
4.4	Integral Action	40
4.5	Performance Criterion and Design Parameters	41
4.5.1	Design Parameters	45
4.6	Controller Reduction	46
5	Experimental Results and Discussion	50
5.1	Graphical User Interface to the Experiment	51
5.2	Experimental Results	52
5.3	Discussion	53
6	Nonlinear Behaviour of the Optical Cavity	56
6.1	Nonlinear Modelling of the Optical Cavity	58
6.2	Separation of Time-scale Approach to Nonlinearity Modelling . .	60
6.3	Piezoelectric Actuator Model	63
6.4	Bounded Noise Model	65
7	Time-Varying LQG Controller Design	70
7.1	Integral Action and Performance Cost Criterion	71
7.2	Discrete-time Kalman Filtering	73
8	Simulation Results	75
9	Conclusion and Future Work	79
II	Modelling, Analysis and Control of an Optical Parametric Oscillator	81
10	Introduction	82
10.1	Squeezed states	83
10.2	Applications of Squeezed states	85
10.3	Generation of Squeezed states	86
10.3.1	Optical Parametric Amplification	86
10.4	Motivation and Problem Description	88
11	Modelling	91
11.1	Optical Resonator Cavity	91
11.2	Model Description using Quadrature Operators	93
11.3	Linearised Model of the OPO	94
11.4	Piezo-Electric Actuator Model	96

12 Steady-state Analysis of the Optical Squeezer	97
12.1 Exact Steady-state solution	97
12.2 Steady-state solution to first order in $\chi^{(2)}$	99
12.2.1 Polar form solution	99
12.2.2 Solution in terms of the field quadratures	100
12.3 Steady-state Behaviour of the Optical Squeezer	101
12.4 Optical Parametric Gain of the Fundamental Intracavity field \hat{a} .	107
13 Preliminary Controller Design	111
13.1 Standard Quantum Limit	111
13.2 Sub-Quantum Noise Limit	114
13.3 Static Approximation to State Equations	115
13.4 Preliminary LQG Controller Design	117
13.4.1 System Interconnections	118
13.4.2 Performance criterion and Kalman filtering	119
13.4.3 Model and controller design parameters	121
13.4.4 Controlled and uncontrolled variance with quantum noises only	122
13.4.5 Controlled and uncontrolled variance with quantum and classical noises	122
14 LQG Controller Design	127
14.1 Complete Model	128
14.2 Performance Criterion	130
14.3 Model and Design Parameters	130
14.4 Simulation Results	131
15 Integral LQG controller design	137
15.1 Complete Model	138
15.2 Performance Criterion and Integral Action	138
15.3 Model and Design Parameters	142
15.4 Simulation Results	142
16 Multivariable Integral LQG Controller	147
16.1 Modelling	147
16.2 LQG Performance Criterion	150
16.3 Model and Design Parameters	153
16.4 Simulation Results	154
17 Conclusion	160

III Robustness of Risk-Sensitive Controllers for Quantum Systems	163
18 Introduction	164
19 Preliminaries	167
19.1 State of a Quantum System	167
19.2 Measurement	168
19.3 Operators and Observables	169
19.4 Density Operator	170
19.5 Evolution of closed and open quantum systems	172
20 Behaviour of Quantum Systems	174
20.1 Discrete-Time Dynamics	174
20.2 Feedback Control and Measurement	175
21 Optimal Control	178
21.1 Risk-Neutral	178
21.2 Risk-Sensitive	180
21.3 Quantum Bellman Equation	184
22 Robustness Properties of Risk-Sensitive Controllers	186
23 Two-level System Example	196
23.1 Conclusion	204
Conclusion	206
References	209

List of Figures

1.1	System setup used for frequency locking	3
1.2	Variation of transmitted intensity with frequency of incident laser beam	4
1.3	Variation of reflected intensity with frequency of incident laser beam	5
1.4	Error signal with low modulation frequency. (Courtesy of [3]) . .	6
1.5	Schematic layout of a PDH laser frequency locking control loop.(Courtesy of [4])	7
1.6	Error signal with high modulation frequency. (Courtesy of [3]) . .	9
2.1	Homodyne detector	16
3.1	Photograph of the frequency locking set-up in our quantum optics laboratory.	20
3.2	Detailed schematic of the experimental set-up.	21
3.3	Cavity locking feedback control loop.	22
3.4	Experimental set-up used to measure the plant frequency response.	28
3.5	Measured plant frequency response.	29
3.6	Measured frequency response data of the augmented plant and frequency response of the identified system model.	30
3.7	Response of the optical cavity to a ramp input signal.	31
3.8	Polyfit for determination of DC gain	31
4.1	Illustration of the separation theorem.	39
4.2	Block diagram of the plant showing all the noises and their respective point of entry.	42
4.3	Typical optical cavity Bode plot from Δ to y	42
4.4	LQG integral controller design configuration.	43
4.5	Bode plots showing the frequency response of the full and the reduced order controllers.	47
4.6	Bode plots of the loop gain transfer function $L(s)$	48
4.7	Closed-loop transfer function from mechanical noise w_1 to control signal u	49
5.1	Simulink interconnection	50

5.2	Control Desk Interface	52
5.3	Set-Up used to measure the closed-loop step response. Here, r is the step input signal	53
5.4	Step Response of the closed-loop system to a step input disturbance of magnitude -0.1 V.	54
5.5	Closed loop transfer function r to e , $\frac{1}{(1+GK)}$	55
6.1	Variation of the derivative of the reflected intensity with frequency of the incident laser beam.	56
6.2	Experimental and simulated step response of the closed-loop system to step input disturbances of varying magnitude.	58
6.3	Cavity locking feedback control loop.	59
6.4	Block diagram of the cavity system.	59
6.5	Two-time scale model of the system.	61
6.6	Behaviour of nonlinear measurement functions $f_1(\Delta)$ and $f_2(\Delta)$ with large variations in Δ	63
6.7	Nonlinear functions $f_1(\Delta)$ and $f_2(\Delta)$	64
6.8	Frequency response of the identified cascaded combination of the piezoelectric actuator and the anti-aliasing filter.	65
6.9	Determination of the set of possible Δ	68
7.1	Complete system model.	70
7.2	Integral LQG controller design configuration.	71
8.1	Laser phase noise modelled as integrated white noise with an initial offset of -1 MHz.	76
8.2	Initial condition response of system using the time-varying LQG controller.	77
8.3	Phase quadrature and transmittance measurement.	77
8.4	Trajectory followed by the system	78
10.1	Minimum uncertainty state	83
10.2	Quantum noises associated with different quantum states. (a) Coherent state, (b) Phase quadrature squeezed state, (c) Amplitude quadrature squeezed state, (d) Arbitrary (Quadrature) squeezed state.	84
11.1	Schematic of the Optical Parametric Oscillator.	92
12.1	Variation of $\bar{\theta}_a$ and $\bar{\theta}_{a,out}$ with respect to $\bar{\theta}_{a,in}$	102
12.2	Variation of $\bar{\theta}_{a,out}$ with respect to $\bar{\theta}_{b,in}$	103
12.3	Variation of $\bar{\theta}_b$ with respect to $\bar{\theta}_{b,in}$	103
12.4	Variation of the magnitude of the intracavity field \hat{a} with respect to $\bar{\theta}_{a,in}$ and $\bar{\theta}_{b,in}$	104

12.5	Variation of gain $ \hat{A}_{out} ^2/ \hat{A}_{in} ^2$ and $ \hat{B}_{out} ^2/ \hat{B}_{in} ^2$	105
12.6	Variation of the gain $ \hat{A}_{out} ^2/ \hat{A}_{in} ^2$ of the fundamental output field with respect to $\theta_{a,in}$ for different $\chi^{(2)}$	106
12.7	Variation of the parametric gain $ \hat{A}_{out} ^2/ \hat{A}_{in} ^2$ of the fundamental field (in dB) with respect to $\chi^{(2)}$	107
12.8	Variation of the gain $ \hat{A}_{out} ^2/ \hat{A}_{in} ^2$ with $\bar{\theta}_{a,in}$ and $\bar{\theta}_{b,in}$	108
12.9	Representation of phase sensitive squeezing.	109
13.1	Set-up used for the standard quantum noise limit determination.	112
13.2	Variance of the filtered controlled variable \tilde{z}	114
13.3	Variance of the controlled variable using approximate static equations	117
13.4	Block diagram of system interconnections.	118
13.5	Variance of filtered controlled variable under open-loop and closed-loop conditions with quantum noise only.	123
13.6	Variance of filtered controlled variable under open-loop and closed-loop conditions with quantum and classical noises.	124
14.1	Schematic for control of an Optical Parametric Oscillator	128
14.2	System interconnections used for LQG Controller Design.	129
14.3	Bode plot of the LQG controller.	131
14.4	Bode plot of the loop gain transfer function.	132
14.5	Simulink block diagram used for simulation of the LQG controller.	133
14.6	Quantum noise limit ($\chi^{(2)} = 0$) and squeezed quantum noise limit ($\chi^{(2)} = 0.03$).	134
14.7	Laser phase noise w_1 and control signal u	135
14.8	The uncontrolled and controlled variable \tilde{z}	135
14.9	Variance of \tilde{z} versus measurement angle θ	136
15.1	System interconnections for integral LQG controller design.	138
15.2	Integral LQG controller design configuration.	140
15.3	Bode plot of the Integral LQG controller.	143
15.4	Bode plot of the loop gain transfer function.	144
15.5	Simulink block diagram used for simulation of the Integral LQG controller.	144
15.6	Laser phase noise w_1 and control signal u	145
15.7	Mirror position.	145
15.8	The uncontrolled and controlled variable \tilde{z}	146
16.1	Schematic of the proposed multivariable controller for the Optical Parametric Oscillator.	149
16.2	Multivariable controller design configuration.	152
16.3	Bode plots of the multivariable LQG controller.	156

16.4	Simulink block diagram used for the multivariable controller simulation	157
16.5	Laser phase noise 1 and the corresponding control signal u_1	157
16.6	Laser phase noise 2 and the corresponding control signal u_2	158
16.7	Error signals e_1 and e_2	158
16.8	Mirror positions 1 and 2.	159
16.9	The uncontrolled and controlled variable \tilde{z}	159

List of Tables

4.1	LQG Controller Design Parameter Values	46
6.1	Optical Cavity Model and Sensor Parameter Values	63
7.1	Time-Varying LQG Controller Design Parameters.	74
8.1	Measurement Noise Bounds	75
12.1	Optical Parametric Oscillator Model Parameter Values.	98
13.1	Laser Noise Model and Controller Design Parameters	121
14.1	Piezoelectric Actuator and OPO Model Parameters used for LQG Controller Design.	130
15.1	Piezoelectric Actuator and OPO Model Parameters used for Inte- gral LQG Controller Design.	142
16.1	Piezoelectric Actuators and OPO Model Parameters used for Mul- tivariable LQG Controller Design.	154
16.2	Design Parameters used for the Multivariable LQG Controller. . .	155

Part I

Frequency Locking of an Optical Resonant Cavity

Chapter 1

Introduction

In many high precision applications of quantum optics, it is required to have lasers and optical cavities with resonant frequencies that are locked to each other. Applications range from precision measurement, laser cooling, interferometric gravitational wave detectors, atomic interferometry, high-resolution spectroscopy, high-performance atomic clocks and Bose-Einstein condensate experiments, among others. For a laser and an optical cavity to remain locked and at resonance, feedback is necessary. The laser frequency tends to drift with time while the length of the optical cavity changes due to external factors. Usually, either the length of the laser resonator or that of the optical cavity is continuously adjusted, and the uncontrolled cavity is taken as the reference. For example, with the use of feedback, a dye laser can have its linewidth (see Section 2.6) reduced from the order of megahertz(MHz) to kilohertz(kHz) [5]. In some applications, where very accurate frequency locking is desired, both the laser resonator cavity and the optical cavity are controlled.

There are numerous factors that adversely affect the performance and hence the quality of a laser. The interested reader is referred to [6] for a detailed discussion which is unfortunately beyond the scope of this thesis. While the effect of some of these factors can be minimised with better design, accounting for technical imperfections and by limiting exposure to environmental conditions, other factors are simply an intrinsic part of any laser and are thus inevitable. These include temperature changes, mechanical vibration and phase drift over time. One popular and all encompassing standard used to quantify the performance of lasers in terms of frequency stability is the Allan variance; see [7–9].

Different frequency stabilisation techniques have been developed over the years to suppress laser disturbances in an effort to obtain very stable lasers. These have extended the range of practical applications of lasers which have in turn allowed predictions of the theory of quantum mechanics to be tested experimentally. In the physics literature, stabilisation techniques are usually classified in two categories in terms of those that use:

- modulation and synchronous detection,
- direct detection.

The modulation techniques usually provide better performance but at the expense of greater cost and complexity. In this introduction, we will briefly describe the different frequency stabilisation techniques used for lasers before motivating our research contribution.

1.1 Side Locking

Side locking is probably the simplest modulation-free locking technique in use. It uses a frequency sensitive optical device to generate a voltage V (proportional to the transmitted intensity) which is dependent on the laser frequency; see, e.g., [10]. If we wish to lock the laser frequency at a given frequency ω_o , then we determine the error signal generated by

$$e = V(\omega) - V(\omega_0) \quad (1.1)$$

and we use this error signal to drive the laser and in turn reduce the error signal to zero. The setup for this approach is as shown in Figure 1.1. It is assumed

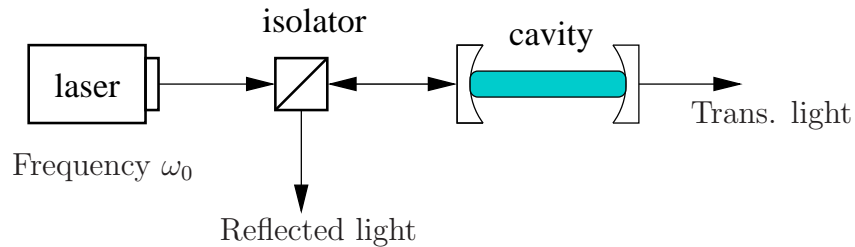


Figure 1.1: System setup used for frequency locking

here that the chosen frequency ω_0 is close to the resonant frequency of the laser such that some light is transmitted and small deviations about this frequency will cause proportional changes in the generated voltage used to drive the laser. However, there are a few problems associated with this method:

1. The laser intensity and hence the generated voltage is symmetric about the resonant frequency; see Figure 1.2. A linear control scheme therefore cannot

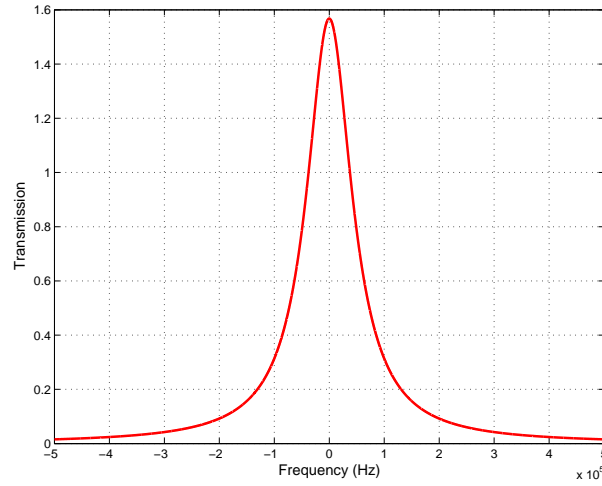


Figure 1.2: Variation of transmitted intensity with frequency of incident laser beam

bring the system back onto resonance on the basis of that measurement only, as it will be unclear whether the frequency needs to be increased or decreased. It must be clear beforehand on which side of resonance the system is operating.

2. Given that the method can work only on one side of resonance, we cannot lock the laser to the peak of resonance (where $dV/d\omega = 0$), which is more often than not desirable.
3. The method is sensitive to variations in intensity of the laser. In other words, the system cannot differentiate between fluctuations in frequency and fluctuations in the intensity of the laser itself, thus locking it to an undesirable frequency. Here, it must be mentioned that efforts have been made to control the laser intensity separately with some success (see [11]),

and that more recently, work was done to make this technique partially insensitive to laser intensity; see, e.g., [12].

1.2 Dither Locking

To decouple frequency variation and intensity variation, it is proposed that the reflected intensity be used instead of the transmitted intensity. In this way, the reflected intensity is maintained at zero and thus the system becomes insensitive to variation of laser intensity; see Figure 1.3. The problem remains though that

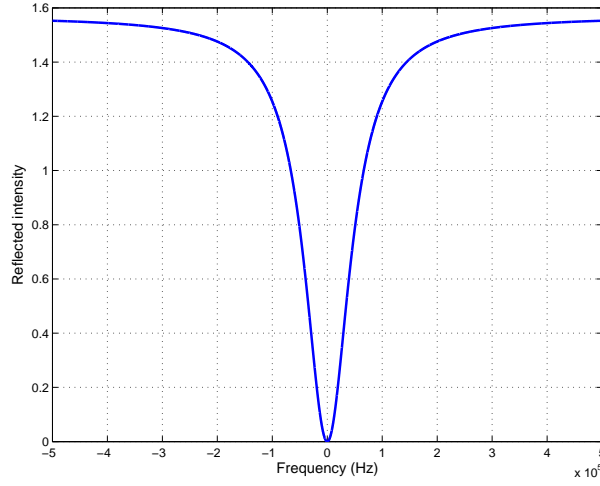


Figure 1.3: Variation of reflected intensity with frequency of incident laser beam

the signal from the reflected intensity is also symmetric about resonance. However, if the derivative of this signal is used, then it is clear which side of resonance the system is. The derivative can be determined by dithering the frequency a small amount and then measuring the reflected intensity. The reflected intensity will be 180° out of the phase with the frequency below resonance since the derivative is negative. Above resonance, the two will be in phase and at resonance, a small frequency variation will not result in any change in the reflected intensity. The variation of the error signal as a function of frequency is shown in Figure 1.4.

Clearly, to achieve locking using the error signal in Figure 1.4 would require that we operate close to resonance; i.e., in the linear portion of the curve. For the case considered in Figure 1.4, the capture region extends up to $\pm 0.1\%$ of the free spectral range (FSR) (see Section 2.6). Also, it is worthwhile noting that the

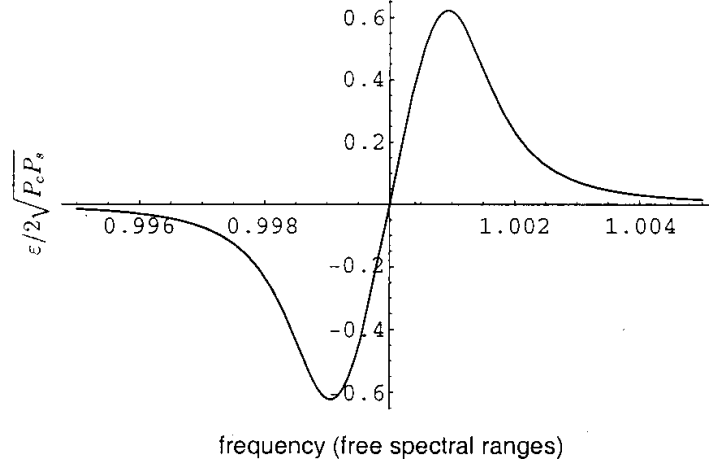


Figure 1.4: Error signal with low modulation frequency. (Courtesy of [3])

error signal approaches zero very quickly once the system is operating outside the linear region. Moreover, to obtain the error signal in Figure 1.4, the rate at which the frequency of the laser is dithered cannot be too fast or the cavity will not have enough time to settle down, in which case the relationship between the reflected intensity and frequency will not be valid. In practise, this would mean a modulation frequency of the order of 10-100 kHz. The bandwidth of the control system in turn needs to be much less than the dithering frequency and could thus be too restricted to be of use for practical applications. The need for fast control resulted in the development of the Pound-Drever-Hall (PDH) technique, as described next.

1.3 Pound-Drever-Hall technique

When the dithering (modulation) frequency is increased such that it is as much as or even greater than the laser frequency deviation, it is found (rather surprisingly perhaps) that the approach described previously still works; see [3]. In this case, it is the “phase quadrature” (see Section 2.4) of the reflected field that is being modulated. The phase is modulated much more rapidly than the characteristic time-scale of the optical cavity and hence the dynamics of the cavity mode remains unaffected by the modulation. Small variations of the laser frequency away from the cavity resonance then convert phase modulation on the reflected field

to amplitude modulation which is detected and demodulated. The basic layout used for Pound-Drever-Hall (PDH) locking is as shown in Figure 1.5.

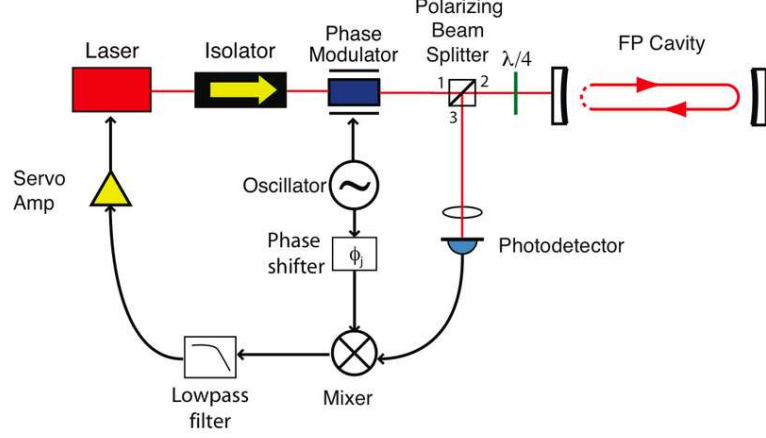


Figure 1.5: Schematic layout of a PDH laser frequency locking control loop.(Courtesy of [4])

A phase modulator driven at a frequency ω_m is placed between the laser and the optical cavity. The phase modulated light incident on the optical cavity consists of a carrier and two modulation sidebands. The magnitude of the incident electric field can be written as

$$E_{inc} = E_0 e^{i\omega t}, \quad (1.2)$$

and after modulation, it is given by

$$E_{inc} = E_0 e^{i(\omega t + \beta \sin \omega_m t)}. \quad (1.3)$$

Here, β is the modulation depth and the total power in the incident beam is denoted by $P_0 = |E_0|^2$. Using Bessel functions, this expression can be approximated as

$$\begin{aligned} E_{inc} &\approx E_0 [J_0(\beta) + 2iJ_1(\beta) \sin \omega_m t] e^{i\omega t} \\ &= E_0 [J_0(\beta) e^{i\omega t} + J_1(\beta) e^{i(\omega + \omega_m)t} - J_1(\beta) e^{i(\omega - \omega_m)t}]. \end{aligned} \quad (1.4)$$

Equation (1.4) shows clearly the presence of three beams with a carrier at frequency ω and two sidebands at frequencies $(\omega - \omega_m)$ and $(\omega + \omega_m)$ respectively.

The reflected beam is then

$$E_{ref} = E_0 \left[F(\omega) J_0(\beta) e^{i\omega t} + F(\omega + \omega_m) J_1(\beta) e^{i(\omega + \omega_m)t} - F(\omega - \omega_m) J_1(\beta) e^{i(\omega - \omega_m)t} \right]. \quad (1.5)$$

Here, $F(\omega)$ is the reflection coefficient and is the ratio of E_{ref} and E_{inc} ; see [3]. The photo-detector voltage is proportional to the power in the reflected field and the power reflected is given by

$$\begin{aligned} P_{ref} &= E_{ref}^* E_{ref} \\ &= P_0 |R(\omega)|^2 + P_0 \frac{\beta^2}{4} |R(\omega + \omega_m)|^2 + P_0 \frac{\beta^2}{4} |R(\omega - \omega_m)|^2 \\ &\quad + \frac{\beta}{2} \{ \text{Re} [R(\omega) R^*(\omega + \omega_m) - R^*(\omega) R(\omega - \omega_m)] \cos \omega_m t \\ &\quad + \text{Im} [R(\omega) R^*(\omega + \omega_m) - R^*(\omega) R(\omega - \omega_m)] \sin \omega_m t \} \\ &\quad + 2\omega_m \text{ terms.} \end{aligned} \quad (1.6)$$

We are interested in the phase of the reflected carrier from which we can then deduce which side and how far we are from the resonant frequency of the cavity. This information is available in the sine and cosine terms in (1.6) as they oscillate at the modulation frequency ω_m , thus providing us with the derivative. We isolate these two terms from the photo-detector measurement through the use of a mixer. A phase shifter is included to account for unequal delays in the signal paths such that pure sinusoidal functions are present at the mixer. This phase delay can be checked and adjusted by checking the error signal (after being low pass filtered) while scanning the optical cavity or the laser frequency. The error signal should look as shown in Figure 1.6.

After going through the mixer, the reflected signal becomes

$$\begin{aligned} P'_{ref} &= P_{ref} \cos(\omega_m t + \phi) \\ &= P_0 \beta \{ \text{Re} [R(\omega) R^*(\omega + \omega_m) - R^*(\omega) R(\omega - \omega_m)] \cos \phi \\ &\quad + \text{Im} [R(\omega) R^*(\omega + \omega_m) - R^*(\omega) R(\omega - \omega_m)] \sin \phi \} \\ &\quad + \text{other sinusoidal terms.} \end{aligned} \quad (1.7)$$

Low-pass filtering allows us to remove the sinusoidal terms and the amplitude

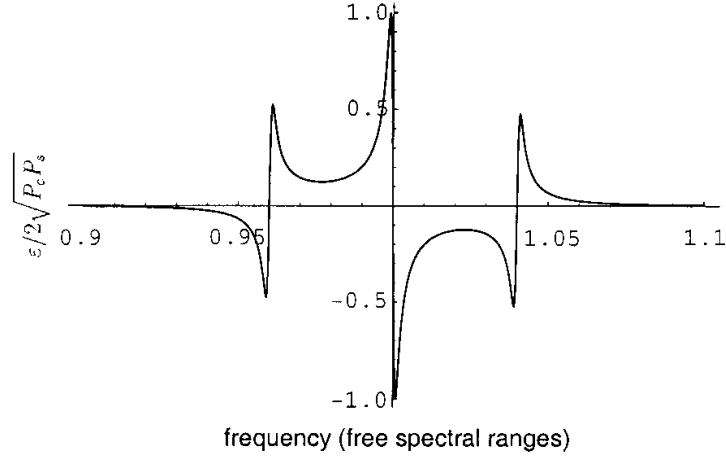


Figure 1.6: Error signal with high modulation frequency. (Courtesy of [3])

of the resulting d.c. signal provides the necessary error signal to lock the laser. It should be noted here that the linear region of operation near the resonant frequency in Figure 1.6 is again very small and that the error signal is larger in magnitude; c.f. with Figure 1.4. Moreover, the error signal is zero at frequencies other than the resonant frequency of the cavity, where there are other smaller linear regions of operation. This can result in frequency locking at frequencies other than the resonant frequency if the system is initialised/disturbed into one of these other linear regions of operation.

Recently, an attempt was made in [13] to model and to lock an external-cavity diode laser (ECDL) to an ultra-high finesse cavity in an effort to achieve levels of stability suitable for optical-frequency atomic clocks. The frequency of the laser was controlled by actuating (rotating/sliding) a grating which in turn varies the length of the cavity or changes the refractive index of the laser diode and the error signal was generated using the PDH approach. In [13], the plant and the noise models were identified using rather simple low-order systems for which a series of PID controllers were designed (using analog circuitry) and tested on the system. The controllers, whilst effective in the linear region of operation, were not the outcome of systematic design. More sophisticated controller design techniques could make better use of information gathered about the noise model allowing for the design of stable controllers which would also optimise the level of performance achieved.

1.4 Motivation

From the previous discussion, it can be noted from a control systems perspective that the frequency-locking problem has not been addressed in the most rigorous of ways. The controllers traditionally used to lock optical cavities are the outcome of ad-hoc processes and were not optimally designed. The absence of first principle models and the presence of strong nonlinearities at the sensor did not help in establishing a systematic way of approaching this problem. We aim to address this problem in two ways:

1. We initially investigate the linear problem with a view to lock an optical cavity to a laser while the system is operating in the linear region. We start by experimentally locking an optical cavity to a free running laser in our optics laboratory. For our experiment, we however do not use the Pound-Drever-Hall approach to lock our cavity. Instead, we use a homodyne detector (see Section 2.5) and use the phase quadrature (see Section 2.4) of the reflected field as the error signal. The system is first identified under closed-loop conditions with a stabilising PI controller in place. This allows us to model the overall system and in particular take into account the resonant dynamics of the piezoelectric actuator (PZT) used to control the mirror position. An LQG controller is then designed from the system model obtained from measurement data. Due to the nature of the noise present in the system, it was also necessary to include integral action in our design and this was done by introducing an integrated state in the performance criterion. Experimental results showed that the controller was effective in achieving frequency lock; see [14]. Moreover, the system could also handle small constant disturbances with the controller in place. We showed that as long as the error signal is within the capture range, the “detuning” will be reduced and the system will eventually come back to resonance; see [15]. The “detuning” or “detuning variable” refers to the difference between the laser frequency and the resonant frequency of the optical cavity. As expected however, the system would go out of lock if the applied disturbance is large enough to push it outside the “capture range”. Outside the linear region, the system will move away from resonance.
2. To resolve this problem, we propose a control algorithm that will lock the

laser frequency at a selected frequency from any given initial operating point. The capture region is then enlarged to include not only the linear region of operation of the laser-cavity system but the whole operating region. In this way, the control algorithm is also able to handle disturbances that may be large enough to push the system outside its linear region of operation. We propose a novel time-varying Kalman filtering approach together with an optimal state-feedback control law. We assume an instantaneous bounded noise model for our measurements which are now the phase quadrature of the reflected field and the transmittance of the optical cavity. The detuning variable Δ and its corresponding variance are estimated from these two noisy measurements by solving a set of quartic equations and the gain of the Kalman filter is varied accordingly. The Kalman filter is combined with a state feedback optimal control law obtained by minimizing a given cost functional, generating the overall controller. For reasons stated previously, we also include integral action in our design. Conclusive simulation results were obtained using this approach; see [16].

Chapter 2

Background

The material presented in this chapter aims to provide a brief overview of concepts and background information needed to fully appreciate future work presented in this part of the thesis. It is by no means exhaustive and the interested reader will find an excellent concise reference to the material discussed in this section in [5]. A more detailed discussion on lasers can also be found in [6].

2.1 Laser

Laser radiation is generated in a resonator cavity when the frequency of the atomic transitions of the molecules inside the cavity corresponds to the resonant frequency of the cavity. As the energy in the optical field at the resonant frequency (also called the laser mode) increases, the probability of atomic transitions in that particular mode, a process known as stimulated emission, also increases. This process continues exponentially until the cavity saturates and nonlinear effects come into play with the losses in the system balancing out the gain. When the cavity saturates, the laser achieves steady continuous wave operation. From a control perspective, the laser can be viewed to operate using feedback, feeding part of the light, in phase, back to the input. The gain is provided by an external source (commonly known as the pump) through the excitation of atoms or molecules. In this way, the laser behaves much like an electronic circuit and is usually termed an optical oscillator. To summarise, two conditions are necessary for lasing to occur:

1. The gain must be greater than the loss in the feedback system;

2. The total phase in a single round trip must be an integer multiple of 2π to provide phase matching (see, e.g., [17]) to the feedback signal.

The cavity properties and the gain profile (see, e.g., [6]) determine the frequency distribution of the laser output. In our case, we shall only consider the “homogeneous” profile whereby the spectral modes compete with each other and the output spectrum consists of a single dominant spectral mode. This single laser mode has an associated bandwidth which is a measure of the size of frequency fluctuations. The frequency variations are not primarily determined in practice by quantum mechanical fluctuations but rather by technical imperfections, temperature variation, mechanical vibration, electrical and acoustic noise, among other sources. The frequency of lasers can vary greatly over time as a result. Moreover, the phase also drifts uncontrollably over a long period of time, a process known as phase diffusion. These features of lasers make the frequency locking problem of a cavity especially challenging.

2.2 Coherent States

A light bulb radiates light in a continuum of modes. In a laser, however, light is emitted into a resonant mode and that mode is highly coherent. By coherent, it is meant here that if two detectors are placed apart in space, or in time, the amplitude at the two points will be in phase and will fluctuate in the same way. In practise, any source of light has an associated coherence length and coherent time. Laser light is idealised as a coherent state $|\alpha\rangle$ and is a minimum uncertainty quantum state, i.e., it has the minimal product of the amplitude and phase quadrature uncertainties; see Section 2.4. $|\cdot\rangle$ represents the state of a quantum mechanical system in a separable Hilbert space and uses Dirac’s notation. It is defined as the eigenstate of the annihilation operator \hat{a} , i.e.,

$$\hat{a}|\alpha\rangle = \alpha|\alpha\rangle. \quad (2.1)$$

Here, α is complex and can be represented as

$$\alpha = |\alpha|e^{i\theta},$$

where $|\alpha|$ and θ are the amplitude and phase of the state respectively. The annihilation operator \hat{a} lowers the excitation level of a system (by one). Similarly, the creation operator raises the excitation level; see [18].

2.3 Quantum Noise

Due to the quantum nature of light, quantum noise is of great interest in quantum optics. It is an intrinsic property of lasers and any measurement of the properties of light (amplitude, phase or intensity) is limited by quantum noise.

Its origin can be explained using the Heisenberg uncertainty principle (see [19]) and the associated operators used to describe the light field. From a more experimental point of view however, it can be explained by viewing the natural state of light as a stream of photons whose arrival times at a photodetector are statistically modelled using a Poisson distribution. The photo-current measured by the detector will then show features of this Poissonian distribution. Moreover, the magnitude of the noise is strongly linked to the intensity of light (number of photons) detected. Quantum noise is an unavoidable source of noise and quantum experiments conducted under optimal conditions with all other sources of noise (electronic noise due to the detector, amplifiers, etc. and technical noises due to light source instabilities, gas fluctuations, etc.) eliminated, are still restricted by what is known as the “quantum noise limit” (QNL).

Quantum noise is frequency independent at different time instances and can be conveniently classified as white noise for control purposes.

2.4 Quadratures

Given certain assumptions about the spatial modes, an electromagnetic wave can be described by the complex amplitude

$$\alpha = \alpha_0 e^{i\phi}; \quad (2.2)$$

with magnitude α_0 and phase ϕ .

The quadrature values X^+ and X^- provide an alternative description of electromagnetic waves which is particularly useful for distinguishing between relative

and absolute phase; see [5]. The quadrature values are defined as:

$$X^+ = \alpha + \alpha^*; \quad (2.3a)$$

$$X^- = i(\alpha^* - \alpha). \quad (2.3b)$$

When electromagnetic waves have fluctuations in their amplitude and phase, these variations can in turn be described in terms of the quadratures as follows:

$$\alpha(t) = \alpha + \delta X^+(t) + i\delta X^-(t). \quad (2.4)$$

In the limit when $\alpha \gg \delta X^+$, it can be shown that δX^+ and δX^- correspond to changes in the amplitude and phase of the wave respectively; see [5]. X^+ is usually referred to as the “amplitude quadrature” and X^- as the “phase quadrature” in the physics literature.

2.5 Homodyne Detection

Homodyne detection is a method of measuring frequency-modulated radiation by nonlinear mixing with radiation of a reference frequency. When the reference frequency is derived from the same source as the signal, the method of detection is called “homodyne”. Alternatively, if the reference frequency (also referred to as local oscillator) is frequency shifted, the detection method is known as “heterodyne”. Homodyne detection has the advantage of being insensitive to variations in the frequency of the laser. In this scheme, the laser beam is split into two parts, one of which then acts as the reference signal and the other beam is sent to the system to be probed. The laser beam is split to allow for determination of the phase and amplitude quadratures which direct detection will not permit. A schematic of the homodyne detection set-up is shown in Figure 2.1.

Mirror M_1 has a 95/5 reflectivity and mirrors M_2 and M_3 are fully reflecting. M_4 has a balanced 50/50 reflectivity and combines the two beams α_{in} and α_{lo} . The phase shifter is used to control the relative phase difference between the local oscillator beam and the input beam. In practise, this can be done by rotating a glass plate in the local oscillator beam. The photo-detectors D_1 and D_2 convert the optical interference signals into electrical currents. The two beams can be

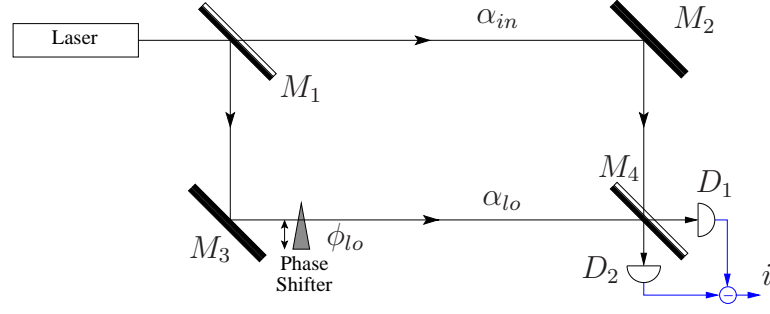


Figure 2.1: Homodyne detector

represented as

$$\alpha_{in}(t) = \alpha_{in} + \delta X_{in}^+(t) + i\delta X_{in}^-(t); \quad (2.5a)$$

$$\alpha_{lo}(t) = [\alpha_{lo} + \delta X_{lo}^+(t) + i\delta X_{lo}^-(t)] e^{i\phi_{lo}}. \quad (2.5b)$$

Provided the intensity of the local oscillator is far more intense than the input beam, the current generated by the two detectors is given by (see, e.g., [5]):

$$i(t) \approx 2\alpha_{lo}(\delta X_{in}^+(t) \cos \phi_{lo} + i\delta X_{in}^-(t) \sin \phi_{lo}). \quad (2.6)$$

This scheme allows for the complete suppression of noise from the local oscillator and the current is unaffected by the power of the input beam, as long as it is well below that of the local oscillator. Furthermore, by choosing suitable values for ϕ_{lo} , the variance in specific quadratures (or along any projection angle) can be measured.

2.6 Fabry-Perot Cavity

Fabry-Perot cavities have been widely used even before the advent of lasers. They are formed by two partially transmitting mirrors facing each other and which are spaced apart by distances large compared to the size of the mirrors. The mirrors are curved such that the desired optical modes (transverse modes) set-up inside the cavity are well-defined with smooth and regular transverse patterns resembling Hermite-Gaussian cross-sections; see [6]. They also reduce leakage and diffraction losses out of the open-sides of the cavity or past the edges of

the finite-diameter mirrors. The two waves travelling in the forward and reverse direction in a Fabry-Perot cavity set up an optical standing-wave which has a periodic spatial variation along the axis with a period equal to one-half the optical wavelength. Depending on the length of the cavity, the plane waves propagating inside the cavity can interact constructively resulting in stable optical modes and in a resonant mode, or destructively giving rise to unstable optical modes; see, e.g., [6, 20]. Thus, a Fabry-Perot interferometer can act like a filter as light can only pass through it if twice the length of the cavity is equal to an integer number of wavelengths of the light.

In practise, multiple frequencies are present inside a Fabry-Perot cavity, setting up their own standing waves and distorting the characteristics of the desired standing-wave. The desired standing-wave is (usually) the lowest-order transverse mode of the cavity which has the lowest leakage and diffraction losses. With the proper use of lenses and other mode-matching optics (see [21]), an optical cavity can be excited in just one of its transverse modes although in practise, the field patterns can only approximate ideal plane waves. As such, in this work, we will ignore the effect of these other modes in our analysis of the cavity, and will consider variations of the fields only along z direction. The set-up of the standing waves do not happen instantaneously as it requires the interference of waves which have travelled the entire length of the cavity and back. The time it takes to achieve a steady-state is denoted as t_{cav} and this also determines the decay rate of the cavity in the absence of an incident light field. The cavity “linewidth” is defined as

$$\gamma = 1/t_{cav} \text{ (Hz)}. \quad (2.7)$$

Frequencies larger than γ present in the incident field will be reflected. Fabry-Perot cavities, if aligned properly, can have sharp resonances at specific optical frequencies. They have thus been widely used as passband filters, used for measuring the frequency spectrum of particularly narrow optical lines, such as laser beams. The cavity resonance frequencies are equally spaced and we define the “free spectral range” (FSR) as the difference between two adjacent resonance frequencies:

$$\text{FSR} = c/2L \text{ (Hz)}. \quad (2.8)$$

Here c is the speed of light and $2L$ is the optical path length for one round trip

through the cavity. In the case of a linear cavity, $L = nd$, where n is the refractive index of the material inside the cavity and d is the physical separation between the two mirrors. Finally, the “finesse” of an optical cavity is defined as

$$F = \text{FSR}/\gamma. \quad (2.9)$$

Cavities with high finesse have sharp transmission peaks but are more difficult to stabilise.

Chapter 3

Cavity Modelling and Identification of the Overall System

We first describe in detail the experimental set-up and derive a model of the cavity system which will be investigated from first principles. This model is however inadequate for the design of an appropriate controller as the dynamics responsible for the actuation mechanism are not taken into account. Moreover, the exact parameter values of the optical system are hard to determine experimentally. For these reasons, we resort to the determination of the overall system model by gathering frequency domain data and then using a subspace identification method as described in [22].

Our aim as described previously is to frequency lock an optical cavity to a free running laser. The resonant frequency of an optical cavity depends upon its optical path length, as explained in Section 2.6. We modify the optical path length by controlling a piezoelectric actuator attached to one of the mirrors of the cavity. In this way, the piezoelectric actuator regulates the error between the laser frequency and the natural frequency of the cavity. This error is also known as the “detuning variable” and is denoted by Δ .

3.1 Schematic of Experimental Set-Up

Figure 3.1 shows a photograph of the experimental set-up taken in our quantum optics laboratory. The laser as well as the optical cavity are highlighted. Also, quantum optical components such as mirrors, beam-splitters can be seen. The control signal is applied to the mirror which is furthest from the laser (in the optical beam path). A PZT is attached to the mirror and the wiring leading to the PZT from a high-voltage amplifier can also be seen in the picture.

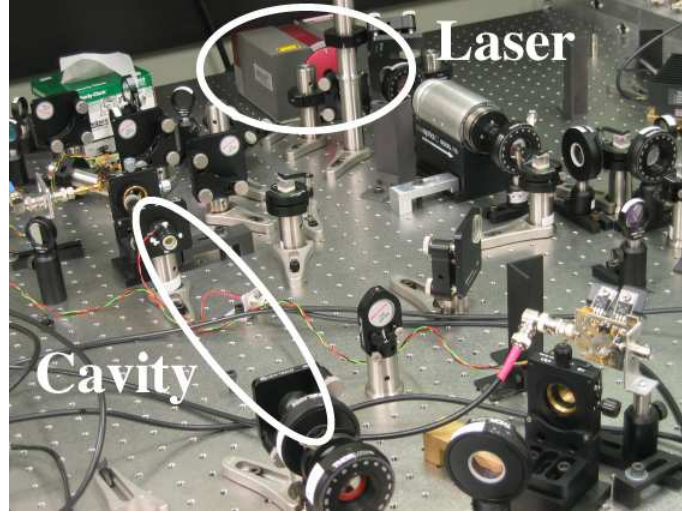


Figure 3.1: Photograph of the frequency locking set-up in our quantum optics laboratory.

A schematic of the experimental set-up given in Figure 3.2 shows in more detail the optical components used in our system. The specifications of the optical elements as well as the PZT are described next. Approximately 1 mW of the 1064 nm, single-mode output of a diode-laser pumped, miniature monolithic Nd:YAG laser operating at 235 mW, is used as the input to the linear cavity. Both mirrors of the linear cavity have 98 % reflectivity, with the input coupler (the mirror closest to the laser) being plane, the output coupler having a 300 mm radius of curvature and the mirrors being separated by a nominal 200 mm. Such a cavity has a free-spectral range of 750 MHz, a finesse of approximately 150 and a waist of approximately 220 microns, located at the input coupler to the cavity; see [6, 21]. The waist size is a measure of mismatch between the laser beam and the cavity, which can result in the coupling of transverse modes rather

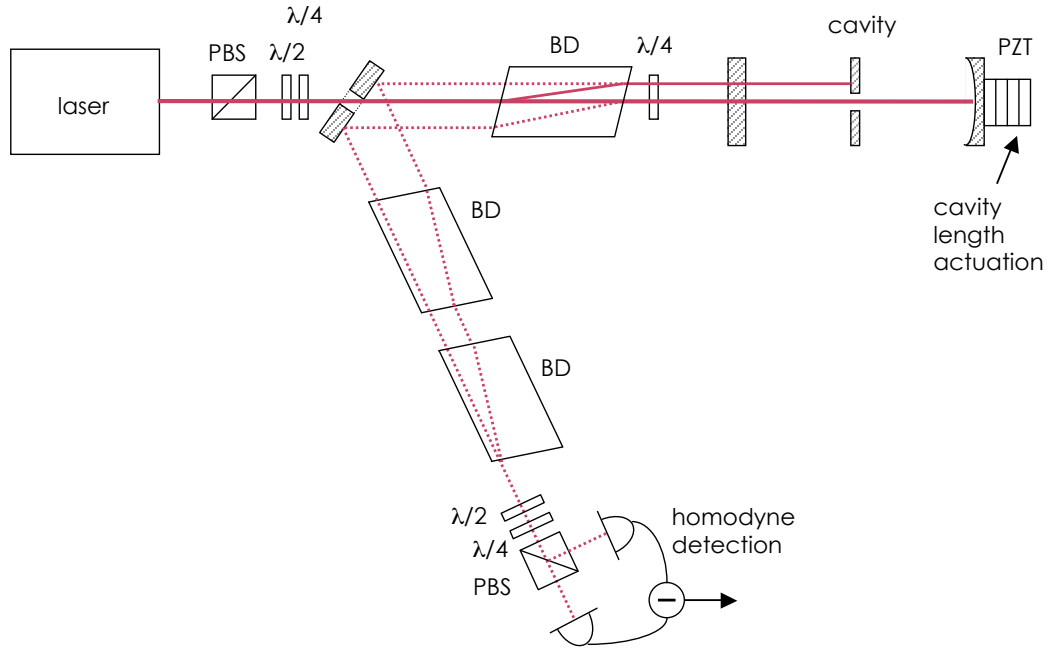


Figure 3.2: Detailed schematic of the experimental set-up.

than the fundamental longitudinal mode; see [23] for more details. In Figure 3.2, BD stands for beam displacer, $\lambda/2$ and $\lambda/4$ stands for half-wave plates and quarter-wave plates respectively and PBS for polarising beam-splitter. Also, the dashed lines represent the reflected field from the cavity.

The field reflected from the optical cavity is extracted via an optical circulator. The circulator is implemented by a mirror with a 2 mm aperture in its centre, a calcite beam displacer and a quarter-wave plate placed immediately prior to the input coupler of the cavity. This arrangement is used as it provides a co-propagating, and hence automatically phase-locked, local oscillator for the homodyne detection system; see [24]. The fringe visibility of the homodyne detection system is measured to be greater than 98 %. Less than 5 % of power is measured in higher-order modes of the cavity. The length of the cavity, and hence its resonant frequency, is actuated via a tubular piezoelectric transducer with a stroke of 10 microns when the maximum 500 V is applied.

The system illustrated in Figure 3.2 is referred to as the “plant” with the homodyne detector output being the measurement signal y and the input voltage applied to the high-voltage amplifier driving the PZT being the control signal u .

3.2 Cavity Model

A schematic of the frequency stabilisation system is depicted in Figure 3.3. The

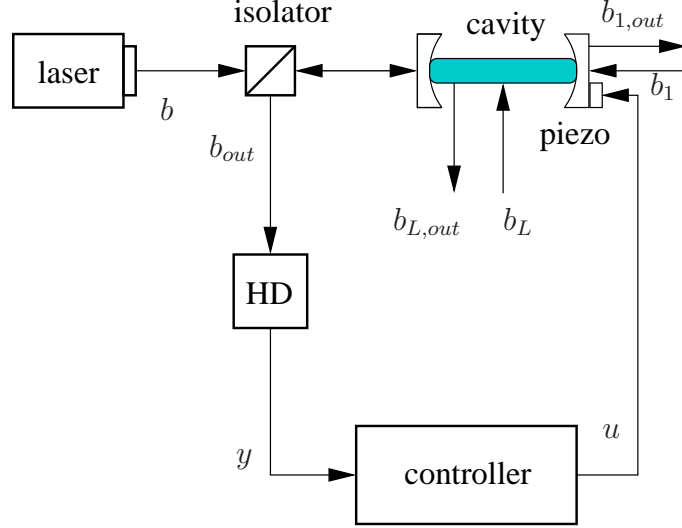


Figure 3.3: Cavity locking feedback control loop.

laser mode b of frequency ω_0 is modelled by a boson field $b = \beta + b_0$ where β is a real number (without loss of generality) and b_0 is a vacuum field, a standard quantum Gaussian white noise with unit variance; see [25]. b is also usually represented in Dirac's notation as a coherent state $|\beta\rangle$. The cavity is also coupled to two other optical fields: a transmitted mode b_1 , and a loss mode b_L .

The cavity can be described in the Heisenberg picture by the following quantum stochastic differential equations; e.g., see [5, 25]:

$$\dot{a} = -\left(\frac{\kappa}{2} - i\Delta\right)a - \sqrt{\kappa_0}(\beta + b_0) - \sqrt{\kappa_1}b_1 - \sqrt{\kappa_L}b_L; \quad (3.1a)$$

$$b_{out} = \sqrt{\kappa_0}a + \beta + b_0. \quad (3.1b)$$

Here, the annihilation operator for the cavity mode is denoted by a and the annihilation operator for the coherent input mode is denoted by $b = \beta + b_0$, both defined in an appropriate rotating reference frame (see [26]), where b_0 is quantum noise. We write

$$\kappa = \kappa_0 + \kappa_1 + \kappa_L; \quad (3.2)$$

where κ represents the decay rate of the cavity and is usually measured in

hertz(Hz). κ_0 quantifies the coupling strength of the field b_0 to the cavity. Similarly, κ_1 and κ_L quantify the strength of the couplings of the optical fields b_1 and b_L to the cavity respectively.

The input to the cavity is taken to be a coherent state with amplitude β which is assumed to be real. The assumption of a coherent state is well-justified since homodyne detection cancels out any common-mode quadrature amplitude and phase variations in the laser. Δ denotes the frequency detuning between the laser frequency and the resonant frequency of the cavity. The objective of the frequency stabilisation scheme is to maintain $\Delta = 0$. The detuning is given by

$$\Delta = f_c - f_L = q \frac{c}{nL} - f_L, \quad (3.3)$$

where f_c is the resonant frequency of the cavity, f_L is the laser frequency, nL is the optical path length of the cavity, c is the speed of light in a vacuum and q is a large integer indicating that the q^{th} longitudinal cavity mode is being excited.

The cavity locking problem is formally a nonlinear control problem since the equations governing the cavity dynamics in (3.1b) contain the nonlinear product term Δa . In order to apply linear optimal control techniques, we need to linearise these equations about the zero-detuning point. Let α denote the steady state average of a when $\Delta = 0$ such that $a = \alpha + \tilde{a}$. The perturbation operator \tilde{a} satisfies the linear quantum stochastic differential equation (neglecting higher order terms)

$$\dot{\tilde{a}} = -\frac{\kappa}{2}\tilde{a} + i\Delta\alpha - \sqrt{\kappa_0}b_0 - \sqrt{\kappa_1}b_1 - \sqrt{\kappa_L}b_L. \quad (3.4)$$

The perturbed output field operator \tilde{b}_{out} is given by

$$\tilde{b}_{out} = \sqrt{\kappa_0}\tilde{a} + b_0; \quad (3.5)$$

which implies $b_{out} = \sqrt{\kappa_0}\alpha + \beta + \tilde{b}_{out}$.

We model the measurement of the X_ϕ quadrature of \tilde{b}_{out} with homodyne detection (see Section 2.5) by changing the coupling operator for the laser mode to $\sqrt{\kappa_0}e^{-i\phi}a$, and measuring the real quadrature of the resulting field. The measurement signal is then given by

$$\tilde{y} = \tilde{b}_{out} + \tilde{b}_{out}^\dagger = \sqrt{\kappa_0}(e^{-i\phi}\tilde{a} + e^{i\phi}\tilde{a}^\dagger) + q_0; \quad (3.6)$$

where $q_0 = b_0 + b_0^\dagger$ is the intensity noise in the input coherent state.

If we define the quadratures $\tilde{q} = \tilde{a} + \tilde{a}^\dagger$ and $\tilde{p} = i(\tilde{a}^\dagger - \tilde{a})$, then the cavity dynamics and homodyne measurement are expressed in state-space form in terms of the quadratures of the operators \tilde{a}, b_0, b_1, b_L as

$$\begin{bmatrix} \dot{\tilde{q}} \\ \dot{\tilde{p}} \end{bmatrix} = \begin{bmatrix} -\frac{\kappa}{2} & 0 \\ 0 & -\frac{\kappa}{2} \end{bmatrix} \begin{bmatrix} \tilde{q} \\ \tilde{p} \end{bmatrix} + \begin{bmatrix} 0 \\ 2\alpha \end{bmatrix} \Delta - \sqrt{\kappa_0} \begin{bmatrix} \cos \phi & -\sin \phi \\ \sin \phi & \cos \phi \end{bmatrix} \begin{bmatrix} q_0 \\ p_0 \end{bmatrix} \\ - \sqrt{\kappa_1} \begin{bmatrix} 1 & 0 \\ 0 & 1 \end{bmatrix} \begin{bmatrix} q_1 \\ p_1 \end{bmatrix} - \sqrt{\kappa_L} \begin{bmatrix} 1 & 0 \\ 0 & 1 \end{bmatrix} \begin{bmatrix} q_L \\ p_L \end{bmatrix}; \quad (3.7a)$$

$$y = k_2 \sqrt{\kappa_0} \begin{bmatrix} \cos \phi & \sin \phi \end{bmatrix} \begin{bmatrix} \tilde{q} \\ \tilde{p} \end{bmatrix} + k_2 \begin{bmatrix} 1 & 0 \end{bmatrix} \begin{bmatrix} q_0 \\ p_0 \end{bmatrix} + w_2; \quad (3.7b)$$

with noise quadratures $q_j = b_j + b_j^\dagger$, $p_j = -i(q_j - p_j^\dagger)$, for $j = 0, 1, L$ (all standard Gaussian white noises). Here, y is the homodyne detector output in which we have included an electronic noise term w_2 . Also, k_2 represents the trans-impedance gain of the homodyne detector, including the photodetector quantum efficiency.

3.3 Subspace System Identification

The state-space model of the cavity given in (3.7b) is incomplete as it does not include an explicit model, including the actuation mechanism, for the dynamics of the detuning, Δ . The dynamics of the detuning and actuation mechanism are sufficiently complex that direct measurement is a more experimentally reasonable approach than *a priori* modelling of the system.

We use a system identification method to determine a state-space model for the system from gathered input-output frequency response data. The method of system identification which is applied here is the frequency domain subspace system identification method; see, e.g., [27] for more details. We now provide a brief overview of the subspace system identification method.

The frequency domain subspace system identification method enables the model system matrices A , B , C and D to be constructed from measurements of the system frequency response. The transfer function of the system is given by $G(s) = C(sI - A)^{-1}B + D$ and the measured frequency response data is assumed to take the form of a set of noisy measurements of this transfer function evaluated

at a range of frequency points:

$$G_k = G(j\omega_k) + n_k, \quad k = 1, 2, \dots, N. \quad (3.8)$$

In practise, the measured frequency response data can be obtained using an instrument such as a swept sine digital signal analyser. The frequency domain subspace system identification method is a non-iterative method of constructing the state space matrices A , B and C from the frequency response data G_k , $k = 1, 2, \dots, N$.

The subspace system identification method is based on the realisation theory of [28] and [29] which involves constructing a state space model using impulse response data. This approach was generalised to allow for general time domain input-output data in the papers [30, 31] and the resulting system identification method is referred to as the time domain subspace method. A frequency domain counterpart to this approach was first proposed in [32] and the actual algorithm we implement is based on the more recent paper [22]. Two algorithms are presented in [22] for the case when frequency domain data is available at uniformly and non-uniformly spaced intervals respectively. The algorithms work by first solving for the matrices \check{A} and \check{C} algebraically and then solving for \check{B} and \check{D} using a least-squares approach for the discrete system G . Controller design can then be directly carried out using suitable discrete-time control design techniques or alternatively, the discrete-time system model can be converted to a continuous-time system model before controller design is performed. In our case, this is the approach we choose and we use the bilinear transformation method (see [33]) to obtain the continuous-time state-space matrices A , B , C and D .

The subspace identification method delivers minimal state-space mathematical models and is fast compared to methods such as the iterative prediction error methods used in the classical system identification problem. Subspace identification algorithms are particularly suited for highly resonant and/or flexible structures which are infinite dimensional and require high-order models. This feature makes this method suitable for our application which includes a piezoelectric actuator coupled to the cavity mirror. The frequency domain version of the subspace identification method also allows data from different runs of the experiment to be easily combined in the frequency domain. Moreover, the algorithm we use accommodates arbitrary frequency spacing, and is guaranteed to

exactly estimate any finite-dimensional transfer function, given a finite amount of data (depending on the model order). A detailed discussion of the theory and algorithms can be found in [27], [34] and the references therein.

We now outline the main steps in the frequency domain subspace system identification method of [22]. The first step is to convert the continuous time frequency domain data (3.8) into frequency domain data for a corresponding discrete time system via a bilinear transformation:

$$\check{G}_k = G_k, \quad k = 1, 2, \dots, N; \quad (3.9a)$$

$$\check{\omega}_k = 2 \tan^{-1} \left(\frac{\omega_k T}{2} \right), \quad k = 1, 2, \dots, N. \quad (3.9b)$$

This operation, which involves simply scaling the frequency values, is carried out because direct application of the subspace method to the continuous-time frequency response data would lead to severe numerical problems; see [35]. The scaling “time constant” T is typically chosen to be the reciprocal of the maximum frequency of the available frequency response data: $T = \frac{2\pi}{\omega_N}$.

The next step is to use the discrete time frequency response data to construct the matrices

$$\mathcal{G} = \frac{1}{\sqrt{N}} \begin{bmatrix} \check{G}_1 & \check{G}_2 & \dots & \check{G}_N \\ e^{j\check{\omega}_1} \check{G}_1 & e^{j\check{\omega}_2} \check{G}_2 & \dots & e^{j\check{\omega}_N} \check{G}_N \\ e^{j2\check{\omega}_1} \check{G}_1 & e^{j2\check{\omega}_2} \check{G}_2 & \dots & e^{j2\check{\omega}_N} \check{G}_N \\ \vdots & \vdots & \ddots & \vdots \\ e^{j(q-1)\check{\omega}_1} \check{G}_1 & e^{j(q-1)\check{\omega}_2} \check{G}_2 & \dots & e^{j(q-1)\check{\omega}_N} \check{G}_N \end{bmatrix}; \quad (3.10a)$$

$$\mathcal{W} = \frac{1}{\sqrt{N}} \begin{bmatrix} I & I & \dots & I \\ e^{j\check{\omega}_1} I & e^{j\check{\omega}_2} I & \dots & e^{j\check{\omega}_N} I \\ e^{j2\check{\omega}_1} I & e^{j2\check{\omega}_2} I & \dots & e^{j2\check{\omega}_N} I \\ \vdots & \vdots & \ddots & \vdots \\ e^{j(q-1)\check{\omega}_1} I & e^{j(q-1)\check{\omega}_2} I & \dots & e^{j(q-1)\check{\omega}_N} I \end{bmatrix}. \quad (3.10b)$$

We then use QR factorisation to determine R_{22} :

$$\begin{bmatrix} \text{Re } \mathcal{W} & \text{Im } \mathcal{W} \\ \text{Re } \mathcal{G} & \text{Im } \mathcal{G} \end{bmatrix} = \begin{bmatrix} R_{11} & 0 \\ R_{21} & R_{22} \end{bmatrix} \begin{bmatrix} Q_1^T \\ Q_2^T \end{bmatrix}. \quad (3.11)$$

To obtain suitable and consistent estimates, the method in [22] also requires *a priori* information about the noise covariance present in the measurement data. We use the noise information to weight the measurement data and construct a matrix \mathbf{K} using Cholesky factorisation. This matrix is then used to calculate the singular value decomposition:

$$\mathbf{K}^{-1}R_{22} = \begin{bmatrix} U_s & U_o \end{bmatrix} \begin{bmatrix} \Sigma_s & 0 \\ 0 & \Sigma_o \end{bmatrix} \begin{bmatrix} V_s \\ V_o \end{bmatrix}. \quad (3.12)$$

The system order n is determined by inspecting the singular values of Σ_s and Σ_o . The largest singular value of Σ_o should be significantly smaller than the n^{th} singular value of Σ_s . From these, the matrices \check{A} and \check{C} for the discrete time state space model can be easily constructed; see [22]. Then, the matrices \check{B} and \check{D} from the discrete time state space model are computed by solving the least squares problem:

$$\min_{\check{B}, \check{D}} \sum_{k=1}^N \|\check{G}_k - \check{D} - \check{C} (e^{j\omega_k} I - \check{A})^{-1} \check{B}\|_F^2; \quad (3.13)$$

where the notation $\|\cdot\|_F$ denotes the matrix Frobenius norm. Finally, the required continuous time state space matrices are constructed according to the bilinear transformation formulae:

$$A = \frac{2}{T} (I + \check{A})^{-1} (\check{A} - I); \quad (3.14a)$$

$$B = \frac{2}{\sqrt{T}} (I + \check{A})^{-1} \check{B}; \quad (3.14b)$$

$$C = \frac{2}{\sqrt{T}} \check{C} (I + \check{A})^{-1}; \quad (3.14c)$$

$$D = \check{D} - \check{C} (I + \check{A})^{-1} \check{B}. \quad (3.14d)$$

3.4 Subspace Identification of the cavity system

The transfer function of the cavity and measurement system described in Section 3.2 (or alternatively the “plant”) is identified under closed-loop conditions. The error signal is linear over a very narrow region near equilibrium and since the typical noise would perturb the system into the nonlinear region, it is neces-

sary to use feedback to minimise the effect of noise and maintain the system in the linear region while collecting data. We use an analog proportional-integral (PI) controller to stabilise the system for the duration of the measurement. This controller was obtained by trial-and-error in the absence of a model. The experimental set-up in which a digital signal analyser was used to measure the plant frequency response data is shown in Figure 3.4. The digital signal analyser which is used to measure the plant frequency response, excites the system with a series of sinusoidal inputs (r) at a discrete set of frequencies, and correlates the sinusoidal input signal with the sinusoidal output signals u and y . In this way, we can determine the gain and phase of the system at each frequency.

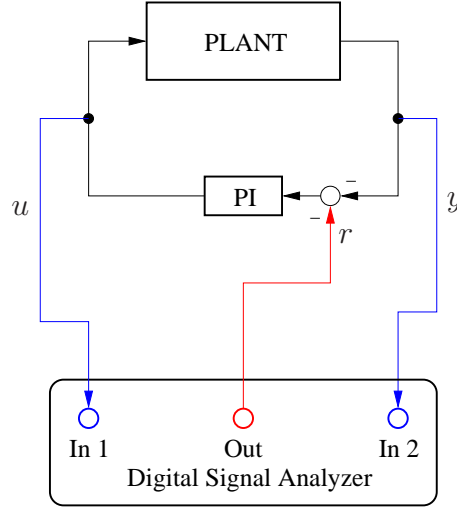


Figure 3.4: Experimental set-up used to measure the plant frequency response.

It is straightforward to show, using Figure 3.4, that the transfer function from r to y is given by

$$G_{yr} = \frac{-PK_{PI}}{I + PK_{PI}}. \quad (3.15)$$

Similarly, the transfer function from r to u can be shown to be

$$G_{ur} = \frac{-K_{PI}}{I + PK_{PI}}. \quad (3.16)$$

The digital signal analyser directly determines the ratio of these two transfer

functions, thus generating the frequency response from u to y ; i.e.,

$$G_{yu} = G_{yr}/G_{ur} = P. \quad (3.17)$$

Also, to minimise the effect of noise, each data point at each given frequency is averaged over a suitably selected number of measurements. The frequency response data thus obtained for the plant is plotted in Figure 3.5. From the data, at least three resonances can be clearly identified, occurring at frequencies of about 520, 2100 and 5000 Hz respectively.

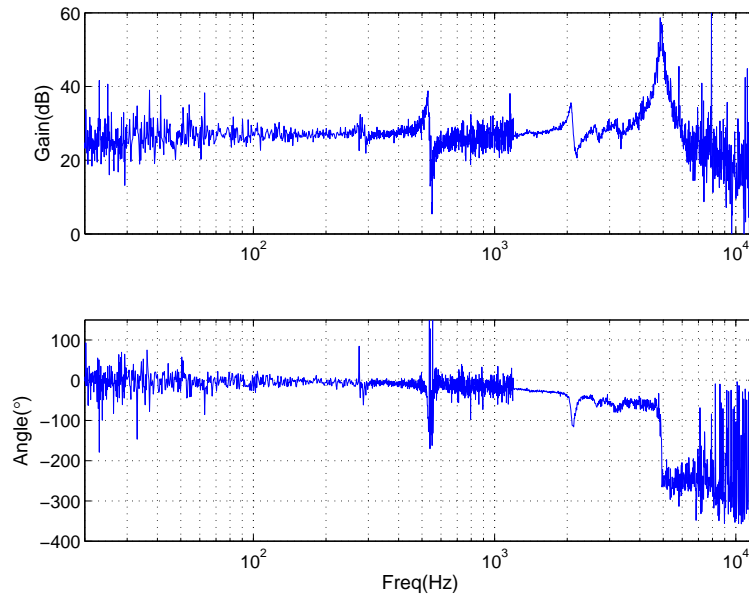


Figure 3.5: Measured plant frequency response.

An 8th-order anti-aliasing filter with a corner frequency of 2.5 kHz (chosen because it is far greater than the unity-gain bandwidth of the controller and far less than the 50 kHz sampling frequency) was then placed immediately prior to the controller. Such filters are commonly used in digital control systems (see, e.g., [36]) in order to ensure that the bandwidth of the signal being sampled satisfies the Nyquist condition. The anti-aliasing filter is regarded as augmenting the plant so that the augmented plant has a frequency response that is the product of the plant data gathered previously and the anti-aliasing filter which is identified separately.

The frequency response data obtained is then used to determine a 13th or-

der model using the frequency domain subspace identification method of [22]. Figure 3.6 compares the gain (in dB) and the phase (in deg) of the measured frequency data for the augmented plant with that of the identified system model. This identified system model is then used for controller design in the sequel.

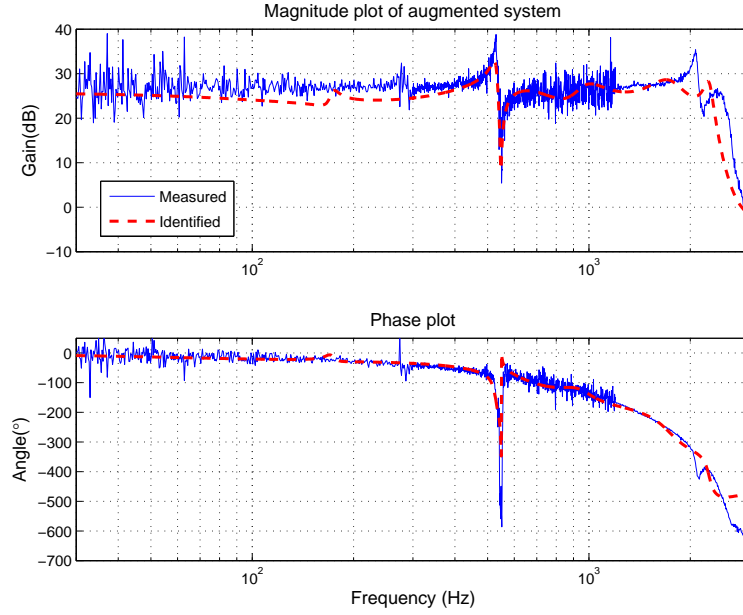


Figure 3.6: Measured frequency response data of the augmented plant and frequency response of the identified system model.

Furthermore, we also determine the steady-state d.c. gain of the system using a separate method. The d.c. gain can be measured by applying a suitable voltage (a ramp input) to the system, causing the mirror attached to the piezoelectric actuator to move in such a way that the system goes in and out of lock with time, as shown in Figure 3.7. The linear region of operation is highlighted in Figure 3.7. Within this region, small variations of Δ will result in proportional changes in y . When we are ramping the control signal u , we are actually scanning the optical cavity for resonance and the process is equivalent to varying Δ . Close to resonance and within the linear region, the gain of the system $\frac{y}{u}$ can therefore be equivalently determined from the magnitude of the gradient of the curve. This is determined by approximating the curve with a straight line, as shown in Figure 3.8 using the POLYFIT function in MATLAB®. The magnitude of the d.c. gain is found to be of the order of 23.6 dB which compares well with the d.c. gain

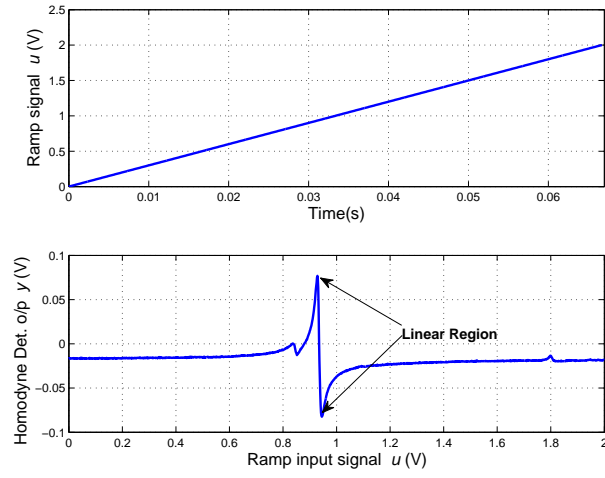


Figure 3.7: Response of the optical cavity to a ramp input signal.

obtained from the identified frequency response plot (c.f. 25.6 dB) obtained in Figure 3.6. It must be emphasised here that the steady state gain of the system as measured above can vary by a factor of ± 3 dB as the dynamics of the laser and the cavity change with time.

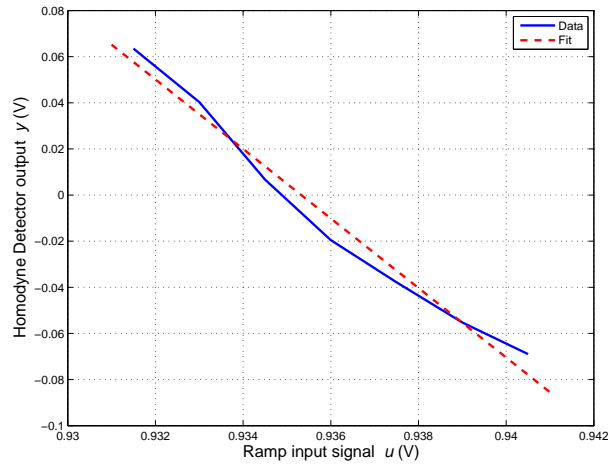


Figure 3.8: Polyfit for determination of DC gain

Chapter 4

Controller Design

In this chapter, we consider the application of a systematic controller design approach to the cavity locking problem. This approach is a variant of the linear quadratic Gaussian control method which allows us to take into account the specific requirements of this problem.

The solution to the linear quadratic Gaussian (LQG) optimal control problem originated with the work of Kalman. In the paper [37], the state feedback linear quadratic optimal control problem was solved in terms of Riccati equations. Also, in the papers [38, 39], the linear filtering or optimal state estimation problem was solved using a method which has become known as the Kalman-Bucy filter. Combining the state-feedback method of [37] and the state estimation method of [39] leads to the solution of the LQG optimal control problem. This result is known as the “separation principle” and is explained next in more detail.

4.1 Deterministic Linear Optimal Regulator Problem

Consider a linear time-invariant system described by the state-space equations:

$$\dot{x} = Ax + Bu, \quad (4.1)$$

where $A \in \mathbb{R}^{n \times n}$, $x \in \mathbb{R}^n$, $B \in \mathbb{R}^{n \times m}$, and $u \in \mathbb{R}^m$. For our application, we shall consider the “regulator problem”, whereby we apply a control signal to take the plant from a non-zero state to the zero state. In other words, we wish to bring the

system output and its derivatives to zero. This problem is typically found in a wide range of applications where systems are subjected to unwanted disturbances. An equivalent control problem which follows along similar lines to the approach that will be presented next is the “tracking problem”. This is however beyond the scope of our current work and the interested reader is referred to [40, 41] for more details.

We now consider the question: how effectively can one manipulate the state x using the given input u ? In particular, if some of the components of x cannot be influenced by u , there will be a limit on what can be achieved using feedback control. This question gives rise to the concept of “controllability”. The system (4.1) is controllable if the system controllability matrix (see [42, 43]):

$$\mathcal{C} = \begin{bmatrix} B & AB & A^2B & \dots & A^{n-1}B \end{bmatrix}. \quad (4.2)$$

has full rank; i.e.,

$$\text{rank}(\mathcal{C}) = n.$$

Thus, it can be shown that a control law of the form

$$u = -Kx \quad (4.3)$$

can arbitrarily locate the characteristic values of $(A - BK)$ in the complex plane by choosing K suitably if and only if (4.1) is controllable.

It may happen that some of the states of a system are not controllable and in such cases, we usually check whether such systems can be stabilised. “Stabilizability” is a weaker condition than controllability that is useful in such cases. We say that the pair (A, B) is stabilizable if there exists a state-feedback gain K such that the closed-loop system matrix $(A - BK)$ is stable, that is all of its eigenvalues have strictly negative real parts.

In designing K for a controllable system, we can place the closed-loop poles far to the left in the complex plane such that the system has an arbitrarily fast response. For our problem, we would like the states to converge quickly to zero. Of course, this requires large control signals to be applied to the system. In practice, the available control energy is bounded and this puts a restriction on the location of the closed-loop poles in the left-half plane. The requirement for a fast response and the constraint on control energy naturally leads to an optimisation

problem where both the speed of convergence of the states and the magnitude of the control inputs are taken into account in our design. A very attractive measure that is used to formulate this problem is the quadratic integral criteria:

$$\int_0^T [x^T Q x + u^T R u] dt, \quad (4.4)$$

where $Q \geq 0$ is a positive semi-definite symmetric matrix determining the weight that is attached to each state. Also, $R > 0$ is a positive-definite symmetric weighting matrix which minimises the control amplitude. The integral in (4.4) represents the cumulative deviation of the state x and control u from zero during the interval $[0, T]$. Usually, we have a controlled variable z that we would like to minimise, which can be defined in terms of the states as

$$z = C_2 x. \quad (4.5)$$

Our objective is then to minimise $z^T z$ which can be equivalently expressed as $x^T C_2^T C_2 x$. A suitable candidate for the weighting matrix is then $Q = C_2^T C_2$. Having set the stage for the deterministic linear optimal problem, the next step is to determine u^* that will minimise (4.4). The optimal control signal u^* can be determined using the calculus of variations; see [44]. We shall omit the derivation and simply state the result. The interested reader is referred to [41] for details of the derivation.

Theorem 4.1 *For the system described in (4.1), the optimal control law for the deterministic optimal linear regulator problem given a quadratic integral criterion of the form (4.4), is given by*

$$u^* = -K(t)x, \quad (4.6)$$

where

$$K(t) = R^{-1} B^T P(t). \quad (4.7)$$

Here, the symmetric positive semi-definite matrix $P(t)$ satisfies the matrix Riccati

equation:

$$-\dot{P}(t) = Q - P(t)BR^{-1}B^TP(t) + P(t)A + A^TP(t); \quad P(T) = 0. \quad (4.8)$$

A control law (4.6) is guaranteed to exist provided that the system (4.1) is controllable. Furthermore, for practical problems, it is natural to consider time periods for $T \rightarrow \infty$. Under such circumstances and provided the system is time-invariant, the solution of $P(t)$ of the matrix Riccati equation (13.23) approaches a steady-state solution \bar{P} which is a constant and is a solution of the algebraic Riccati equation

$$0 = Q - \bar{P}BR^{-1}B^T\bar{P} + \bar{P}A + A^T\bar{P}. \quad (4.9)$$

This allows for a convenient predetermined fixed control law to be implemented in practise.

4.2 Optimal Observer

The deterministic optimal regulator works under the assumption that all the states of the system are available and are accurately measured. This idealistic scenario exists in very few practical cases and in most cases, only a combination of the states are available for measurement:

$$y = Cx, \quad (4.10)$$

where $y \in \mathbb{R}^l$ and $l \leq n$.

We then ask the following question: when can the internal state x be reconstructed from measurements of the available output y ? In particular, if some of the state components do not influence y , then the measurements are somehow deficient and there are some limitations on what can be achieved using feedback of the output y . This leads to the concept of “observability” which allows us to determine whether it is possible to determine the behaviour of the states of a system from the behaviour of its output. A system defined by (4.1) and (4.10) is

said to be observable if the system observability matrix defined by

$$\mathcal{O} = \begin{bmatrix} C \\ CA \\ CA^2 \\ \vdots \\ CA^{k-1} \end{bmatrix} \quad (4.11)$$

has full rank; i.e.,

$$\text{rank}(\mathcal{O}) = n.$$

The dynamical system

$$\dot{\hat{x}} = A\hat{x} + Bu + L(y - C\hat{x}), \quad (4.12)$$

is an observer for the system described by (4.1) and (4.10); see, e.g., [41, 42]. Here, L is an arbitrary matrix (also known as the output injection matrix) which is chosen such that all the poles of $(A - LC)$ lie in the left-half complex plane. The pair (A, C) is observable if and only if all the poles of $(A - LC)$ may be placed arbitrarily by proper choice of the matrix L . The requirement for this condition can be clearly seen by defining the reconstruction error

$$\tilde{x} \triangleq x - \hat{x}, \quad (4.13)$$

from which it can then be shown that (see, e.g., [42])

$$\dot{\tilde{x}} = (A - LC)\tilde{x}. \quad (4.14)$$

Equation (4.14) implies that the state estimate \hat{x} approaches the actual state x asymptotically provided that the matrix $(A - LC)$ is stable. A weaker condition than observability often used in modern control is “detectability”. We say the pair (A, C) is detectable if there exists an output injection matrix L such that the matrix $(A - LC)$ is stable.

We would ideally place the observer poles far in the left-half of the complex plane to obtain fast convergence of the reconstruction error \tilde{x} to zero. This can generally be achieved by a large gain matrix L which in turn can make

the observer sensitive to measurement noise present in the measurement y . A knowledge of the statistical properties of the noise processes present in our system allows us to make an optimal choice in the determination of the observer gain matrix L . Let us redefine our system equations to include noise terms as follows:

$$\dot{x} = Ax + Bu + w, \quad (4.15a)$$

$$y = Cx + v; \quad (4.15b)$$

where w is the process noise or state excitation noise and v is the measurement or observation noise. We assume that the joint process $[w^T; v^T]$ can be described as white noise with covariance matrix (see [45]),

$$V = \begin{bmatrix} V_1 & V_{12} \\ V_{12}^T & V_2 \end{bmatrix}. \quad (4.16)$$

Furthermore, we assume that the initial state $x(0)$ is uncorrelated with w and v ; i.e.,

$$\mathbf{E}[x(0)] = \bar{x}_0, \quad \mathbf{E}\{[x(0) - \bar{x}_0][x(0) - \bar{x}_0]^T\} = Q_0. \quad (4.17)$$

where Q_0 is the assumed initial state covariance matrix. The optimal observer problem is to find a matrix L so as to minimise

$$\mathbf{E}\{\tilde{x}^T W \tilde{x}\}, \quad (4.18)$$

where W is a positive-definite symmetric weighting matrix. We shall limit our interest to the non-singular case; i.e., when $V_2 > 0$. Singular observation problems arise when the measurements are free of noise or when the measurement noise cannot be assumed to be white noise. We will state the solution for two cases (see [41] for a derivation of these results):

Theorem 4.2 *For the case when the process noise and measurement noise are uncorrelated ($V_{12} = 0$), the optimal observer gain matrix is given by*

$$L(t) = Q(t)C^T V_2^{-1}, \quad (4.19)$$

where $Q(t)$ is the solution of the matrix Riccati equation

$$\dot{Q}(t) = AQ(t) + Q(t)A^T + V_1 - Q(t)C^T V_2^{-1} C Q(t), \quad (4.20)$$

with initial condition

$$\hat{x}(0) = \bar{x}_0 \text{ and } Q(0) = Q_0.$$

Moreover, the mean square reconstruction error is given by

$$\mathbf{E}\{[x - \hat{x}]^T W [x - \hat{x}]\} = \text{tr}[QW]. \quad (4.21)$$

The optimal observer described in Theorem 4.2 is known as the Kalman-Bucy filter.

Theorem 4.3 *For the more general case when the process noise and measurement noise are correlated ($V_{12} \neq 0$), the optimal observer gain matrix is given by*

$$L(t) = (Q(t)C^T + V_{12})V_2^{-1}, \quad (4.22)$$

where $Q(t)$ is the solution of the matrix Riccati equation

$$\begin{aligned} \dot{Q}(t) = & (A - V_{12}V_2^{-1}C)Q(t) + Q(t)(A - V_{12}V_2^{-1}C)^T \\ & - Q(t)C^T V_2^{-1} C Q(t) + V_1 - V_{12}V_2^{-1}V_{12}^T, \end{aligned} \quad (4.23)$$

with initial condition

$$\hat{x}(0) = \bar{x}_0 \text{ and } Q(0) = Q_0.$$

It can be easily seen that (4.22) and (4.23) reduce to (4.19) and (4.20) respectively when $V_{12} = 0$. Also, as for the regulator problem, it can be shown for the time-invariant case that $Q(t)$ converges to a steady-state solution \bar{Q} as $T \rightarrow \infty$. \bar{Q} is, in general, the unique solution of the observer algebraic Riccati equation and is obtained by setting $\dot{Q} = 0$:

$$0 = A\bar{Q} + \bar{Q}A^T + V_1 - \bar{Q}C^T V_2^{-1} C \bar{Q}. \quad (4.24)$$

As the steady-state optimal observer then becomes time-invariant, it is attractive for practical implementation.

4.3 Separation Principle

We can combine the results from Theorems 4.1, 4.2 and 4.3 so that any linear system (that is stabilizable and detectable) with incomplete and noisy measurements can be optimally controlled. The end product is a linear quadratic Gaussian (LQG) controller. This result is known as the separation principle as it allows us to solve for the optimal state-feedback gain matrix and the optimal observer gain matrix separately, as if they are two unrelated problems. Figure 4.1 illustrates the resulting interconnection when the separation theorem is applied to a noisy linear system. The separation theorem can also be regarded as a special case of “certainty equivalence principle”; see [46, 47].

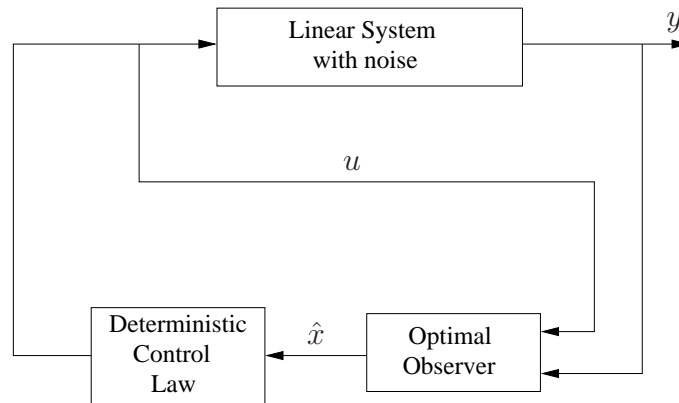


Figure 4.1: Illustration of the separation theorem.

Given the random nature of the noise present in the system and of the initial state of the system, we modify the deterministic quadratic integral criteria as defined in (4.4) to be

$$\mathbf{E} \left\{ \int_0^T [x^T Q x + u^T R u] dt \right\} \quad (4.25)$$

for the LQG optimal control problem. Here, the expectation is with respect to the initial state and the process and measurement noises.

Theorem 4.4 *The optimal solution of the stochastic linear optimal output feedback regulator problem is the same as the solution of the corresponding deterministic optimal state feedback regulator (Theorem 4.1) with the exception that the state x is replaced by its minimum mean square linear estimator \hat{x} ; i.e.,*

$$u = -K\hat{x}. \quad (4.26)$$

Here, K is given by (4.7) and \hat{x} is the output of the optimal observer obtained from (4.12). The optimal observer gain L is obtained from (4.19) and (4.22) for the case of uncorrelated and correlated process and measurement noises respectively.

The LQG controller design methodology provides a neat and elegant approach for a wide range of problems. It does not however directly address some important engineering issues in control system design such as controller bandwidth and the robustness of the control system against variations in the plant dynamics and errors in the plant model. These issues can however be taken into account in the controller design process by suitable choice of the noise terms in the plant model and of the quadratic cost functional (4.25).

4.4 Integral Action

The system we are interested in controlling is also subjected to constant disturbances or slowly varying low frequency noises. The LQG control method described previously is not able to reject that kind of disturbance because a constant (or slowly varying) control signal will be necessary to drive the steady-state error to zero. The performance criterion as defined by (4.25) cannot cater for constant non-zero control signals as the cost function will become infinite as $T \rightarrow \infty$. If the disturbance is a fixed constant, the performance criterion could be reformulated as

$$\mathbf{E} \left\{ \int_0^T [x^T Q x + \delta u^T R \delta u] dt \right\}, \quad (4.27)$$

where

$$\delta u = u - \bar{u}$$

and \bar{u} is the control signal determined beforehand that will satisfy the requirement of zero steady-state error. However, in our case, this is not feasible as the magnitude of the constant disturbance is not known *a priori*.

We need to include integral action in our controller design to eliminate the effect of constant disturbances. Integral action has been introduced by including an integral state in the system variables for the state feedback case and then by treating the augmented system using the standard approach; see, e.g., [40] and [41]. A few different integral control configurations have been suggested in those references. One approach given in [48] provides an elegant way to include an integral state in the system for the case of output feedback. However, the approach is only useful for regulating systems to obtain zero steady-state error when the set-point is constant but known.

For our problem, we include integral action by adding an additional term in the cost function which involves the integral of the output y . Moreover, we include the “integral state” as another state variable of the system. The new variable $\int y d\tau$ is also fed to the Kalman filter, which when combined with an optimal state-feedback control law leads to an integral LQG optimal controller. In this way, the controller will meet the desired performance requirements.

4.5 Performance Criterion and Design Parameters

Our system comprises of an electro-mechanical subsystem (high-voltage amplifier and piezo-electric actuator) and an electro-optical subsystem (the optical cavity and homodyne detector) which can be subdivided as shown in Figure 4.2.

The control objective is to minimise the cavity detuning Δ , which is not available for measurement. Instead, the measurement signal y is the output of the homodyne detector and to include Δ in the performance criterion, we need to relate Δ to y . It can be easily derived from (3.7b) that the transfer function of the optical cavity from Δ to y is a first-order low-pass filter with a corner frequency of $\kappa/2$. A typical gain response for the optical subsystem is shown in Figure 4.3. Physically, this arises from the well-known (see, e.g., [6, 49] and the references therein) transfer function of the optical cavity from Δ to a phase shift, which is then measured by the homodyne detector. In the experimental system described

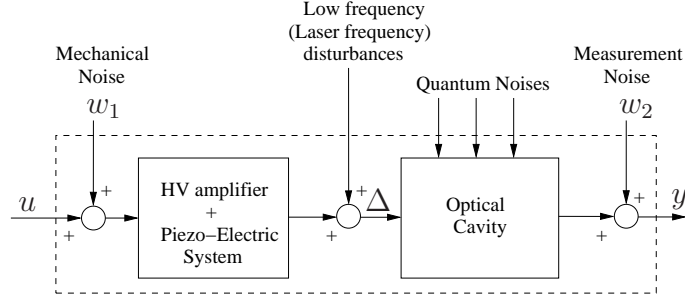


Figure 4.2: Block diagram of the plant showing all the noises and their respective point of entry.

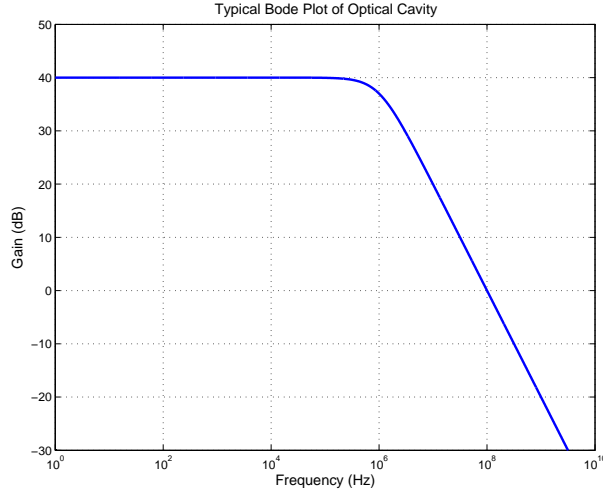


Figure 4.3: Typical optical cavity Bode plot from Δ to y

herein $\kappa/2 \approx 10^6$ Hz, which is well beyond the frequency range of interest for the integral LQG controller. Hence we can consider y to be proportional to Δ under these conditions, and therefore minimising variations in Δ can be regarded as being equivalent to minimising variations in y .

The LQG performance criterion to be used for our problem is chosen to reflect the desired control system performance. That is, (i) to keep the cavity detuning Δ small (ideally zero), and (ii) to limit the control energy. However, as explained before, these requirements are not sufficient to generate a suitable controller as the system is subject to a large d.c. offset and slowly varying disturbances. Integral action is included by splitting the output and generating an integrated version of the output and by changing the corresponding cost function accordingly

to include this new output. The integrator then forms part of the augmented plant for which we design an LQG controller using the standard approach. After designing the LQG controller, the integrator is then made part of the integral LQG controller. The desired performance requirements and more specifically the requirement to reject the constant disturbance are thus satisfied.

The integral LQG controller design configuration is shown in Figure 15.2.

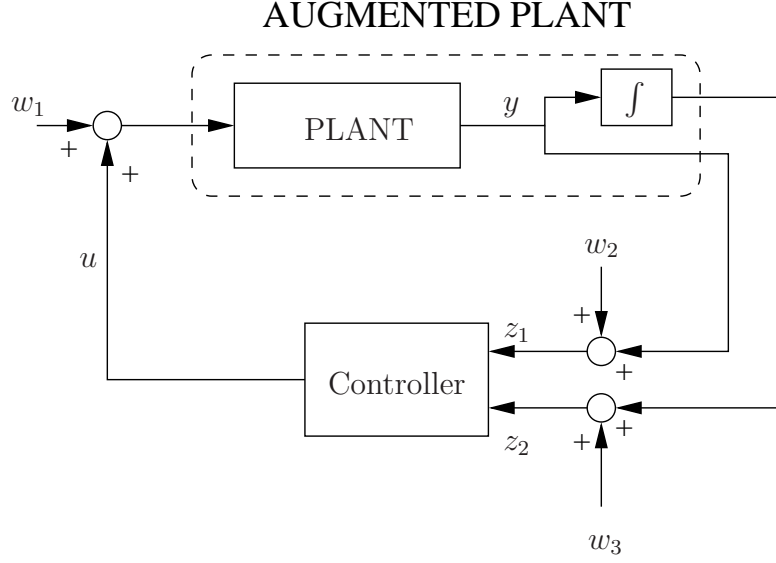


Figure 4.4: LQG integral controller design configuration.

The overall system can then be described in state-space form as follows:

$$\dot{\tilde{x}} = \tilde{A}\tilde{x} + \tilde{B}w_1 + \tilde{B}u; \quad (4.28a)$$

$$\tilde{z} = \tilde{C}\tilde{x} + \begin{bmatrix} w_2 \\ w_3 \end{bmatrix}; \quad (4.28b)$$

where

$$\tilde{x} = \begin{bmatrix} x \\ \int y d\tau \end{bmatrix} \quad \text{and} \quad \tilde{z} = \begin{bmatrix} z_1 \\ z_2 \end{bmatrix}.$$

Here the system matrices $\tilde{A}, \tilde{B}, \tilde{C}$ of the overall system are constructed from the original system matrices A, B, C as follows:

$$\tilde{A} = \begin{bmatrix} A & 0 \\ C & 0 \end{bmatrix}, \quad \tilde{B} = \begin{bmatrix} B \\ 0 \end{bmatrix}, \quad \text{and} \quad \tilde{C} = \begin{bmatrix} C & 0 \\ 0 & I \end{bmatrix}.$$

In (4.28), the quantity w_1 represents mechanical noise entering the system, w_2 represents the sensor noise present in the system output y and w_3 is included to represent the sensor noise added to the quantity $\int y dt$. They are all assumed to be Gaussian white noise. In particular, the noise w_3 is fictitious and is included to fit into the standard framework of the non-singular LQG controller design process.

The integral LQG performance criterion can be written as:

$$\mathcal{J} = \lim_{T \rightarrow \infty} \mathbf{E} \left[\frac{1}{T} \int_0^T [x^T Q x + L(y)^T \bar{Q} L(y) + u^T R u] dt \right] \quad (4.29)$$

where

$$L(y) = \int_0^t y(\tau) d\tau.$$

We choose the matrices Q, R and \bar{Q} such that

$$x^T Q x = |y|^2, \quad u^T R u = r|u|^2, \text{ and } \bar{Q} = \bar{q},$$

where $r > 0$ and $\bar{q} > 0$ are also treated as design parameters. The first term of the integrand in (4.29) ensures that the controlled variable y goes to zero, while the second term forces the integral of the controlled variable to go to zero. Finally, the third term serves to limit the control input magnitude. The expectation in (4.29) is with respect to the classical Gaussian noise processes described previously, and the assumed Gaussian initial conditions. Given the system as described by (4.28), the optimal LQG controller is given by (see (4.26) and (4.7))

$$u = -r^{-1} \tilde{B}^T X \hat{x}, \quad (4.30)$$

where X is the solution of the following matrix Riccati equation (see (4.9))

$$0 = X \tilde{A} + \tilde{A}^T X + \tilde{Q} - r^{-1} X \tilde{B} \tilde{B}^T X, \quad (4.31)$$

and

$$\tilde{Q} = \tilde{C}^T \begin{bmatrix} 1 & 0 \\ 0 & \bar{q} \end{bmatrix} \tilde{C}.$$

In (4.30), $\hat{\tilde{x}}$ is an optimal estimate of the vector of plant variables \tilde{x} obtained via a steady state Kalman filter which can be described by the state equations (see (4.12))

$$\dot{\hat{\tilde{x}}} = \tilde{A}\hat{\tilde{x}} + \tilde{B}u + L[\tilde{y} - \tilde{C}\hat{\tilde{x}}]. \quad (4.32)$$

For the case of uncorrelated process and measurement noises, the steady state Kalman filter is obtained by choosing the observer gain matrix L in (15.13) as (see (4.19))

$$L = P\tilde{C}^T V_2^{-1}, \quad (4.33)$$

where P is the solution of the matrix Riccati equation (see (4.20))

$$0 = \tilde{A}P + P\tilde{A}^T + V_1 - P\tilde{C}^T V_2^{-1} \tilde{C}P. \quad (4.34)$$

Here,

$$V_1 = \epsilon_1^2 \tilde{B}\tilde{B}^T = \tilde{B}\mathbf{E}[w_1 w_1^T] \tilde{B}^T \quad \text{and} \quad V_2 = \begin{bmatrix} \epsilon_2^2 & 0 \\ 0 & \epsilon_3^2 \end{bmatrix}$$

define the covariance of the process and measurement noises respectively.

4.5.1 Design Parameters

In designing the LQG controller, the parameters ϵ_1^2 (the mechanical noise variance), ϵ_2^2 (the sensor noise variance of y), ϵ_3^2 (the variance of the sensor noise added to $\int y$), r (the control energy weighting in the LQG cost function) and \bar{q} (the integral output weighting in the LQG cost function) were used as design parameters. The LQG design methodology does not automatically guarantee that the resulting controller will have a suitable bandwidth or robustness properties. However, by suitably choosing the parameters ϵ_1 , ϵ_2 and ϵ_3 , these essential control engineering requirements can be satisfied. Also, the true variances of the noises w_1 and w_2 are not easy to determine in practise. In addition, the noise w_3 does not exist at all in the physical plant but has been added to the plant model in order to satisfy the mathematical requirements of the LQG controller synthesis procedure. The general principles used in choosing ϵ_1 , ϵ_2 and ϵ_3 , are roughly as follows. The effect of increasing ϵ_1 or decreasing ϵ_2 and ϵ_3 is to increase the

overall bandwidth of the control system. However, if the overall bandwidth of the control system is made too large, then this will result in a control system with poor robustness. Also, the relative size of ϵ_2 and ϵ_3 determines the amount of integral action in the control system. Decreasing ϵ_3 increases the amount of integral action.

The parameters were chosen to ensure suitable gain and phase robustness margins and that the magnitude of the required control signal u was not too large. The specific values used for the design are shown in Table 4.1.

Design parameter	Value
ϵ_1	5×10^{-2}
ϵ_2	500
ϵ_3	3×10^{-4}
r	1×10^3
\bar{q}	1×10^6

Table 4.1: LQG Controller Design Parameter Values

4.6 Controller Reduction

Using the design parameter values given in Table 4.1, the LQG controller synthesis methodology leads to a 15th order controller. The digital implementation of such a high order controller would require a long sampling time which would degrade the performance of the control system. Also, the use of such high order controllers often leads to numerical problems when implemented digitally. Hence, it is desirable to approximate this 15th order controller by a controller with a reduced state dimension.

We use a frequency-weighted balanced controller reduction approach to obtain a 6th order controller. The technique we use allows for the inclusion of weighting transfer function matrices in the controller reduction process which puts emphasis on a selected frequency range of interest. The new lower order model for the controller is determined by minimising the weighted frequency response error between the original controller transfer function and the reduced controller transfer function; see [50]. Formally, the reduced order controller is constructed so that

the quantity

$$\left\| \frac{P(s)H(s)}{(I + P(s)H(s))} (H(s) - H_r(s)) \right\|_{\infty} \quad (4.35)$$

is minimised. Here, $P(s) = \tilde{C}(sI - \tilde{A})^{-1}\tilde{B}$, is the plant transfer function matrix and $H(s) = F(sI - \tilde{A} + K\tilde{C} - \tilde{B}F)^{-1}K$ is the original full controller transfer function matrix. Also, $H_r(s)$ is the reduced dimension controller transfer function matrix. The notation $\|M(s)\|_{\infty}$ refers to the \mathcal{H}^{∞} norm of a transfer function matrix $M(s)$ which is defined to be the maximum of $\sigma_{max}[M(i\omega)]$ over all frequencies $\omega \geq 0$. Here $\sigma_{max}[M(i\omega)]$ refers to the maximum singular value of the matrix $M(i\omega)$. Figure 4.5 shows Bode plots of the full-order controller and the reduced order controller.

This approach to controller reduction however does not guarantee the stability of the closed loop system with the reduced controller. We check for closed loop stability separately after the controller reduction process.

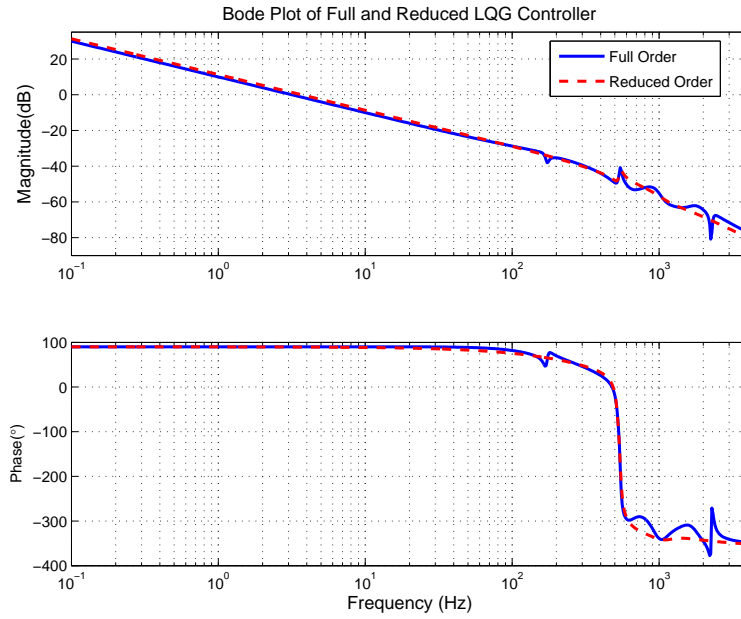


Figure 4.5: Bode plots showing the frequency response of the full and the reduced order controllers.

The reduced controller is then discretized at a sampling rate of 50 kHz to be implemented and the corresponding Bode plot of the discrete-time loop gain is shown in Figure 4.6. This discretized controller provides good gain and phase

margins of 16.2 dB and 63° respectively.

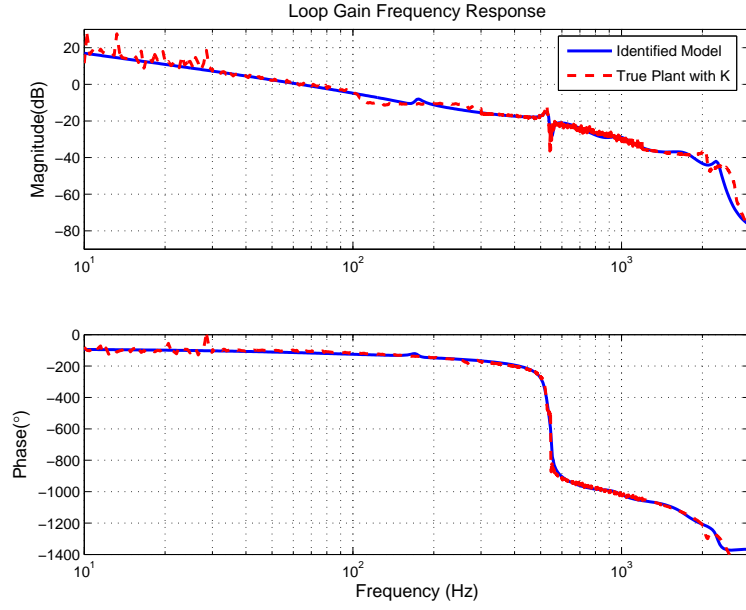


Figure 4.6: Bode plots of the loop gain transfer function $L(s)$.

Finally, Figure 4.7 shows the bode plot of the closed-loop transfer function from the mechanical noise w_1 to the control signal u for the full-order and reduced controllers. This plot shows good tracking by the reduced controller of the low frequency noises up to about 100 Hz.

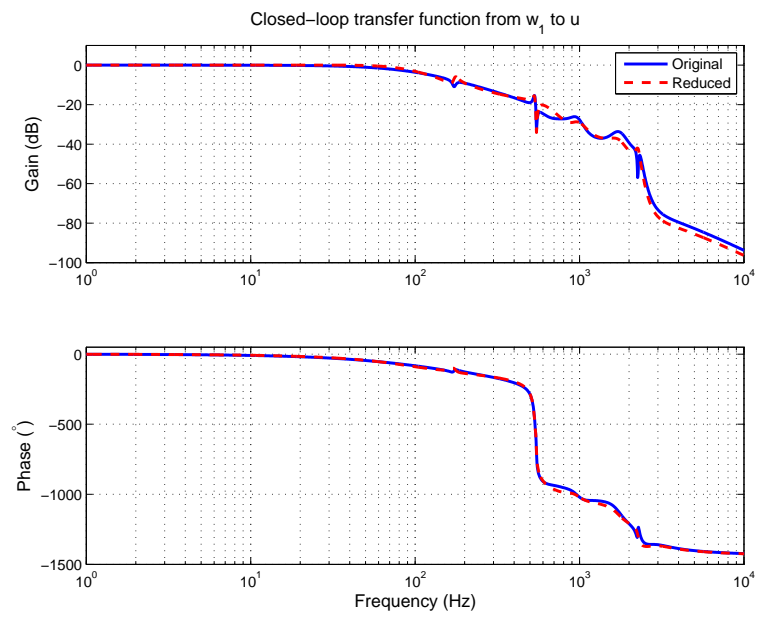


Figure 4.7: Closed-loop transfer function from mechanical noise w_1 to control signal u .

Chapter 5

Experimental Results and Discussion

The discrete controller is implemented on a dSPACE DS1103 Power PC DSP Controller Board. This board is fully programmable from SIMULINK[®] and uses 16-bit resolution. The Simulink block diagram used is shown in Figure 5.1.

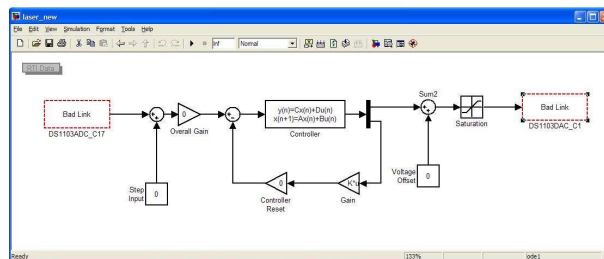


Figure 5.1: Simulink interconnection

The “DS1103ADC_C17” block represents the interface where the measurement signal from the plant enters the computer through channel 17 of the analogue-to-digital (A/D) converter of the dSPACE board. The measurement signal is discretized by the A/D converter, before being supplied to the controller. The “Overall gain” block is used to vary the gain of the controller to take into account variations in the parameters of the plant. As discussed previously in Section 3.4, the gain of the plant can vary by a factor of about ± 3 dB and for optimal performance, the gain of the controller needs to be adjusted accordingly. The discretized controller is shown and a feedback loop around the controller is added

to reset/clear all the states of the controller once the system is ready to place the controller in the loop. It is necessary to reset the controller before running the experiment. As explained in Section 4.5, our controller includes integral action and therefore will have a pole at zero, which will integrate constant signals feeding into the controller. A non-zero average measurement signal feeding into the controller will drive the states of the controller to large values in a relatively small amount of time. We design a dead-beat controller which takes as measurements all the states of the controller and resets/clears all of them in 6 sampling periods (since we have a 6th order controller). Note that the chosen sampling rate was 50 kHz and one sampling period $T_s = 20\mu\text{s}$. Another block which is added is the “Voltage Offset” block. The voltage offset generates the control signal that is necessary to first bring the system within the linear region of operation of the optical cavity. Before switching on the controller, we manually adjust this voltage until we obtain a linear error signal. As explained previously, varying this voltage is equivalent to scanning the optical cavity. The “Saturation” block ensures that the control signal does not exceed the limits determined by the digital-to-analogue (D/A) card. Finally, the “DS1103DAC_C1” block converts the control signal generated by the controller into a suitable analogue voltage which is then fed to the plant.

The .mdl code generated from the above Simulink block diagram is compiled to generate corresponding .ppc (Compiled object file for execution on DS1103) and .sdf (System description file). The .sdf file contains references to the executable file as well as the platform for the simulation.

5.1 Graphical User Interface to the Experiment

CONTROLDESK provides a powerful experimental environment for managing Simulink based controller development. It allows for virtual instrumentation and parameter handling in a single working environment.

We used the interface shown in Figure 5.2 to control our system online and to collect data for further analysis. Instrumentation to manually change the “Overall Gain” as well as the “Offset Voltage” online and corresponding to the SIMULINK[®] blocks in Figure 5.1 can be seen. Also, radio buttons are used to implement the “Step input” disturbance as well as the “Controller Reset” functions. The

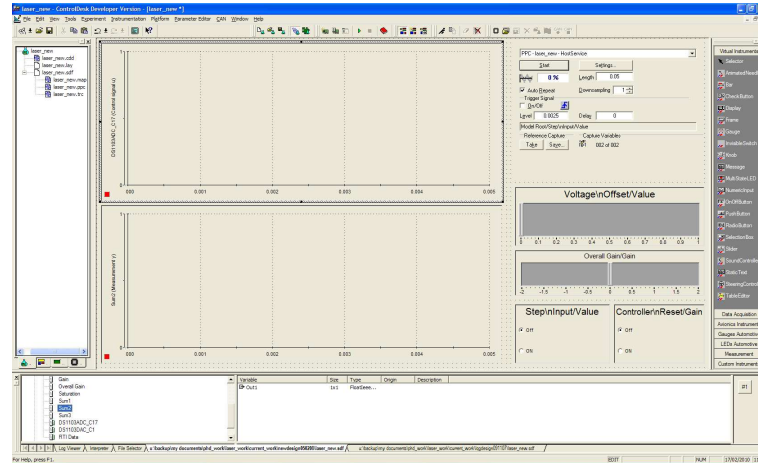


Figure 5.2: Control Desk Interface

measurement signal y and the generated control signal u are monitored on the two plotters.

5.2 Experimental Results

The controller regulating the position of the piezoelectric actuator successfully stabilises the frequency in the optical cavity, locking its resonant frequency to that of the laser frequency, f_0 ; see [14]. In addition, we also show that the control system is able to withstand significant disturbances that are introduced into the system. A step input r of magnitude 0.1 V is applied to the closed-loop system as shown in Figure 5.3. This step input can also be seen in the SIMULINK[®] interconnection in Figure 5.1 occurring just before the controller. The plant output response y is monitored. The aim here is to show that the controlled system does not go out of lock as a result of this disturbance and that the experimental system behaves as predicted by theory.

Figure 5.4 shows the experimentally measured step response which is also compared with the corresponding simulated step response obtained by using the identified plant model and the designed controller. The rise time and the general behaviour of the two are consistent with each other, except for the noise level seen in the measurement data, which has not been accounted for in the simulation.

Also, in Figure 5.5, we consider the disturbance rejection capability of our

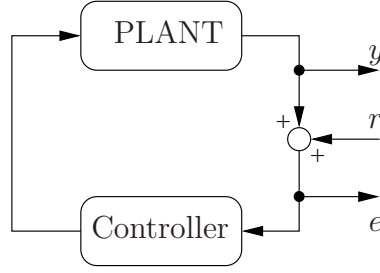


Figure 5.3: Set-Up used to measure the closed-loop step response. Here, r is the step input signal

controlled system. We compare frequency response data obtained experimentally with the closed loop transfer function determined using the identified plant and the designed controller. We are interested in the transfer function from input r to the output e , corresponding to $T = (1 + GK)^{-1}$. It is expected that the closed-loop system will attenuate the effect of disturbance r over a suitable range of frequencies (from DC up to a high enough frequency). Figure 5.3 shows that the experimental and simulated frequency response plots agree well, rejecting disturbances up to a frequency of about 60 Hz.

5.3 Discussion

The optical cavity has been successfully locked onto the laser frequency using an integral LQG controller. Simulation results obtained show that the system is also robust to the different sources of noise present as well as to external disturbances applied to the system. As can be seen from the experimental results obtained, the closed-loop system is subjected to high-frequency noises which have not been properly damped by the controller. Given the nature of the piezo-electric actuator used, the controller's bandwidth was restricted and we could not afford high enough gain at high frequencies to reject such disturbances and maintain the overall stability of the system. Also, external sources of noise not accounted for in our design such as cavity noise could be responsible. The mechanical vibration due to the mirror movement and the nonlinearities present in the HV amplifier also add to the noise in the system. With a vacuum enclosed cavity, we would have a quieter environment which would have allowed operation closer to the

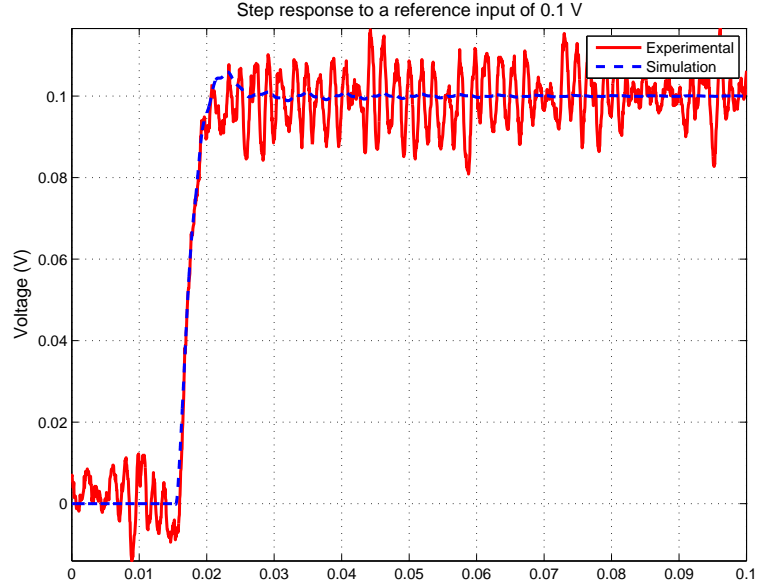


Figure 5.4: Step Response of the closed-loop system to a step input disturbance of magnitude -0.1 V.

fundamental limits of performance of the closed-loop system.

Cavity-locking controller design has been traditionally done by hand in an ad-hoc manner in the physics literature. As a general rule, controller designs start off as some combination of proportional, integral and differential transfer functions (PID controller). The final controller depends on a number of engineering trade-offs and the quality of the final product relies on the imagination and experience of the individual designer. On the other hand, the LQG approach we have investigated provides a systematic approach to controller design, codifying the engineering trade-offs using the identified state-space model of the plant in the form of an integral LQG cost functional. The design parameters listed in Table 4.1 were then chosen such that we obtained a controller with suitable gain and phase margins. Our LQG controller can provide better performance than a traditionally-designed one, since it is not confined to a modified proportional-integral-differential architecture. More importantly, our approach takes into account the dynamics of the plant and in particular the piezoelectric actuator integrated into the plant. Our method also guarantees the optimality of the solution for a given set of engineering trade-offs, practical limitations and constraints.

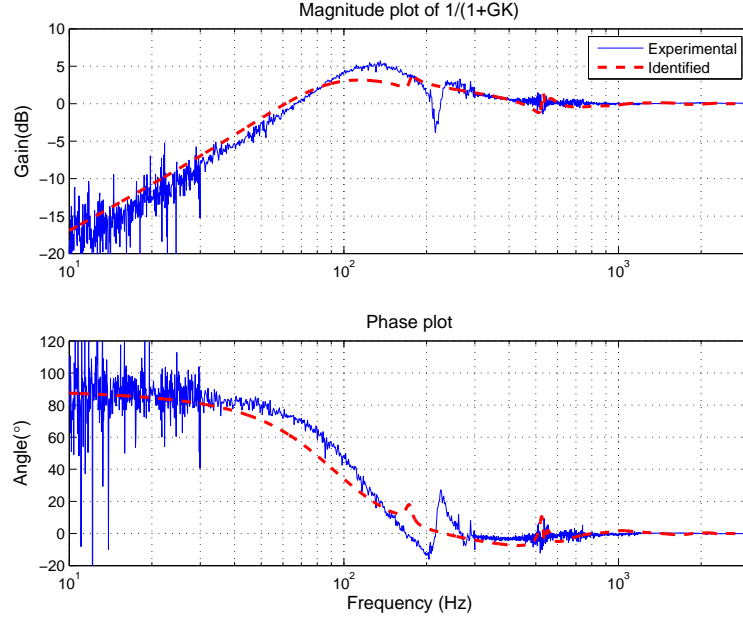


Figure 5.5: Closed loop transfer function r to e , $\frac{1}{(1+GK)}$

At a more general level, we know that due to the quantum nature of light, there is a limit to how quiet the error signal can be. The basic physical principles that set those fundamental limits are unchanged by the methodology used to design the controller. The ultimate limits to metrics such as the linewidth, Allan variance on long and short timescales, pointing stability or intensity noise of the closed-loop system are still set by the same physical limits of cavity-locking. Such performance metrics depend on things such as the power of the laser, the noise-floor of the laser and the linewidth of the frequency discriminator, irrespective of the controller design methodology. Also, those ultimate limits assume that there is no limitation on the energy that can be supplied and/or the bandwidth of the controller. Thus, the performance of a frequency-locking feedback system cannot exceed the level which is set by these limits.

Chapter 6

Nonlinear Behaviour of the Optical Cavity

The PDH approach to frequency stabilisation suppresses variations in the frequency of the laser by continuously comparing the laser's frequency with the resonant frequency of a Fabry-Perot cavity. The error signal generated using this method is proportional to the derivative of the reflected intensity and is anti-symmetric about resonance as shown in Figure 6.1.

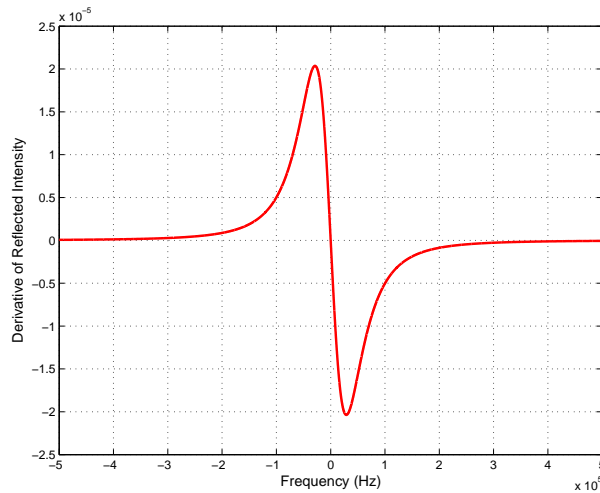


Figure 6.1: Variation of the derivative of the reflected intensity with frequency of the incident laser beam.

We use this signal to drive the piezoelectric actuator connected to one of the mirrors of the optical cavity in the appropriate direction. While this scheme

works well when the laser frequency is close to the resonant frequency of the cavity with the error signal being proportional to the reflected intensity of light, it often breaks down when the difference between the two frequencies is large. In particular, the PDH approach becomes unreliable as the derivative of the reflected intensity goes to zero; see Figure 6.1. We experience the same issues using our scheme as shown in [15] where the error signal is generated using the homodyne detection method.

This problem has been a difficult one to deal with in the physics community mainly because of an almost complete loss of observability when the system goes out of lock into the nonlinear region. We shall explain this statement further later in this chapter. To show the nonlinear behaviour experimentally, we subject the closed-loop system with a linear controller (as designed in Section 4.5) in place to step disturbances r of varying magnitude. We use the set-up shown in Figure 5.3. We seek to determine how large the measurement signal y can be to reject the disturbances introduced in the system and in turn drive the error signal to zero. Figure 6.2 shows that the controller is able to completely reject the first two step disturbances of magnitude 0.05 and 0.08 V respectively. However, it is unable to cope with a disturbance of 0.15 V resulting in an error signal which does not decay to zero. The larger disturbances push the system outside its linear region of operation and once that happens, the measurement y does not reflect a proportional deviation in Δ . The system loses observability and the linear controller will push the system further away from resonance.

In this chapter, we propose a novel controller design approach which achieves a frequency lock from any given initial operating point. In this way, our approach also caters for large perturbations which can abruptly drive the system away from the linear operating region. Also, in addition to using the phase quadrature, we use the transmitted intensity (transmittance) as a second measurement. The transmittance is measured using a photodiode and is readily available in most experimental set-ups used for optical frequency locking of cavities. We propose an approach which works by allowing for unknown but bounded measurement noises in our two observations. We determine the set of all frequency errors Δ compatible with the output measurements. Information from this set is then used to update the parameters of a time-varying Kalman filter at each time instant. In this respect, the filtering problem is related to the deterministic interpretation

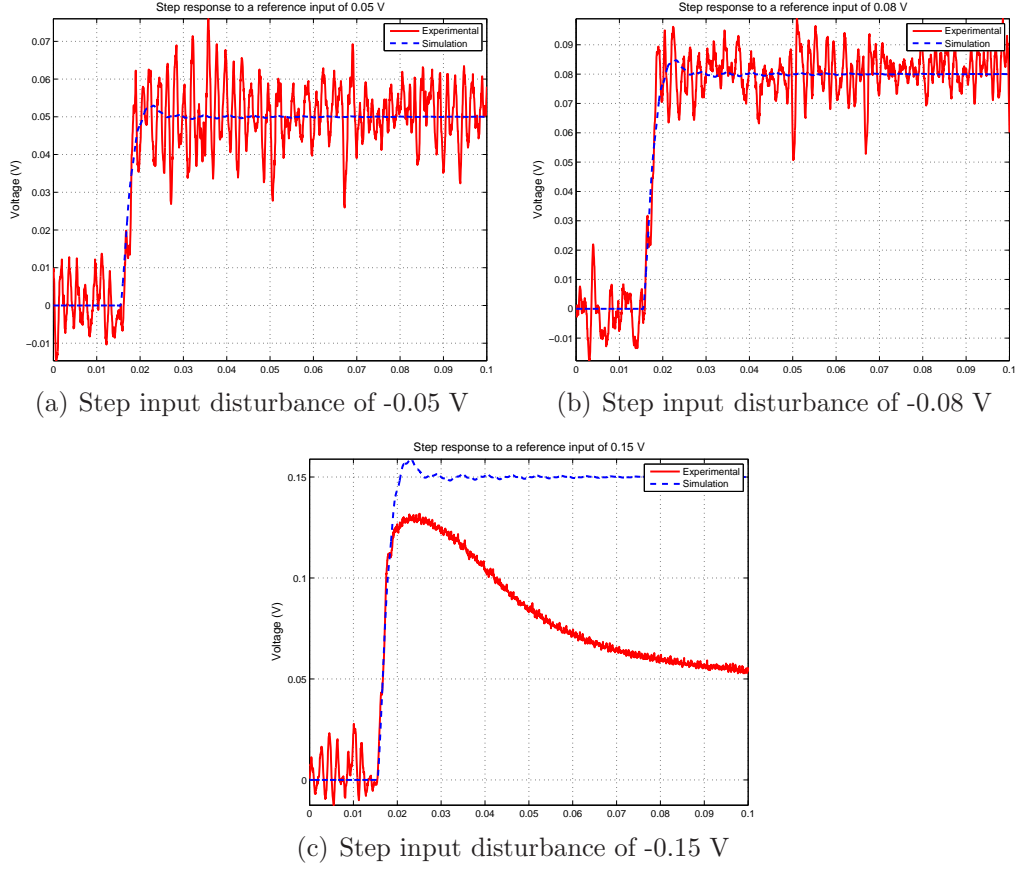


Figure 6.2: Experimental and simulated step response of the closed-loop system to step input disturbances of varying magnitude.

of the Kalman filter as described in [51] where a set-membership description of the disturbance was used. Our method also allows for laser phase noise (or $1/f^2$ noise) which acts like a slowly varying disturbance by including integral action in our design. We do so by introducing an integral state at the plant input or equivalently at the controller output.

6.1 Nonlinear Modelling of the Optical Cavity

For convenience, we depict the relevant components of the cavity locking system here again in Figure 6.3.

We continuously measure a quadrature of the laser field reflected by the cavity b_{out} using homodyne detection, producing a classical electrical signal y_1 . The

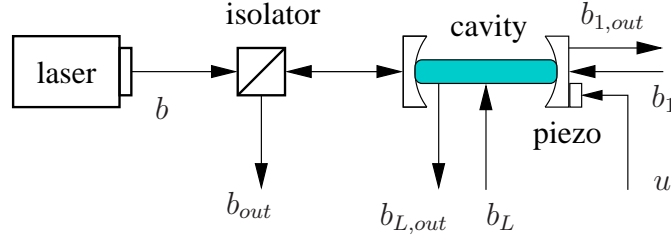


Figure 6.3: Cavity locking feedback control loop.

second measurement y_2 is obtained from $b_{1,out}$ and represents the transmitted light intensity (transmittance) from the cavity. The signal y_1 is measured using the standard homodyne detection method and includes a sensor noise v_1 . Similarly, y_2 is measured using a photodiode and includes a sensor noise v_2 . Figure 6.4 shows a block diagram of our system. The detuning Δ representing the difference between the cavity's resonant frequency from the laser frequency f_L is generated by the mechanical subsystem represented by the HV-amplifier and the piezoelectric actuator. The other noises that enter the optical cavity are the quantum noises.

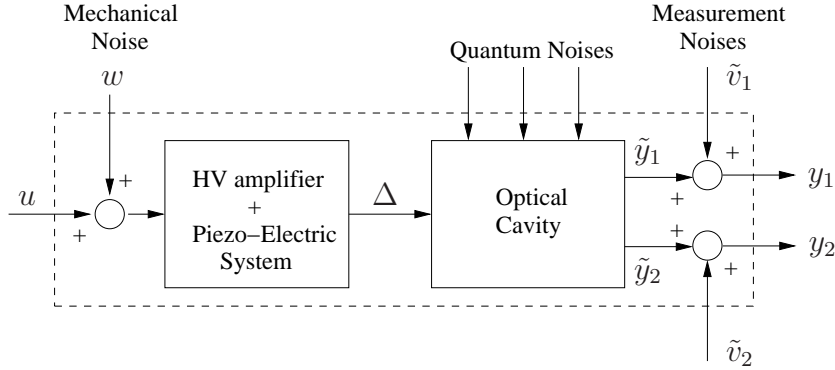


Figure 6.4: Block diagram of the cavity system.

We rewrite the equations describing the dynamics of the optical cavity (see Figure 6.3) as follows:

$$\dot{a} = -\left(\frac{\kappa}{2} - i\Delta\right)a - \sqrt{\kappa_0}(\beta + b_0) - \sqrt{\kappa_1}b_1 - \sqrt{\kappa_L}b_L; \quad (6.1a)$$

$$b_{out} = \sqrt{\kappa_0}a + \beta + b_0; \quad (6.1b)$$

$$b_{1,out} = \sqrt{\kappa_1}a + b_1. \quad (6.1c)$$

As was done with the linearised model (see (3.4)–(3.5)), we model the measurement of the X_ϕ quadrature of b_{out} via homodyne detection by changing the coupling operator for the laser mode to $\sqrt{\kappa_0}e^{-i\phi}a$, and measuring the real quadrature of the resulting field. The two output signals are respectively given by:

$$\begin{aligned}\tilde{y}_1 &= e^{-i\phi}b_{out} + e^{i\phi}b_{out}^\dagger \\ &= \sqrt{\kappa_0}(e^{-i\phi}a + e^{i\phi}a^\dagger) + 2\beta \cos \phi + q_0;\end{aligned}\tag{6.2a}$$

$$\begin{aligned}\tilde{y}_2 &= b_{1,out}^\dagger b_{1,out} \\ &= \kappa_1 a^\dagger a + \sqrt{\kappa_1}(a^\dagger b_1 + b_1^\dagger a) + b_1^\dagger b_1;\end{aligned}\tag{6.2b}$$

where $q_0 = e^{-i\phi}b_0 + e^{i\phi}b_0^\dagger$ is a standard Gaussian white noise. The cavity dynamics can then be expressed in state-space form in terms of the amplitude and phase quadrature variables as follows:

$$\begin{aligned}\begin{bmatrix} \dot{q} \\ \dot{p} \end{bmatrix} &= \begin{bmatrix} -\frac{\kappa}{2} & -\Delta \\ \Delta & -\frac{\kappa}{2} \end{bmatrix} \begin{bmatrix} q \\ p \end{bmatrix} - \begin{bmatrix} 2\beta\sqrt{\kappa_0} \\ 0 \end{bmatrix} - \sqrt{\kappa_0} \begin{bmatrix} \cos \phi & \sin \phi \\ -\sin \phi & \cos \phi \end{bmatrix} \begin{bmatrix} q_0 \\ p_0 \end{bmatrix} \\ &\quad - \sqrt{\kappa_1} \begin{bmatrix} 1 & 0 \\ 0 & 1 \end{bmatrix} \begin{bmatrix} q_1 \\ p_1 \end{bmatrix} - \sqrt{\kappa_L} \begin{bmatrix} 1 & 0 \\ 0 & 1 \end{bmatrix} \begin{bmatrix} q_L \\ p_L \end{bmatrix};\end{aligned}\tag{6.3a}$$

$$\begin{aligned}y_1 &= k_2\sqrt{\kappa_0} \begin{bmatrix} \cos \phi & \sin \phi \end{bmatrix} \begin{bmatrix} q \\ p \end{bmatrix} + k_2 \begin{bmatrix} 1 & 0 \end{bmatrix} \begin{bmatrix} q_0 \\ p_0 \end{bmatrix} \\ &\quad + 2k_2\beta \cos \phi + \tilde{v}_1;\end{aligned}\tag{6.3b}$$

$$y_2 = \tilde{k}_2 \left(\frac{\kappa_1}{4}(p^2 + q^2) + \frac{\sqrt{\kappa_1}}{2} \begin{bmatrix} q & p \end{bmatrix} \begin{bmatrix} q_1 \\ p_1 \end{bmatrix} \right) + \tilde{v}_2.\tag{6.3c}$$

Here, y_1 is the output of the first sensor in which we have included the noise term \tilde{v}_1 and k_2 is the trans-impedance gain of the homodyne detector. Similarly, y_2 represents the measurement of the transmitted light intensity which includes the sensor noise \tilde{v}_2 and \tilde{k}_2 is the sensor gain of the associated photodiode.

6.2 Separation of Time-scale Approach to Nonlinearity Modelling

With the detuning variable Δ treated as an input signal in (6.3a), this system is clearly nonlinear. The system (6.3a) only behaves linearly when the variations

of Δ about the linearised operating point are small. Under such circumstances, we used linear control design techniques to control the system. In the more general case, the detuning variable Δ is not necessarily small. In fact, it tends to be quite large and the linear control techniques discussed previously will not be appropriate anymore. In this section, we investigate the nonlinear behaviour of the measurement signals which will enable us to control the system for large values of Δ . Ignoring the noise terms q_0, p_0, q_1, p_1, q_L and p_L in (6.3a), we can write

$$\dot{q} = -\frac{\kappa}{2}q - p\Delta - 2\sqrt{\kappa_0}\beta; \quad (6.4)$$

$$\dot{p} = -\frac{\kappa}{2}p + q\Delta. \quad (6.5)$$

In most problems of interest, the optical cavity has a very large value of κ , implying that it has a large bandwidth and is a very fast system compared to the mechanical subsystem. This feature allows for a decomposition of the system into stages that are dictated by a separation of time-scales. The end result is then a reduced model representing the dominant slowest phenomena together with a “boundary layer” model which evolves much faster and which represents deviations from the predicted slow behaviour. We use this approach to represent the optical cavity as a “boundary layer” model that acts like a static nonlinearity on Δ ; see Figure 6.5.

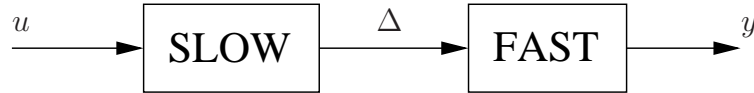


Figure 6.5: Two-time scale model of the system.

In Figure 6.5, the slow block whose output is Δ is followed by the fast block which can be thought of as a sensor information about the variable Δ . The amplification provided then varies depending on the operating point. This way of modelling and simplifying systems has been widely used in practical control applications. More formally, it is known as singular perturbation control in the literature; see, e.g., [52].

To determine the characteristics of this static nonlinearity, we set $\dot{q} = \dot{p} = 0$

in (6.4) and (6.5) and obtain

$$\begin{aligned} \begin{bmatrix} q \\ p \end{bmatrix} &= \begin{bmatrix} -\frac{\kappa}{2} & -\Delta \\ \Delta & -\frac{\kappa}{2} \end{bmatrix}^{-1} \begin{bmatrix} 2\sqrt{\kappa_0}\beta \\ 0 \end{bmatrix} \\ &= \frac{-1}{(\frac{\kappa}{2})^2 + \Delta^2} \begin{bmatrix} \kappa\beta\sqrt{\kappa_0} \\ 2\beta\sqrt{\kappa_0}\Delta \end{bmatrix}. \end{aligned} \quad (6.6)$$

For the case when $\phi = \frac{\pi}{2}$ in (6.3b), the two measurements available can then be written as:

$$\begin{aligned} y_1 &= k_2\sqrt{\kappa_0}p + 2k_2\beta\cos\phi + v_1 \\ &= -\frac{2k_2\beta\kappa_0\Delta}{(\frac{\kappa}{2})^2 + \Delta^2} + v_1 \quad (\text{since } \cos\phi = 0) \\ &= f_1(\Delta) + v_1; \end{aligned} \quad (6.7a)$$

$$\begin{aligned} y_2 &= k_3(p^2 + q^2) + v_2 \\ &= \frac{k_3\beta^2\kappa_0}{(\frac{\kappa}{2})^2 + \Delta^2} + v_2 \\ &= f_2(\Delta) + v_2. \end{aligned} \quad (6.7b)$$

Here, we have combined all the noise terms together such that:

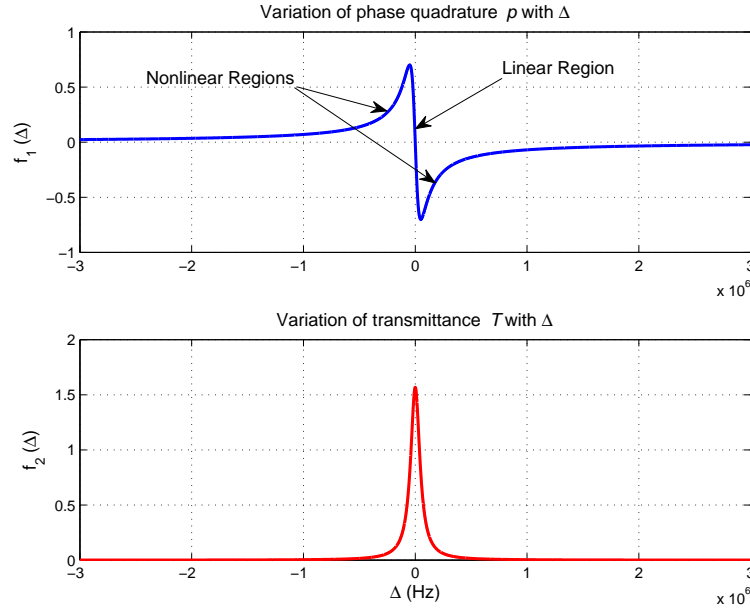
$$\begin{aligned} v_1 &= \tilde{v}_1 + k_2 q_0; \\ v_2 &= \tilde{v}_2 + \frac{1}{2}\tilde{k}_2\sqrt{\kappa_1} \begin{bmatrix} q & p \end{bmatrix} \begin{bmatrix} q_1 \\ p_1 \end{bmatrix}; \\ \text{and } k_3 &= \frac{1}{4}\tilde{k}_2\kappa_1. \end{aligned}$$

Note that ϕ can be chosen by changing the orientation of the quarter-wave/half-wave plate along the beam path. Using suitable experimental values for the parameters of the optical system (see Table 6.1), the plots shown in Figure 6.6 were generated to show the nonlinear effect of the detuning variable Δ on the measurement signals y_1 and y_2 .

It is clear from Figure 6.6 that maximum transmission occurs when the detuning variable Δ is zero. This occurs when the frequency of the laser's electromagnetic field is equal to the cavity's free spectral range (FSR) = $c/2L$. Furthermore, Figure 6.7 shows the characteristic experimental curves that would be obtained if

Simulation parameters	Value	Units
β	7×10^7	Hz
κ	1×10^5	Hz
κ_0	1×10^4	Hz
k_2	5×10^{-8}	V/Hz
k_3	8×10^{-9}	V

Table 6.1: Optical Cavity Model and Sensor Parameter Values

Figure 6.6: Behaviour of nonlinear measurement functions $f_1(\Delta)$ and $f_2(\Delta)$ with large variations in Δ .

the cavity length were scanned with a piezoelectric transducer attached to one of the cavity mirrors; see also [53, 54]. The characteristic curves repeat themselves at integer multiples of the cavity's FSR. We shall take advantage of this periodic feature of the system in designing our controller.

6.3 Piezoelectric Actuator Model

We use the same piezoelectric actuator model that was obtained experimentally in Section 3.4 as the mechanical subsystem. We augmented the model of the

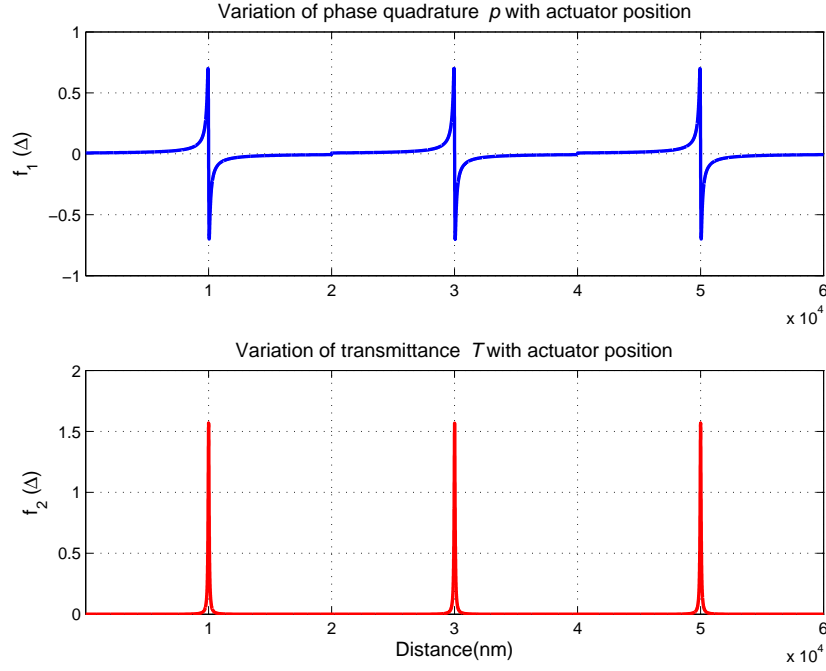


Figure 6.7: Nonlinear functions $f_1(\Delta)$ and $f_2(\Delta)$.

piezoelectric actuator with a low-pass anti-aliasing filter placed just before the controller. The cut-off frequency of this anti-aliasing filter is 2.5 kHz which was chosen to be much less than the sampling frequency of 50 kHz but high enough so as not to adversely affect the performance of the controller. This choice of cut-off frequency also suppresses resonances present at high frequencies. As explained in Section 3.4, the cascaded system of the piezoelectric actuator and anti-aliasing filter was identified using a subspace identification approach (see, e.g., [22]) and is shown again here for convenience; see Figure 6.8.

This system identification process led to a continuous time linear state-space model which was then discretized at a sampling frequency of 50 kHz. The resulting discrete-time state-space plant model is of the form:

$$x_{k+1} = A_d x_k + B_d u_k; \quad (6.8a)$$

$$\Delta_k = C_d x_k. \quad (6.8b)$$

Here, Δ is measured in hertz (Hz) and the control signal u is applied in volts (V).

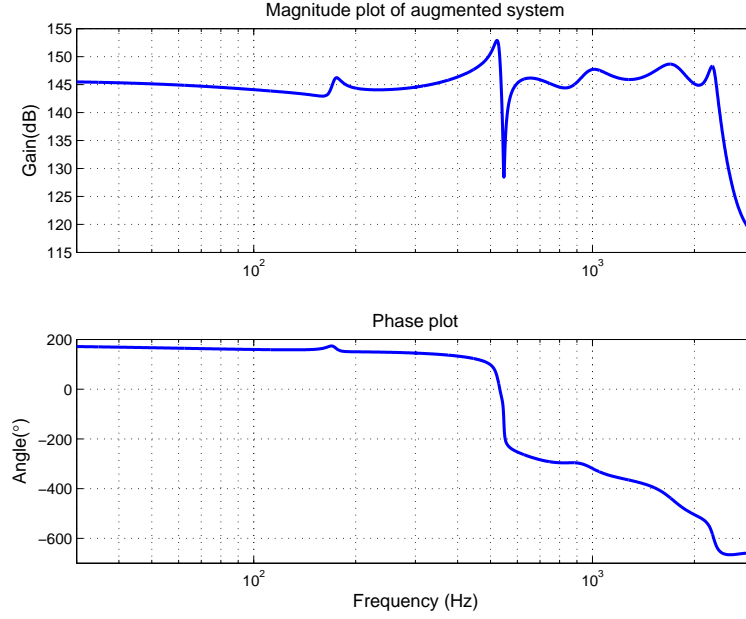


Figure 6.8: Frequency response of the identified cascaded combination of the piezoelectric actuator and the anti-aliasing filter.

6.4 Bounded Noise Model

Our system operates linearly only for small values of Δ ; see Figure 6.6. If the system is perturbed strongly enough (which is often the case in practise) and goes outside the linear operating region, it becomes effectively unobservable (with y_1 only as measurement). We seek to construct a control law that would overcome this problem and that would be capable of taking the system from the nonlinear region into the linear region. Using both measurements y_1 and y_2 to control the cavity system may at first sight seem to provide a trivial solution to the problem. However, both measurement signals tend to zero for large values of $|\Delta|$, as shown in Figure 6.6 and in the presence of measurement noises, the system then becomes extremely sensitive to measurement errors. Moreover, outside the linear region, the effective sensor gain may change sign and drive the system away from resonance. Here, we propose an approach that enables us to estimate the state of a dynamical system using noise corrupted measurements when the measurement noise is assumed to be unknown but bounded. We consider a model of measurement noise involving instantaneous constraints on the noise variables v_1 and v_2 in (6.7a) and (6.7b) respectively. Thus, we bound the measurement

errors v_{1_k} and v_{2_k} at each instant of time k ; i.e.,

$$v_{1_k}^2 \leq \mu_1^2, \quad v_{2_k}^2 \leq \mu_2^2; \quad (6.9)$$

where μ_1 and μ_2 are fixed constants denoting the magnitude of the noise. Let

$$y_{1_k} = f_1(\Delta_k) + v_{1_k}, \quad \text{where } f_1(\Delta_k) = \frac{-2k_2\beta\kappa_0\Delta_k}{(\frac{\kappa}{2})^2 + \Delta_k^2}; \quad (6.10a)$$

$$y_{2_k} = f_2(\Delta_k) + v_{2_k}, \quad \text{where } f_2(\Delta_k) = \frac{k_3\beta^2\kappa_0}{(\frac{\kappa}{2})^2 + \Delta_k^2}. \quad (6.10b)$$

We then consider the problem of characterising the set of all possible Δ_k compatible with the given observations y_{1_k} and y_{2_k} ; i.e., to find the set

$$\mathcal{S} = \{ \Delta_k \in \mathbb{R} : (y_{1_k} - f_1(\Delta_k))^2 \leq \mu_1^2 \text{ and } (y_{2_k} - f_2(\Delta_k))^2 \leq \mu_2^2 \}. \quad (6.11)$$

It is straightforward to verify from (6.11) that \mathcal{S} is the set of $\Delta_k \in \mathbb{R}$ that satisfies the following inequalities:

$$(16\Delta_k^4 + \kappa^4)(y_{1,k}^2 - \mu_1^2) + 64\Delta_k^3 k_2 \beta \kappa_0 y_{1,k} + 8\Delta_k^2 (8k_2^2 \beta^2 \kappa_0^2 + \kappa^2 y_{1,k}^2 - \kappa^2 \mu_1^2) + 16\Delta_k k_2 \beta \kappa_0 \kappa^2 y_{1,k} \leq 0; \quad (6.12a)$$

$$(16\Delta_k^4 + \kappa^4)(y_{2,k}^2 - \mu_2^2) + 8\Delta_k^2 (\kappa^2 y_{2,k}^2 - 4k_3 \kappa_0 \beta^2 y_{2,k} - \kappa^2 \mu_2^2) - 8\kappa^2 k_3 \beta^2 \kappa_0 y_{2,k} + 16k_3^2 \beta^4 \kappa_0^2 \leq 0. \quad (6.12b)$$

The set \mathcal{S} is constructed by first equating the two quartic expressions in (6.12a) and (6.12b) to zero. We next summarise the steps used in determining the solutions to these quartic equations; for more details, see, e.g., [55]. Given a general equation of the form

$$ax^4 + bx^3 + cx^2 + dx + e = 0, \quad (6.13)$$

we let

$$\alpha = -\frac{3b^2}{8a^2} + \frac{c}{a}; \quad (6.14a)$$

$$\beta = \frac{b^3}{8a^3} - \frac{bc}{2a^2} + \frac{d}{a}; \quad (6.14b)$$

$$\gamma = -\frac{3b^4}{256a^4} + \frac{cb^2}{16a^3} - \frac{bd}{4a^2} + \frac{e}{a}; \quad (6.14c)$$

and

$$P = -\frac{\alpha^2}{12} - \gamma; \quad (6.15a)$$

$$Q = -\frac{\alpha^3}{108} + \frac{\alpha\gamma}{3} - \frac{\beta^2}{8}; \quad (6.15b)$$

$$R = -\frac{Q}{2} \pm \sqrt{\frac{Q^2}{4} + \frac{P^3}{27}} \quad (\text{either root is chosen}); \quad (6.15c)$$

$$U = \sqrt[3]{R}. \quad (6.15d)$$

Then we determine

$$y = \begin{cases} -\frac{5}{6}\alpha + U - \frac{P}{3U} & : U \neq 0; \\ -\frac{5}{6}\alpha + U - \sqrt[3]{Q} & : U = 0. \end{cases}; \quad (6.16)$$

and

$$W = \sqrt{\alpha + 2y}. \quad (6.17)$$

Finally, we set

$$x = -\frac{b}{4a} + \frac{\pm_s W \pm_t \sqrt{-(3\alpha + 2y \pm_s \frac{2\beta}{W})}}{2}, \quad (6.18)$$

where \pm_s have the same sign and \pm_t are independent, giving the 4 roots of (6.13). Solving the two quartic equations results in 8 roots $\Delta_{k,i}$ for $i = 1, \dots, 8$. These

8 roots bound 9 corresponding regions of interest which are defined as:

$$\begin{aligned}
 \mathcal{S}_1 &= \{\Delta_k \in \mathbb{R} : -\infty < \Delta_k < \Delta_{k,1}\}; \\
 \mathcal{S}_2 &= \{\Delta_k \in \mathbb{R} : \Delta_{k,1} < \Delta_k < \Delta_{k,2}\}; \\
 &\vdots \\
 \mathcal{S}_8 &= \{\Delta_k \in \mathbb{R} : \Delta_{k,7} < \Delta_k < \Delta_{k,8}\}; \\
 \mathcal{S}_9 &= \{\Delta_k \in \mathbb{R} : \Delta_{k,8} < \Delta_k < \infty\}.
 \end{aligned} \tag{6.19}$$

The union of the sets \mathcal{S}_i , which have a point satisfying (6.12a) and (6.12b), defines the set \mathcal{S} . It may be that the set \mathcal{S} is a disjoint non-convex set when the system is operating far from resonance. In those cases, we may end up with two large regions on either side of resonance where the inequalities are satisfied. We then consider the convex hull of the set \mathcal{S} . As an illustrative example, for $\mu_1 = \mu_2 = 0.01$ and assuming that the true value of $\Delta = 1 \times 10^6$ Hz (outside the linear region), the set within which Δ can lie given the two noise corrupted measurement signals is determined to be between $8.4 \times 10^5 - 11 \times 10^5$ Hz; see Figure 6.9.

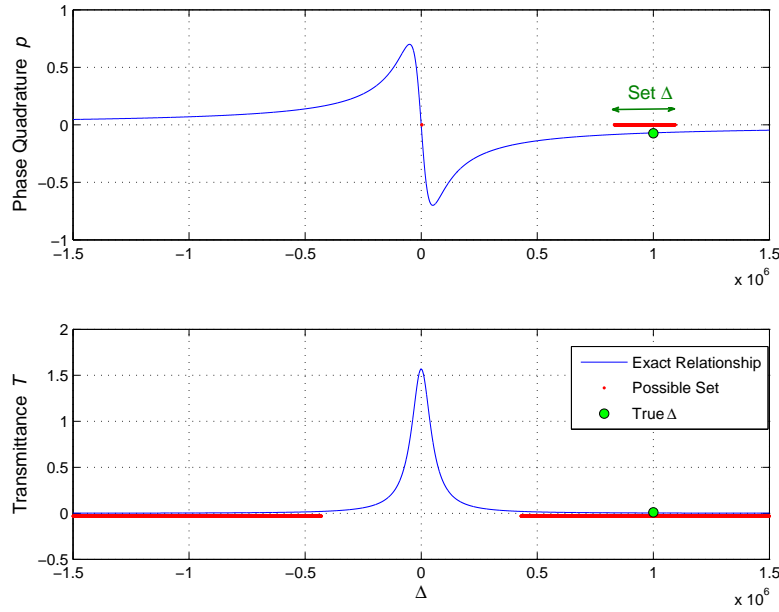


Figure 6.9: Determination of the set of possible Δ .

Given the set $\text{conv } \mathcal{S}_k$ at time step k , its centre and standard deviation are determined as follows (assuming a uniform probability distribution on $\text{conv } \mathcal{S}$):

$$\bar{\Delta} = \frac{1}{2} \left[\min_{\Delta \in \mathcal{S}_k}(\Delta) + \max_{\Delta \in \mathcal{S}_k}(\Delta) \right]; \quad (6.20a)$$

$$\sigma = \frac{1}{6} \left[\max_{\Delta \in \mathcal{S}_k}(\Delta) - \min_{\Delta \in \mathcal{S}_k}(\Delta) \right]. \quad (6.20b)$$

$\bar{\Delta}$ and σ in (6.20a) and (6.20b) are used to update the inputs of a discrete-time Kalman filter where they define the new measurement Δ_k and the measurement covariance σ_k^2 respectively. This process is described next.

Chapter 7

Time-Varying LQG Controller Design

The system we want to control is a cascade combination of the electro-mechanical subsystem and the static nonlinearity introduced by the optical cavity. Two measurements y_1 of the phase quadrature and y_2 of the transmittance are available from the optical cavity. Assuming that the observation errors are bounded, the measurements are used to determine the set \mathcal{S} within which the true value of the detuning variable Δ lies. The centre of this set is used as the new measurement $\bar{\Delta}$ and its variance σ^2 is determined from the range of the set \mathcal{S} ; see Figure 7.1.

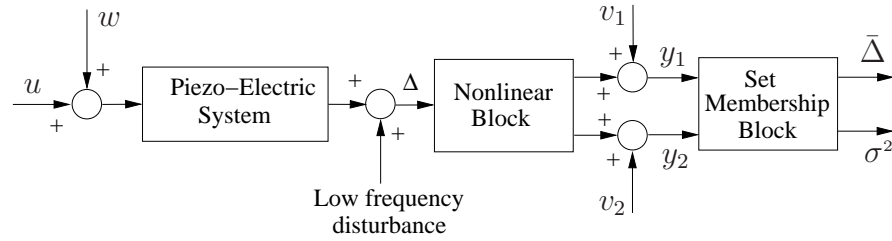


Figure 7.1: Complete system model.

The state of a time-varying Kalman filter is updated using the new measurement $\bar{\Delta}_k$ and the variance σ_k^2 available at each instant of time. In this way, the nonlinear problem becomes one which fits into the standard framework of the LQG controller design approach.

7.1 Integral Action and Performance Cost Criterion

As explained in Section 4.3, an LQG controller consists of an estimation block defined by a Kalman filter followed by a deterministic linear quadratic regulator state feedback gain. The regulator assumes that the estimates are the actual states and determines the optimal control law corresponding to a given performance criterion. The system is subjected to laser phase noise ($1/f^2$ noise) in the form of low frequency disturbances as well as a large constant disturbance. A standard LQG controller is not able to drive the detuning variable Δ to zero in the face of such disturbances; see Section 4.4. In order to achieve this, we require integral action and it is included in our LQG design by placing an integrator at the input of the plant. The general set-up for the new proposed integral LQG design is shown in Figure 7.2.

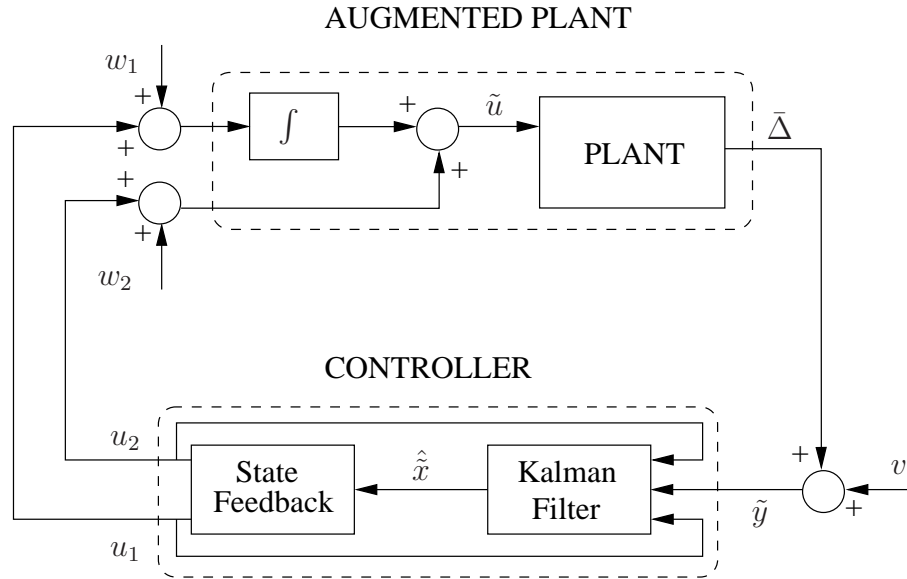


Figure 7.2: Integral LQG controller design configuration.

The plant to be controlled as seen by the controller is then the “augmented plant”. When the integral LQG controller is implemented, the integrator is then included as part of the controller. The two control signals generated by the controller u_1 and u_2 are combined through the integrator at the input of the plant to form the control signal \tilde{u} that is then fed to the plant. The integrated

u_1 takes care of the low-frequency and/or constant disturbance acting on the system while u_2 caters for the higher frequency components of noise present in the system. The fictitious process noise w_1 is included to help in the shaping of the controller such that suitable bandwidth and robustness is achieved. The measurement noise v is included to model the variance of the detuning variable $\bar{\Delta}$.

The discretized augmented system we use for the controller design can then be described as follows:

$$\tilde{x}_{k+1} = \tilde{A}_d \tilde{x}_k + \tilde{B}_d u_k + \tilde{B} w_k; \quad (7.1a)$$

$$\tilde{y} = \tilde{C}_d \tilde{x}_k + v_k; \quad (7.1b)$$

where

$$\tilde{x}_k = \begin{bmatrix} x_k \\ x_{i,k} \end{bmatrix}, \quad u_k = \begin{bmatrix} u_{1,k} \\ u_{2,k} \end{bmatrix}, \quad w_k = \begin{bmatrix} w_{1,k} \\ w_{2,k} \end{bmatrix}; \quad (7.2)$$

and $x_{i,k}$ is the state of the integrator introduced at the input of the plant. The augmented system matrices \tilde{A}_d , \tilde{B}_d and \tilde{C}_d are constructed from the original system matrices A_d , B_d and C_d as follows:

$$\tilde{A}_d = \begin{bmatrix} A_d & B_d \\ 0 & 0 \end{bmatrix}, \quad \tilde{B}_d = \begin{bmatrix} 0 & B_d \\ 1 & 0 \end{bmatrix}, \quad \text{and } \tilde{C}_d = \begin{bmatrix} C_d & 0 \end{bmatrix}. \quad (7.3)$$

The mechanical noises $w_{i,k}$ for $i = 1, 2$, are assumed to be Gaussian white noise with variance ϵ_1^2 and ϵ_2^2 respectively. The measurement noise v_k is assumed to be Gaussian white noise with variance σ_k^2 . We also assume that the initial state x_0 is unknown but that $x_0 \sim N(\bar{x}_0, P_{x_0})$.

An LQG performance criterion is chosen to minimise the detuning variable Δ while at the same time limit the magnitude of the control signal. This requirement is reflected in the following quadratic cost function:

$$\mathcal{J} = \lim_{k \rightarrow \infty} \mathbf{E} \left[\sum_{k=1}^{\infty} (\tilde{x}_k^T Q \tilde{x}_k + u_k^T R u_k) \right]. \quad (7.4)$$

The matrices Q and R are chosen such that

$$\tilde{x}_k^T Q \tilde{x}_k = |\tilde{y}_k|^2 \quad \text{and} \quad u_k^T R u_k = r_1 |u_{1,k}|^2 + r_2 |u_{2,k}|^2 \quad (7.5)$$

where $r_1, r_2 > 0$ are treated as design parameters. The expectation in (7.4) is with respect to the Gaussian white noise present in the system. The optimal control is given by

$$u_k = \begin{bmatrix} u_{1,k} \\ u_{2,k} \end{bmatrix} = -F \hat{\tilde{x}}_k; \quad (7.6)$$

where

$$F = (\tilde{B}_d^T S \tilde{B}_d + R)^{-1} \tilde{B}_d^T S \tilde{A}_d; \quad (7.7)$$

and S satisfies the algebraic Riccati equation

$$0 = \tilde{A}_d^T [S - S \tilde{B}_d (\tilde{B}_d^T S \tilde{B}_d + R)^{-1} \tilde{B}_d S] \tilde{A}_d - S + Q. \quad (7.8)$$

7.2 Discrete-time Kalman Filtering

We now turn our attention to the estimation of the states of the system given a noise corrupted system as described by (7.1b).

If the *a posteriori* estimate and error covariance are given by $\hat{\tilde{x}}_k$ and P_k respectively and $\hat{\tilde{x}}_k^-, P_k^-$ are the respective *a priori* quantities, then the state of the system is estimated recursively using the following Kalman filter equations (see, e.g., [42, 45]):

$$K_k = P_k^- \tilde{C}_d^T (\tilde{C}_d P_k^- \tilde{C}_d^T + \sigma_k^2)^{-1}, \quad P_0^- = P_{\tilde{x}_0}; \quad (7.9a)$$

$$\hat{\tilde{x}}_k = \hat{\tilde{x}}_k^- + K_k (\tilde{y}_k - \tilde{C}_d \hat{\tilde{x}}_k^-), \quad \hat{\tilde{x}}_0^- = \tilde{\tilde{x}}_0; \quad (7.9b)$$

$$P_k = (I - K_k \tilde{C}_d) P_k^-; \quad (7.9c)$$

and

$$\hat{\tilde{x}}_{k+1}^- = \tilde{A}_d \hat{\tilde{x}}_k + \tilde{B}_d u_k; \quad (7.10a)$$

$$P_{k+1}^- = \tilde{A}_d P_k \tilde{A}_d^T + \tilde{B}_d W \tilde{B}_d^T; \quad (7.10b)$$

where

$$W = \begin{bmatrix} \epsilon_1 & 0 \\ 0 & \epsilon_2 \end{bmatrix}. \quad (7.11)$$

At each time instant, the new measurement $\tilde{y}_k = \bar{\Delta}_k$ and measurement covariance σ_k are determined from the set \mathcal{S} in (6.11) and are used to update \hat{x}_k in (11.6b) and P_k using (11.9a) and (7.9a). In designing the LQG controller, the following parameters were chosen for good controller performance:

Simulation parameters	Value
ϵ_1	5
ϵ_2	5
r_1	0.01
r_2	0.1

Table 7.1: Time-Varying LQG Controller Design Parameters.

Chapter 8

Simulation Results

We simulate the system with the given control law (7.6) for a time period of 10 ms and with a sampling rate of 50 kHz which can be easily attained in practise using standard ADC/DAC cards. The simulation parameters used reflect those of an experimental set-up used in our optics laboratory (see Table 6.1) and the noise models are specifically chosen to reflect experimental conditions. The selected bounds on the noise inputs are shown in Table 8.1. The system is initialised

Noise Bounds	Value	Units
μ_1	1×10^{-2}	V
μ_2	1×10^{-2}	V

Table 8.1: Measurement Noise Bounds

outside the linear region, with $\Delta = -1 \times 10^6$ Hz. Also, we include a disturbance on Δ to represent the low-frequency laser phase noise. This disturbance is modelled as integrated white noise with an initial offset of -1×10^6 Hz as shown in Figure 8.1.

The process noise w_2 is modelled as Gaussian white noise with variance $\sigma_1^2 = 1 \times 10^{-4}$ and w_1 being a fictitious process noise input (used for the controller design process only) is ignored in the simulation stage. The measurement noises v_1 and v_2 are uniformly distributed and bounded such that

$$v_1^2 \leq \mu_1^2 \quad \text{and} \quad v_2^2 \leq \mu_2^2.$$

Figure 8.2 shows the response of the true Δ as well as the estimated $\hat{\Delta}$ obtained

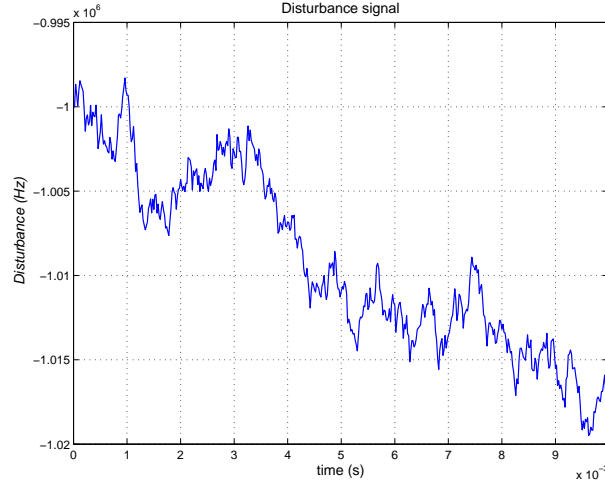


Figure 8.1: Laser phase noise modelled as integrated white noise with an initial offset of -1 MHz.

from the time-varying Kalman filter. The generated control signal u in volts (V) is also shown.

Figure 8.3 shows the variation of the two measurement signals y_1 and y_2 representative of the phase quadrature p (V) and the transmittance I (V) respectively. The measurement signal y_1 is highly sensitive to small disturbances. The transmittance I reaches and settles close to its peak value after about 4 ms.

Figure 8.4 shows the trajectory of the phase quadrature measurement p and of the transmittance I . The starting point and the end point at the end of the simulation time of 10 ms are also shown. It can be seen that the closed-loop system stabilises very quickly. The controller is effective in transferring the system from the nonlinear region into the linear region and regulates Δ close to zero in the presence of process noise, laser phase noise and bounded measurement noises on the two measurement channels y_1 and y_2 . The oscillatory response seen is due to the resonant nature of the specific piezoelectric actuator, as modelled in Section 3.4; see also [15]. Also, we note that the system stabilises with a non-zero value of the control signal to counteract the effect of the low-frequency laser phase noise.

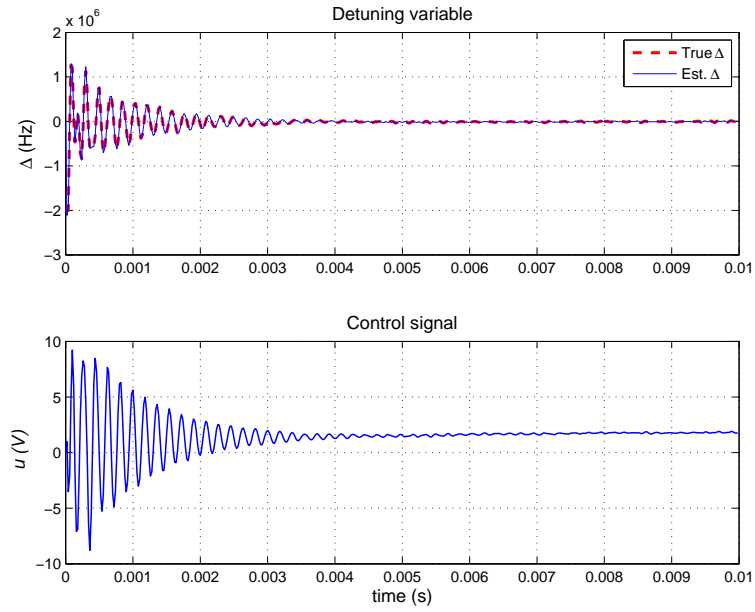


Figure 8.2: Initial condition response of system using the time-varying LQG controller.

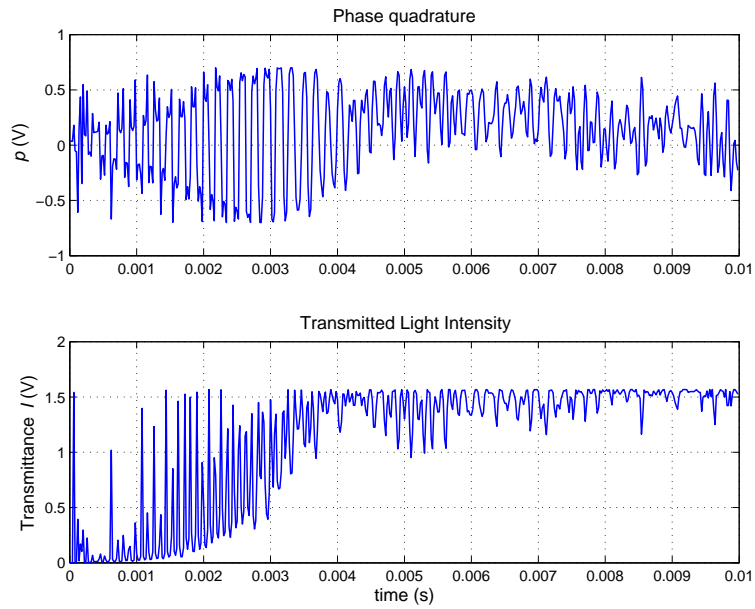


Figure 8.3: Phase quadrature and transmittance measurement.

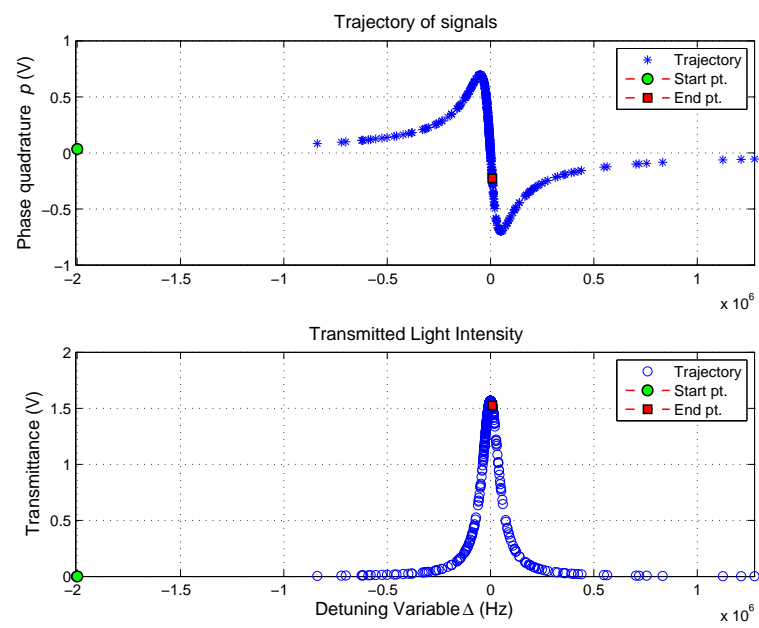


Figure 8.4: Trajectory followed by the system

Chapter 9

Conclusion and Future Work

The frequency locking problem of an optical resonant cavity forms an integral part of just about every experimental work performed in the area of quantum optics. In the first part of this work, we have modelled an optical cavity system from frequency response data gathered on an experimental test-bed in our optics laboratory. We used a subspace identification method to model the system. A modified version of the LQG control approach which includes integral action is then used to design, implement and test a controller which successfully locks the resonant frequency of the cavity to that of the laser frequency.

The ultimate performance of a cavity-locking system is however still limited by the underlying physics and by the prevailing experimental laboratory conditions and constraints. The approach we use guarantees optimal results within those constraints. We believe that with the use of additional sensors and actuators, and with a quieter cavity, this work can be extended to improve the quality of frequency lock achieved. Moreover, the subspace identification method is also particularly suited for identifying multivariable systems and the LQG control technique can be easily extended for MIMO systems. Also, future work along this line could include, for example, the control of the laser pump power using a similar scheme as the one used here. This work can be expected to pave the way for extremely stable lasers with fluctuations approaching the quantum noise limit and which could be potentially used in a wide range of applications in high precision metrology.

The technique described and implemented in the first part, is however only applicable for the linear region of operation of the optical cavity. It is only valid

for frequency deviations that are not large. In the second part of this work, we addressed the nonlinear problem of stabilising an optical cavity system from any initial operating point. Using a singular perturbation approach and taking advantage of the different time-scales of the interconnected systems, the piezo-electric actuator and the inherent nonlinearity present in the optical cavity were modelled separately. We then placed instantaneous error bounds on the measurement noises and computed a convex set within which the detuning variable lies. Information from this set was then used to update estimates of the states of the system. In this way, the nonlinear problem was formulated into the framework of an integral LQG control problem with a time-varying Kalman filter. Simulation results showed that the controller was successful in regulating the detuning variable Δ in the presence of realistic noise models from any given initial operating point. Future research will involve validating our design on an experimental laboratory system and if successful, would provide experimentalists with a powerful frequency locking scheme for optical resonator cavities. Another avenue of research could involve the design of robust controllers that would allow for variations in the parameters of the optical subsystem, which are usually difficult to determine to a high level of accuracy.

Part II

Modelling, Analysis and Control of an Optical Parametric Oscillator

Chapter 10

Introduction

Advances in nano-technology and atomic systems have led to devices which are sensitive enough to detect quantities at the quantum level. It is well known in the physics literature that experiments performed at the quantum level are restricted by the quantum noise limit (QNL); see Section 2.3. The QNL sets a fundamental limit to the performance of quantum systems and puts a bound on the signal to noise ratio that can be achieved, restricting the usefulness of applications involving quantum technology. With the use of nonlinear effects (see [17, 56]) and nonlinear media in quantum optics, it is possible to change the statistics of quantum noise, allowing for measurements that are better than permitted by the standard quantum limit (SQL). Here, SQL refers to the minimum level of quantum noise that can be obtained with the use of states of light that possess classical quantum noise properties.

If we define the amplitude and phase quadrature operators (see Section 2.4 and [5]) of an optical field as \mathbf{X}^+ and \mathbf{X}^- respectively, then the Heisenberg uncertainty principle (see [19, 25]) implies that the variance of the operators in any given state is constrained by

$$\langle \Delta \mathbf{X}^{+2} \rangle \langle \Delta \mathbf{X}^{-2} \rangle \geq 1; \quad (10.1)$$

where $\langle \cdot \rangle$ denotes the quantum expectation value. In the case of laser light which can be idealised as being in a coherent state $|\alpha\rangle$ (see Section 2.2) or minimum uncertainty state (with a minimal product of the amplitude and phase quadrature uncertainties), the uncertainty associated with the quantum state is equally

divided between the two quadratures such that

$$\langle \Delta \mathbf{X}^{+2} \rangle = \langle \Delta \mathbf{X}^{-2} \rangle = 1. \quad (10.2)$$

The uncertainty can thus be visualised as corresponding to a circular and symmetric area, as shown in Figure 10.1. The “uncertainty ball” arises as a result of the quantum nature of light, affecting a given system and restricts how close two measurable quantum states can be if they are to be distinguished from each other. Indeed, classical noises affect measurement of classical states in a similar fashion. Classical noises can (in theory) however be completely suppressed with improved measurement techniques. This is not the case for quantum noises whose sizes are dictated by the laws of quantum mechanics rather than as a result of the limitations of the measurement devices. It is possible, however to partly circumvent this problem by concentrating the quantum noises in specific quadratures of light. In other words, we can rearrange the noise distribution between the quadratures such that one quadrature has less noise than the other. Quantum states of light which have this property of asymmetric quadrature noise distributions are known as “squeezed” or “non-classical” states of light.

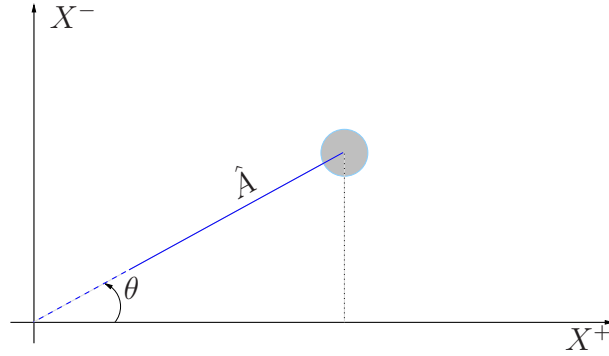


Figure 10.1: Minimum uncertainty state

10.1 Squeezed states

Figure 10.2 shows some of the different types of squeezed states that can be achieved from a coherent state. Squeezed states of light have their *quantum*

noises squeezed and possess noise distribution which are less than those of the coherent states of light in specified directions.

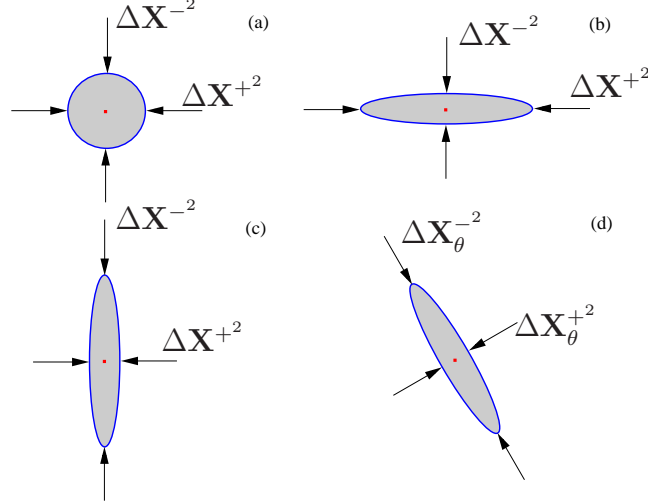


Figure 10.2: Quantum noises associated with different quantum states. (a) Coherent state, (b) Phase quadrature squeezed state, (c) Amplitude quadrature squeezed state, (d) Arbitrary (Quadrature) squeezed state.

A coherent state of light has a Gaussian distribution such that (10.2) is satisfied. Pauli [57] showed that both a coherent quantum state and squeezed state can be completely described using only 2-dimensional Gaussian distribution functions. For a squeezed state, the only requirement is that the width of these functions need to satisfy the uncertainty principle for any chosen direction θ . The contour line for such a 2-dimensional function turns out to be always elliptical, while that for a coherent state is circular. The total area inside the contour can however never be less than that of the uncertainty area of a coherent state. For the case of phase squeezed states (see Figure 10.2(b)), they have a narrow axis aligned with the phase axis and the widest distribution orthogonal to the phase axis. Similarly for the amplitude squeezed state (see Figure 10.2(c)), there is less noise along the amplitude quadrature and the fluctuations along the phase quadrature are above the standard quantum noise limit. Furthermore, in the presence of external sources of noise, the phase quadrature fluctuations can be even larger than required by the Heisenberg uncertainty principle. External sources of noise will also affect the squeezed quadrature but as long as the excess noise introduced does not drive the fluctuations above the standard quantum

noise limit, squeezed states are obtained. In this way, depending on whether the amplitude or the phase quadrature is being measured, the state can be squeezed such that the measurement can become more sensitive in a given direction, thus containing a level of noise which is below the SQL. Moreover, a quantum state can be squeezed along any arbitrary angle with respect to the predefined amplitude and phase quadratures, as shown in Figure 10.2(d) and it is then described as quadrature squeezed state. In the presence of external sources of noise, (10.1) applies. Squeezed states are of course, going to be most useful in applications where the standard quantum noise limit has already been reached.

10.2 Applications of Squeezed states

As a result of the fact that they possess less noise in one quadrature than the standard quantum noise limit, squeezed states of light have a wide range of applications. One application of squeezed states of light is in gravitational wave detection (see [58, 59]) where the use of phase-squeezed light allows for a reduction in the necessary laser power to achieve a given signal to noise ratio. Quantum teleportation, which is an integral part of quantum communication and information processing, has also been demonstrated using squeezed light; see [60]. Amplitude-squeezed light, on the other hand, is used for the measurement of weak spectroscopic signals. Other applications include quantum cryptography whereby secret keys are securely distributed to two distant parties.

Also, experimental quantum optics has enabled many fundamental theories of quantum mechanics to be tested at unprecedented level. In particular, nonlinear processes in quantum optics have proved useful in checking the counter-intuitive predictions of the theory of quantum mechanics. For example, entangled states of light are produced from squeezed states and have been used to demonstrate the Einstein-Podolsky-Rosen (EPR) paradox [61]; see [62]. The EPR paradox had been a highly controversial topic among physicists, questioning the completeness of quantum theory.

10.3 Generation of Squeezed states

Squeezed light is generated from coherent light using nonlinear optical crystals (such as magnesium oxide doped with lithium niobate) in what is known as an optical parametric amplifier/oscillator (OPA/OPO). Squeezed light was first demonstrated in 1985; see [63]. Recently, the OPO was used to successfully generate squeezed vacuum states, achieving a suppression level of about 10 dB [64]. The OPO ensures noiseless *phase-sensitive amplification* of the quadratures of light such that one of the quadratures is amplified by an amount and the other quadrature is de-amplified by an amount. In this way, the product of the gains in the two quadratures is unity (assuming initial minimum uncertainty).

Traditional amplifiers (such as electronic amplifiers) affect both the signal and the noise in the same way, maintaining more or less the same signal to noise ratio. Optical amplifiers behave quite differently. In particular, they introduce additional sources of noise (referred to as vacuum states which are at the quantum noise limit) in the amplification process. These vacuum states are then amplified just like the signal such that the signal to noise ratio suffers a penalty of 3 dB; see [5]. This is however only the case when the amplifier acts equally on both quadratures and such amplifiers are called *phase insensitive*.

To avoid this problem, we use phase sensitive amplifiers, also known as parametric amplifiers. In the next section, we give a brief overview of how the OPA works; see [17, 65] for more details.

10.3.1 Optical Parametric Amplification

Certain classes of crystals show nonlinear dielectric properties which in addition to a linear response to an electric field, propagate electromagnetic radiation whose polarization is proportional to the square of the field. With incident fields of high strength (as is the case with lasers) and appropriate index-matching techniques (see [17]), these second order nonlinear effects (also known as susceptibilities) become significant. Crystals capable of showing such properties are responsible for the exchange of energy between electromagnetic fields of different frequencies, which can happen in a few different ways as follows:

1. The electromagnetic field going through a dielectric material forms temporary dipoles in the material which at high enough field strengths form

a polarization wave and is re-radiated as an electromagnetic field. The re-radiated field contains numerous frequency components but for our purposes, we shall consider only second-order harmonic frequencies and optical $\chi^{(2)}$ processes. Thus, part of the energy of an optical field at frequency f results in the generation of another optical field at frequency $2f$ in a process called “second harmonic generation” (SHG).

2. A fraction of a strong electromagnetic field at frequency f_3 simultaneously generates optical fields at frequencies f_1 and f_2 , with $f_1 + f_2 = f_3$ in a process called “difference frequency generation” (DFG). In the presence of a field at frequency f_2 , this results in what is known as a two-photon stimulated emission process and the lower frequency input field f_2 is amplified. This process is known as “optical parametric amplification” (OPA). Furthermore, if the nonlinear material is placed inside an optical resonator, the generated fields can build up to large values and the device is known as an “optical parametric oscillator” (OPO). Optical parametric oscillation occurs at some threshold intensity when the parametric gain causes simultaneous oscillations at frequencies f_1 and f_2 . The output frequencies can be altered by using some phase matching properties (angle of orientation/temperature) of the nonlinear crystal.
3. A weak optical field of low frequency f_1 is converted to an optical field of higher frequency f_3 by interacting with a strong optical field f_2 , with $f_2 = f_3 - f_1$ in a process called “frequency up-conversion”.

Optical parametric amplification is fundamentally similar to second harmonic generation, with the only difference being in the direction of power flow. In the special case where $f_1 = f_2$, the two processes are exactly the reverse of each other and this results in what is known as “degenerate parametric amplification”. It can be shown that for parametric oscillation to occur, the pump frequency f_3 needs to be twice that of the signal frequency f_1 (or f_2), and that the pump phase ϕ relative to the signal phase must be 0 or an integer multiple of π ; see, e.g., [65]. Here, the pump signal refers to the high intensity electromagnetic field and the input signal is the low intensity fundamental field. Moreover, a phase shift of $\pi/2$ or $(2n + 1)\pi/2$ between the two fields, where n is an integer, results in the attenuation of the input signal. The degenerate parametric amplifier thus

acts as a “phase sensitive amplifier”. Our focus in this part of the thesis is to model and control this particular process which is the basis of “squeezing” effects observed in optical experiments.

10.4 Motivation and Problem Description

One of the main problems associated with the generation of squeezed states is due to what is known in the physics literature as “dephasing”; see [6]. Dephasing adds considerable phase noise to both the fundamental and second-harmonic fields inside the optical cavity. Moreover, it also directly affects the detuning variables Δ_a and Δ_b which need to be minimised or kept close to zero if any squeezing is to be obtained. The detuning variables here refer to the frequency difference between the input laser beams and the respective optical fields set-up inside the optical cavity, as would be used to generate squeezed states of light; see (3.3). This noise is also referred to as laser phase noise and if unaccounted for, it can completely destroy any squeezing achieved.

The approach traditionally used in the physics literature for the control of optical squeezer has been a combination of proportional, integral and derivative control. While this approach can work well, it relies on the designer’s experience and does not efficiently use information available about the system to be controlled. We propose a systematic approach to control optical squeezers. Our approach generates an optimal controller, given information about the dynamics of the system, the noises entering the system, and using a performance criterion which quantifies a suitable control objective. Here, we address the problem of optimally squeezing the amplitude quadrature of the fundamental optical field of light in the presence of external disturbances which include quantum and classical noises. We take into account the complete model of the OPA system, which also includes actuator dynamics used to control the system. It is expected that with the proposed control technique, larger squeezing factors can be achieved. The range of potential applications and also the possibility of better understanding the nature of experiments using squeezed states of light, provide enough motivation to further research this area.

Using suitable parameter values for the optical squeezer, we first calculate the steady-state operating point (intra-cavity field magnitudes and phases) by

solving a set of nonlinear coupled equations for different input phase angles. The strength of the input fields are assumed to be constant. We also explicitly determine analytical expressions for the steady-state operating points (to first order in $\chi^{(2)}$) and compare them with numerical results obtained using exact methods. Depending on the phase angles at which the quantum state noise is squeezed, different types of squeezed states are generated. To determine which type of squeezed state we end up with, we derive the relationship that exists between the output fields and input fields as a result of the application of the input fields of varying phases. In particular, at each operating point, we determine the optical gains of the fundamental and second harmonic fields. We show that depending on the operating point, the fundamental field is amplified or de-amplified to varying extents. More specifically, we show that the level of amplification/de-amplification (gain) follows a cyclical pattern with respect to the phase angles of the input fields. The optical gain then determines the light quadrature that is squeezed. In this way, depending on the type of squeezed states desired (amplitude or phase squeezed states), appropriate field angles are applied and we address the problem of controlling small variations of the input field angles, thus minimising deviations about the given operating point using an LQG controller.

We shall consider three separate approaches to the LQG controller design based on assumptions that we make about the nature of the noises present in the optical squeezer but also on the value of the detuning variables :

1. We consider the detuning variables $\Delta_a = \Delta_b = 0$, and we assume that the laser phase noise can be modelled as integrated white noise without a constant d.c. component associated with it; see [66].
2. We again consider the detuning variables to be zero but this time assume a more realistic model of the laser phase noise. This model has a constant or low frequency component which can only be offset by a constant or slowly varying control signal. Thus we include integral action in our LQG design; see [67].
3. Finally, we consider the more general case where the detuning variables are also subjected to laser phase noise as modelled in Case 2. Here, we propose a multivariable integral LQG controller to regulate the position

of 2 mirrors to achieve frequency lock as well as squeezing in the chosen quadrature; see [68].

Chapter 11

Modelling

The optical parametric oscillator (OPO) primarily consists of a second-order non-linear optical medium enclosed within an optical resonator. Materials showing second-order nonlinearities $\chi^{(2)}$ have the ability to couple a fundamental field (f) to a second harmonic field ($2f$). This coupling forms the basis of operation of the OPO which works by converting an input laser wave into two output waves of lower frequency through nonlinear optical interaction; see also Section 10.3.1. Feedback in a resonator cavity results in the build-up of the waves in a process similar to that seen in an optical laser cavity and in this way, the intracavity fields become quantum correlated, resulting in the generation of squeezed states of light. For more details, the interested reader is referred to [5, 25] and [17].

11.1 Optical Resonator Cavity

A schematic of an OPO driven by two optical fields \hat{A}_{in} and \hat{B}_{in} is shown in Figure 11.1. The quantities \hat{A}_{in} and \hat{B}_{in} are the input fields which set-up the fundamental and second-harmonic intracavity fields \hat{a} and \hat{b} . $\kappa_{a,in}$ and $\kappa_{b,in}$ are the loss rates of the input/output mirrors for the \hat{a} and \hat{b} fields respectively. The parameters $\kappa_{a,l}$ and $\kappa_{b,l}$ are the internal loss rates for the corresponding two fields. Also, $\kappa_a = \kappa_{a,in} + \kappa_{a,l}$ and $\kappa_b = \kappa_{b,in} + \kappa_{b,l}$ are the associated total resonator decay rates. Furthermore, $\delta\hat{A}_l$ and $\delta\hat{B}_l$ represent the vacuum fields due to the internal losses. The output fields are given by \hat{A}_{out} and \hat{B}_{out} .

The quantum mechanical Hamiltonian describing the $\chi^{(2)}$ interactions is given

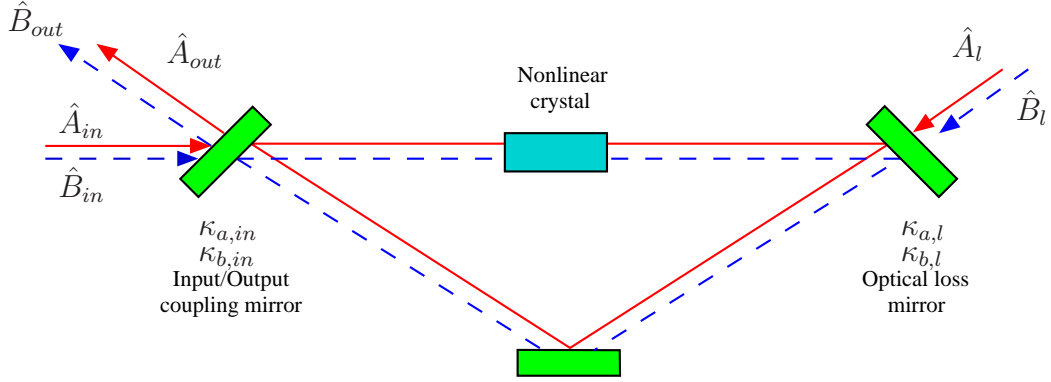


Figure 11.1: Schematic of the Optical Parametric Oscillator.

by

$$\hat{H} = i\chi^{(2)}(\hat{b}^\dagger \hat{a}^2 - \hat{a}^{\dagger 2} \hat{b}), \quad (11.1)$$

where $a(a^\dagger)$ and $b(b^\dagger)$ are the annihilation (creation) operators for the fundamental and second harmonic fields respectively; see [5]. The first term in (11.1) can be interpreted as the annihilation of two photons at the fundamental frequency and the creation of a single photon at the second harmonic frequency. Similarly, the second term in (11.1) can be interpreted as the annihilation of a single photon at the second harmonic frequency and the creation of two photons at the fundamental frequency.

The Heisenberg equations of motion are given by (see [5]):

$$\dot{\hat{a}} = -2\chi^{(2)}\hat{a}^\dagger \hat{b}; \quad (11.2a)$$

$$\dot{\hat{b}} = -i[\hat{b}, \hat{H}] = \chi^{(2)}\hat{a}^2. \quad (11.2b)$$

Bosonic fields (such as photons) obey canonical commutation relations which govern the relationship between canonical conjugate quantities. For example, the relationship between position x and momentum p of a particle is given by

$$[x, p] = i\hbar, \quad (11.3)$$

where $[x, p] = xp - px$ and \hbar is the reduced Planck's constant ($h/2\pi$); see, e.g., [69] for more details. This relationship implies Heisenberg uncertainty principle. Using canonical quantisation of the equations of motion of a ring cavity (a procedure

first undertaken by P. Dirac) and combining it with (11.2), we obtain the dynamics of the OPO for the internal cavity modes as (see also [70]):

$$\dot{\hat{a}} = -(\kappa_a + i\Delta_a)\hat{a} + \chi^{(2)}\hat{a}^\dagger\hat{b} + \sqrt{2\kappa_{a,in}}\hat{A}_{in} + \sqrt{2\kappa_{a,l}}\delta\hat{A}_l; \quad (11.4a)$$

$$\dot{\hat{b}} = -(\kappa_b + i\Delta_b)\hat{b} - \frac{1}{2}\chi^{(2)}\hat{a}^2 + \sqrt{2\kappa_{b,in}}\hat{B}_{in} + \sqrt{2\kappa_{b,l}}\delta\hat{B}_l; \quad (11.4b)$$

where Δ_a and Δ_b represent the frequency mismatches (detuning variables) which are defined as the difference between the respective resonant frequency of the cavity and the laser frequency. The output fields are given by:

$$\hat{A}_{out} = \sqrt{2\kappa_{a,in}}\hat{a} - \hat{A}_{in}; \quad (11.5a)$$

$$\hat{B}_{out} = \sqrt{2\kappa_{b,in}}\hat{b} - \hat{B}_{in}. \quad (11.5b)$$

11.2 Model Description using Quadrature Operators

As explained in Section 2.4, the amplitude and phase quadratures operators provide a particularly useful description of the properties of light. For convenience, we define them here again for the optical fields \hat{a} and \hat{b} :

$$X_a^+ = \hat{a} + \hat{a}^\dagger; \quad X_a^- = i(\hat{a}^\dagger - \hat{a}); \quad (11.6a)$$

$$X_b^+ = \hat{b} + \hat{b}^\dagger; \quad X_b^- = i(\hat{b}^\dagger - \hat{b}). \quad (11.6b)$$

The quadratures of the input and noise fields can similarly be defined as:

$$X_{Ain}^+ = \hat{A}_{in} + \hat{A}_{in}^\dagger; \quad X_{Ain}^- = i(\hat{A}_{in}^\dagger - \hat{A}_{in}); \quad (11.7a)$$

$$X_{\delta A,l}^+ = \delta\hat{A}_l + \delta\hat{A}_l^\dagger; \quad X_{\delta A,l}^- = i(\delta\hat{A}_l^\dagger - \delta\hat{A}_l); \quad (11.7b)$$

$$X_{Bin}^+ = \hat{B}_{in} + \hat{B}_{in}^\dagger; \quad X_{Bin}^- = i(\hat{B}_{in}^\dagger - \hat{B}_{in}); \quad (11.7c)$$

$$X_{\delta B,l}^+ = \delta\hat{B}_l + \delta\hat{B}_l^\dagger; \quad X_{\delta B,l}^- = i(\delta\hat{B}_l^\dagger - \delta\hat{B}_l). \quad (11.7d)$$

Then, the dynamics of the optical subsystem can be rewritten in terms of the quadratures as:

$$\begin{aligned}\dot{X}_a^+ &= -\kappa_a X_a^+ + \Delta_a X_a^- + \frac{1}{2}\chi^{(2)}(X_a^+ X_b^+ + X_a^- X_b^-) \\ &\quad + \sqrt{2\kappa_{a,in}} X_{Ain}^+ + \sqrt{2\kappa_{a,l}} X_{\delta A,l}^+;\end{aligned}\quad (11.8a)$$

$$\begin{aligned}\dot{X}_a^- &= -\kappa_a X_a^- - \Delta_a X_a^+ + \frac{1}{2}\chi^{(2)}(X_a^+ X_b^- - X_a^- X_b^+) \\ &\quad + \sqrt{2\kappa_{a,in}} X_{Ain}^- + \sqrt{2\kappa_{a,l}} X_{\delta A,l}^-;\end{aligned}\quad (11.8b)$$

$$\begin{aligned}\dot{X}_b^+ &= -\kappa_b X_b^+ + \Delta_b X_b^- - \frac{1}{4}\chi^{(2)}(X_a^{+2} - X_a^{-2}) \\ &\quad + \sqrt{2\kappa_{b,in}} X_{Bin}^+ + \sqrt{2\kappa_{b,l}} X_{\delta B,l}^+;\end{aligned}\quad (11.8c)$$

$$\begin{aligned}\dot{X}_b^- &= -\kappa_b X_b^- - \Delta_b X_b^+ - \frac{1}{2}\chi^{(2)} X_a^+ X_a^- \\ &\quad + \sqrt{2\kappa_{b,in}} X_{Bin}^- + \sqrt{2\kappa_{b,l}} X_{\delta B,l}^-.\end{aligned}\quad (11.8d)$$

The output fields are similarly expressed as

$$X_{Aout}^+ = \sqrt{2\kappa_{a,in}} X_a^+ - X_{Ain}^+; \quad (11.9a)$$

$$X_{Aout}^- = \sqrt{2\kappa_{a,in}} X_a^- - X_{Ain}^-; \quad (11.9b)$$

$$X_{Bout}^+ = \sqrt{2\kappa_{b,in}} X_b^+ - X_{Bin}^+; \quad (11.9c)$$

$$X_{Bout}^- = \sqrt{2\kappa_{b,in}} X_b^- - X_{Bin}^-. \quad (11.9d)$$

11.3 Linearised Model of the OPO

While nonlinear properties are essential for the generation of squeezed states of light, we only need to consider first order terms in the variations to obtain elliptical contours and Gaussian distribution functions for the states; see [5]. Thus, we can linearise the dynamics of the optical subsystem (11.8a)–(11.8d) without losing the important characteristic features of the optical squeezer. In this way, we model the behaviour of the system for small perturbations about a steady state operating point of the system. The linearised dynamics of the OPO

are given by:

$$\begin{aligned}\delta\dot{X}_a^+ &= -\kappa_a\delta X_a^+ + \bar{X}_a^-\Delta_a \\ &\quad + \frac{1}{2}\chi^{(2)}(\bar{X}_b^+\delta X_a^+ + \bar{X}_b^-\delta X_a^- + \bar{X}_a^+\delta X_b^+ + \bar{X}_a^-\delta X_b^-) \\ &\quad + \sqrt{2\kappa_{a,in}}\delta X_{Ain}^+ + \sqrt{2\kappa_{a,l}}X_{\delta A,l}^+;\end{aligned}\quad (11.10a)$$

$$\begin{aligned}\delta\dot{X}_a^- &= -\kappa_a\delta X_a^- - \bar{X}_a^+\Delta_a \\ &\quad + \frac{1}{2}\chi^{(2)}(\bar{X}_b^-\delta X_a^+ - \bar{X}_b^+\delta X_a^- - \bar{X}_a^-\delta X_b^+ + \bar{X}_a^+\delta X_b^-) \\ &\quad + \sqrt{2\kappa_{a,in}}\delta X_{Ain}^- + \sqrt{2\kappa_{a,l}}X_{\delta A,l}^-;\end{aligned}\quad (11.10b)$$

$$\begin{aligned}\delta\dot{X}_b^+ &= -\kappa_b\delta X_b^+ + \bar{X}_b^-\Delta_b - \frac{1}{2}\chi^{(2)}(\bar{X}_a^+\delta X_a^+ - \bar{X}_a^-\delta X_a^-) \\ &\quad + \sqrt{2\kappa_{b,in}}\delta X_{Bin}^+ + \sqrt{2\kappa_{b,l}}X_{\delta B,l}^+;\end{aligned}\quad (11.10c)$$

$$\begin{aligned}\delta\dot{X}_b^- &= -\kappa_b\delta X_b^- - \bar{X}_b^+\Delta_b - \frac{1}{2}\chi^{(2)}(\bar{X}_a^-\delta X_a^+ + \bar{X}_a^+\delta X_a^-) \\ &\quad + \sqrt{2\kappa_{b,in}}\delta X_{Bin}^- + \sqrt{2\kappa_{b,l}}X_{\delta B,l}^-.\end{aligned}\quad (11.10d)$$

The corresponding linearised output field equations are expressed as

$$\delta X_{Aout}^+ = \sqrt{2\kappa_{a,in}}\delta X_a^+ - \delta X_{Ain}^+;\quad (11.11a)$$

$$\delta X_{Aout}^- = \sqrt{2\kappa_{a,in}}\delta X_a^- - \delta X_{Ain}^-;\quad (11.11b)$$

$$\delta X_{Bout}^+ = \sqrt{2\kappa_{b,in}}\delta X_b^+ - \delta X_{Bin}^+.\quad (11.11c)$$

$$\delta X_{Bout}^- = \sqrt{2\kappa_{b,in}}\delta X_b^- - \delta X_{Bin}^-.\quad (11.11d)$$

Here, \bar{X}_a^+ , \bar{X}_a^- , \bar{X}_b^+ and \bar{X}_b^- denote the steady-state values of the respective quadratures. These are determined for the given set of input fields and phase angles by solving the nonlinear coupled equations obtained by setting the derivatives of (11.8a)–(11.8d) to zero. We will use the linearised dynamics of the system for designing controllers. Our aim is to maximise the amplitude quadrature squeezing of the fundamental field \hat{a} observed at a given operating point by optimally suppressing the different sources of noise feeding into the system. This aim will be translated into a specific quadratic cost functional to define an LQG optimal control problem; the underlying assumption being that the conditional state associated with a quantum system can be equivalently modelled using a classical system; see [71–74].

11.4 Piezo-Electric Actuator Model

Depending on the particular control configuration we will be working with, one or two piezo-electric actuators will be used to control the phase of the optical input fields entering the system. We describe the piezo-actuators attached to corresponding mirrors as general second-order systems as follows:

$$\begin{aligned} \begin{bmatrix} \dot{\xi}_1 \\ \dot{\xi}_2 \end{bmatrix} &= \begin{bmatrix} 0 & 1 \\ -r_2 & -r_1 \end{bmatrix} \begin{bmatrix} \xi_1 \\ \xi_2 \end{bmatrix} + \begin{bmatrix} 0 \\ 1 \end{bmatrix} w_1 + \begin{bmatrix} 0 \\ 1 \end{bmatrix} u; \\ \delta X_{pzt} &= [c_2 \ c_1] \begin{bmatrix} \xi_1 \\ \xi_2 \end{bmatrix} + w_2. \end{aligned} \quad (11.12)$$

Here, ξ_1 represents deviation in the position of the mirror which controls the phase of a given input field, and ξ_2 represents the velocity of the mirror. The quantity w_1 represents process noise which arises due to mechanical fluctuations in the beam path and w_2 represents quantum/classical output noises entering the piezo-actuator. The complete linearised system can then be modelled in state-space form as:

$$\dot{x} = Ax + B_1u + B_2w; \quad (11.13a)$$

$$y = Cx + Dw. \quad (11.13b)$$

We leave the detailed description of the system represented by (11.13) for specific cases that we shall consider in future chapters.

Chapter 12

Steady-state Analysis of the Optical Squeezer

At steady-state, there is a steady flow of energy between the intracavity optical fields. For the optical squeezer, the flow of energy is predominantly from the second-harmonic field to the fundamental field. In this chapter, we determine the relationship that exists between the phase of the intracavity fields and the type of squeezed states obtained. It is not possible to have both amplitude and phase quadrature squeezing at a given operating point. We choose the phase of the input fields such that suitable stable steady-state operating points are obtained, which in turn allows quantum noise squeezing in specific quadratures.

12.1 Exact Steady-state solution

The nonlinearity present in the system makes it difficult to explicitly determine expressions to describe the behaviour of the optical squeezer at steady-state. We solve for the exact stable steady-state operating point of the system numerically using conventional software such as MATLAB[®]. In particular, we used the MATLAB[®] command `fsolve` which uses the ‘Trust-Region’ technique and computes the step size using Powell procedure; see [75]. The algorithm is efficient and can be more robust than the Gauss-Newton method especially when starting far from a solution. The parameter values we used are chosen to reflect those of an optical squeezer in our optics laboratory and are shown in Table 12.1.

Using this numerical approach, it was found that for any combination of

Model parameter	Value	Units
κ_a	1×10^5	rad/s
κ_b	1×10^9	rad/s
$\kappa_{a,l}$	5×10^3	rad/s
$\kappa_{b,l}$	5×10^7	rad/s
$\kappa_{a,in}$	9.5×10^4	rad/s
$\kappa_{b,in}$	9.5×10^8	rad/s
$\chi^{(2)}$	3×10^{-2}	—
\bar{A}_{in}	2×10^6	$\sqrt{\text{rad/s}}$
\bar{B}_{in}	2×10^{10}	$\sqrt{\text{rad/s}}$

Table 12.1: Optical Parametric Oscillator Model Parameter Values.

field inputs \hat{A}_{in} and \hat{B}_{in} , we always obtain one stable steady-state solution. An analytical examination of the steady-states and the stability of nonlinear optical systems is given in [76], where the interaction of a light beam with its second-harmonic is investigated. The paper focuses on non-equilibrium steady-states and considers the use of the device as a switch, when the system transitions from different steady-states. More importantly, it is shown (see Section 5 of [76]) that provided

$$\delta = \left(\frac{C}{2}\right)^2 + \left(\frac{B-A}{3}\right)^3 \geq 0; \quad (12.1)$$

where

$$A = \frac{2|\bar{B}_{in}|}{\chi^{(2)}}, \quad B = \frac{2\kappa_a\kappa_b}{\chi^{(2)^2}}, \quad \text{and} \quad C = \frac{2\kappa_b|\bar{A}_{in}|}{\chi^{(2)^2}};$$

then there exists only one stable equilibrium point for the nonlinear system. Condition (12.1) is satisfied by our chosen optical parameters in Table 12.1. The stability of the steady-state solution can be checked by substituting the steady-state values \bar{X}_a^+ , \bar{X}_a^- , \bar{X}_b^+ and \bar{X}_b^- in (11.10a)–(11.10d) and calculating the eigenvalues of the corresponding linearised system.

12.2 Steady-state solution to first order in $\chi^{(2)}$

It is also possible to obtain explicit expressions for the steady-state solution if we allow for some approximation in solving for \hat{a} and \hat{b} in (11.4a)–(11.4b). Since $\chi^{(2)}$ represents the nonlinearity that couples the two optical fields, we approximate the solution to our system by considering only first order terms in $\chi^{(2)}$. It is known that the higher order terms contribute only small components to the exact solution and this justifies our assumption. We here determine expressions for those equilibrium operating point(s) using both polar coordinates and the field quadratures.

12.2.1 Polar form solution

The steady-state solution of the system (to first-order in $\chi^{(2)}$) is determined by equating (11.4a) and (11.4b) to zero and solving for \hat{a} and \hat{b} :

$$-\kappa_a \hat{a} + \chi^{(2)} \hat{a}^\dagger \hat{b} + \sqrt{2\kappa_{a,in}} \hat{A}_{in} = 0; \quad (12.2a)$$

$$-\kappa_b \hat{b} - \frac{1}{2} \chi^{(2)} \hat{a}^2 + \sqrt{2\kappa_{b,in}} \hat{B}_{in} = 0. \quad (12.2b)$$

From (12.2b),

$$\hat{b} = -\frac{1}{\kappa_b} \left(\frac{1}{2} \chi^{(2)} \hat{a}^2 - \sqrt{2\kappa_{b,in}} \hat{B}_{in} \right). \quad (12.3)$$

Substituting (12.3) into (12.2a), and keeping terms linear in $\chi^{(2)}$, we have

$$-\kappa \hat{a} + \chi^{(2)} \hat{a}^\dagger \frac{\sqrt{2\kappa_{b,in}}}{\kappa_b} \hat{B}_{in} + \sqrt{2\kappa_{a,in}} \hat{A}_{in} = 0. \quad (12.4)$$

Taking the conjugate transpose of (12.4), we have

$$-\kappa \hat{a}^\dagger + \chi^{(2)} \hat{a} \frac{\sqrt{2\kappa_{b,in}}}{\kappa_b} \hat{B}_{in}^\dagger + \sqrt{2\kappa_{a,in}} \hat{A}_{in}^\dagger = 0. \quad (12.5)$$

From (12.5),

$$\hat{a}^\dagger = \chi^{(2)} \frac{\sqrt{2\kappa_{b,in}}}{\kappa_a \kappa_b} \hat{a} \hat{B}_{in}^\dagger + \frac{\sqrt{2\kappa_{a,in}}}{\kappa_a} \hat{A}_{in}^\dagger. \quad (12.6)$$

Substituting (12.6) into (12.4) and keeping terms linear in $\chi^{(2)}$, we can determine

$$\hat{a} = 2\chi^{(2)} \frac{\sqrt{\kappa_{a,in}\kappa_{b,in}}}{\kappa_a^2\kappa_b} \hat{A}_{in}^\dagger \hat{B}_{in} + \frac{\sqrt{2\kappa_{a,in}}}{\kappa_a} \hat{A}_{in}^\dagger. \quad (12.7)$$

Finally substituting (12.7) into (12.3), we have

$$\hat{b} = \frac{\sqrt{2\kappa_{b,in}}}{\kappa_b} \hat{B}_{in} - \chi^{(2)} \frac{\kappa_{a,in}}{\kappa_a^2\kappa_b} \hat{A}_{in}^2. \quad (12.8)$$

If we denote the steady-state values of the fields \hat{f} by \bar{f} , we can rewrite the steady-state values of the fundamental and the second-harmonic fields as:

$$\bar{a} = e^{i\bar{\theta}_{a,in}} \left[\frac{\sqrt{2\kappa_{a,in}}}{\kappa_a} |\bar{A}_{in}| + 2\chi^{(2)} \frac{\sqrt{\kappa_{a,in}\kappa_{b,in}}}{\kappa_a^2\kappa_b} |\bar{A}_{in}| |\bar{B}_{in}| e^{i(\bar{\theta}_{b,in}-2\bar{\theta}_{a,in})} \right]; \quad (12.9a)$$

$$\bar{b} = e^{i\bar{\theta}_{b,in}} \left[\frac{\sqrt{2\kappa_{b,in}}}{\kappa_b} |\bar{B}_{in}| - \chi^{(2)} \frac{\kappa_{a,in}}{\kappa_a^2\kappa_b} |\bar{A}_{in}|^2 e^{-i(\bar{\theta}_{b,in}-2\bar{\theta}_{a,in})} \right]; \quad (12.9b)$$

where the steady state values of the input fields are expressed in polar coordinates as $\bar{A}_{in} = |\bar{A}_{in}|e^{i\bar{\theta}_{a,in}}$ and $\bar{B}_{in} = |\bar{B}_{in}|e^{i\bar{\theta}_{b,in}}$. Also, we write $\bar{a} = |\bar{a}|e^{i\bar{\theta}_a}$ and $\bar{b} = |\bar{b}|e^{i\bar{\theta}_b}$.

12.2.2 Solution in terms of the field quadratures

The steady-state solution of the optical system (to first-order in $\chi^{(2)}$) can also be expressed by expanding the field quadratures in terms of their coherent amplitude and quantum noise operators, so that a quadrature $X_i^\pm = \bar{X}_i^\pm + \delta X_i^\pm, i = a, b$ where \bar{X}_i^\pm and δX_i^\pm represent the expectation value and small variations of the field quadratures respectively. The expectation value of the field quadratures (to

first order in $\chi^{(2)}$) are correspondingly given by:

$$\bar{X}_a^+ = \frac{\sqrt{2\kappa_{a,in}}}{\kappa_a}(\bar{A}_{in} + \bar{A}_{in}^\dagger) + 2\chi^{(2)}\frac{\sqrt{\kappa_{a,in}\kappa_{b,in}}}{\kappa_a^2\kappa_b}(\bar{A}_{in}^\dagger\bar{B}_{in} + \bar{A}_{in}\bar{B}_{in}^\dagger); \quad (12.10a)$$

$$\bar{X}_a^- = i \left[\frac{\sqrt{2\kappa_{a,in}}}{\kappa_a}(\bar{A}_{in}^\dagger - \bar{A}_{in}) + 2\chi^{(2)}\frac{\sqrt{\kappa_{a,in}\kappa_{b,in}}}{\kappa_a^2\kappa_b}(\bar{A}_{in}\bar{B}_{in}^\dagger - \bar{A}_{in}^\dagger\bar{B}_{in}) \right]; \quad (12.10b)$$

$$\bar{X}_b^+ = \frac{\sqrt{2\kappa_{b,in}}}{\kappa_b}(\bar{B}_{in} + \bar{B}_{in}^\dagger) - \chi^{(2)}\frac{\kappa_{a,in}}{\kappa_a^2\kappa_b}(\bar{A}_{in}^2 + \bar{A}_{in}^{\dagger 2}); \quad (12.10c)$$

$$\bar{X}_b^- = i \left[\frac{\sqrt{2\kappa_{b,in}}}{\kappa_b}(\bar{B}_{in}^\dagger - \bar{B}_{in}) - \chi^{(2)}\frac{\kappa_{a,in}}{\kappa_a^2\kappa_b}(\bar{A}_{in}^{\dagger 2} - \bar{A}_{in}^2) \right]. \quad (12.10d)$$

12.3 Steady-state Behaviour of the Optical Squeezer

In this section, we analyse the effect of various parameters (in particular the phase angles of the input fields) on the system at steady-state, using both the exact numerical method and the approximate equations described in Section 12.2. The results are represented graphically below. Unless mentioned, all parameters are kept constant (as shown in Table 12.1) except for the ones specifically identified.

1. First, we investigate the effect of changing the phase $\bar{\theta}_{a,in}$ of the input field \hat{A}_{in} on the intracavity field phase angle $\bar{\theta}_a$. The phase of the input field is varied from 0 to $2\pi(360^\circ)$. Figure 12.1(a) shows that the phase of the fundamental intracavity field follows that of the fundamental input field very closely for $\bar{\theta}_{b,in} = 0$. Moreover, the solution obtained using only linear terms in $\chi^{(2)}$ and the numerical solution can be seen to agree very well with each other. The procedure is repeated at a different phase angle $\bar{\theta}_{b,in} = \pi$ for the harmonic input field \hat{B}_{in} and a similar relationship is seen; see Figure 12.1(b). We also show the variation of the phase $\bar{\theta}_{a,out}$ of the fundamental output field \hat{A}_{out} , with the phase of the input field $\bar{\theta}_{a,in}$. We choose the same combination of phase angles $\bar{\theta}_{b,in}$ in Figure 12.1(c) and 12.1(d). It can be seen that the following approximations hold at steady-state:

$$\bar{\theta}_{a,out} \simeq \bar{\theta}_a \simeq \bar{\theta}_{a,in}. \quad (12.11)$$

The variation of the phase of the intracavity field \hat{b} and the output field

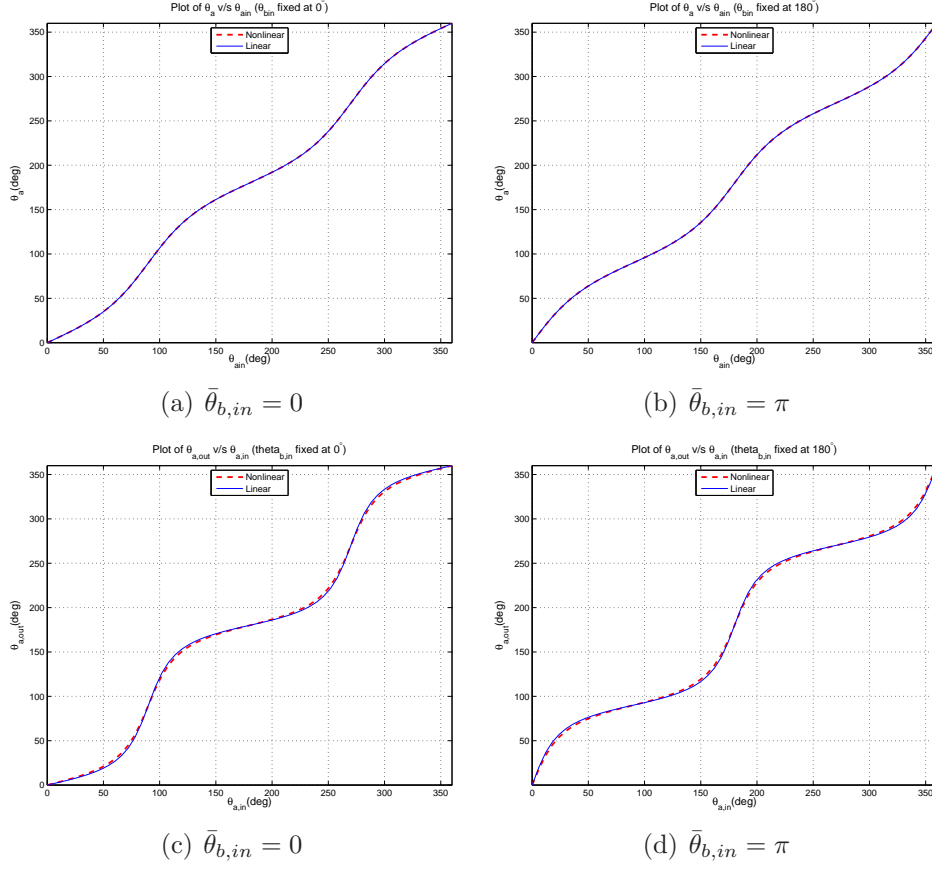
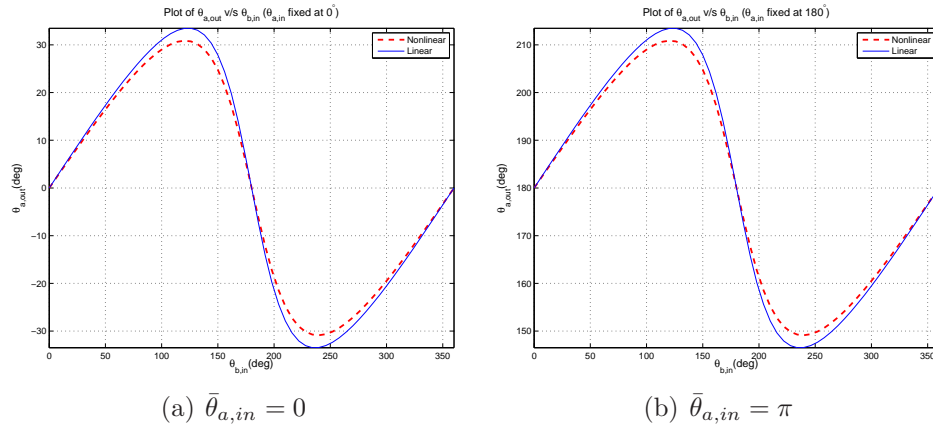


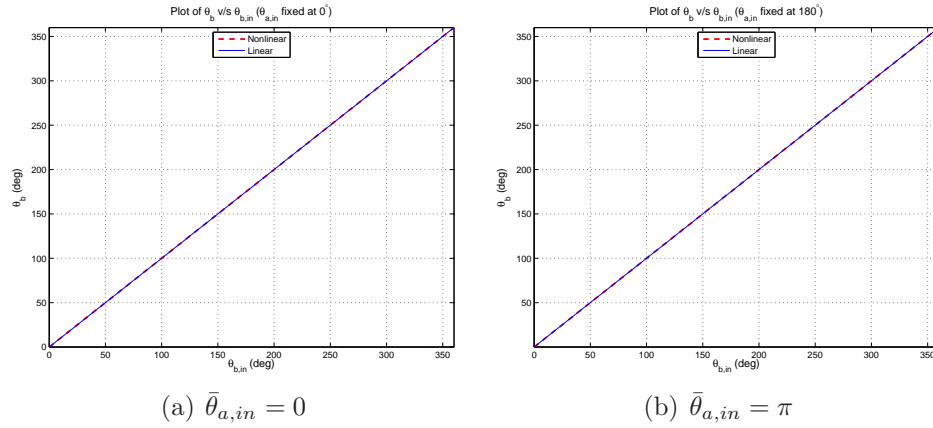
Figure 12.1: Variation of $\bar{\theta}_a$ and $\bar{\theta}_{a,out}$ with respect to $\bar{\theta}_{a,in}$.

\hat{B}_{out} with the phase of the input field \hat{A}_{in} is also determined. We found that varying $\bar{\theta}_{a,in}$ does not have any noticeable effect on the second harmonic output fields. This result is as expected given the large difference in the field strengths of the input fields \hat{A}_{in} and \hat{B}_{in} and the predominant direction of energy flow in the OPO at steady-state.

2. Next, we consider the variation of the phase angle $\bar{\theta}_{a,out}$ of the output field \hat{A}_{out} , with respect to the phase $\bar{\theta}_{b,in}$ of the second harmonic input field \hat{B}_{in} . Figure 12.2 shows that the input field \hat{B}_{in} has considerable effect on the output field \hat{A}_{out} . This is as expected given the strength of the second harmonic field.
3. We repeat the above procedure for the second harmonic field. It is found that the phase $\bar{\theta}_b$ of the intracavity field \hat{b} varies linearly with respect to

Figure 12.2: Variation of $\bar{\theta}_{a,out}$ with respect to $\bar{\theta}_{b,in}$.

the phase $\theta_{b,in}$ of the input field \hat{B}_{in} , as shown in Figure 12.3. Moreover, the phase of the output field $\bar{\theta}_{b,out}$ follows $\bar{\theta}_b$ very closely. We thus obtain

Figure 12.3: Variation of $\bar{\theta}_b$ with respect to $\bar{\theta}_{b,in}$.

the approximations:

$$\bar{\theta}_{b,out} \simeq \bar{\theta}_{b,in} \simeq \bar{\theta}_b. \quad (12.12)$$

4. Figure 12.4(a) and Figure 12.4(b) show the variation of the magnitude of the intracavity field \hat{a} with respect to $\bar{\theta}_{a,in}$. We consider two cases when $\bar{\theta}_{b,in} = 0$ and π . It is clear that there is a large cyclic change in the strength of the intracavity field \hat{a} as the phase angle $\bar{\theta}_{a,in}$ is varied. Similarly, Figure 12.4(c)

and Figure 12.4(d) show the variation of the magnitude of intracavity field \hat{a} with respect to $\bar{\theta}_{b,in}$. Here, we consider two cases when $\bar{\theta}_{a,in} = 0$ and π . The variation of field \hat{a} goes through only one cycle as we vary $\bar{\theta}_{b,in}$ from 0 to 2π in this case. This is as expected since the frequency of input field \hat{B}_{in} is twice that of the input field \hat{A}_{in} . The behaviour of the system as a “phase sensitive” amplifier is thus apparent. Also, it should be noted that the approximate and numerical solutions show a significant difference in this case.

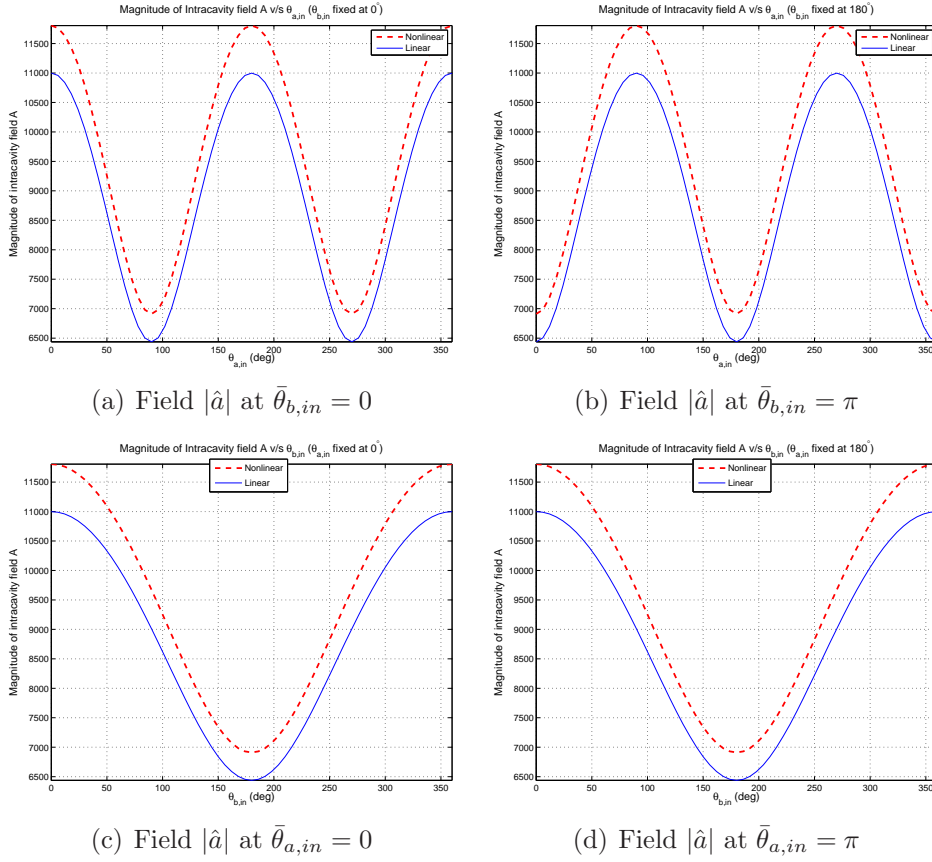


Figure 12.4: Variation of the magnitude of the intracavity field \hat{a} with respect to $\bar{\theta}_{a,in}$ and $\bar{\theta}_{b,in}$.

- Next, we analyse the optical parametric gain of the fundamental and harmonic fields, i.e., the ratio of $|\hat{A}_{out}|^2/|\hat{A}_{in}|^2$ and $|\hat{B}_{out}|^2/|\hat{B}_{in}|^2$. Figures 12.5(a) and 12.5(b) show the variation of $|\hat{A}_{out}|^2/|\hat{A}_{in}|^2$ and $|\hat{B}_{out}|^2/|\hat{B}_{in}|^2$ with respect to the phase angle $\bar{\theta}_{a,in}$ of the fundamental input field \hat{A}_{in} . Similarly,

Figures 12.5(c) and 12.5(d) show the variation of the gain $|\hat{A}_{out}|^2/|\hat{A}_{in}|^2$ and $|\hat{B}_{out}|^2/|\hat{B}_{in}|^2$ with respect to the phase angle $\bar{\theta}_{b,in}$ of the harmonic input field \hat{B}_{in} . The gain $|\hat{B}_{out}|^2/|\hat{B}_{in}|^2$ of the harmonic field is negligible

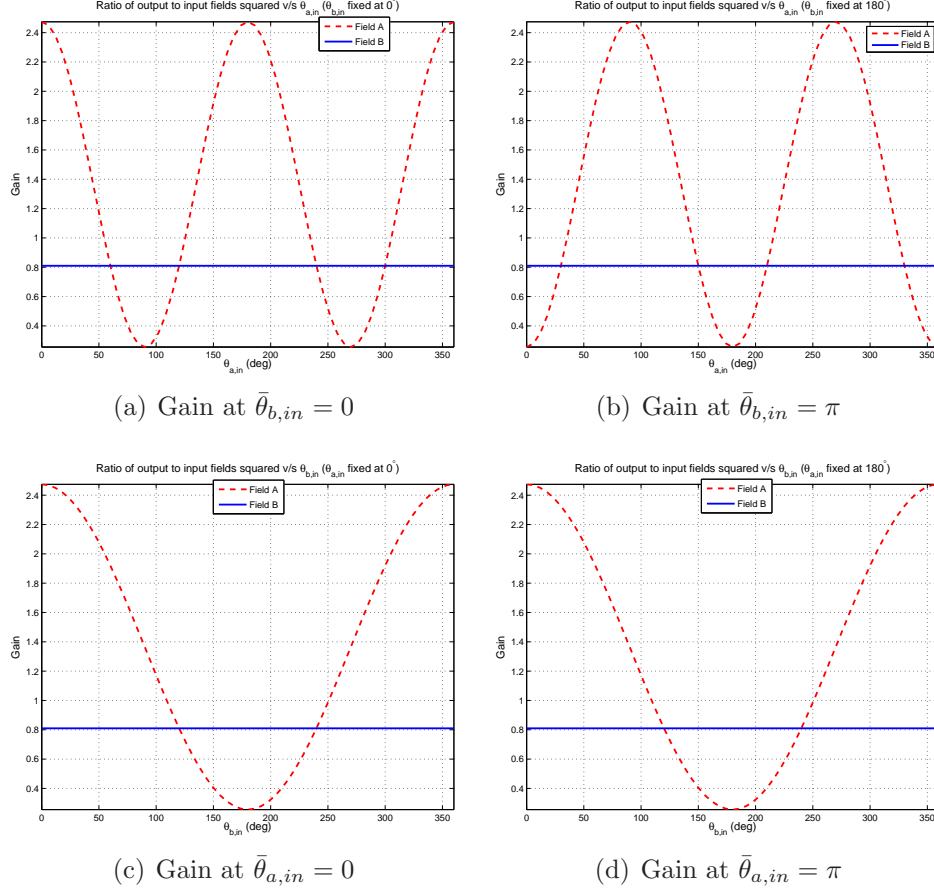


Figure 12.5: Variation of gain $|\hat{A}_{out}|^2/|\hat{A}_{in}|^2$ and $|\hat{B}_{out}|^2/|\hat{B}_{in}|^2$.

and barely changes with the phase angles of the input fields. On the other hand, the optical field \hat{A}_{out} is clearly affected in all of the figures. Again, the variation of the gain $|\hat{A}_{out}|^2/|\hat{A}_{in}|^2$ is seen to go through 2 cycles when $\bar{\theta}_{a,in}$ is varied, compared to only one cycle with variation in $\bar{\theta}_{b,in}$. Figure 12.5 shows that the gain $|\hat{A}_{out}|^2/|\hat{A}_{in}|^2$ can be controlled by fixing either $\bar{\theta}_{a,in}$ or $\bar{\theta}_{b,in}$ and varying the other field angle.

6. In Figure 12.6, we vary the phase $\bar{\theta}_{a,in}$ of the input field \hat{A}_{in} and determine its effect on the gain $|\hat{A}_{out}|^2/|\hat{A}_{in}|^2$ of the fundamental field. We repeat the process for different parameter values of $\chi^{(2)}$. We find that the parameter

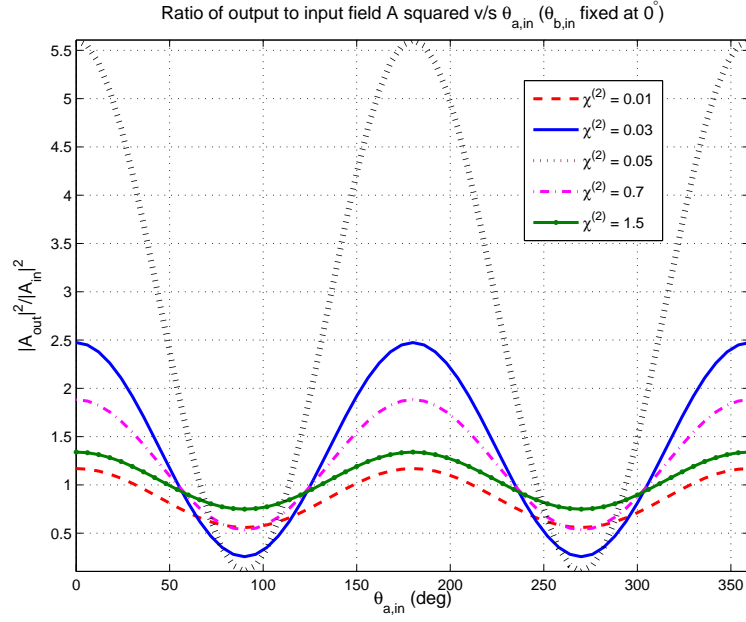


Figure 12.6: Variation of the gain $|\hat{A}_{out}|^2/|\hat{A}_{in}|^2$ of the fundamental output field with respect to $\theta_{a,in}$ for different $\chi^{(2)}$.

$\chi^{(2)}$ significantly affects the gain of the optical field $|\hat{A}_{out}|^2/|\hat{A}_{in}|^2$. Increasing $\chi^{(2)}$ increases the coupling between the fields \hat{A} and \hat{B} which in turn increases the steady-state energy flow from intracavity field \hat{b} to \hat{a} . However, this effect is reversed beyond a certain value of $\chi^{(2)}$. This was shown in Figure 12.6 for the cases $\chi^{(2)} = 0.7$ and 1.5 .

7. Next, we select a given pair of $\bar{\theta}_{a,in}$ and $\bar{\theta}_{b,in}$ and investigate the effect of varying $\chi^{(2)}$ on the gain $|\hat{A}_{out}|^2/|\hat{A}_{in}|^2$ of the fundamental field, as shown in Figure 12.7. This plot shows that optimal gain $|\hat{A}_{out}|^2/|\hat{A}_{in}|^2$ can be achieved at a $\chi^{(2)} \approx 0.115$. However, nonlinear materials with such large values of $\chi^{(2)}$ are not practically realisable. Moreover, it is well known that $\chi^{(2)}$ is a function of numerous factors, including temperature, electromagnetic field strength and angle of orientation (see [17]), making it extremely difficult to operate at any optimally chosen value. For all future work presented from this point onwards, we will assume that $\chi^{(2)}$ is constant.

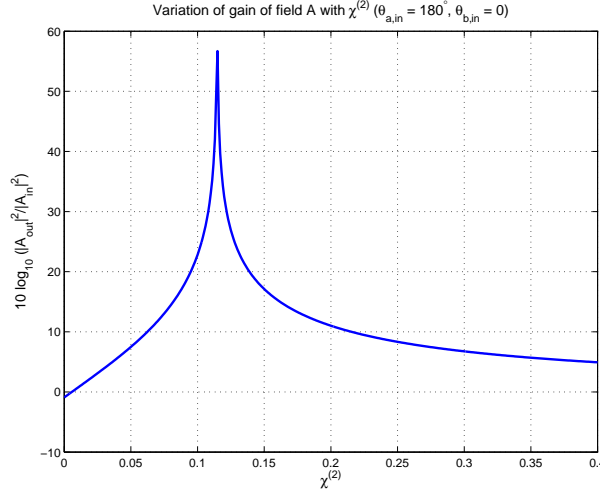


Figure 12.7: Variation of the parametric gain $|\hat{A}_{out}|^2/|\hat{A}_{in}|^2$ of the fundamental field (in dB) with respect to $\chi^{(2)}$.

12.4 Optical Parametric Gain of the Fundamental Intracavity field \hat{a}

In this section, we put together some of the analysis performed in the previous section in an attempt to formulate some suitable mathematical condition that result in the generation of specific type of squeezed states of light. We consider the variation of the steady-state gain of the OPO under some specific conditions which are satisfied in our set-up shown in Figure 11.1. If $\kappa_a \ll \kappa_b$, and the harmonic field \hat{B}_{in} is much more intense than the fundamental field \hat{A}_{in} , then energy will be predominantly transferred from field \hat{b} to field \hat{a} . The steady-state optical gain of the fundamental field $|\hat{A}_{out}|^2/|\hat{A}_{in}|^2$, is then of much greater magnitude than the corresponding gain with respect to the field \hat{b} . In fact, we have shown that field \hat{b} is virtually undepleted by its interaction with field \hat{a} when the above conditions are met; see Figure 12.5. Here, we determine the variation of the gain $|\hat{A}_{out}|^2/|\hat{A}_{in}|^2$ with respect to the quantities $\bar{\theta}_{a,in}$ and $\bar{\theta}_{b,in}$. This is equivalent to combining numerous plots of the type shown in Figure 12.5 for the fundamental field for different phase angles and the result is shown in Figure 12.8. The parameter values we use are the same as shown in Table 12.1. The variation of the gain $|\hat{A}_{out}|^2/|\hat{A}_{in}|^2$ with respect to the phase angles of the input fields,

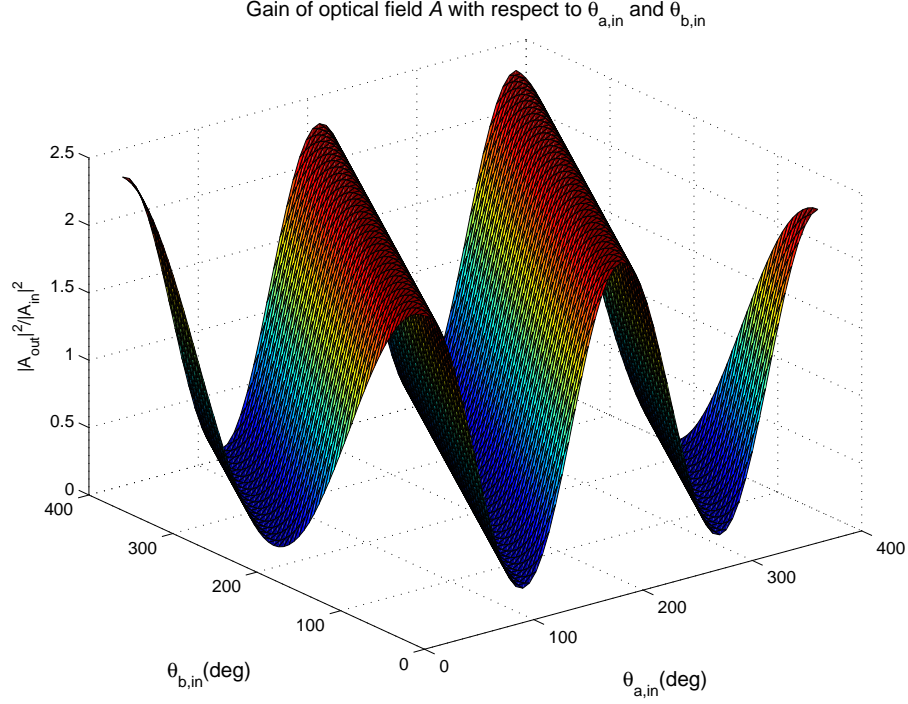


Figure 12.8: Variation of the gain $|\hat{A}_{out}|^2/|\hat{A}_{in}|^2$ with $\bar{\theta}_{a,in}$ and $\bar{\theta}_{b,in}$.

as shown in Figure 12.8 is used in the determination of the operating point we would choose to obtain maximum squeezing. In particular, depending on the quadrature we would like to squeeze, we choose appropriate operating point(s) corresponding to a given pair of input field angles $\bar{\theta}_{a,in}$ and $\bar{\theta}_{b,in}$ such that we have the appropriate level of steady-state gain $|\hat{A}_{out}|^2/|\hat{A}_{in}|^2$.

Figure 12.9 illustrates the way in which we determine the type and extent of the quadrature squeezing achieved. It shows the effect of varying the steady-state gain $|\hat{A}_{out}|^2/|\hat{A}_{in}|^2$ of a coherent state of light (minimum uncertainty state) denoted \hat{A}_{out} . The symmetric circular region represents the uncertainty associated with a given coherent state due to quantum noise. This noise is equally divided between the two quadratures. The diagram shows how amplifying one quadrature by a given amount and de-amplifying the other quadrature by the same amount, a process which does not violate the Heisenberg uncertainty relation, results in a quadrature with an uncertainty level below the SQL. The gain here is, of course, introduced by a phase-sensitive amplifier or parametric amplifier, as provided by an OPO. Using our set-up, we can thus change the noise distribution about the

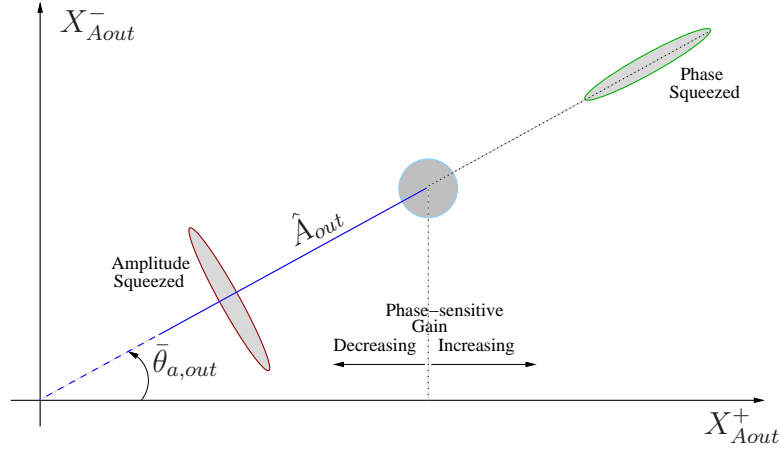


Figure 12.9: Representation of phase sensitive squeezing.

state from being circular and symmetric about the quadratures to elliptical and asymmetric. In particular, the noise variance along a given quadrature increases while that along the other (orthogonal) quadrature decreases proportionately such that the Heisenberg uncertainty principle is not violated

$$\langle \delta X_{Aout}^{+2} \rangle \langle \delta X_{Aout}^{-2} \rangle \geq 1. \quad (12.13)$$

Here $\langle \cdot \rangle$ denotes the quantum expectation value. It should be emphasised that this is only the case because the gain is introduced by a phase-sensitive amplifier (OPO). A simple optical active medium used for this purpose would amplify both quadratures equally, resulting in amplified light with a signal to noise ratio that is worse by about 3 dB; see [5].

Figure 12.9 shows that increasing the steady-state gain results in phase squeezing while decreasing the gain gives rise to amplitude squeezing. In our case, we are interested in maximising the level of amplitude squeezing and we would therefore ideally operate in a region where the optical steady-state gain is at its minimum. From Figure 12.8 and Figure 12.5, we can determine the relationship between $\bar{\theta}_{a,in}$ and $\bar{\theta}_{b,in}$ when the optical gain is at its minimum. To achieve optimal amplitude squeezing, we would then choose the operating point so that

$$\bar{\theta}_{b,in} - 2\bar{\theta}_{a,in} = n\pi; \quad \text{where } n \in \mathbb{Z}. \quad (12.14)$$

Furthermore, the relationship between $\bar{\theta}_{a,in}$ and $\bar{\theta}_a$ and between $\bar{\theta}_{b,in}$ and $\bar{\theta}_b$

as determined from (12.11)–(12.12) show that an equivalent condition to (12.14) for maximum amplitude squeezing of the fundamental field \hat{a} would be

$$\bar{\theta}_b - 2\bar{\theta}_a = n\pi. \tag{12.15}$$

Chapter 13

Preliminary Controller Design

13.1 Standard Quantum Limit

As explained in Sections 2.2 and 2.3, quantum coherent states of light impose equal quantum noise limits on all quadratures, which we shall refer to as the standard quantum limit (SQL). The coupling of the electromagnetic fields inside the resonator cavity of an OPO results in squeezed states of light with quadratures which have noise levels that are less than the SQL. From Equations (11.10a)–(11.10d), it is clear that $\chi^{(2)}$ is responsible for the interaction of the optical fields inside an optical squeezer and we can therefore deduce that SQL is the noise level observed in the output field equations (11.11a)–(11.11d) when $\chi^{(2)}$ is set to zero. Our aim here is to first determine numerical values for the SQL for the optical squeezer under consideration.

As explained before, we are interested in minimising the variance along the quadratures of the fundamental output field \hat{A}_{out} . Depending on the phase angle of the output field, the appropriate quadratures are chosen by rotating the reference axis accordingly. In general, an arbitrary amplitude quadrature, X^θ , can be described as a function of the phase angle θ , according to

$$X^\theta = X^+ \cos \theta + X^- \sin \theta. \quad (13.1)$$

Thus, if we wish to control the amplitude quadrature of the fundamental output

field, the variable whose magnitude we would minimise can be defined as

$$z = \delta X_a^+ \cos \bar{\theta}_{a,out} + \delta X_a^- \sin \bar{\theta}_{a,out}. \quad (13.2)$$

To control the phase quadrature, we would similarly minimise the magnitude of the quantity

$$\begin{aligned} z &= \delta X_a^+ \cos(\bar{\theta}_{a,out} + \frac{\pi}{2}) + \delta X_a^- \sin(\bar{\theta}_{a,out} + \frac{\pi}{2}) \\ &= \delta X_a^- \cos \bar{\theta}_{a,out} - \delta X_a^+ \sin \bar{\theta}_{a,out}. \end{aligned} \quad (13.3)$$

Since in this case, the output of interest is only a function of δX_a^+ and δX_a^- , we only need to consider the two state equations (11.10a)–(11.10b) to determine the SQL. The quantum noises feeding into the optical squeezer are modelled as Gaussian white noise processes with unit covariance. To obtain a finite value for the SQL, we model our measurement device as a first order low pass filter. This is necessary as quantum noises also feed directly through to the controlled variable. In this way, rather than penalising variations at all frequencies equally, we restrict our interest to a more reasonable region. We choose a bandwidth of 1×10^5 rad/s which reflect standard capability of optical measurement devices used for this purpose. Note that choosing a larger bandwidth results in a larger reference value of the SQL. However, our primary concern here is to investigate the reduction or amplification level of noise achieved about this reference value and this is unaffected by the specific numerical value of the SQL. The set-up we used for the SQL determination is as shown in Figure 13.1. Given the filtered

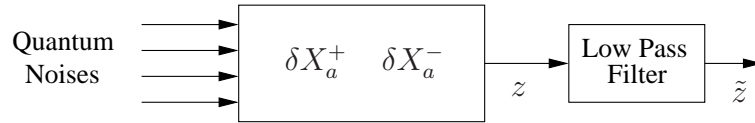


Figure 13.1: Set-up used for the standard quantum noise limit determination.

controlled output \tilde{z} from Figure 13.1, the resulting linearised equations when

$\chi^{(2)} = 0$, including the equations of the first-order low pass filter, is described by:

$$\delta\dot{X}_a^+ = -\kappa_a\delta X_a^+ + \sqrt{2\kappa_{a,in}}\delta X_{Ain}^+ + \sqrt{2\kappa_{a,l}}X_{\delta A,l}^+; \quad (13.4a)$$

$$\delta\dot{X}_a^- = -\kappa_a\delta X_a^- + \sqrt{2\kappa_{a,in}}\delta X_{Ain}^- + \sqrt{2\kappa_{a,l}}X_{\delta A,l}^-; \quad (13.4b)$$

$$\tau\dot{x}_f = -x_f + z; \quad (13.4c)$$

where τ denotes the time-constant of the filter and x_f is the state of the low-pass filter. The controlled output is a filtered version of the output z which is defined to determine variations about the amplitude quadrature of the fundamental output field as in (13.2):

$$\tilde{z} = x_f. \quad (13.5)$$

The linearised system (13.4)–(13.5) can be represented in the form

$$\dot{x} = Ax + B_2w, \quad \tilde{z} = Cx; \quad (13.6)$$

where $x = [\delta X_a^+ \ \delta X_a^- \ x_f]^T$ and $w = [\delta X_{Ain}^+ \ \delta X_{Ain}^- \ X_{\delta A,l}^+ \ X_{\delta A,l}^-]^T$. The quantum fluctuations associated with coherent states of light are known to possess Gaussian distribution with unit variance; see [5]. Here, w are zero mean, unit covariance, stationary white noise processes, with $\mathbf{E}[w(t)w(\tau)'] = Q\delta(t - \tau)$, where Q is an identity matrix. If $\mathbf{Re} \ \lambda_i(A) < 0$, then $\mathbf{E}[x(t)x(t)'] = P$ where P is the state covariance matrix and is the unique solution of (see [41]):

$$PA' + AP + B_2QB_2' = 0. \quad (13.7)$$

The covariance of the controlled output can then be computed as

$$\mathbf{E}[\tilde{z}(t)\tilde{z}(t)'] = \mathbf{E}[Cx(t)x(t)'C'] = CPC', \quad (13.8)$$

using numerical values for the model from Table 12.1. It was found that the expectation $\mathbf{E}[\tilde{z}(t)\tilde{z}(t)^T]$ is also independent of $\bar{\theta}_{a,out}$ and hence the SQL is the same irrespective of the operating point. This result confirms that the noise levels at any measured angle around a coherent state are equal, as expected from the Heisenberg uncertainty principle.

13.2 Sub-Quantum Noise Limit

Similarly, we can also numerically determine the quantum noise level when there is coupling between the intracavity fields; i.e., when $\chi^{(2)}$ is not zero. We model the optical squeezer described by (11.10)–(11.11) together with the low-pass filter in state-space form as in (13.6). The quantum noise terms feeding into the system are however modified to include

$$w = [\delta X_{Ain}^+ \delta X_{Ain}^- \delta X_{Bin}^+ \delta X_{Bin}^- X_{\delta A,l}^+ X_{\delta A,l}^- X_{\delta B,l}^+ X_{\delta B,l}^-]^T. \quad (13.9)$$

We again excite the system with Gaussian white noise of unit variance on all of the quantum input channels and determine the noise covariance of the controlled output \tilde{z} using (13.7) and (13.8). This time however the dynamical equations are affected by the operating point of the system. Here, the operating point is determined by solving the nonlinear equations (11.8) for a given combination of $\bar{\theta}_{a,in}$ and $\bar{\theta}_{b,in}$. The steady-state values of \bar{X}_a^\pm and \bar{X}_b^\pm are then substituted in (11.10) to determine the state matrix in the state-space model (13.6).

Figure 13.2 shows a plot of the variance of the filtered controlled variable \tilde{z} in dB at various operating points. In this case, we choose a fixed value of $\bar{\theta}_{a,in} = 0^\circ$ and vary $\bar{\theta}_{b,in}$. The straight horizontal line corresponds to the SQL,

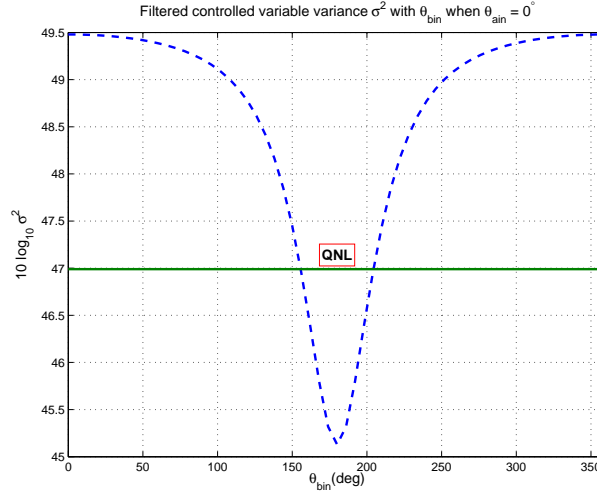


Figure 13.2: Variance of the filtered controlled variable \tilde{z}

which is constant at all operating points and was determined to be about 47 dB.

The change in the variance of the controlled variable \tilde{z} shows that the interaction between the electromagnetic fields inside the optical resonator cavity results in noise levels that are below the SQL at some operating points, and above the SQL at other operating points, along the chosen direction of measurement. In this case, we are measuring along the amplitude quadrature of the fundamental output field. This behaviour confirms the result from the discussion in Section 12.4 since the point at which maximum squeezing is observed ($\bar{\theta}_{a,in} = 0, \bar{\theta}_{b,in} = 180^\circ$) corresponds to the condition specified in (12.14).

13.3 Static Approximation to State Equations

The covariance of the controlled output can also be approximately determined as follows. Since $\kappa_b \gg \kappa_a$, the dynamics due to the intracavity field \hat{b} are much faster than those of field \hat{a} . This feature of the optical squeezer allows the use of a singular perturbation approach (see [52]), where we can use a separation of the time-scales of the system to simplify the dynamical equations describing the behaviour of the system. We thus neglect the linearised equations (11.10c) and (11.10d) and equate all components related to variations of the quadratures of field \hat{b} in (11.10a)–(11.10b) to zero. Then, we only consider the following two equations to obtain a good approximation to the behaviour of the optical squeezer:

$$\begin{aligned} \delta \dot{X}_a^+ &= -\kappa_a \delta X_a^+ + \frac{1}{2} \chi^{(2)} (\bar{X}_b^+ \delta X_a^+ + \bar{X}_b^- \delta X_a^-) \\ &\quad + \sqrt{2\kappa_{a,in}} \delta X_{Ain}^+ + \sqrt{2\kappa_{a,l}} X_{\delta A,l}^+; \end{aligned} \quad (13.10a)$$

$$\begin{aligned} \delta \dot{X}_a^- &= -\kappa_a \delta X_a^- + \frac{1}{2} \chi^{(2)} (\bar{X}_b^- \delta X_a^+ - \bar{X}_b^+ \delta X_a^-) \\ &\quad + \sqrt{2\kappa_{a,in}} \delta X_{Ain}^- + \sqrt{2\kappa_{a,l}} X_{\delta A,l}^-. \end{aligned} \quad (13.10b)$$

Furthermore, at steady-state, we can equate the left hand side of (13.10a) and (13.10b) to zero and determine solutions for δX_a^+ and δX_a^- from

$$\begin{bmatrix} 2\kappa_a - \chi^{(2)}\bar{X}_b^+ & -\chi^{(2)}\bar{X}_b^- \\ -\chi^{(2)}\bar{X}_b^- & 2\kappa_a + \chi^{(2)}\bar{X}_b^+ \end{bmatrix} \begin{bmatrix} \delta X_a^+ \\ \delta X_a^- \end{bmatrix} = 2\sqrt{2} \begin{bmatrix} \sqrt{\kappa_{a,in}} & \sqrt{\kappa_{a,l}} & 0 & 0 \\ 0 & 0 & \sqrt{\kappa_{a,in}} & \sqrt{\kappa_{a,l}} \end{bmatrix} \begin{bmatrix} \delta X_{Ain}^+ \\ X_{\delta A,l}^+ \\ \delta X_{Ain}^- \\ X_{\delta A,l}^- \end{bmatrix}. \quad (13.11)$$

The resulting equations for δX_a^+ and δX_a^- are then given by:

$$\begin{aligned} \delta X_a^+ &= \begin{bmatrix} \frac{2\sqrt{2\kappa_{a,in}}(2\kappa_a + \chi^{(2)}\bar{X}_b^+)}{4\kappa_a^2 - \chi^{(2)2}(\bar{X}_b^{+2} + \bar{X}_b^{-2})} & \frac{2\sqrt{2\kappa_{a,l}}(2\kappa_a + \chi^{(2)}\bar{X}_b^+)}{4\kappa_a^2 - \chi^{(2)2}(\bar{X}_b^{+2} + \bar{X}_b^{-2})} \\ \frac{2\sqrt{2\kappa_{a,in}}\chi^{(2)}\bar{X}_b^-}{4\kappa_a^2 - \chi^{(2)2}(\bar{X}_b^{+2} + \bar{X}_b^{-2})} & \frac{2\sqrt{2\kappa_{a,l}}\chi^{(2)}\bar{X}_b^-}{4\kappa_a^2 - \chi^{(2)2}(\bar{X}_b^{+2} + \bar{X}_b^{-2})} \end{bmatrix} \begin{bmatrix} \delta X_{Ain}^+ \\ X_{\delta A,l}^+ \\ \delta X_{Ain}^- \\ X_{\delta A,l}^- \end{bmatrix}; \\ \delta X_a^- &= \begin{bmatrix} \frac{2\sqrt{2\kappa_{a,in}}\chi^{(2)}\bar{X}_b^-}{4\kappa_a^2 - \chi^{(2)2}(\bar{X}_b^{+2} + \bar{X}_b^{-2})} & \frac{2\sqrt{2\kappa_{a,l}}\chi^{(2)}\bar{X}_b^-}{4\kappa_a^2 - \chi^{(2)2}(\bar{X}_b^{+2} + \bar{X}_b^{-2})} \\ \frac{2\sqrt{2\kappa_{a,in}}(2\kappa_a - \chi^{(2)}\bar{X}_b^+)}{4\kappa_a^2 - \chi^{(2)2}(\bar{X}_b^{+2} + \bar{X}_b^{-2})} & \frac{2\sqrt{2\kappa_{a,l}}(2\kappa_a - \chi^{(2)}\bar{X}_b^+)}{4\kappa_a^2 - \chi^{(2)2}(\bar{X}_b^{+2} + \bar{X}_b^{-2})} \end{bmatrix} \begin{bmatrix} \delta X_{Ain}^+ \\ X_{\delta A,l}^+ \\ \delta X_{Ain}^- \\ X_{\delta A,l}^- \end{bmatrix}. \end{aligned}$$

We are interested in minimising the variance of the amplitude quadrature and as before, the variable of interest is given by:

$$z = \delta X_a^+ \cos \bar{\theta}_{a,out} + \delta X_a^- \sin \bar{\theta}_{a,out}. \quad (13.12)$$

The covariance of the variable z denoted by $\mathbf{E}[z(t)z(t)^T]$ is then dependent on the variance of the inputs only. As an example, the case when the variance of all the inputs is unity and $\bar{\theta}_{a,in} = 45^\circ$ is shown in Figure 13.3.

The level of squeezing determined using this method though numerically easier to compute is an approximation to what is achieved using equations (13.6)–(13.8)

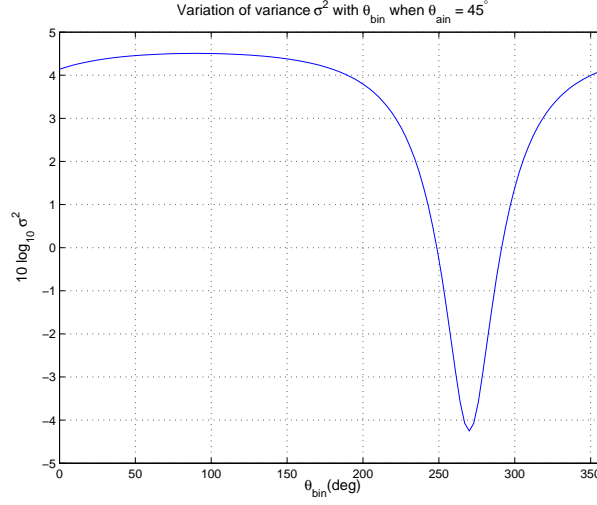


Figure 13.3: Variance of the controlled variable using approximate static equations

and serves as a good rough estimate.

13.4 Preliminary LQG Controller Design

We have shown in Section 13.2 that it is possible to obtain noise levels that are below the SQL using an optical squeezer at selected operating points. The operating points depend primarily on the phase angle of the input fields. For the optical squeezer model considered, we achieved a maximum reduction in the noise level of about 2 dB. This result was attained without the use of feedback control when the system is subjected to quantum noises only and when the phase angle of the input fields are suitably chosen. The next logical question to ask is whether it is possible to achieve further improvement of the noise level with the use of an appropriate controller.

In this section, we begin by designing LQG controllers at numerous operating points for the optical squeezer when the system is exposed to quantum noises only. The objective is to minimise the variance along a given quadrature of the system. The variance of the controlled variable for the closed-loop systems with the controllers in place is then determined and compared with the open-loop cases at each corresponding operating point.

Then, we consider the more general case where the optical squeezer is subjected to classical noises as well as quantum noises. We model the different types of classical noises and determine their cumulative effect on the level of squeezing achieved in the open-loop case at various operating points. The controller design process iterated above is then repeated in an effort to improve the noise level observed in the controlled variable.

13.4.1 System Interconnections

A novel feature of our approach is that we propose to minimise the variance of the fundamental output field of the optical squeezer by regulating the phase quadrature of the second-harmonic input field (δX_{Bin}^-) and by using the phase quadrature of the second-harmonic output field (δX_{Bout}^-) as measurement. As we are only concerned with the determination of the noise limits which can be attained at this stage, we shall not unnecessarily complicate the controller design process by including the dynamics of the piezo-electric actuator. The piezo-electric actuators (as modelled in (11.12)) will however be taken into account for the complete controller design to be discussed in future chapters. The plant to be controlled can be represented as shown in Figure 15.1. Here, w_1 is used

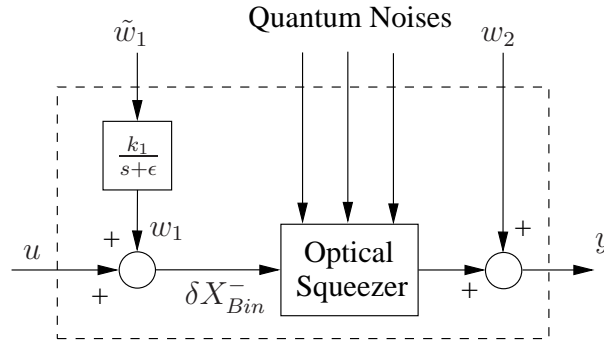


Figure 13.4: Block diagram of system interconnections.

to represent laser phase noise which arises due to mechanical fluctuations in the beam path. This noise is modelled as approximately integrated white noise using the state equations:

$$\dot{\xi} = -\epsilon\xi + \tilde{w}_1, \quad w_1 = k_1\xi; \quad (13.13)$$

where \tilde{w}_1 is a Gaussian white noise with variance ϵ_{ln}^2 . ϵ defines the noise model pole location and k_1 is a gain parameter denoting the size of the mechanical noise signal w_1 . The complete linearised model can then be modelled in state-space form as:

$$\dot{x} = Ax + B_1u + B_2w; \quad (13.14a)$$

$$y = Cx + Dw, \quad (13.14b)$$

where

$$\begin{aligned} x &= \begin{bmatrix} \delta X_a^+ & \delta X_a^- & \delta X_b^+ & \delta X_b^- & \xi \end{bmatrix}^T; \\ w &= \begin{bmatrix} \tilde{w}_1 & \delta X_{Ain}^+ & \delta X_{Ain}^- & \delta X_{Bin}^+ & p_{Bin} & \\ & X_{\delta A,l}^+ & X_{\delta A,l}^- & X_{\delta B,l}^+ & X_{\delta B,l}^- & w_2 \end{bmatrix}^T; \end{aligned}$$

and w_2 is used to represent Gaussian white sensor noise. Also, p_{Bin} represents the phase quadrature of the quantum noise present in the input field \hat{B}_{in} . The variance of the quantum noises ϵ_1^2 , sensor noise ϵ_2^2 and the laser noise ϵ_{ln}^2 are then treated as controller design parameters.

13.4.2 Performance criterion and Kalman filtering

The LQG approach involves separately estimating the system variables using a Kalman filter and determining an optimal state feedback control law using a quadratic cost functional. The Kalman filter is then combined with the optimal feedback control law to give an LQG controller; see Section 4.3. The performance requirement in our case is to minimise the variance of a function of the quadratures of the output field \hat{A}_{out} , to achieve optimal squeezing in the presence of both quantum and classical noises. The controlled variable, as explained previously, is chosen such that the variations of the quadratures are measured along or orthogonal to the direction of the steady-state output field, in particular along the phase angle $\bar{\theta}_{a,out}$. In either case, our requirement is to minimise the variance along the direction of measurement. If we choose to measure along the direction of the steady-state output field (along the amplitude quadrature), then

the variable of interest is given by

$$\begin{aligned} z &= \delta X_a^+ \cos \bar{\theta}_{a,out} + \delta X_a^- \sin \bar{\theta}_{a,out} \\ &= Hx + Gw. \end{aligned} \quad (13.15)$$

Furthermore, as explained previously, we are limited by the bandwidth of the measuring device which is modelled as a first-order low-pass filter. We thus will use the filtered variable \tilde{z} in the LQ performance criterion (13.18). The augmented system we use for the controller design is then completely characterised by:

$$\dot{\tilde{x}} = \tilde{A}\tilde{x} + \tilde{B}_1 u + \tilde{B}_2 w; \quad (13.16a)$$

$$y = \tilde{C}\tilde{x} + Dw, \quad (13.16b)$$

where $\tilde{x} = [x^T \ x_f^T]^T$ and

$$\tilde{A} = \begin{bmatrix} A & 0 \\ H & -\frac{1}{\tau} \end{bmatrix}; \quad \tilde{B}_1 = \begin{bmatrix} B_1 \\ 0 \end{bmatrix}; \quad \tilde{B}_2 = \begin{bmatrix} B_2 \\ G \end{bmatrix}; \quad \tilde{C} = \begin{bmatrix} C & 0 \end{bmatrix}. \quad (13.17)$$

The control objective can then be formulated as the minimisation of the following cost function:

$$\mathcal{J} = \lim_{T \rightarrow \infty} \mathbf{E} \left[\frac{1}{T} \int_0^T \tilde{x}(t)^T \tilde{Q} \tilde{x}(t) + u(t)^T R u(t) dt \right], \quad (13.18)$$

where \tilde{Q} and R are positive definite matrices. The matrix \tilde{Q} is chosen such that $\tilde{x}^T \tilde{Q} \tilde{x} = |\tilde{z}|^2$ and R is chosen to weight the control energy required. The expectation in (13.18) is with respect to the Gaussian quantum and classical noise processes, and the assumed Gaussian initial conditions.

The LQG optimal controller is constructed from the solution to a deterministic regulator problem and an optimal observer problem as follows (see, e.g., [41, 77] and Chapter 4):

$$u = -R^{-1} \tilde{B}_1^T X \hat{\tilde{x}}, \quad (13.19)$$

where X satisfies the following matrix algebraic Riccati equation

$$Q - X \tilde{B}_1 R^{-1} \tilde{B}_1^T X + X \tilde{A} + \tilde{A}^T X = 0. \quad (13.20)$$

The optimal observer dynamics (Kalman filter) are described by

$$d\hat{x} = \tilde{A}\hat{x} dt + \tilde{B}_1 u dt + K[dy - \tilde{C}\hat{x} dt]; \quad (13.21)$$

and the solution of the optimal observer is obtained by choosing the gain matrix

$$K = (P_e \tilde{C}^T + \tilde{B}_2 D^T)(DD^T)^{-1}, \quad (13.22)$$

where P_e is the solution to the matrix Riccati equation:

$$\begin{aligned} &(\tilde{A} - \tilde{B}_2 D^T (DD^T)^{-1} \tilde{C})P_e + P_e(\tilde{A} - \tilde{B}_2 D^T (DD^T)^{-1} \tilde{C})^T \\ &- P_e \tilde{C}^T (DD^T)^{-1} \tilde{C} P_e + \tilde{B}_2 \tilde{B}_2^T - \tilde{B}_2 D^T (DD^T)^{-1} D \tilde{B}_2^T = 0. \end{aligned} \quad (13.23)$$

13.4.3 Model and controller design parameters

The parameter values we used for the optical model are shown in Table 12.1. In designing the LQG controllers, the design parameters we chose for good performance are shown in Table 13.1. Using these parameters, a series of LQG

Parameters	Value
ϵ	3×10^{-4}
k_1	1×10^5
ϵ_1	1
ϵ_2	1
ϵ_{ln}	1
R	1×10^{-10}

Table 13.1: Laser Noise Model and Controller Design Parameters

controllers are designed at different operating points for the following two cases:

1. Only quantum noises acting on the system;
2. Both quantum and classical noises act on the system.

13.4.4 Controlled and uncontrolled variance with quantum noises only

Using (13.7) and (13.8), the open-loop and closed-loop variances of the filtered controlled variable are computed at numerous operating points. We consider two choices of the variable of interest. First, we take measurements along the steady state output field as given by (13.2). The results obtained for three different values of $\bar{\theta}_{a,in}$ and for $\bar{\theta}_{b,in}$ varying from 0 to 2π are shown in Figures 13.5(a), 13.5(c) and 13.5(e). Clearly, the noise variances under open-loop and closed-loop conditions are the same in this case. This shows that at any operating point, a classical LQG controller cannot suppress the quantum noises further than what is already achieved with the optical squeezer. For comparison and to confirm the result above, we repeat the controller design process with the controlled variable chosen to correspond to measurement of the variance perpendicular to the direction of the output field, using (13.3). The corresponding variances are shown in Figures 13.5(b), 13.5(d), 13.5(f). Again, no improvement in the noise level is observed with the controller in place. It is interesting to note however that the operating points at which the minima and maxima were obtained using (13.2) are reversed since the measurement axis is now along the direction of anti-squeezing.

13.4.5 Controlled and uncontrolled variance with quantum and classical noises

In this case, in addition to the quantum noises present in the system, we also include laser noise and sensor noise and design a series of LQG controllers at different operating points. As before, the variable of interest (13.2) corresponds to taking measurement along the direction of the output field. The results obtained for the same three cases considered previously are shown in Figures 13.6(a), 13.6(c), and 13.6(e). As expected, we find that the open-loop variances are larger this time as a result of the inclusion of laser phase noise and sensor noise in the system. With the use of controllers, the closed-loop noise level is however brought down to the same level as seen in Figure 13.5. Thus, the controllers are effective in completely attenuating the laser phase noise and sensor noise introduced into the system. Also, as was done previously, with the controlled variable chosen

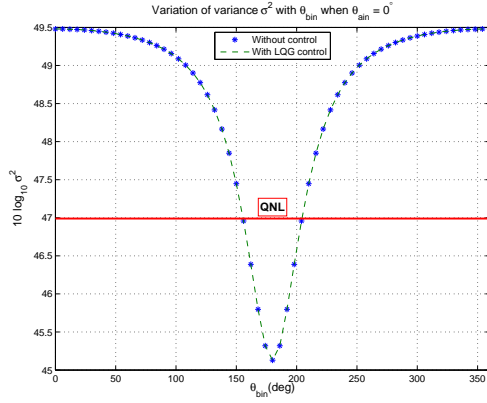
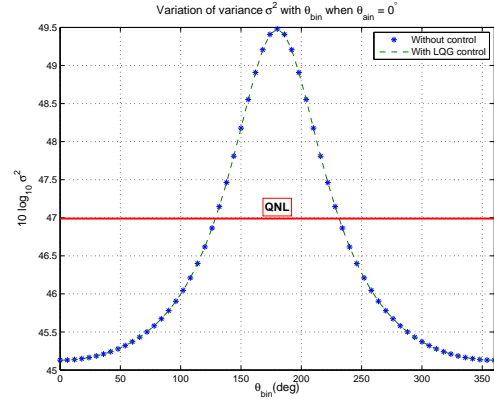
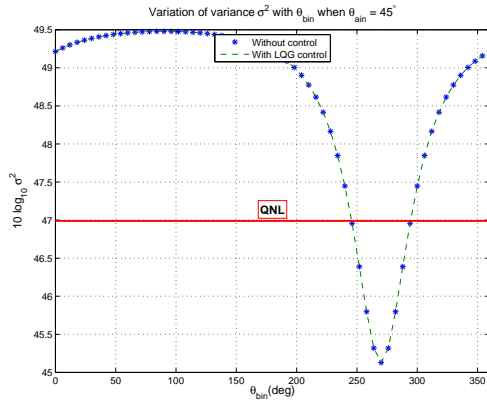
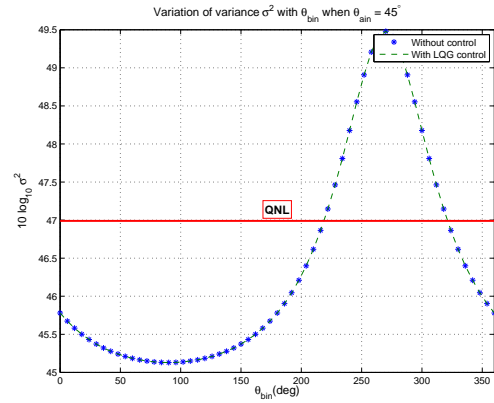
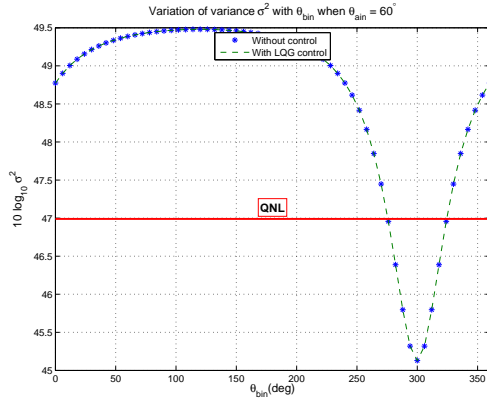
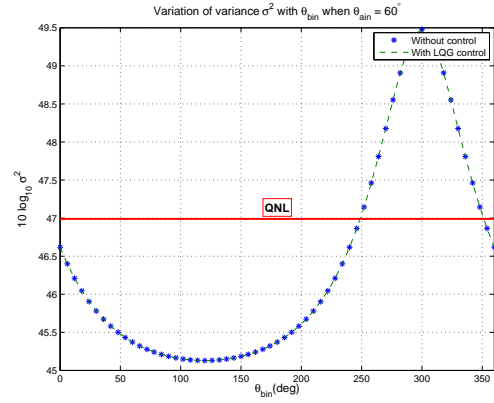
(a) Variance at $\bar{\theta}_{a,in} = 0^\circ$ (b) Variance at $\bar{\theta}_{a,in} = 0^\circ$ (c) Variance at $\bar{\theta}_{a,in} = 45^\circ$ (d) Variance at $\bar{\theta}_{a,in} = 45^\circ$ (e) Variance at $\bar{\theta}_{a,in} = 60^\circ$ (f) Variance at $\bar{\theta}_{a,in} = 60^\circ$

Figure 13.5: Variance of filtered controlled variable under open-loop and closed-loop conditions with quantum noise only.

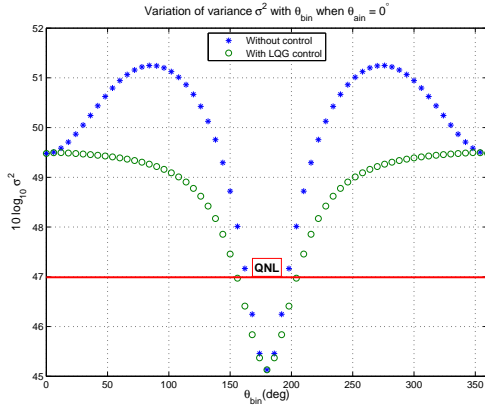
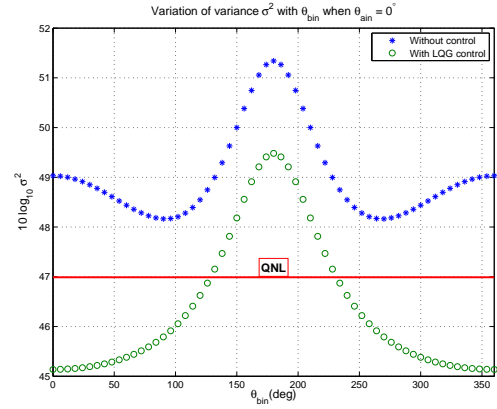
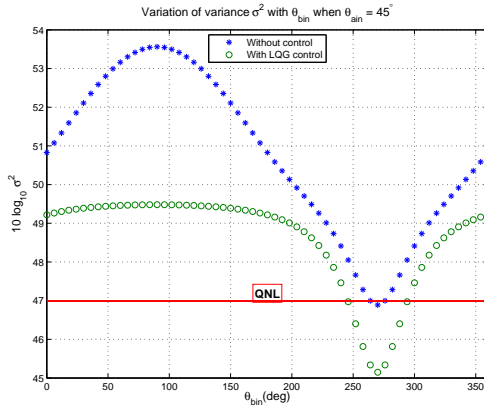
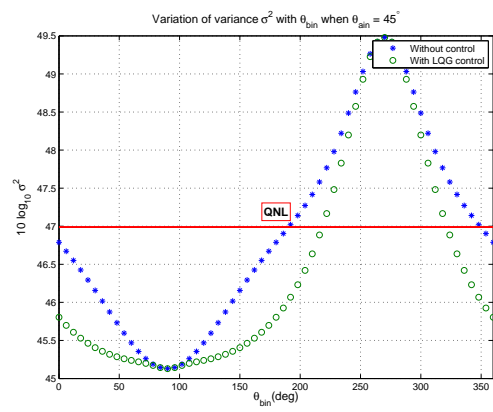
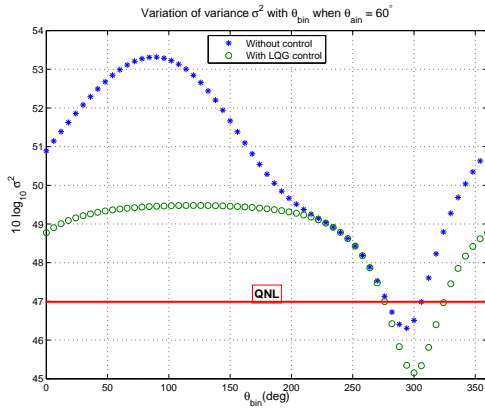
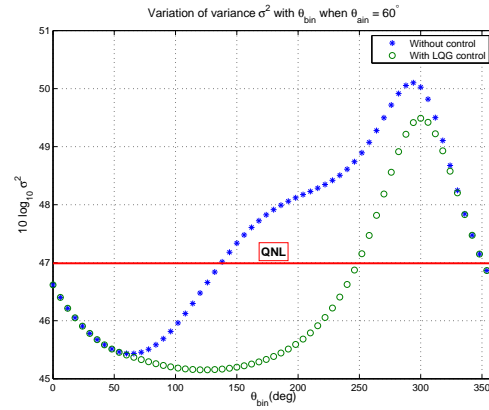
(a) Variance at $\bar{\theta}_{a,in} = 0$ (b) Variance at $\bar{\theta}_{a,in} = 0$ (c) Variance at $\bar{\theta}_{a,in} = 45^\circ$ (d) Variance at $\bar{\theta}_{a,in} = 45^\circ$ (e) Variance at $\bar{\theta}_{a,in} = 60^\circ$ (f) Variance at $\bar{\theta}_{a,in} = 60^\circ$

Figure 13.6: Variance of filtered controlled variable under open-loop and closed-loop conditions with quantum and classical noises.

to reflect measurements taken perpendicular to the direction of the output field, the corresponding anti-squeezing effects are shown in Figures 13.6(b), 13.6(d), 13.6(f). One feature observed in some of these figures however, (e.g., see Figure 13.6(a)), seems problematic. We note that at some operating points (e.g., see the pair $(\theta_{a,in}, \theta_{b,in}) = (0, \pi)$), the open-loop and closed-loop noise variances do not seem to differ by much. This would suggest that to obtain optimal squeezing, we would not require a controller in the presence of additional sources of noise, other than quantum noises. This aspect of the system was investigated further. In particular, we determine the controllability of the system at the problematic points. Controllability is necessarily to be able to assign arbitrary sets of poles which are determined by the cost function. Since the system does not show improvement in the noise level after the inclusion of a controller at some points, it can be expected that is due to numerical difficulties when the system is close to an uncontrollable problem. It is well known that direct determination of the rank of the controllability matrix is numerically sensitive for large systems (of order more than 3). Moreover, a “yes/no” answer can be misleading. A better measure of computing controllability is obtained by computing the distance $\delta(A, B)$ of a given pair $(A, B) \in \mathbb{R}^{n \times n} \times \mathbb{R}^{n \times p}$ to the nearest uncontrollable matrix pair,

$$\delta(A, B) = \inf \{ \|\delta A, \delta B\| : (A + \delta A, B + \delta B) \text{ is not controllable}, \quad [\delta A, \delta B] \in \mathbb{R}^{n \times n} \times \mathbb{R}^{n \times p} \}, \quad (13.24)$$

where $\|\cdot\|$ may denote the matrix 2-norm. Eising [78] showed that this measure of conditioning of a system is equivalent to:

$$\delta(A, B) = \inf_{\lambda \in \mathbb{C}} \sigma_{\min}([A - \lambda I, B]), \quad (13.25)$$

where σ_{\min} denotes the minimum singular value. Determining an exact solution to (13.25) can be challenging as it involves solving a non-convex optimisation problem in two variables $\mathbf{Re}(\lambda)$ and $\mathbf{Im}(\lambda)$. However, efficient algorithms for determining $\delta(A, B)$ do exist; see [79–81]. For our case, knowing where we desire the closed-loop poles to be as specified by fixed control design parameters, we can determine a measure of controllability for any given pair of phase angles $(\theta_{a,in}, \theta_{b,in})$. We compute the singular value decomposition of the controllability

matrix $\mathcal{C} \in \mathbb{R}^{n \times m}$ as follows:

$$\mathcal{C} = U\Sigma V^T, \quad (13.26a)$$

$$\text{where } U^T U = V^T V = VV^T = I_m, \quad (13.26b)$$

$$\text{and } \Sigma = \text{diag}(\sigma_1, \sigma_2, \dots, \sigma_m), \quad \sigma_1 \geq \sigma_2 \geq \dots \geq \sigma_m \geq 0. \quad (13.26c)$$

The real scalars $\sigma_1, \sigma_2, \dots, \sigma_m$ are the singular values of \mathcal{C} . Thus if $\sigma_1 \geq \sigma_2 \geq \dots \geq \sigma_r > 0$ and $\sigma_{r+1} = \dots = \sigma_m = 0$, then the system has rank r . Moreover, if $\tilde{\sigma}_1 \geq \tilde{\sigma}_2 \geq \dots \geq \tilde{\sigma}_m$ are the singular values of a perturbed matrix $\mathcal{C} + \delta\mathcal{C}$, then

$$|\sigma_i - \tilde{\sigma}_i| \leq \|\delta\mathcal{C}\|_2. \quad (13.27)$$

Thus, for any $j \leq r$, a change of $\|\delta\mathcal{C}\|_2 \geq \sigma_j$ is needed to obtain a perturbed controllability matrix $\mathcal{C} + \delta\mathcal{C}$ of lesser rank than j . Singular values in this way not only provide information about the rank of a system but also determines how far the system is from a system of lesser rank.

For our case, some of the elements of the state matrix of the optical cavity system become almost negligible (but not zero) at some operating points, making the system close to uncontrollable in the sense as described above. In particular, for the pair $(\theta_{a,in}, \theta_{b,in}) = (0, \pi)$, the states δX_a^+ and δX_b^+ become uncontrollable. All the states however remain observable. This problem occurs at numerous operating points, explaining the unexpected behaviour observed in the generated plots in Figure 13.6. For the controller designs performed in the following chapters, we shall choose operating points that do not suffer from this condition.

Chapter 14

LQG Controller Design

In this chapter, we consider the complete model of the system under consideration (optical parametric oscillator with the piezo-electric actuator) and design an LQG controller at a suitably chosen operating point. The operating point is chosen such that we obtain amplitude quadrature squeezing of the fundamental output field \hat{A}_{out} . One important assumption we make at this stage is that the intracavity fields are locked to the incoming laser beams; i.e., the detuning variables satisfy $\Delta_a = \Delta_b = 0$. It is necessary to have the optical squeezer in lock before any squeezed states of light can be observed and the system is kept in lock by using an external simple PI controller. In future designs, we shall consider the more general case when the detuning variables are not zero.

As mentioned previously, we propose a scheme to optimise the level of squeezing achieved in the fundamental field by both taking measurement and providing actuation on the second harmonic field only. In our case, the available measurement is the phase quadrature of the second harmonic field (δX_{Bout}^-) which is measured using the homodyne detection method. Actuation is provided by a piezoelectric actuator connected to a mirror which adjusts the phase quadrature of the second harmonic input field (δX_{Bin}^-), thus minimising the effect of laser phase noise and other sources of classical noise on the system. In turn, this regulates the phase angles of the fundamental and second-harmonic intracavity fields, allowing for optimal amplitude quadrature squeezing of the fundamental field.

Figure 14.1 shows the set-up used for the OPO control problem. The requirement to regulate the phase angles and meet the phase-matching conditions on the intracavity fields is reflected in an LQG cost functional defined using the

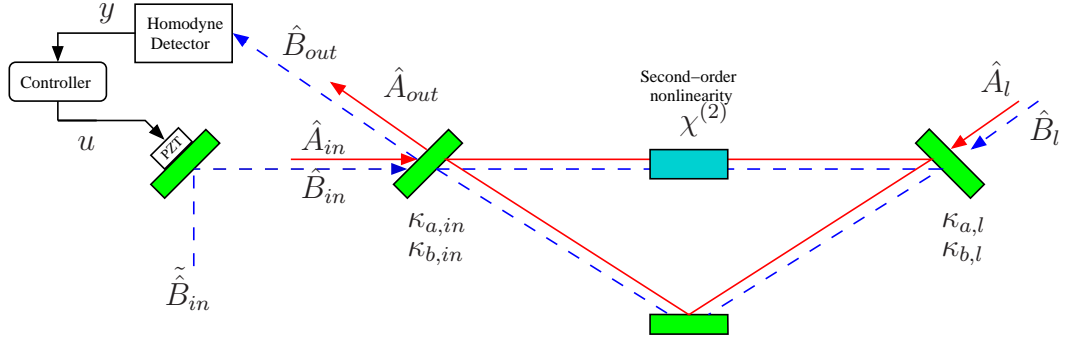


Figure 14.1: Schematic for control of an Optical Parametric Oscillator

phase angle of the steady-state output field through a rotation of the axes of measurement.

14.1 Complete Model

The complete model we use for the controller design and subsequent simulations is derived from the linearised quantum dynamics of the OPO (optical subsystem) and from a piezo-electric actuator (mechanical subsystem). Also, laser phase noise, which is predominantly at low frequencies and which drives the cavity, is modelled as (approximately) integrated white noise. The parameter values used for simulations are typical of an experimental test-bed in our laboratory.

Given the effect of the operating point as explained previously, we linearise the optical system about a set point defined by setting \bar{A}_{in} and \bar{B}_{in} so as to obtain a suitable pair $\bar{\theta}_a$ and $\bar{\theta}_b$ satisfying the condition $\bar{\theta}_b - 2\bar{\theta}_a = \pi$. The results presented in Figure 12.8 show that these values lead to maximum amplitude quadrature squeezing of the field \hat{a} . The pair of phase angles we choose for controller design in this and future chapters is $\bar{\theta}_a = \frac{\pi}{3}$ and $\bar{\theta}_b = \frac{5\pi}{3}$.

The piezo-electric actuator attached to the mirror (the mechanical subsystem) is approximated as a second order system; see (11.12). For convenience, we

include a model description of it here:

$$\begin{bmatrix} \dot{\xi}_1 \\ \dot{\xi}_2 \end{bmatrix} = \begin{bmatrix} 0 & 1 \\ -r_2 & -r_1 \end{bmatrix} \begin{bmatrix} \xi_1 \\ \xi_2 \end{bmatrix} + \begin{bmatrix} 0 \\ 1 \end{bmatrix} w_1 + \begin{bmatrix} 0 \\ 1 \end{bmatrix} u; \quad (14.1a)$$

$$\delta X_{Bin}^- = [c_2 \ c_1] \begin{bmatrix} \xi_1 \\ \xi_2 \end{bmatrix} + p_{Bin}. \quad (14.1b)$$

Furthermore, laser phase noise w_1 modelled as approximately integrated white noise is described in (13.13). The complete linearised system is then modelled in state-space form as:

$$\dot{x} = Ax + B_1u + B_2w; \quad (14.2a)$$

$$y = Cx + Dw, \quad (14.2b)$$

where

$$x = \begin{bmatrix} \delta X_a^+ & \delta X_a^- & \delta X_b^+ & \delta X_b^- & \xi_1 & \xi_2 & \xi \end{bmatrix}^T;$$

$$w = \begin{bmatrix} \tilde{w}_1 & \delta X_{Ain}^+ & \delta X_{Ain}^- & \delta X_{Bin}^+ & p_{Bin} & X_{\delta A,l}^+ & X_{\delta A,l}^- & X_{\delta B,l}^+ & X_{\delta B,l}^- & w_2 \end{bmatrix}^T.$$

The plant to be controlled is represented as shown in Figure 14.2.

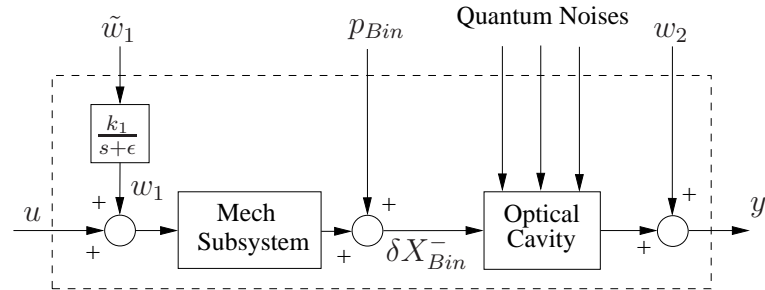


Figure 14.2: System interconnections used for LQG Controller Design.

14.2 Performance Criterion

The performance requirement for our control system is to minimise the variance of the amplitude quadrature of the fundamental output field \hat{A}_{out} , and to achieve squeezing in the presence of both quantum and classical noises. The controlled variable is chosen such that the variations of the quadratures are measured along the direction of the steady-state output field. As before, we consider the controlled variable described by (13.2). Also, we include a low-pass filter at the output of the controlled variable z as modelled in (13.4c). We then use the filtered controlled variable \tilde{z} in the LQ performance criterion (13.18). The augmented system we use for the controller design is completely characterised by (13.16) and (13.17) and we then construct the LQG optimal controller from the solution to a deterministic regulator problem and an optimal observer problem using (13.19)–(13.23).

14.3 Model and Design Parameters

The parameter values of the piezoelectric actuator, the low pass filter and the steady-state phase angles of the input fields are shown in Table 14.1.

Model parameter	Value
r_1	1×10^5
r_2	1×10^9
c_1	-5×10^3
c_2	1.5×10^{10}
τ	1×10^{-5}
$\bar{\theta}_{a,in}$	$\pi/3$
$\bar{\theta}_{b,in}$	$5\pi/3$

Table 14.1: Piezoelectric Actuator and OPO Model Parameters used for LQG Controller Design.

In designing the LQG controller, the design parameters ϵ_{ln}^2 (laser noise variance), ϵ_1^2 (quantum noise variance), ϵ_2^2 (sensor noise variance), ϵ (phase noise model pole location), k_1 (phase noise gain parameter), and R (the control energy weighting in the cost functional) were adjusted until good performance was obtained in the controller simulations. The values used were $\epsilon = 3 \times 10^{-5}$, $\epsilon_1 = 1$,

$\epsilon_2 = 0.1$, $\epsilon_{ln} = \sqrt{10}$, $k_1 = 1 \times 10^6$ and $R = 1 \times 10^{-10}$. These parameters led to an LQG controller with Bode plots as shown in Figure 14.3.

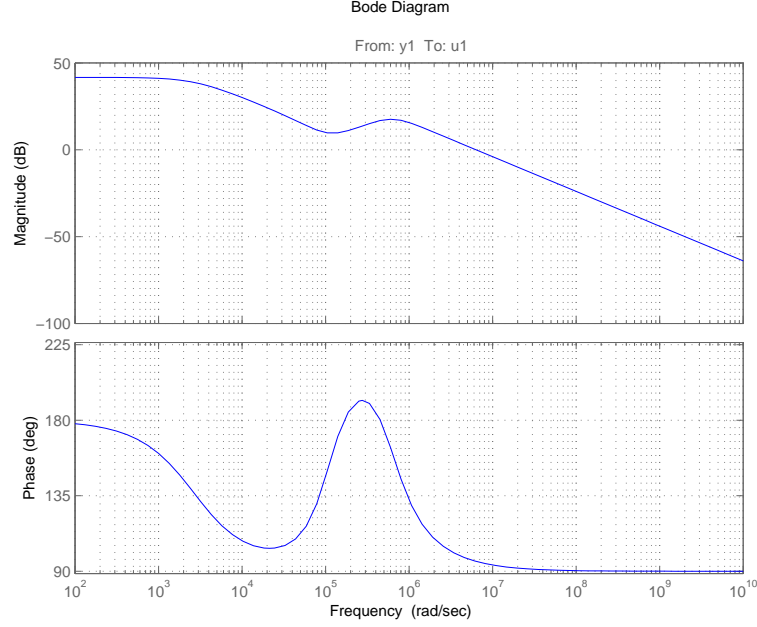


Figure 14.3: Bode plot of the LQG controller.

The corresponding loop gain Bode plot in Figure 14.4 shows that the controlled system has high gain at low frequencies where the slowly varying phase noise predominates. It also has a large bandwidth of 4.8×10^5 rad/s and a gain margin of about 30° .

14.4 Simulation Results

Using the model parameters specified in Table 12.1 and 14.1 and the designed controller, we simulate the system using the SIMULINK[®] block diagram shown in Figure 14.5.

First, we show the effect of the nonlinearity $\chi^{(2)}$ on the variance of the controlled filtered output \tilde{z} . We simulate the open-loop system with only quantum noises exciting the system and with $\chi^{(2)} = 0$. This corresponds to the case where there is no interaction between the fundamental and second harmonic fields inside the optical cavity. The controlled variable \tilde{z} is then representative of the SQL.

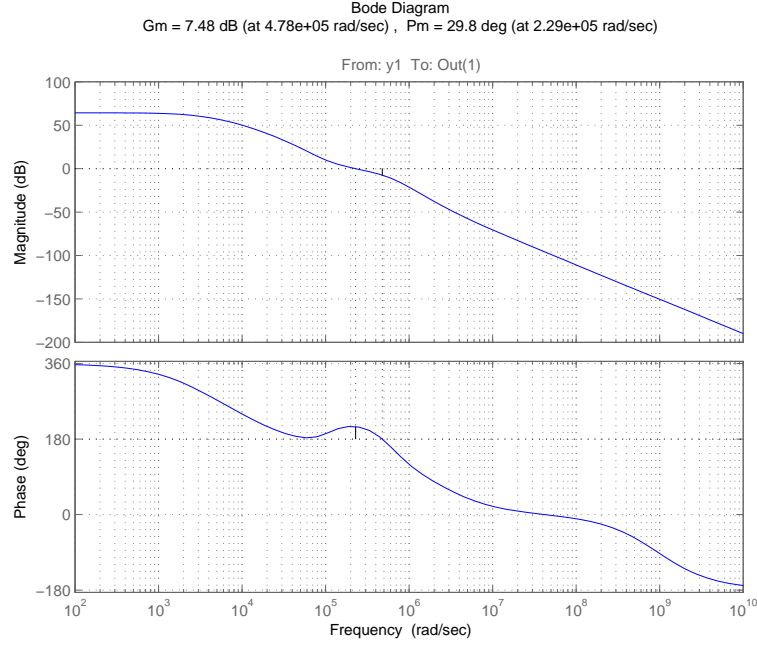


Figure 14.4: Bode plot of the loop gain transfer function.

We repeat the process with $\chi^{(2)} = 0.03$ and the corresponding plots are shown in Figure 14.6. As expected, the interaction between the optical fields results in a reduction of the variance of the controlled variable \tilde{z} . Physically, a non-zero value of $\chi^{(2)}$ causes squeezing of the amplitude quadrature, which in turn reduces the degree of uncertainty along the chosen axis of measurement as defined by (13.2).

We next simulate the closed-loop system to determine the effectiveness of the designed controller. We consider the case where the system is excited with both classical and quantum noises for $\chi^{(2)} = 0.03$ (as shown in Table 12.1). Figure 14.7 shows the laser phase noise w_1 and the corresponding control signal generated by the controller to counteract the effect of this noise. Note that the laser phase noise is generated using the same noise model as was used in the controller design. Figure 14.8 compares the time history of the filtered controlled variable \tilde{z} for the open-loop and the closed-loop case. It can be seen that the controller successfully minimises the variance of the controlled variable to a level below the SQL and close to the sub-quantum noise limit achieved with the system exposed to quantum noises only; cf. Figure 14.6.

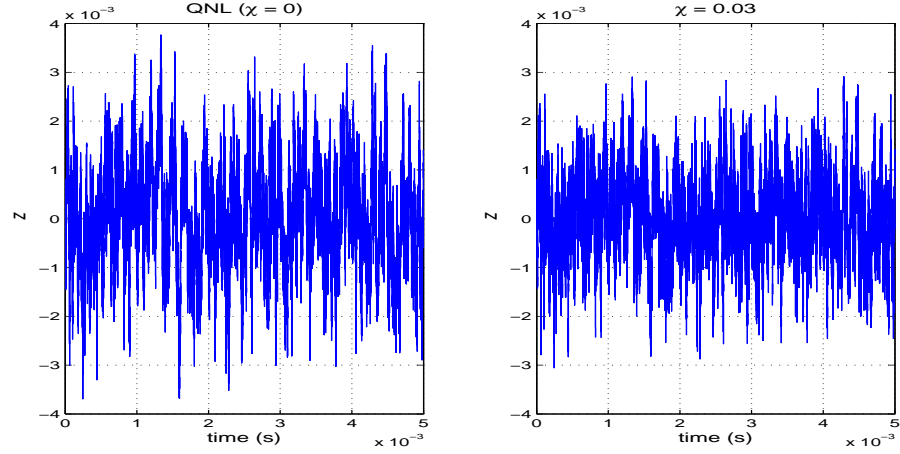
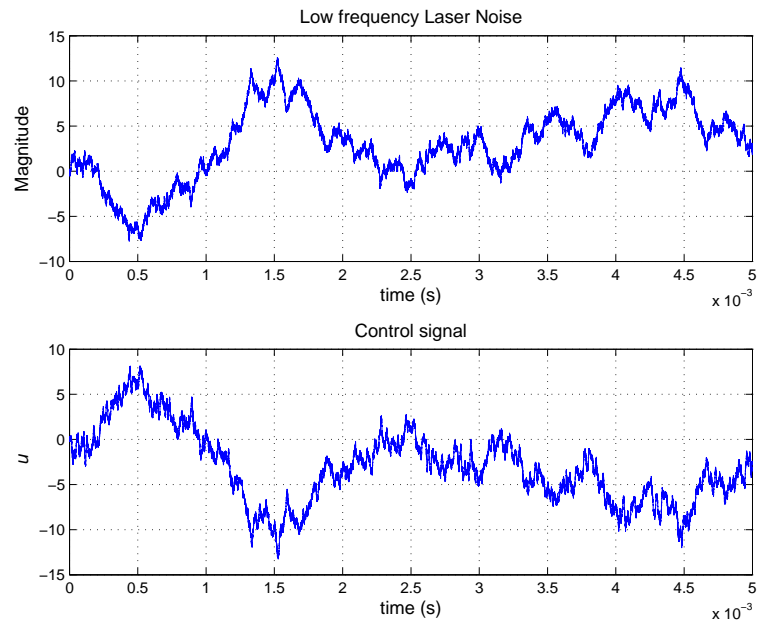
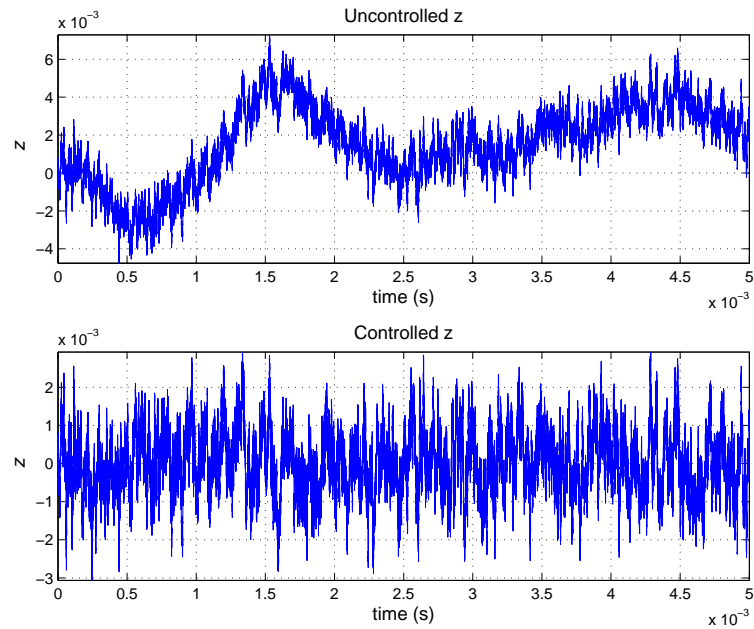


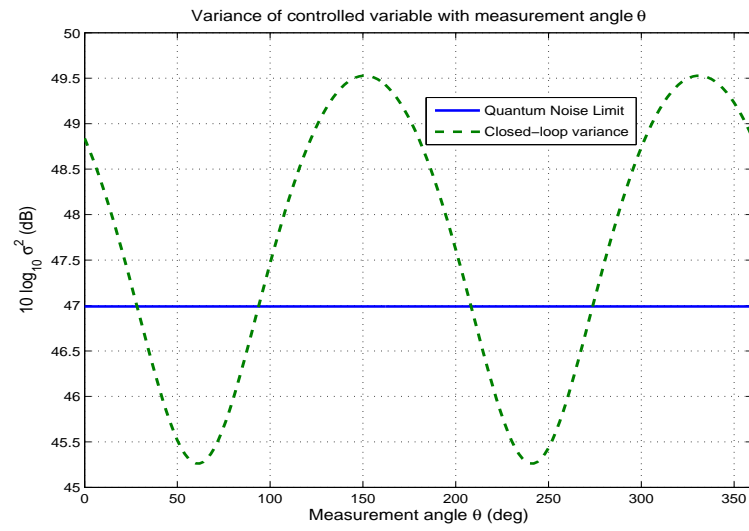
Figure 14.6: Quantum noise limit ($\chi^{(2)} = 0$) and squeezed quantum noise limit ($\chi^{(2)} = 0.03$).

able \tilde{z} when the open-loop system is excited with only quantum noises and with $\chi^{(2)} = 0$. Figure 14.9 shows that maximum squeezing is achieved at a value of $\theta = 60^\circ = \frac{\pi}{3}$ rad. This is as expected since $\bar{\theta}_{a,in} = \pi/3$ and as was explained in Section 12.4, a very good steady-state approximation is to assume that

$$\bar{\theta}_{a,out} = \bar{\theta}_{a,in} = \bar{\theta}_a.$$

Also, maximum anti-squeezing is observed at $\theta = 150^\circ$, or orthogonal to the angle of maximum squeezing. The cycle can be seen to repeat itself for every π radians change in the measurement angle θ .

Figure 14.7: Laser phase noise w_1 and control signal u .Figure 14.8: The uncontrolled and controlled variable \tilde{z} .

Figure 14.9: Variance of \tilde{z} versus measurement angle θ .

Chapter 15

Integral LQG controller design

We showed through the simulation results in Section 14.4 that the laser phase noise, which was modelled previously as integrated white noise, can be completely suppressed using a standard LQG controller. However, in practice, the laser phase noise also has an unknown d.c. or low frequency component superimposed on it. This property of the noise was not accounted for in our previous model and to reject this constant or low frequency disturbance, we require a constant/slowly varying control signal. The standard LQG controller approach, as described in Chapter 14, cannot deal with this particular requirement (see Section 4.4) and we cater for this offset by including integral action in the LQG controller design.

We consider the same complete model as in Chapter 14, with the same choice of operating point, although one parameter of the piezo-electric actuator is slightly modified. As before, the operating point is chosen such that we obtain maximum amplitude squeezing of the fundamental output field \hat{A}_{out} . We also assume that the intracavity fields are locked to the incoming laser beams; i.e., the detuning variables satisfy $\Delta_a = \Delta_b = 0$. As before, the measurement available is the phase quadrature of the second harmonic field (δX_{Bout}^-) and actuation is provided by a piezo-electric actuator connected to a mirror which adjusts the phase quadrature of the second harmonic input field (δX_{Bin}^-).

15.1 Complete Model

For ease of reference, we again describe the complete linearised model which includes the dynamics of the piezo-electric actuator in state-space form as:

$$\dot{x} = Ax + B_1u + B_2w; \quad (15.1a)$$

$$y = Cx + Dw, \quad (15.1b)$$

where

$$x = \begin{bmatrix} \delta X_a^+ & \delta X_a^- & \delta X_b^+ & \delta X_b^- & \xi_1 & \xi_2 \end{bmatrix}^T;$$

$$w = [\delta X_{Ain}^+ \ \delta X_{Ain}^- \ \delta X_{Bin}^+ \ pBin \ X_{\delta A,l}^+ \ X_{\delta A,l}^- \ X_{\delta B,l}^+ \ X_{\delta B,l}^-]^T.$$

Note that this time however, we do not include the dynamical model of the laser phase noise in the system description. Figure 15.1 shows the plant to be controlled, where w_1 is used to represent laser phase noise. This noise is simply modelled as a fixed d.c. offset feeding into the system and we shall account for it through the inclusion of integral action in the controller design process.

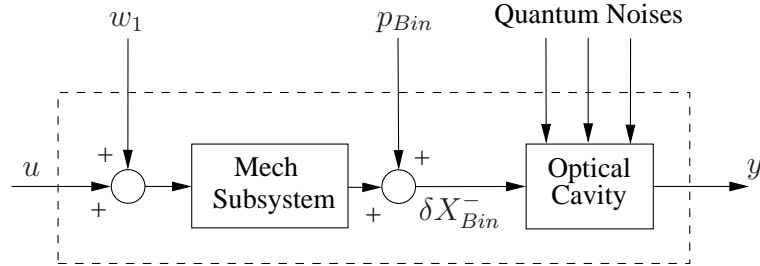


Figure 15.1: System interconnections for integral LQG controller design.

15.2 Performance Criterion and Integral Action

As before, the performance requirement for our control system is to minimise the variance of the amplitude quadrature of the fundamental output field \hat{A}_{out} , and to achieve squeezing in the presence of both quantum and classical noises. We consider the controlled variable described by (13.2) and also include a low-pass filter at the output of the controlled variable z as modelled in (13.4c). We then

consider minimising the filtered controlled variable \tilde{z} in a new LQ performance criterion as defined by (15.4).

Also, our system is subjected to laser phase noise (w_1) which is most prominent at low frequencies, presenting itself as an initial d.c. offset acting on the system. Our application requires the elimination of such effects but standard LQG techniques do not provide satisfactory performance in the face of such constant disturbances. We can fortunately however cater for this offset by including integral action in the LQG controller design process. We introduce integral action by adding an additional term in the cost function which involves the integral of the controlled output. To achieve this, we introduce the integral operator L , where

$$L(x) = \int_0^T A_2 x dt. \quad (15.2)$$

Here, A_2 is a constant matrix which is formed by selecting the state variables which are to be driven to zero in the steady-state. In our case, we choose

$$A_2 = [\cos \bar{\theta}_{a,out} \quad \sin \bar{\theta}_{a,out} \quad 0 \quad 0 \quad 0 \quad 0 \quad 0], \quad (15.3)$$

so that $z = A_2 x$. The integral LQG performance criterion is then formulated as the minimisation of the following cost function:

$$\mathcal{J} = \lim_{T \rightarrow \infty} \mathbf{E} \left[\frac{1}{T} \int_0^T x^T Q_1 x + L(x)^T Q_2 L(x) + u^T R u dt \right]. \quad (15.4)$$

We choose the matrices Q_1 , Q_2 and R such that

$$x^T Q_1 x = |z|^2, \quad u^T R u = r|u|^2, \quad Q_2 = q_2; \quad (15.5)$$

where $q_2, r > 0$ are treated as design parameters. The expectation in (15.4) is with respect to the Gaussian quantum and classical noise processes, and the assumed Gaussian initial conditions. Figure 15.2 shows the set-up used for the integral LQG controller design.

The integral LQG controller is formed by combining the Kalman filter with an optimal state feedback control law. The Kalman filter produces an optimal estimate of all the states of the system from the available measurement. The feedback control law is made up of two parts, K_1 and K_2 , which are present in the

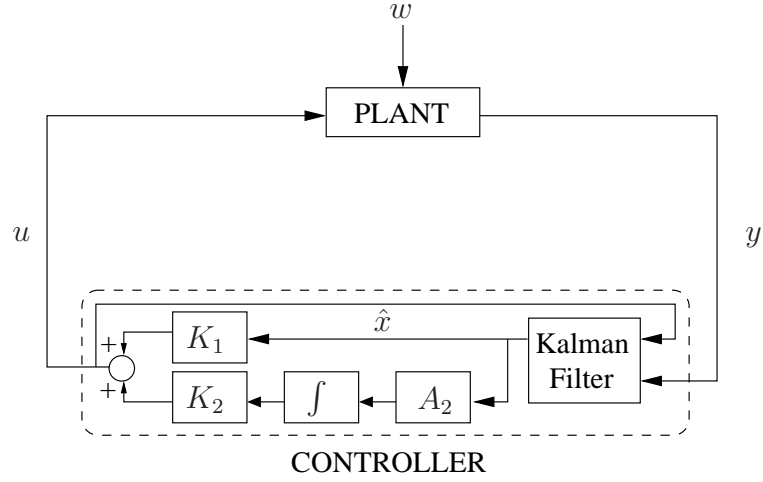


Figure 15.2: Integral LQG controller design configuration.

integrator path; see Figure 15.2. We will describe next how K_1 and K_2 are computed. This controller will then satisfy the specified performance requirements as described above and formulated in (15.4).

To put the system in a form suitable for standard LQG result to be applied, we transform the problem by augmenting the state variables of the system as follows. We define

$$\tilde{x} = \begin{bmatrix} x \\ L(x) \end{bmatrix}; \quad (15.6)$$

and rewrite the state equations as

$$\dot{\tilde{x}} = \tilde{A}\tilde{x} + \tilde{B}_1u + \tilde{B}_2w; \quad (15.7a)$$

$$y = \tilde{C}\tilde{x} + Dw, \quad (15.7b)$$

where

$$\tilde{A} = \begin{bmatrix} A & 0 \\ A_2 & 0 \end{bmatrix}; \quad \tilde{B}_1 = \begin{bmatrix} B_1 \\ 0 \end{bmatrix}; \quad \tilde{B}_2 = \begin{bmatrix} B_2 \\ 0 \end{bmatrix}; \quad \tilde{C} = \begin{bmatrix} C & 0 \end{bmatrix}. \quad (15.8)$$

The performance criterion can thus be reformulated as

$$\mathcal{J} = \lim_{T \rightarrow \infty} \mathbf{E} \left[\frac{1}{T} \int_0^T \tilde{x}^T \bar{Q} \tilde{x} + u^T R u \, dt \right], \quad (15.9)$$

where

$$\bar{Q} = \begin{bmatrix} Q_1 & 0 \\ 0 & Q_2 \end{bmatrix}. \quad (15.10)$$

We construct the LQG optimal controller from the solution to a deterministic regulator problem and an optimal observer problem as follows (see, e.g., [41, 48]):

$$\begin{aligned} u &= -K\hat{x} \\ &= -K_1\hat{x} - K_2L(\hat{x}). \end{aligned} \quad (15.11)$$

The optimal feedback gain matrix is given by

$$\begin{aligned} K &= [K_1 \quad K_2] \\ &= r^{-1}\tilde{B}_1^T X, \end{aligned}$$

where X satisfies the matrix Riccati equation:

$$\bar{Q} - r^{-1}X\tilde{B}_1\tilde{B}_1^T X + X\tilde{A} + \tilde{A}^T X = 0. \quad (15.12)$$

The optimal observer dynamics (Kalman filter) are described by

$$d\hat{x} = \tilde{A}\hat{x} dt + \tilde{B}_1 u dt + L[dy - \tilde{C}\hat{x} dt]; \quad (15.13)$$

and the solution of the optimal observer is obtained by choosing the gain matrix

$$L = (P_e \tilde{C}^T + \tilde{B}_2 D^T)(DD^T)^{-1}, \quad (15.14)$$

where P_e is the solution to the matrix Riccati equation

$$\begin{aligned} &(\tilde{A} - \tilde{B}_2 D^T (DD^T)^{-1} \tilde{C})P_e + P_e(\tilde{A} - \tilde{B}_2 D^T (DD^T)^{-1} \tilde{C})^T \\ &- P_e \tilde{C}^T (DD^T)^{-1} \tilde{C} P_e + \tilde{B}_2 \tilde{B}_2^T - \tilde{B}_2 D^T (DD^T)^{-1} D \tilde{B}_2^T = 0. \end{aligned} \quad (15.15)$$

15.3 Model and Design Parameters

The parameter values of the piezoelectric actuator and the steady-state phase angles of the input fields are shown in Table 15.1.

Model parameter	Value
r_1	1×10^4
r_2	1×10^9
c_1	-5×10^3
c_2	1.5×10^{10}
$\bar{\theta}_{a,in}$	$\pi/3$
$\bar{\theta}_{b,in}$	$5\pi/3$

Table 15.1: Piezoelectric Actuator and OPO Model Parameters used for Integral LQG Controller Design.

In designing the LQG controller, the design parameters ϵ_1^2 (quantum noise variance), ϵ_2^2 (sensor noise variance), R (the control energy weighting in the cost functional) and Q_2 were adjusted until good performance was obtained in the controller simulations. The values used were $\epsilon_1 = 1 \times 10^{-3}$, $\epsilon_2 = 1 \times 10^{-5}$, $R = 3.2 \times 10^{-7}$ and $Q_2 = 4 \times 10^{15}$. The large value of Q_2 is required to enforce integral action. These parameters led to an LQG controller with Bode plots as shown in Figure 15.3. The controller clearly possesses integral action and has infinite gain at dc to suppress the constant disturbance present in our application. The corresponding loop gain Bode plot is shown in Figure 15.4.

15.4 Simulation Results

Using the model parameters specified in Table 12.1 and 15.1, we simulate the closed-loop system using the SIMULINK[®] block diagram in Figure 15.5 to show the performance of the designed controller.

We consider the case where the system is excited with both classical and quantum noises. Figure 15.6 shows the laser phase noise w_1 , modelled as (approximately) integrated white noise superimposed over a fixed d.c. offset of magnitude 5 V introduced into the system. The laser noise subsystem is modelled as

$$P_{ln} = \frac{k_1}{\tau_1 s + 1}; \quad (15.16)$$

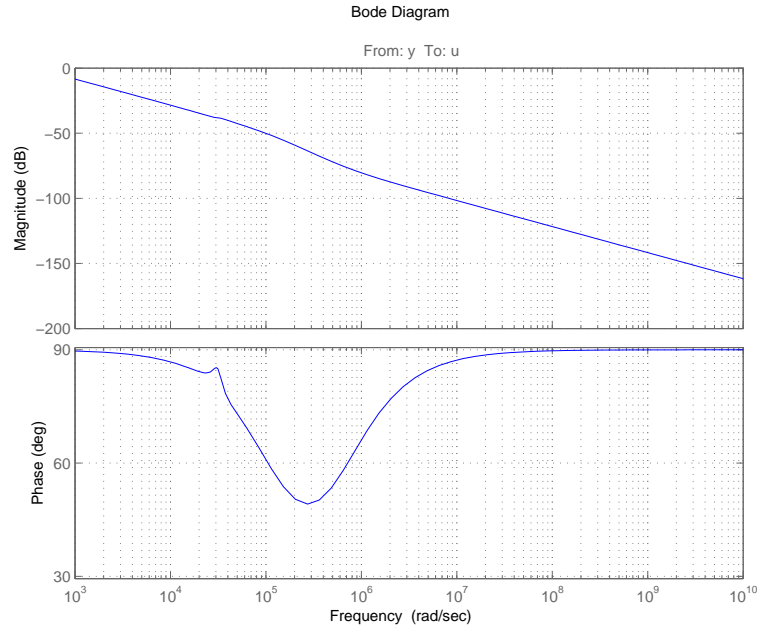


Figure 15.3: Bode plot of the Integral LQG controller.

where $k_1 = 3.33 \times 10^8$ and $\tau_1 = 3.33 \times 10^4$. The corresponding control signal u generated shows the effectiveness of the controller in rejecting the constant disturbance.

The movement of the mirror compensating for the laser phase noise is also shown in Figure 15.7 and finally, Figure 15.8 shows the time history of the filtered controlled and uncontrolled variable \tilde{z} .

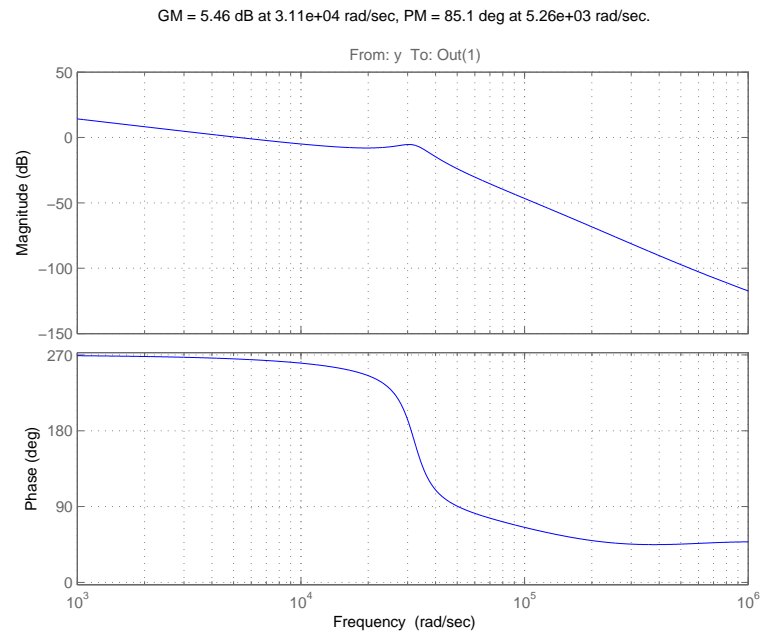


Figure 15.4: Bode plot of the loop gain transfer function.

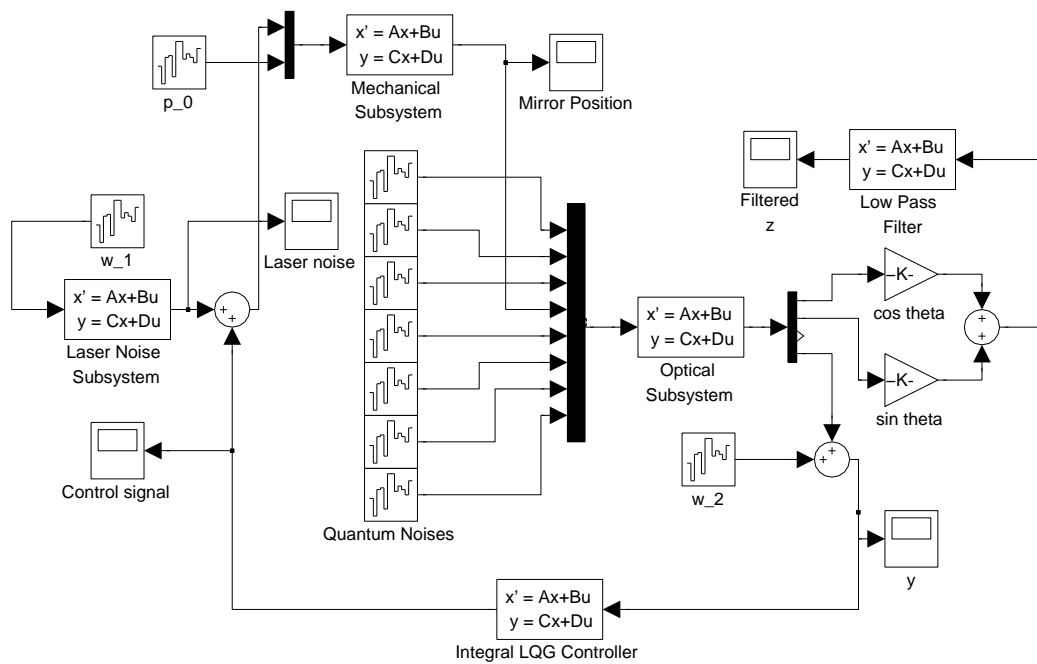


Figure 15.5: Simulink block diagram used for simulation of the Integral LQG controller.

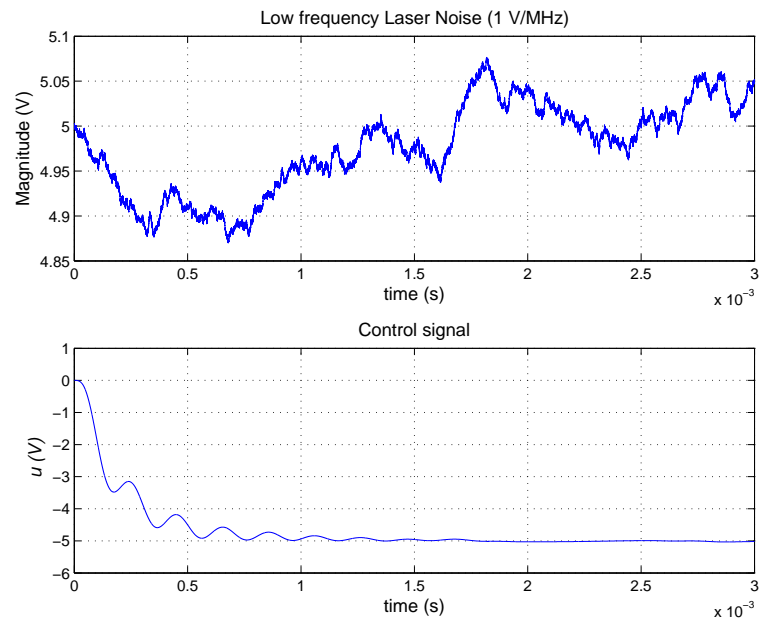
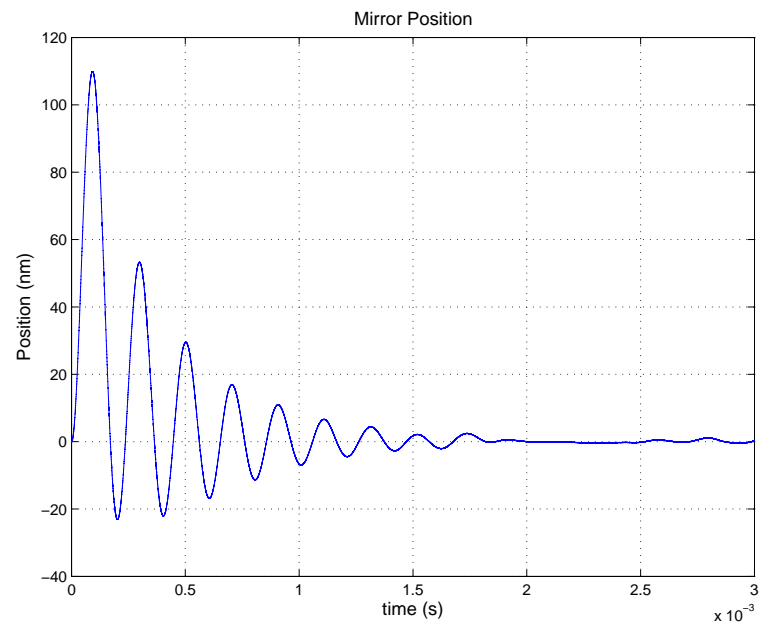
Figure 15.6: Laser phase noise w_1 and control signal u .

Figure 15.7: Mirror position.

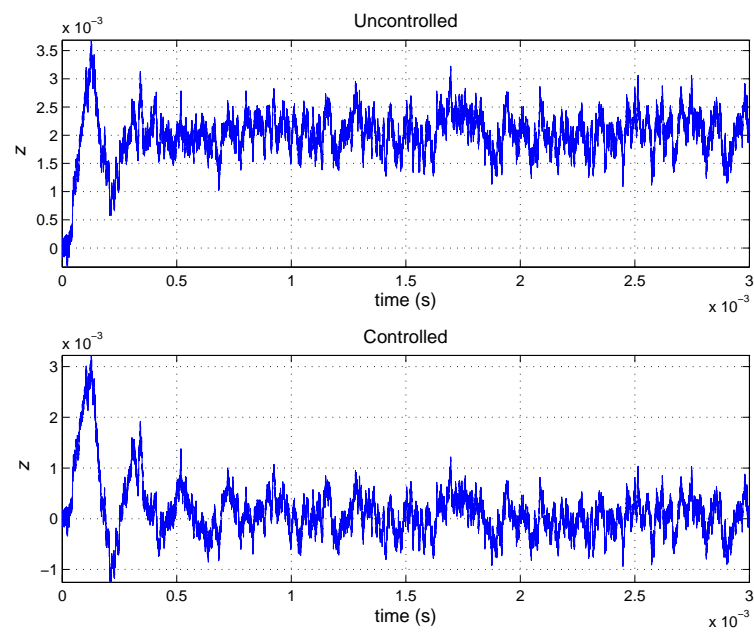


Figure 15.8: The uncontrolled and controlled variable \tilde{z} .

Chapter 16

Multivariable Integral LQG Controller

It is well known that one prerequisite to achieving squeezed states of light is that the optical resonator cavity needs to be frequency locked. The controllers designed in the previous Chapters 14 and 15 assume that the incoming beams and the intracavity fields are at resonance and the control problem then became one of only regulating the phase of the second harmonic input field to optimise the level of squeezing achieved in the amplitude quadrature of the fundamental output field. In this chapter, we consider the more general problem of optimising the level of squeezing achieved with the OPO when the detuning variables Δ_a and Δ_b are not zero. We shall design a multivariable controller that will also regulate the detuning variables Δ_a and Δ_b along with the original requirement to regulate the phase of the incoming harmonic field. Given the strong nonlinearity associated with the frequency locking problem (see Chapter 6), we will however only consider the local behaviour of the OPO. In other words, we assume that the system is operating within the linear region of operation of the resonator cavity and that the frequency locking requirement is to control small variations of Δ_a and Δ_b about $\Delta_a = \Delta_b = 0$.

16.1 Modelling

As was done in the last chapter, we will assume that the OPO is exposed to constant or low frequency disturbances in addition to the high frequency noises, thus

requiring the inclusion of integral action in the LQG controller design process. In particular, we will consider two different sources of laser phase noise acting on the OPO. One of these will offset the detuning variables Δ_a and Δ_b and the other one will adversely influence the phase of the harmonic input field \hat{B}_{in} .

As we are interested in controlling small variations of Δ_a and Δ_b about zero, and we only consider interactions between the fundamental and second harmonic optical fields, it is reasonable to assume that in the linear region of operation of the cavity,

$$\Delta_b = 2\Delta_a. \quad (16.1)$$

This linear relationship between the detuning variables simplifies the design problem as regulating one of the detuning variables to zero is then equivalent to regulating both to zero. The dynamics describing the behaviour of the OPO can thus be rewritten from (11.10) as follows:

$$\begin{aligned} \delta\dot{X}_a^+ &= -\kappa_a\delta X_a^+ + \bar{X}_a^-\Delta_a \\ &\quad + \frac{1}{2}\chi^{(2)}(\bar{X}_b^+\delta X_a^+ + \bar{X}_b^-\delta X_a^- + \bar{X}_a^+\delta X_b^+ + \bar{X}_a^-\delta X_b^-) \\ &\quad + \sqrt{2\kappa_{a,in}}\delta X_{Ain}^+ + \sqrt{2\kappa_{a,l}}X_{\delta A,l}^+; \end{aligned} \quad (16.2a)$$

$$\begin{aligned} \delta\dot{X}_a^- &= -\kappa_a\delta X_a^- - \bar{X}_a^+\Delta_a \\ &\quad + \frac{1}{2}\chi^{(2)}(\bar{X}_b^-\delta X_a^+ - \bar{X}_b^+\delta X_a^- - \bar{X}_a^-\delta X_b^+ + \bar{X}_a^+\delta X_b^-) \\ &\quad + \sqrt{2\kappa_{a,in}}\delta X_{Ain}^- + \sqrt{2\kappa_{a,l}}X_{\delta A,l}^-; \end{aligned} \quad (16.2b)$$

$$\begin{aligned} \delta\dot{X}_b^+ &= -\kappa_b\delta X_b^+ + 2\bar{X}_b^-\Delta_a - \frac{1}{2}\chi^{(2)}(\bar{X}_a^+\delta X_a^+ - \bar{X}_a^-\delta X_a^-) \\ &\quad + \sqrt{2\kappa_{b,in}}\delta X_{Bin}^+ + \sqrt{2\kappa_{b,l}}X_{\delta B,l}^+; \end{aligned} \quad (16.2c)$$

$$\begin{aligned} \delta\dot{X}_b^- &= -\kappa_b\delta X_b^- - 2\bar{X}_b^+\Delta_a - \frac{1}{2}\chi^{(2)}(\bar{X}_a^-\delta X_a^+ + \bar{X}_a^+\delta X_a^-) \\ &\quad + \sqrt{2\kappa_{b,in}}\delta X_{Bin}^- + \sqrt{2\kappa_{b,l}}X_{\delta B,l}^-. \end{aligned} \quad (16.2d)$$

The corresponding linearised output field equations remain unchanged; see (11.11). In (16.2), we choose to keep Δ_a in the equations but we could equivalently have chosen Δ_b . Moreover, we select the same operating point for the optical squeezer as in Chapters 14–15 such that we obtain amplitude squeezing of the fundamental output field \hat{A}_{out} . Also, in addition to δX_{Bout}^- , we use a second measurement

to control the system. In this case, we choose the amplitude quadrature of the fundamental output field, δX_{Aout}^+ . Actuation is provided by two piezo-electric actuators acting on two mirrors, thus regulating the detuning variables $\Delta_a(\Delta_b)$ and the phase quadrature of the second harmonic input field, δX_{Bin}^- . As before, the requirement is to minimise the variance of the amplitude quadrature of the fundamental output field.

Figure 16.1 shows a schematic for the multivariable control of the OPO. The rightmost mirror is chosen as the point of actuation for the control of the detuning variables Δ_a and Δ_b .

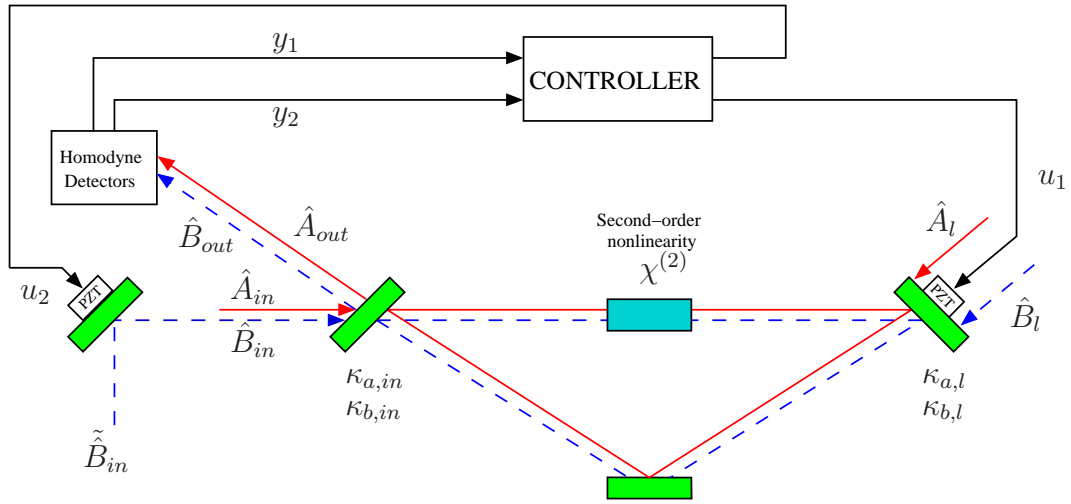


Figure 16.1: Schematic of the proposed multivariable controller for the Optical Parametric Oscillator.

The piezo-electric actuators attached to the mirrors (the mechanical subsystems) are modelled as a second order systems. The dynamics of the actuator used to control the phase of the harmonic input field is described by:

$$\begin{bmatrix} \dot{\xi}_1 \\ \dot{\xi}_2 \end{bmatrix} = \begin{bmatrix} 0 & 1 \\ -r_2 & -r_1 \end{bmatrix} \begin{bmatrix} \xi_1 \\ \xi_2 \end{bmatrix} + \begin{bmatrix} 0 \\ 1 \end{bmatrix} w_1 + \begin{bmatrix} 0 \\ 1 \end{bmatrix} u_2; \quad (16.3a)$$

$$\delta X_{Bin}^- = [c_2 \ c_1] \begin{bmatrix} \xi_1 \\ \xi_2 \end{bmatrix} + p_{Bin}. \quad (16.3b)$$

Similarly, the actuator used to control the detuning variables Δ_a and Δ_b can be

described as follows:

$$\begin{bmatrix} \dot{\xi}_3 \\ \dot{\xi}_4 \end{bmatrix} = \begin{bmatrix} 0 & 1 \\ -r_4 & -r_3 \end{bmatrix} \begin{bmatrix} \xi_3 \\ \xi_4 \end{bmatrix} + \begin{bmatrix} 0 \\ 1 \end{bmatrix} w_2 + \begin{bmatrix} 0 \\ 1 \end{bmatrix} u_1; \quad (16.4a)$$

$$\Delta_a = [c_4 \ c_3] \begin{bmatrix} \xi_3 \\ \xi_4 \end{bmatrix} + p_0. \quad (16.4b)$$

The complete linearised system can then be modelled in state-space form as:

$$\dot{x} = Ax + B_1 u + B_2 w; \quad (16.5a)$$

$$y = Cx + Dw; \quad (16.5b)$$

$$\Delta_a = Fx, \quad (16.5c)$$

where

$$\begin{aligned} x &= \begin{bmatrix} \delta X_a^+ & \delta X_a^- & \delta X_b^+ & \delta X_b^- & \xi_1 & \xi_2 & \xi_3 & \xi_4 \end{bmatrix}^T; \\ w &= \begin{bmatrix} \delta X_{Ain}^+ & \delta X_{Ain}^- & \delta X_{Bin}^+ & p_{Bin} & X_{\delta A,l}^+ & X_{\delta A,l}^- & X_{\delta B,l}^+ & X_{\delta B,l}^- & w_1 & w_2 \end{bmatrix}^T; \\ y &= [\delta X_{Bout}^- \ \delta X_{Aout}^+]^T. \end{aligned}$$

16.2 LQG Performance Criterion

It is not mathematically obvious that the detuning variables need to be minimised to achieve squeezed states of light. The original performance requirement to minimise the variance of the amplitude quadrature of the fundamental output field \hat{A}_{out} is still valid but needs to be supplemented with the additional requirement to minimise the detuning variables Δ_a and Δ_b . We thus define the control variables as:

$$z_1 = \delta X_a^+ \cos \bar{\theta}_{a,out} + \delta X_a^- \sin \bar{\theta}_{a,out}; \quad (16.6a)$$

$$z_2 = \Delta_a. \quad (16.6b)$$

Moreover, in the presence of laser phase noise which presents itself as a slowly varying or constant dc offset, there is a need to include integral action in the LQG controller design process. Note that in this problem, there are two different

sources of low frequency noise. The standard LQG cost functional is thus modified to include an additional term which involves the integral of the outputs. Let us first introduce the integral operator L , where

$$L(y) = \begin{bmatrix} L(y_1) \\ L(y_2) \end{bmatrix} = \begin{bmatrix} \int_0^T y_1(\tau) d\tau \\ \int_0^T y_2(\tau) d\tau \end{bmatrix}. \quad (16.7)$$

We can now formulate the integral LQG performance criterion as the minimisation of the following cost function:

$$\mathcal{J} = \lim_{T \rightarrow \infty} \mathbf{E} \left[\frac{1}{T} \int_0^T x^T Q x + L(y)^T \bar{Q} L(y) + u^T R u dt \right]. \quad (16.8)$$

We choose the matrices Q , \bar{Q} , and R such that:

$$x^T Q x = x^T \begin{bmatrix} q_1 & 0 \\ 0 & q_2 \end{bmatrix} x = q_1 |z_1|^2 + q_2 |z_2|^2; \quad (16.9a)$$

$$L(y)^T \bar{Q} L(y) = L(y)^T \begin{bmatrix} q_3 & 0 \\ 0 & q_4 \end{bmatrix} L(y) = q_3 |L(y_1)|^2 + q_4 |L(y_2)|^2; \quad (16.9b)$$

$$u^T R u = u^T \begin{bmatrix} r_{w1} & 0 \\ 0 & r_{w2} \end{bmatrix} u = r_{w1} |u_1|^2 + r_{w2} |u_2|^2. \quad (16.9c)$$

Here, $q_1, q_2, q_3, q_4, r_{w1}, r_{w2} > 0$ are treated as design parameters. The expectation in (16.8) is with respect to the Gaussian quantum and classical noise processes, and the assumed Gaussian initial conditions.

Figure 16.2 shows the set-up used for the multivariable integral LQG controller design. In order to apply the standard LQG approach to the system, we include the integrators as part of an augmented system which we define next. If we allow

$$\tilde{x} = \begin{bmatrix} x \\ L(y) \end{bmatrix}; \quad \tilde{y} = \begin{bmatrix} \tilde{y}_1 \\ \tilde{y}_2 \\ \tilde{y}_3 \\ \tilde{y}_4 \end{bmatrix}; \quad \text{and} \quad \tilde{w} = \begin{bmatrix} w \\ v_1 \\ v_2 \\ v_3 \\ v_4 \end{bmatrix}; \quad (16.10)$$

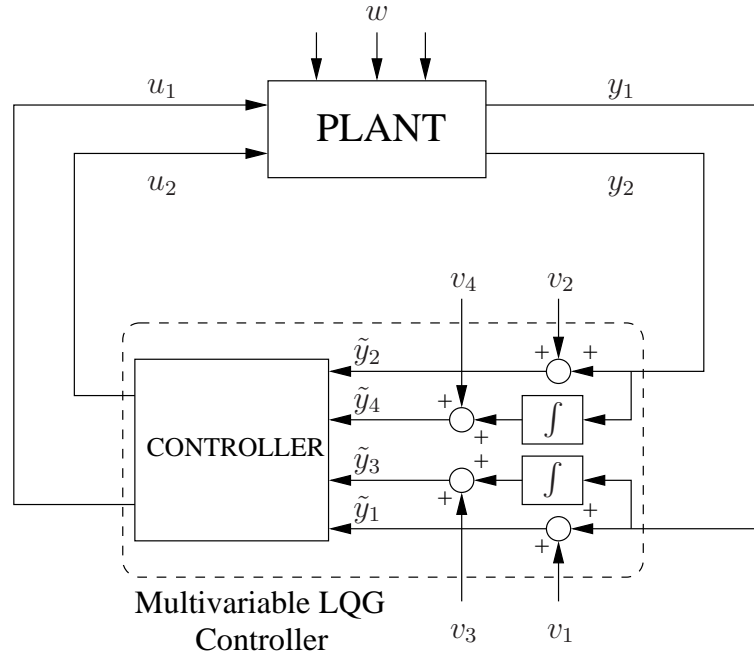


Figure 16.2: Multivariable controller design configuration.

we can rewrite the dynamics of the complete system as

$$\dot{\tilde{x}} = \tilde{A}\tilde{x} + \tilde{B}_1 u + \tilde{B}_2 \tilde{w}; \quad (16.11a)$$

$$\tilde{y} = \tilde{C}\tilde{x} + \tilde{D}\tilde{w}. \quad (16.11b)$$

Here,

$$\tilde{A} = \begin{bmatrix} A & 0 \\ C & 0 \end{bmatrix}; \quad \tilde{B}_1 = \begin{bmatrix} B_1 \\ 0 \end{bmatrix}; \quad \tilde{B}_2 = \begin{bmatrix} B_2 & 0 \\ 0 & 0 \end{bmatrix}; \quad (16.12a)$$

$$\tilde{C} = \begin{bmatrix} C & 0 \\ 0 & I \end{bmatrix}; \quad \tilde{D} = \begin{bmatrix} D & \\ 0 & I_{4 \times 4} \end{bmatrix}. \quad (16.12b)$$

After the controller design, the integrators are pulled back from the augmented system and included as part of the controller. The performance criterion can now be reformulated as

$$\mathcal{J} = \lim_{T \rightarrow \infty} \mathbf{E} \left[\frac{1}{T} \int_0^T \tilde{x}^T \tilde{Q} \tilde{x} + u^T R u \, dt \right], \quad (16.13)$$

where

$$\tilde{Q} = \begin{bmatrix} Q & 0 \\ 0 & \bar{Q} \end{bmatrix}. \quad (16.14)$$

The multivariable controller is then constructed by estimating the states of the augmented system described by (16.11) using a Kalman filter and combining it with an optimal state feedback control law as follows:

$$u = -K\hat{x}.$$

The optimal feedback gain matrix is given by

$$K = r^{-1}\tilde{B}_1^T X,$$

where X satisfies the matrix Riccati equation:

$$\bar{Q} - r^{-1}X\tilde{B}_1\tilde{B}_1^T X + X\tilde{A} + \tilde{A}^T X = 0. \quad (16.15)$$

The optimal observer dynamics (Kalman filter) are described by

$$d\hat{x} = \tilde{A}\hat{x} dt + \tilde{B}_1 u dt + L[d\tilde{y} - \tilde{C}\hat{x} dt]; \quad (16.16)$$

and the solution of the optimal observer is obtained by choosing the gain matrix

$$L = (P_e \tilde{C}^T + \tilde{B}_2 \tilde{D}^T)(\tilde{D}\tilde{D}^T)^{-1}, \quad (16.17)$$

where P_e is the solution to the matrix Riccati equation

$$\begin{aligned} & (\tilde{A} - \tilde{B}_2 \tilde{D}^T (\tilde{D}\tilde{D}^T)^{-1} \tilde{C}) P_e + P_e (\tilde{A} - \tilde{B}_2 \tilde{D}^T (\tilde{D}\tilde{D}^T)^{-1} \tilde{C})^T \\ & - P_e \tilde{C}^T (\tilde{D}\tilde{D}^T)^{-1} \tilde{C} P_e + \tilde{B}_2 \tilde{B}_2^T - \tilde{B}_2 \tilde{D}^T (\tilde{D}\tilde{D}^T)^{-1} \tilde{D} \tilde{B}_2^T = 0. \end{aligned} \quad (16.18)$$

16.3 Model and Design Parameters

The parameter values of the piezo-electric actuators and the steady-state phase angles of the input fields used for the controller design are shown in Table 16.1. The parameters of the OPO are as in Table 12.1.

Model Parameters	Value
r_1	8×10^3
r_2	1×10^9
c_1	-5×10^3
c_2	1.5×10^{10}
r_3	5×10^4
r_4	3×10^9
c_3	-4×10^3
c_4	3×10^{10}
$\bar{\theta}_{a,in}$	$\pi/3$
$\bar{\theta}_{b,in}$	$5\pi/3$

Table 16.1: Piezoelectric Actuators and OPO Model Parameters used for Multi-variable LQG Controller Design.

Table 16.2 shows the design parameters used for the generation of the LQG controller. The quantity ϵ_{qn}^2 represents the quantum noise variance, ϵ_{w1}^2 and ϵ_{w2}^2 represent the variance of the process noises feeding into the respective piezoelectric actuators, and $\epsilon_{p_{Bin}}^2$ and $\epsilon_{p_0}^2$ model the respective sensor noise variances on the piezo-actuators. Also, ϵ_{v1}^2 , ϵ_{v2}^2 , ϵ_{v3}^2 and ϵ_{v4}^2 are used to model the variance of the sensor noise on the measurements. In particular, note that the sensor noises present in \tilde{y}_3 and \tilde{y}_4 are fictitious and are included for design purposes only. These design parameters were adjusted until a suitable controller is obtained and good performance is observed in the computer simulations. Figure 16.3 shows the Bode plots of the 2×2 multivariable controller.

16.4 Simulation Results

Using the model parameters in Table 12.1 and 16.1, we simulate the system using the SIMULINK[®] block diagram shown in Figure 16.4. The laser noise blocks used in the simulation are modelled as (approximately) integrated white noise superimposed over a fixed dc offset. They are described by

$$P_{ln1} = \frac{k_1}{\tau_1 s + 1}, \quad \text{and} \quad P_{ln2} = \frac{k_2}{\tau_2 s + 1}; \quad (16.19)$$

Design Parameters	Value
q_1	1×10^{10}
q_2	1×10^8
q_3	5×10^{15}
q_4	5×10^{15}
r_{w1}	5×10^3
r_{w2}	3×10^6
ϵ_{qn}	1
ϵ_{w1}	1
ϵ_{w2}	1
$\epsilon_{p_{Bin}}$	$\sqrt{10}$
ϵ_{p_0}	1
ϵ_{v1}	1×10^{-2}
ϵ_{v2}	10
ϵ_{v3}	1×10^{-2}
ϵ_{v4}	1×10^{-6}

Table 16.2: Design Parameters used for the Multivariable LQG Controller.

respectively, where $k_1 = 6.67 \times 10^7$, $\tau_1 = 3.33 \times 10^4$, $k_2 = 6 \times 10^8$, and $\tau_2 = 5 \times 10^4$. The offset introduced in P_{ln1} affecting Δ_a is chosen to be of magnitude -15 V and the fixed d.c. offset affecting the phase quadrature δX_{Bin}^- is similarly chosen to be 20 V. It is of course assumed that these offsets will not push the system outside its linear region of operation. We simulate the closed-loop system to show the performance of the designed controller. We consider the case where the system is excited with both classical and quantum noises. Figure 16.5 shows the laser phase noise 1 and the corresponding control signal u_1 generated by the controller. Similarly, Figure 16.6 shows the effectiveness of the controller in counteracting the laser phase noise affecting the phase quadrature of the harmonic input field.

To show the effect of the controller more clearly at high frequencies, we also generate a plot of the error signals as shown in Figure 16.7.

Figure 16.8 shows the movement of the mirrors compensating for the laser phase noises. We note that the movement of mirror 1 controlling the detuning variables needs to stabilise first to get the system in frequency lock before the phase quadrature of the input field can be properly controlled by mirror 2.

Finally, we also simulate the open-loop and closed-loop system to compare the effect of having no controller on the filtered controlled variable \tilde{z} . Figure 16.9

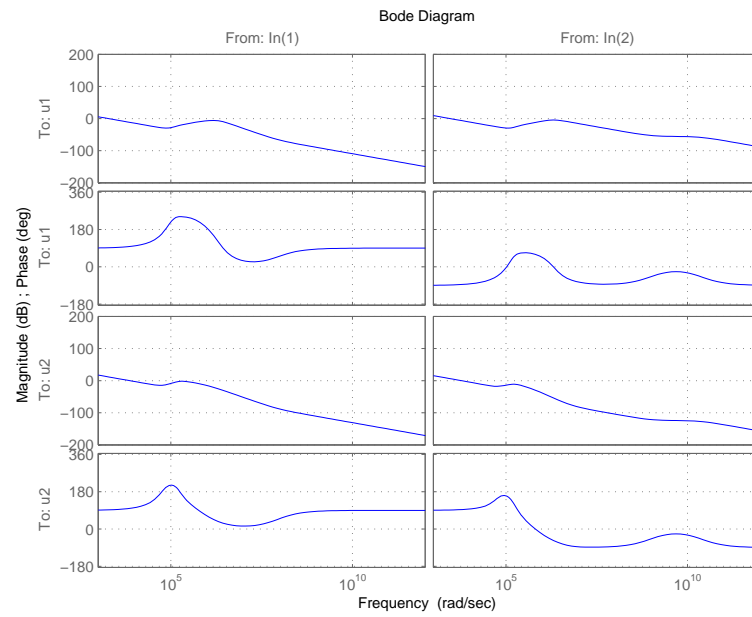


Figure 16.3: Bode plots of the multivariable LQG controller.

compares the time-history for the two cases.

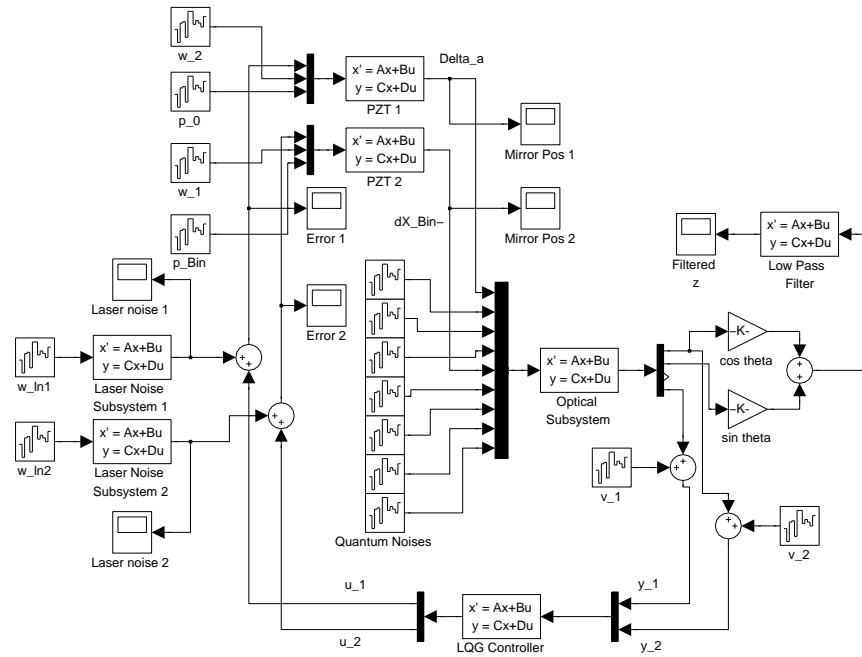


Figure 16.4: Simulink block diagram used for the multivariable controller simulation

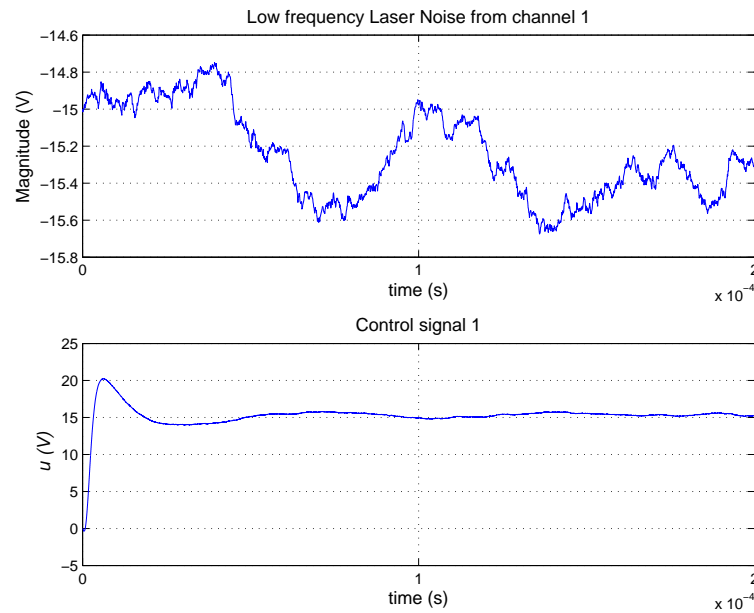


Figure 16.5: Laser phase noise 1 and the corresponding control signal u_1 .



Figure 16.6: Laser phase noise 2 and the corresponding control signal u_2 .

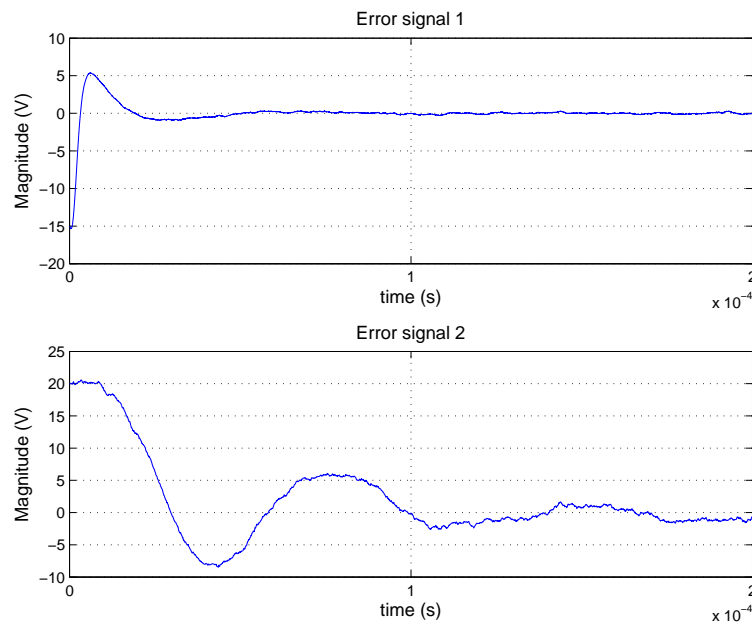


Figure 16.7: Error signals e_1 and e_2 .

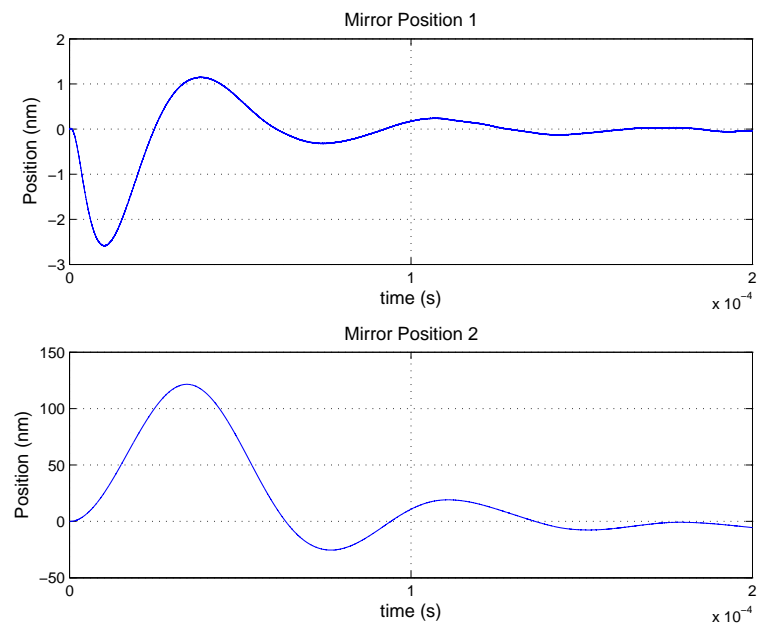
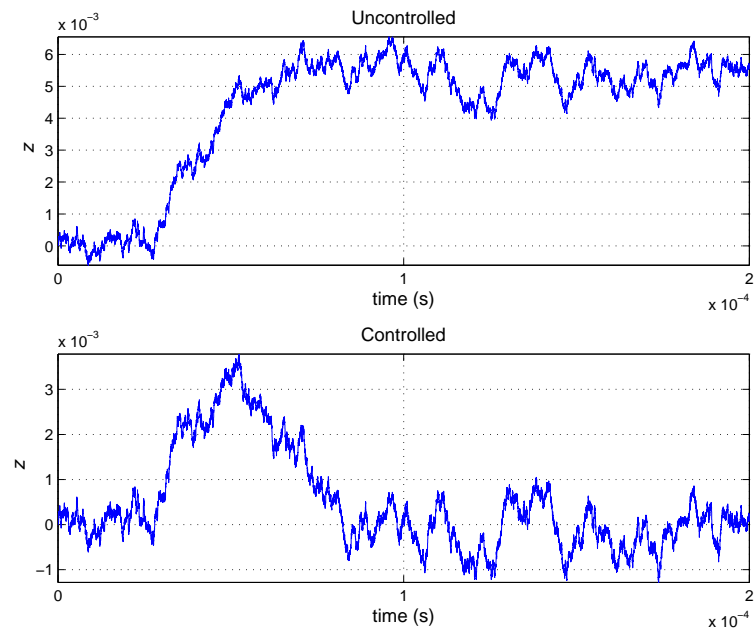


Figure 16.8: Mirror positions 1 and 2.

Figure 16.9: The uncontrolled and controlled variable \tilde{z}

Chapter 17

Conclusion

We have studied the optical parametric oscillator which is a widely used non-linear device in quantum optics. We began by briefly explaining the process by which squeezed states of light are generated in an OPO and motivated our research. The nonlinear dynamics of the optical resonator cavity were then derived in terms of the quadrature operators and we analysed the steady-state behaviour of the system. In particular, we investigated the steady-state conditions that resulted in the generation of specific types of squeezed states of light. We showed that depending on the phase of the input optical fields, we can determine the type and the extent of squeezing achieved. Furthermore, depending on the type of squeezed states desired, we determined a relationship that must exist between the phase of the input fields to achieve maximum squeezing. A selected direction of measurement was chosen corresponding to the axis of the quadrature we are interesting in minimising. In our present work, we are interested in optimising the amplitude quadrature squeezing of the fundamental field and consequently chose a control variable that reflects this requirement. We initially determined the variance of the control variable in the absence of coupling between the two optical fields with only quantum noises affecting the system. This value corresponds to the standard quantum limit (SQL). Allowing for interaction between the intracavity fields, we showed that the variance of the controlled variable can drop below the SQL at various operating points but is minimal when the pairs of input phase angles satisfy a predetermined relationship for maximum squeezing (12.14). This result confirmed the previous steady-state analysis. Moreover, we also showed that the variance orthogonal to the direction of measurement is

maximal when (12.14) is satisfied.

A natural extension to this work was to determine whether it is possible to reduce the variance of the selected quadrature further along the direction of measurement by using a controller. Thus, we designed a series of LQG controllers at different operating points (corresponding to different input phase angles) and showed that it was not possible to achieve more squeezing with the controllers in place. This result is also as expected. For a given OPO, and in the presence of quantum noises only, the extent of squeezing achieved should not be affected by the use of external devices (controllers). However, in practice, OPOs are subjected to both quantum and classical noises and our aim is to minimise the effect of the classical noises entering the system.

We considered three separate cases. In the first scenario, we model laser phase noise entering the system as integrated white noise and incorporate that noise model in the design of an LQG controller for the system at a given operating point. Simulation results showed the effectiveness of the controller in cancelling out classical noises and showed that the system performance is limited only by the sub-quantum noise limit. Next, we consider the more practical case where laser phase noise is modelled as integrated white noise superimposed over a fixed d.c. offset. An LQG controller which included integral action was designed to cater for this scenario and we validated our design with simulation results. We showed that good performance can be achieved in the presence of steady-state offsets. For the two cases considered however, one important assumption we made was that the optical resonator cavity was frequency locked and that the detuning variables were zero. This assumption was removed for the final case when we considered the more realistic situation with the optical cavity operating away from resonance, i.e., the detuning variables are not zero and laser phase noise with d.c. offset is acting at two different points in our system. In this case, a multivariable controller is designed and successfully simulated with piezo-electric actuators controlling the two mirrors.

Future work would involve implementing the proposed control approaches to an experimental test bed. For practical consideration, we would only implement controllers with integral action. These controllers can potentially provide considerable improvement to the quality of the squeezed states of light generated. Another avenue for future research could involve investigating the possibility of

achieving a global lock for the optical resonator cavity. As it is, we assume that the system is operating within a linear region and control small variations about this point. An approach similar to the one considered in Chapter 7 could provide a suitable starting point. The situation is however more complicated given the fact that there are two optical fields and the convenient relationship we assume between the two detuning variables Δ_a and Δ_b is not necessarily applicable outside the linear region of operation.

Part III

Robustness of Risk-Sensitive Controllers for Quantum Systems

Chapter 18

Introduction

In recent years, a significant amount of theoretical research work has addressed the feedback control problem of quantum systems; see, e.g., [72, 74, 82–87]. In most cases, control techniques analogous to those used for classical control systems have been directly applied to models of quantum systems (see [84]) and more specifically, there has been a lot of emphasis laid upon a quantum version of the classical linear quadratic Gaussian (LQG) control method. An appealing feature of the LQG method is that it caters for stochastic systems, a class of systems which quantum systems naturally fit into provided that the quantum dynamics and the measurement(s) are linear in the observables (see Section 19.3), and that the measurement process introduces Gaussian noise. Moreover, the LQG approach conveniently allows for a separation principle whereby the states of a system are estimated using appropriate (quantum) filters followed by a feedback control law applied on the estimated states; see [14, 73, 88]. While the similarities between classical and quantum systems allowing us to extend classical control techniques to quantum systems are evident, the main difference remains the effect of measurement on quantum systems, also referred to as “back-action”. Measurements disturb a quantum system under observation in ways that are quite different to those observed for classical systems, making closed-loop control more challenging. For example, since measurements affect the dynamics of a system, it also then becomes more difficult to have a good estimate of the states of the system.

With technological developments, there have been numerous applications or schemes to partly circumvent the problem of quantum measurement. For ex-

ample, an *adaptive* scheme initially proposed by Wiseman in [89] has been implemented to obtain continuous accurate measurements from a quantum system while minimally disturbing the system. It is shown experimentally in [90] that this scheme approached the quantum uncertainty limit more closely than any other measurement technique used at the time in the area of precision metrology. Better measurement techniques allow for improved estimates of the quantum states which in turn can be used to better control a quantum system. This result naturally leads us to consider a quantum version of the classical LQG control approach. While the classical LQG approach seems to be amenable to quantum systems, it is well known that it provides little guarantee of stability when subjected to model uncertainty; see [91]. And even though improved measurement techniques guarantee a certain sense of continuity with regards to the dynamical behaviour of quantum systems, quantum systems can change and vary dramatically at times. It is well known in the control literature that robustness is of critical importance in the design of feedback control systems. In particular, a feedback controller is commonly designed on the basis of a nominal model which only approximates the true behavior of a system being controlled. And the need for robustness in feedback control system design applies equally for quantum systems as it does for classical systems, if not more so. Given the nature of quantum systems and the underlying uncertainties associated with them, it is natural therefore to require any practical quantum control algorithm to be robust. These considerations motivated the work of [1] which deals with the risk-sensitive optimal control of quantum systems.

The interest in the risk-sensitive problem is due to its close connections to robust control and minimax games (see [92, 93]) and the use of a risk sensitive cost criterion in designing optimal feedback controllers is known to lead to useful robustness properties for the resulting controller; see [94–96]. Indeed, in the paper [94], it is shown that the use of a risk sensitive optimal controller enables an upper bound to be obtained for a certain (risk neutral) cost function for a class of true system dynamics which differ from the nominal system model that is used to design the risk sensitive controller. We apply similar results here to quantum systems. The main result in this part of the thesis represents an extension of the work of [1] and [2]. We show that for a class of risk sensitive optimal controllers for quantum systems, a bound on a corresponding risk neutral

cost function can also be obtained. This result represents a quantum version of the result of [94] and provides motivation for the risk sensitive optimal control procedure as a suitable methodology for designing robust feedback controllers for quantum systems. It does so by using the quantum risk sensitive control result of [1] and is based on a duality formula similar to that used in [94]. In this context, we also need to mention the work by Yamamoto et al. in [97] using risk-sensitive estimators and following a related approach to the one presented here. Their approach however addresses the problem of robustness by allowing for perturbations in the density matrix while we consider perturbations in the observables used in the determination of the states of the quantum system, which in turn allows for variation in the cost function used for the determination of the risk-sensitive controller. Moreover, the result of [97] relies on a quantum version of the duality formula which is different from that used here and they obtain a different estimation error band for a different class of uncertainty of the quantum system.

We begin with a brief overview of quantum mechanics in Chapter 19, highlighting the tools used to describe quantum systems and which will be used throughout the rest of this work. In Chapter 20, we describe the behavior of discrete-time quantum systems using a stochastic master equation and we introduce the concept of selective evolution of the states using an appropriate probability distribution. The classical risk-neutral optimal control problem is explained in Section 21.1 and the quantum generalization of the classical cost function as well as the resulting dynamic programming equations are described. The advantages of the risk-sensitive control method over the risk-neutral (LQG) scheme for this particular class of problems are emphasized in Section 21.2 and the robustness properties associated with the risk-neutral control method are developed in Chapter 22, with a set of proofs and lemmas using certain Radon-Nikodym derivatives. Finally, the main result of this work is illustrated with an example involving a simple two-level quantum system.

Chapter 19

Preliminaries

19.1 State of a Quantum System

The state of a quantum mechanical system is represented by a vector in a separable Hilbert space. A Hilbert space \mathcal{H} is a complex vector space with an inner product given by an operation $(\cdot, \cdot) : \mathcal{H} \times \mathcal{H} \rightarrow \mathbb{C}$; see, e.g., [98].

We use the standard Dirac's notation to denote states in quantum mechanics. For example, the quantum mechanical notation for a state vector ψ is $|\psi\rangle$ (also called a “ket”). The vector dual to $|\psi\rangle$ is denoted by $\langle\psi|$ and in the finite dimensional case is the complex conjugate transpose of $|\psi\rangle$ (also called a “bra”). The standard quantum mechanical notation for the inner product between two kets $|\phi\rangle$ and $|\psi\rangle$ is $\langle\phi|\psi\rangle$ (forming a “bra-ket”). The norm of a vector $|\psi\rangle$, is defined as $\| |\psi\rangle \| := \sqrt{\langle\psi|\psi\rangle}$. It is often assumed that the vector representing the state of a quantum system has norm equal to one, i.e., $\langle\psi|\psi\rangle = \| |\psi\rangle \|^2 = 1$ and we then say that $|\psi\rangle$ is normalized.

To model a quantum system, the set of states are chosen so that they have a physical meaning usually corresponding to either a given position, momentum, spin or energy. Accordingly, we work in a given “representation”. The “dimension” of a quantum system is a measure of the number of elements (cardinality) of the chosen set of states and could be finite or infinite. For example, a two dimensional system will have a pair of distinguished orthonormal states, say $|0\rangle$ and $|1\rangle$. In the energy representation, the dimension of a quantum system is called the “number of levels”. However, this appellation is also widely used for other representations as well; see [99].

19.2 Measurement

Before we can apply classical control theory or an equivalent quantum version of the theory to quantum systems, we need to determine the relevant “observables” (see Section 19.3) of the systems. An observable is a linear operator which maps a Hilbert space which contains all the possible quantum states into itself and all the possible outcomes of the measurement are eigenvalues of the observable (which are real since the observable is Hermitian). If a quantum system is prepared and a particular aspect (observable) of it is measured and the process is repeated many times under the same set of conditions, different results will be obtained. In particular, the result follows a probability distribution which can be continuous or discrete, thus making the process non-deterministic. Moreover, different observables may not be exactly measured at the same time due to a lack of commutativity.

It is well known that for feedback control to be effective, we need to act upon some measurement which provides us information about the states of the system. In classical systems, this is not a cause for concern if we can measure some or all of the states. If not all of the states can be measured, we can estimate the states from the measurement of the output of the system using for example, a Kalman filter; see [41]. Quantum systems however are affected by measurement, in such a way that the act of measuring the system (without any control applied) affects the dynamics of the system and adds noise to the state of the system (due to the randomness of the measurement result). This is a well-known effect in quantum mechanics referred to as the back-action of measurement. Different types of measurement performed on a quantum system may affect the system differently, introducing different levels of noise. A direct projective measurement for example, results in an instantaneous and complete collapse of the quantum system into an eigenstate of the measurement operator. This effect is known as state collapse, or von Neumann state reduction and represents a discontinuous evolution of the quantum state due to quantum jumps. Fortunately, there exists ways in which quantum systems can be measured with less abrupt disruptions of the system, referred to as indirect or “weak” measurements. In this scheme, the state of the quantum system can be pictured as being entangled with a meter and the measurement is made on the meter rather than on the system. If the coupling between the meter and the system is kept at a low level, the back-action of the

measurement is reduced and we end up with a continuous stochastic evolution of the quantum states, amenable to control design techniques. The feedback algorithm will depend on the strength of coupling or on the measurement strength which affects the level of noise introduced into the system. This represents a trade-off that is always present in quantum systems and deciding on the measurement strength that will provide the most effective feedback is an ongoing research problem. It is worthwhile pointing out here that in some applications in quantum optics, there is no need for measurement at all as we can directly feed back the physical output of the system to the input via a quantum controller. This naturally leads to the use of optical feedback actuators; see [100, 101].

19.3 Operators and Observables

Quantum mechanics is usually described using linear operators. Physical quantities such as momentum, position and spin can be represented by self-adjoint operators and these are called “observables”. The outcomes of experiments corresponding to an observable A are postulated to take values in the spectrum (the collection of all eigenvalues a) of A , and these are distributed randomly. Upon measuring the state $|\psi\rangle$, the probability of getting the result a is given by (assuming a discrete non-degenerate spectrum for A)

$$p(a|\psi) = \langle \psi, P_a \psi \rangle, \quad (19.1)$$

where $\langle \cdot, \cdot \rangle$ denotes the inner product on \mathcal{H} , and ψ is a normalized state vector ($|\psi|^2 = 1$). P_a denotes the projection on the eigenspace corresponding to the eigenvalue a . In Dirac notation, we write this as an outer product $P_a = |a\rangle\langle a|$, where $|a\rangle$ is the corresponding normalized eigenvector. Hence,

$$p(a|\psi) = \langle \psi | a \rangle \langle a | \psi \rangle = |\langle \psi | a \rangle|^2. \quad (19.2)$$

After such a measurement is taken on a system, the state becomes

$$|\psi'\rangle = \frac{P_a |\psi\rangle}{\sqrt{p(a|\psi)}} = |a\rangle. \quad (19.3)$$

The result of a measurement is certain if and only if the system is already in a state which is an eigenvector of the observable being measured, in which case we obtain the corresponding eigenvalue and the system remains in the same state.

19.4 Density Operator

In practice, we usually study an “ensemble” of a large number of identical systems in different states rather than one system in a given state and we usually require information about the proportion of systems in a given state. This information is recorded using an operator rather than a vector and is called the “density operator” or “density matrix” ω . If there is a fraction $0 < \alpha_j \leq 1$ of systems in the ensemble with state $|\psi_j\rangle$, $\sum_j \alpha_j = 1$, then the density operator describing the state of the ensemble is given by

$$\omega := \sum_j \alpha_j |\psi_j\rangle\langle\psi_j|. \quad (19.4)$$

Density operators are positive semidefinite operators¹ on \mathcal{H} with trace one (since $\sum_j \alpha_j = 1$). In general, it is helpful to consider statistical mixtures of state vectors, since they can be used to model imperfect measurements and other sources of noise and uncertainty in quantum systems. In this way, density operators prove to be a convenient way of describing systems whose states are not completely known. This represents a major difference between classical systems and quantum systems whereby the state of knowledge of the quantum system is described by a matrix, instead of a probability density. Nevertheless, the density matrix can be used to directly determine quantities such as expectation values, variances and probability densities, the same standard physical quantities used in stochastic feedback control. For example, the expected value of a given observable A can be calculated as

$$\langle A \rangle = \sum_j \alpha_j \langle \psi_j | A | \psi_j \rangle = \text{tr}[\omega A], \quad (19.5)$$

¹A Hermitian operator X is positive semi-definite if $\langle \psi | X | \psi \rangle \geq 0$ for all $|\psi\rangle$.

and its variance is given by

$$\begin{aligned}
 (\Delta A)^2 &= \langle A^2 \rangle - \langle A \rangle^2 \\
 &= \sum_j \alpha_j \langle \psi_j | A^2 | \psi_j \rangle - \left(\sum_j \alpha_j \langle \psi_j | A | \psi_j \rangle \right)^2.
 \end{aligned} \tag{19.6}$$

If $\alpha_j = 1$ for some j , the system is described as a “pure ensemble”. A quantum system whose state $|\psi\rangle$ is known exactly is said to be in a “pure state”. The density matrix is then simply given by $\omega = |\psi\rangle\langle\psi|$ and further satisfies $\omega^2 = \omega$. Otherwise, ω is said to be a mixture of the different pure states (mixed states) in the ensemble for ω or a convex combinations of such outer products. In this case, more than one α_j is non-zero.

Using density operators, the probabilities of experiment outcomes are expressed as

$$p(a|\omega) = \langle \omega, P_a \rangle = \text{tr}[\omega^\dagger P_a], \tag{19.7}$$

where ω is a normalized state ($\text{tr}[\omega] = 1$) and † denotes the operation of taking the adjoint. Here, we have used the notation

$$\langle A, B \rangle = \text{tr}[A^\dagger B], \tag{19.8}$$

and so $\langle \omega, P_a \rangle$ specifies the (expected) value of an observable P_a when the system is in state ω . Moreover, in the case of a state represented by density operators, state reduction (c.f. (19.3)) corresponds to

$$\omega' = \frac{P_a \omega P_a}{p(a|\omega)}. \tag{19.9}$$

Note that in the case of a pure state $\omega = |\psi\rangle\langle\psi|$,

$$p(a|\omega) = \langle \omega, P_a \rangle = \text{tr}[|\psi\rangle\langle\psi| P_a] = |\langle\psi|a\rangle|^2 = p(a|\psi), \tag{19.10}$$

as obtained in (19.2).

19.5 Evolution of closed and open quantum systems

The dynamics of “closed” quantum systems are described by unitary operators $U(t)$ obtained by solving the Schrödinger equation. In other words, the state $|\psi(t_1)\rangle$ of a quantum system at time t_1 is related to the state $|\psi(t_2)\rangle$ at time t_2 by a unitary operator $U(t)$ which depends only on the times t_1 and t_2 ; see [102]. This unitary evolution acts on state vectors $\psi = |\psi\rangle$ in a separable complex Hilbert space \mathcal{H} as follows:

$$|\psi(t_2)\rangle = U(t_1, t_2)|\psi(t_1)\rangle. \quad (19.11)$$

The requirement that the dynamics of the system be closed implies that the system is not interacting in any way with other systems. Although, this is not practical, for most purposes, the dynamics of many interesting systems can be closely approximated by unitary evolution.

If we extend the result of (19.11) to an ensemble of identical systems for the general case, the unitary evolution of the density operator can be expressed as

$$\omega(t_2) = U(t_1, t_2)\omega(t_1)U^\dagger(t_1, t_2). \quad (19.12)$$

The state of an “open” system on the other hand evolves in time as a result of a variety of factors including the underlying unitary evolution, interaction with the environment, the effect of repeated measurements and feedback control actions. Like classical systems, the dynamics of a quantum system is dependent on the energy present in the system. In fact, the energy of a system is a very important observable if we want to model or describe the dynamics of a quantum system. The “Hamiltonian” operator, which may be time dependent, is the operator associated with the energy of a system and is derived from an expression of the energy of the system and a process called “canonical quantization” which associates quantum mechanical operators to classical quantities. If we denote the system Hamiltonian as H , the feedback Hamiltonian as H_{fb} and the effect of measurement noise and environmental noise are represented by two “Lindblad” terms $\mathcal{D}[\cdot]$, we obtain a master equation describing the evolution of the state as

$$\dot{\omega} = -i[H + H_{fb}, \omega] + \mathcal{D}[Q]\omega + \mathcal{D}[n]\omega, \quad (19.13)$$

where $\mathcal{D}[A]\omega \equiv \frac{1}{2}(2A\omega A^\dagger - A^\dagger A\omega - \omega A^\dagger A)$ for an arbitrary operator A . When A is Hermitian, this term reduces to $\mathcal{D}[A]\omega = -\frac{1}{2}[A, [A, \omega]]$. Here $[A, B] \equiv AB - BA$ defines the commutator between two arbitrary operators A and B . The Lindblad terms $\mathcal{D}[Q]\omega$ and $\mathcal{D}[n]\omega$ describe the interaction of the system with the measuring device via the system operator Q and the interaction of the system with the environment respectively.

A general framework for describing the dynamics of quantum systems which includes unitary evolution, non-unitary open system evolution, and von Neumann state reduction can be obtained using the notion of “quantum operations”; see also [102].

Chapter 20

Behaviour of Quantum Systems

The behavior of quantum systems are usually described using quantum operations. Quantum operations provide the mathematical framework to predict the trajectory of quantum states for open systems (systems interacting either weakly or strongly with their environment), as well as closed systems which are exposed only to measurements. Furthermore, describing systems using quantum operators can be quite explicit of the passage of time, a technically convenient feature when describing discrete state changes using a given discrete control algorithm.

20.1 Discrete-Time Dynamics

As it is conceptually and technically simpler to work in discrete time, we will be using a model for sampled-data feedback control of quantum systems in which measurements are made and control actions are applied at time instants t_k (sample times). We consider a controlled quantum system whose dynamics are described in discrete-time by the recursion

$$\omega_{k+1} = \Lambda_{\Gamma}(u_k, y_{k+1})\omega_k, \quad (20.1)$$

where

$$\Lambda_{\Gamma}(u, y)\omega = \frac{\Gamma(u, y)\omega}{p_{\Gamma}(y|u, \omega)}. \quad (20.2)$$

Equation (20.1) is a discrete-time “stochastic master equation” (SME) and can be viewed as the result of integrating a stochastic master equation of the Itô type over one time step; see [83, 103]. Also, $\Gamma(u, y)$ is a self-adjoint positive quantum

operator that is used to model (via (20.1)) the state transfer if a control value u is applied and a measurement value y is observed. The probability of a measurement outcome y_{k+1} (assumed to be discrete-valued) is given by

$$p_{\Gamma}(y|u, \omega) = \langle \Gamma(u, y)\omega, I \rangle = \text{tr}[\Gamma(u, y)\omega], \quad (20.3)$$

(since both ω and the operator $\Gamma(u, y)$ are self-adjoint). Furthermore, the operator $\Gamma(u, y)$ is assumed to be normalized; i.e.,

$$\sum_{y \in \mathbf{Y}} \langle \Gamma(u, y)\omega, I \rangle = \langle \omega, I \rangle = 1,$$

so that $p_{\Gamma}(y|u, \omega)$ is a probability distribution, since it satisfies $\sum_{y \in \mathbf{Y}} p(y|u, \omega) = 1$. Here, \mathbf{Y} is the set of possible values of the measured outcome y .

Thus if a quantum system is in state ω_k at time k , and a control u_k is applied, a measurement outcome y_{k+1} will be recorded, and the system will transfer to a new state ω_{k+1} . Since measurements are made, and the outcomes are used to determine control actions, we are interested in the selective or conditional evolution of the states. Conditional evolution here implies that the new state ω_{k+1} depends on the value of the measurement y_{k+1} , a feature not present in classical systems.

20.2 Feedback Control and Measurement

On a time interval $0 \leq k \leq M-1$, a feedback controller is specified by a control law $u = K(y)$, where

$$K = \{K_0, K_1, \dots, K_{M-1}\}, \quad (20.4)$$

and

$$\begin{aligned} u_0 &= K_0, \\ u_1 &= K_1(y_1), \\ u_2 &= K_2(y_1, y_2), \\ &\vdots \\ u_k &= K_k(y_1, \dots, y_k). \end{aligned} \quad (20.5)$$

To simplify notation, we write sequences $u_{k_1}, u_{k_1+1}, \dots, u_{k_2}$ as u_{k_1, k_2} . Then we can write $u_k = K_k(y_{1,k})$. A controller K can be restricted to subintervals $k \leq j \leq M$ by fixing (or omitting) the first arguments in the obvious way. We denote by \mathcal{K} , the class of all such feedback controllers.

A feedback controller K in closed loop with a quantum system operates as follows. The given initial state ω_0 and controller K iteratively define a random sequence of states $\omega_{0,M}$, inputs $u_{0,M-1}$ and outputs $y_{1,M}$ over a given time interval $0 \leq k \leq M$. The control value u_0 is determined by K_0 (no observations are involved yet), and it is applied to the quantum system, which responds by selecting y_1 at random according to the distribution $p_\Gamma(y_1|u_0, \omega_0)$. This then determines the next state ω_1 via (20.1). Next u_1 is given by $K_1(y_1)$, and applied to the system. This process is repeated until the final time.

The controller K therefore determines controlled stochastic processes ω_k , u_k and y_k on the interval $0 \leq k \leq M$. The resulting probability distribution $\mathbf{P}_{\omega_0,0}^K$ of the measurement process $y_{1,M} = y_1, \dots, y_M$ is therefore given by

$$\mathbf{P}_{\omega_0,0}^K(y_1, \dots, y_M) = \prod_{k=0}^{M-1} p_\Gamma(y_{k+1}|u_k, \omega_k) \quad (20.6a)$$

$$= p_\Gamma(y_1|u_0, \omega_0) p_\Gamma(y_2|u_1, \omega_1) \cdots p_\Gamma(y_M|u_{M-1}, \omega_{M-1}). \quad (20.6b)$$

From (20.3), we have

$$p_\Gamma(y_M|u_{M-1}, \omega_{M-1}) = \langle \Gamma(u_{M-1}, y_M) \omega_{M-1}, I \rangle, \quad (20.7)$$

and since

$$\omega_{k+1} = \frac{\Gamma(u_k, y_{k+1})}{p_\Gamma(y_{k+1}|u_k, \omega_k)} \omega_k,$$

we can expand (20.7) as follows:

$$p_\Gamma(y_M|u_{M-1}, \omega_{M-1}) = \left\langle \frac{\Gamma(u_{M-1}, y_M) \Gamma(u_{M-2}, y_{M-1}) \cdots \Gamma(u_0, y_1) \omega_0}{p_\Gamma(y_{M-1}|u_{M-2}, \omega_{M-2}) \cdots p_\Gamma(y_1|u_0, \omega_0)}, I \right\rangle. \quad (20.8)$$

Substituting (20.8) into (20.6b), we then have

$$\begin{aligned} \mathbf{P}_{\omega_0,0}^K(y_1, \dots, y_M) &= p_\Gamma(y_1|u_0, \omega_0) p_\Gamma(y_2|u_1, \omega_1) \cdots p_\Gamma(y_{M-1}|u_{M-2}, \omega_{M-2}) \\ &\quad \times \left\langle \frac{\Gamma(u_{M-1}, y_M) \Gamma(u_{M-2}, y_{M-1}) \cdots \Gamma(u_0, y_1) \omega_0}{p_\Gamma(y_{M-1}|u_{M-2}, \omega_{M-2}) \cdots p_\Gamma(y_1|u_0, \omega_0)}, I \right\rangle. \end{aligned} \quad (20.9)$$

Since the terms $p_\Gamma(y_{k+1}|u_k, \omega_k)$ are scalars representing probabilities, we can simplify (20.9) so that

$$\begin{aligned} \mathbf{P}_{\omega_0,0}^K(y_1, \dots, y_M) &= \langle \Gamma(u_{M-1}, y_M) \Gamma(u_{M-2}, y_{M-1}) \cdots \Gamma(u_0, y_1) \omega_0, I \rangle \\ &= \langle \prod_{k=0}^{M-1, \leftarrow} \Gamma(u_k, y_{k+1}) \omega_0, I \rangle. \end{aligned} \quad (20.10)$$

In the last line of (20.10), the product denotes a time-ordered composition with the most recent operator applied first.

Chapter 21

Optimal Control

21.1 Risk-Neutral

Since the output of the controller K depends on the measurement outcome y which in turn determines the new state of the system, it can be constructed using a function of the form

$$u_k = \mathbf{u}(\omega_k, k), \quad (21.1)$$

where ω_k is given by (20.1) with initial state ω_0 . This controller will have a state estimation part for ω which is determined by (20.1) and another part which is based on the function \mathbf{u} . The controller can therefore be naturally considered to have a “separation structure” whereby the state estimation part and the control action can be performed in two stages, independently of each other. This is also referred to as the “certainty equivalence principle” (see Section 4.3), which is the basis of an optimal solution to the stochastic linear quadratic Gaussian (LQG) control problem with incomplete state information. Furthermore, the separation principle guarantees that in the case that the noise statistics are not Gaussian, then it will still yield the best linear regulator in terms of the best linear estimate of the state; see also [41] and [42].

In this case, a performance index (cost function) is formulated by the designer (over a given time interval of interest) that encodes the desired performance of the system as its minimum,

$$J^{\text{LQG}} = \mathbf{E} \left[x'_M P_M x_M + \sum_{k=0}^{M-1} (x'_k P x_k + u'_k Q u_k) \right]. \quad (21.2)$$

The cost is an expectation \mathbf{E} of a quadratic function, x_k and u_k are the state and control variables respectively, and $P_M \geq 0, P \geq 0, Q > 0$ are weighting matrices. The objective is to find the control u_k^* on the time interval of interest which minimizes the cost. The cost criterion (21.2) is also commonly referred to as the “risk-neutral” cost criterion.

We now present a quantum generalization of the classical cost function as described in (21.2). We introduce a non-negative observable $L(u)$ which depends on u and which encodes our control objective as a running cost function. We also introduce a terminal cost represented by N , which is also a non-negative observable. We then define the risk-neutral cost functional as

$$J_{\omega,0}(K) = \mathbf{E}_{\omega,0}^K \left(\sum_{i=0}^{M-1} \langle \omega_i, L(u_i) \rangle + \langle \omega_M, N \rangle \right), \quad (21.3)$$

where $\omega_i, i = 0, \dots, M$, is the solution of the system dynamics (20.1) with initial state ω_0 under the action of a controller K and the expectation $\mathbf{E}_{\omega_0,0}^K$ is with respect to the probability distribution $\mathbf{P}_{\omega_0,0}^K$ described in (20.10).

We can then define a random sequence of observables Q_k using the approach of [104] to rewrite the cost functional (21.3) in a technically more convenient form as:

$$Q_k = \Gamma^\dagger(u_k, y_{k+1}) Q_{k+1} + L(u_k), \quad 0 \leq k \leq M-1, \quad (21.4a)$$

$$Q_M = N; \quad (21.4b)$$

or using a short-hand notation, we write

$$Q_k = Q_k(u_{k,M-1}, y_{k+1,M}). \quad (21.5)$$

Q_k is referred to as the new cost observable, allowing the reformulation of the cost functional (21.3) as

$$J_{\omega,0}^K = \sum_{y_{1,M} \in \mathbf{Y}^M} \langle \omega, Q_0[K(y_{1,M})_{0,M-1}, y_{1,M}] \rangle. \quad (21.6)$$

This (reformulated) problem can then be solved using the following dynamic

programming equation associated with the risk-neutral problem:

$$V(\omega, k) = \inf_{u \in \mathbf{U}} \{ \langle \omega, L(u) \rangle + \sum_{y \in \mathbf{Y}} V(\Lambda_{\Gamma}(u, y)\omega, k+1) p(y|u, \omega) \}, \quad (21.7a)$$

$$V(\omega, M) = \langle \omega, N \rangle, \quad (21.7b)$$

where $0 \leq k \leq M-1$.

21.2 Risk-Sensitive

Our interest in risk-sensitive optimal control as a robust control scheme is due to its close connections with \mathcal{H}_{∞} control and dynamic games; see [92, 105]. Risk-sensitive controller design, also termed Linear Exponential of Quadratic Gaussian (LEQG) control, is very similar to LQG design. In fact, the LQG problem arises as a special case of the LEQG problem and the structure of the controller we obtain also involves a pair of Riccati equations, one to estimate the states and the other to control the estimated states. As expected, the optimal risk-sensitive controller also has a separation structure but the state estimation equation used is different from the LQG one.

For the LEQG case, we choose a control policy to minimize a new cost function given by

$$J^K(\mu) = \frac{2}{\mu} \ln \left[\mathbf{E}^K \exp\left(\frac{\mu}{2} \mathcal{C}\right) \right], \quad (21.8)$$

where μ is the risk-sensitivity parameter and \mathcal{C} is the cost function associated with an equivalent LQG problem. The idea behind defining this new cost function is to achieve robustness to uncertainty in the performance of the controller. In other words, we aim to have excellent performance when the controller is performing under nominal conditions and reasonable performance otherwise. If $\mu < 0$, the criterion is more weighted on smaller values of \mathcal{C} , implying that the designer is more concerned with occurrence of smaller values than larger ones thus showing a disregard for the worst cases. This strategy is often referred to as “risk-seeking” (optimistic). On the other hand, if $\mu > 0$, the converse is true; i.e., the designer is more concerned with large deviations and wants to control the worst cases. This optimization strategy is known as “risk-averse” (pessimistic). Clearly, the parameter μ allows for an extra degree of freedom, enabling the designer to

modify the optimization using knowledge of variability present. Moreover, it can be easily shown that in the case where $\mu = 0$, the LEQG criterion results in the risk-neutral optimal problem. As is the case with \mathcal{H}_∞ theory, our objective here is to seek a controller that “works” in the worst case (and is hence robust) and we shall therefore adopt a pessimistic approach considering the risk-averse case. The solution to the risk-sensitive problem will then lead to a conservative optimal policy, corresponding to the degree of aversion to risk. Whittle [47] solved the risk-sensitive LQG problem for the case of partial state information in the discrete-time case by making use of the certainty equivalence principle. The corresponding continuous-time problem was subsequently solved by Bensoussan; see [106].

Here, we consider two quantum risk-sensitive criteria, both of which generalize the classical LEQG criterion (a third quantum risk-sensitive criteria is also discussed in [1, 2]). We define the following risk-sensitive performance criteria:

$$J_{\omega,0}^{1,\mu}(K) \triangleq \mathbf{E}_{\omega,0}^K[\exp\left(\sum_{k=0}^{M-1} \langle \omega_k, \mu L(u_k) \rangle + \langle \omega_M, \mu N \rangle\right)], \quad (21.9)$$

and

$$J_{\omega,0}^{2,\mu}(K) \triangleq \mathbf{E}_{\omega,0}^K\left[\prod_{k=0}^{M-1} \langle \omega_k, e^{\mu L(u_k)} \rangle \langle \omega_M, e^{\mu N} \rangle\right]. \quad (21.10)$$

Here, $\mu > 0$ is a positive risk parameter. $L(u)$ and N are the running cost-function and the terminal cost-function respectively as defined in Chapter 21.1. In both of these expressions, the conditional states ω_k are given by the quantum system model (20.1) and the expectation $\mathbf{E}_{\omega,0}^K$ is evaluated with respect to the probability distribution $\mathbf{P}_{\omega,0}^K$ determined by a feedback controller K .

We wish to find controllers that minimize these criteria and for that purpose we need to introduce a new state $\hat{\omega}$ which may be “unnormalized”. This was done in [1] for a class of multiplicative criteria that includes (21.10). We now describe these new states $\hat{\omega}$ for the risk-sensitive criteria (21.9) and (21.10) respectively, and then formulate the solution. We define operators

$$R^1(u)\hat{\omega} \triangleq e^{\langle \hat{\omega}, \mu L(u) \rangle / \langle \hat{\omega}, 1 \rangle} \hat{\omega}, \quad (21.11)$$

and

$$R^2(u)\hat{\omega} \triangleq \frac{\langle \hat{\omega}, e^{\mu L(u)} \rangle}{\langle \hat{\omega}, 1 \rangle} \hat{\omega}, \quad (21.12)$$

for the cost functions (21.9) and (21.10) respectively. These operators map possibly unnormalized states to unnormalized states. They are in general nonlinear but satisfy the real multiplicative homogeneity property; i.e.,

$$R(u)r\hat{\omega} = rR(u)\hat{\omega}, \quad (21.13)$$

for any real number r and any $\hat{\omega}$, u . Here and below, $R(u)$ denotes either $R^1(u)$ or $R^2(u)$. Let us introduce a new operator

$$\Gamma_R(u, y) = \Gamma(u, y)R(u), \quad (21.14)$$

to model the state transfer of the new state $\hat{\omega}$ if a control value u is applied and a measurement y is observed. In general, Γ_R is not normalized; i.e.,

$$\sum_{y \in \mathbf{Y}} \langle \Gamma_R(u, y)\hat{\omega}, I \rangle = \langle R(u)\hat{\omega}, I \rangle \neq \langle \hat{\omega}, I \rangle. \quad (21.15)$$

We define a new operator

$$\Lambda_{\Gamma, R}(u, y)\hat{\omega} = \frac{\Gamma_R(u, y)\hat{\omega}}{p_R(y|u, \hat{\omega})}, \quad (21.16)$$

where

$$p_R(y|u, \hat{\omega}) = \frac{\langle \Gamma_R(u, y)\hat{\omega}, I \rangle}{\langle R(u)\hat{\omega}, I \rangle}, \quad (21.17)$$

to describe the evolution of the new state $\hat{\omega}$. In general, the state $\Lambda_{\Gamma, R}(u, y)\hat{\omega}$ is unnormalized. However, $p_R(y|u, \hat{\omega})$ is a probability distribution, since

$$\sum_{y \in \mathbf{Y}} p_R(y|u, \hat{\omega}) = 1.$$

It can also be deduced from (21.16) and (21.17) that

$$\langle \Lambda_{\Gamma, R}(u, y)\hat{\omega}, I \rangle = \langle R(u)\hat{\omega}, I \rangle. \quad (21.18)$$

Associated with the operator $\Lambda_{\Gamma,R}$ is the dynamics

$$\hat{\omega}_{k+1} = \Lambda_{\Gamma,R}(u_k, y_{k+1})\hat{\omega}_k, \quad (21.19)$$

where y_{k+1} is distributed according to the probability distribution $p_R(y_{k+1}|u_k, \hat{\omega}_k)$ given by (21.17). This is a controlled Markov chain, with unnormalized states $\hat{\omega}_k$. It is also a modified stochastic master equation corresponding to the operator Γ_R . Under the action of a controller $K \in \mathcal{K}$, the stochastic process $\hat{\omega}_k$ is determined by (21.19) and $u_k = K_k(y_{1,k})$.

Given a function $\hat{\mathbf{u}}(\hat{\omega}, k)$ and initial state $\hat{\omega}_0$, we define a (separation structure) controller $K_{\hat{\omega}_0}^{\hat{\mathbf{u}}} \in \mathcal{K}$ by

$$u_k = \hat{\mathbf{u}}(\hat{\omega}_k, k),$$

where $\hat{\omega}_k$ is given by (21.19), $0 \leq k \leq M$, with initial condition $\hat{\omega}_0$.

Let M be a positive integer indicating a finite time interval $k = 0, \dots, M$. For each k , given a sequence of control values $u_{k,M-1} = u_k, \dots, u_{M-1}$ and measurement values $y_{k+1,M} = y_{k+1}, \dots, y_M$, we define random cost observables G_k by the recursion

$$G_k = R^\dagger(u_k)\Gamma^\dagger(u_k, y_{k+1})G_{k+1}, \quad 0 \leq k \leq M-1; \quad (21.20a)$$

$$G_M = F, \quad (21.20b)$$

where F is a non-negative linear observable. Using a short-hand notation, we write

$$G_k = G_k(u_{k,M-1}, y_{k+1,M}), \quad (21.21)$$

and we define the general risk-sensitive cost functional as

$$J_{\hat{\omega}_0}^\mu(K) = \sum_{y_{1,M} \in \mathbf{Y}^M} \langle \hat{\omega}, G_0(K(y_{1,M})_{0,M-1}, y_{1,M}) \rangle, \quad (21.22)$$

where $K \in \mathcal{K}$ is a measurement feedback controller. In Example 7 of [1], it is shown that the risk-sensitive criterion (21.10) can be expressed in the form (21.22) with $R(u) = R^2(u)$ given in (21.12). It can similarly be shown that (21.9) can also be expressed as (21.22) using $R(u) = R^1(u)$ given in (21.11). Furthermore, the cost functional $J_{\hat{\omega}_0}^\mu(K)$ defined by (21.22) can be given by the

alternate expression

$$J_{\hat{\omega},0}^\mu(K) = \mathbf{E}_{\hat{\omega},0}^K[\langle \hat{\omega}_M, F \rangle], \quad (21.23)$$

where $\hat{\omega}_i$, $i = k, \dots, M$ is the solution of the recursion (21.19) with initial state $\hat{\omega}_0 = \hat{\omega}$ under the action of the controller K , as shown in Lemma 1 of [1].

21.3 Quantum Bellman Equation

Dynamic programming [107] allows us to transform a single n -dimensional optimization problem into n one-dimensional optimization problems which can be solved one at a time. The principle that allows us to carry out the transformation is known as the “principle of optimality”, which simply states that whatever the initial state and the optimal first decision (control), the remaining decisions (controls) constitute an optimal policy with regard to the state resulting from the first decision. If the period of control is broken down in a series of stages (as it would be in the discrete-time case), the optimal control strategy will then consist of a series of “optimal first decisions” for a series of processes with a decreasing number of “stages-to-go”. The principle of optimality also implies that the optimal control strategy can be determined only by working backwards from the final stage.

A Bellman equation allows us to formulate a given optimal control problem in a way that is amenable to the dynamic programming approach. For the class of systems we are concerned with (quantum systems), we use an equivalent version of the Bellman equation derived by Belavkin in [104] and referred to as the Quantum Bellman Equation. The optimal control problem described by the cost-functional (21.22) is then solved using dynamic programming in terms of the “cost-to-go”:

$$J_{\hat{\omega},k}^\mu(K) \triangleq \sum_{y_{k+1,M} \in \mathbf{Y}^{M-k}} \langle \hat{\omega}, G_k(K(y_{k+1,M})_{k,M-1}, y_{k+1,M}) \rangle. \quad (21.24)$$

The corresponding dynamic programming equation (associated with the risk-sensitive case) is then given as

$$W(\hat{\omega}, k) = \inf_{u \in \mathbf{u}} \left\{ \sum_{y \in \mathbf{Y}} W(\Lambda_{\Gamma,R}(u, y)\hat{\omega}, k+1) p_R(y|u, \hat{\omega}) \right\}, \quad (21.25a)$$

$$W(\hat{\omega}, M) = \langle \hat{\omega}, F \rangle, \quad (21.25b)$$

where $0 \leq k \leq M - 1$.

Theorem 21.1 (*[1, Theorem 1]*) *Let $W(\hat{\omega}, k)$, $0 \leq k \leq M$, be the solution of the dynamic programming equation (21.25).*

1. *Then for any $K \in \mathcal{K}$ we have*

$$W(\hat{\omega}, k) \leq J_{\hat{\omega}, k}^{\mu}(K). \quad (21.26)$$

2. *Assume in addition that the minimizer*

$$\hat{\mathbf{u}}^*(\hat{\omega}, k) \in \operatorname{argmin}_{u \in \mathbf{U}} \left\{ \sum_{y \in \mathbf{Y}} W(\Lambda_{\Gamma, R}(u, y)\hat{\omega}, k+1) p_R(y|u, \hat{\omega}) \right\}, \quad (21.27)$$

exists for all $\hat{\omega}$, $0 \leq k \leq M - 1$.

Then the separation structure controller $K_{\hat{\omega}_0}^{\hat{\mathbf{u}}^}$ defined by (21.27) is optimal for problem (21.22); i.e., $J_{\hat{\omega}_0, 0}^{\mu}(K) \geq J_{\hat{\omega}_0, 0}^{\mu}(K_{\hat{\omega}_0}^{\hat{\mathbf{u}}^*})$ for all $K \in \mathcal{K}$.*

The proof of Theorem 21.1 is given in [1].

Chapter 22

Robustness Properties of Risk-Sensitive Controllers

We now turn to the main objective of our work which is to provide a robustness interpretation of the risk-sensitive criteria (21.9) and (21.10). Robustness relates to the ability or otherwise of a control system to deal with uncertainty. We seek a performance bound that depends on a measure of the size of uncertainty which may arise due to modelling errors, exogenous disturbances, etc.

The quantum model used in this paper is determined by the operator $\Gamma(u)$. Any optimal controller design will depend on the knowledge of $\Gamma(u)$. Suppose that a controller is to be obtained using a particular $\Gamma_{nom}(u, y)$, which defines the nominal model. However, the nominal model may not exactly equal the true model, assumed to be determined by $\Gamma_{true}(u, y)$, that governs the actual physical system being controlled. We seek a bound on the (risk-neutral) performance of the control system

$$J_{\omega,0}(K) = \mathbf{E}_{\omega,0}^K \left[\sum_{k=0}^{M-1} \langle \omega_k, L(u_k) \rangle + \langle \omega_M, N \rangle \right], \quad (22.1)$$

where the state $\omega_k = \omega_k^{true}$ evolves according to the true model (see (22.7) below) and the control is determined by the nominal model

$$u_k = \hat{\mathbf{u}}_{nom}^*(\hat{\omega}_k, k), \quad (22.2)$$

via (21.27) with $\Gamma = \Gamma_{nom}$ and

$$\hat{\omega}_{k+1} = \Lambda_{\Gamma_{nom}, R}(u_k, y_{k+1})\hat{\omega}_k. \quad (22.3)$$

This controller is denoted $K_{nom}^* = K_{\hat{\omega}_0}^{\hat{\mathbf{u}}_{nom}^*}$. In constructing this controller, we use either criteria (21.9) or (21.10), and when necessary to distinguish between them, we write $\hat{\mathbf{u}}_{nom,1}^*(\hat{\omega}_k, k)$ or $\hat{\mathbf{u}}_{nom,2}^*(\hat{\omega}_k, k)$, and $K_{nom,1}^*$ or $K_{nom,2}^*$.

A bound for (22.1) is sought in terms of a measure of the “distance” between $\Gamma_{nom}(u)$ and $\Gamma_{true}(u)$. The way in which we measure the “distance” between $\Gamma_{nom}(u)$ and $\Gamma_{true}(u)$ is to consider the “distance” between the probability distributions \mathbf{P}_{nom} and \mathbf{P}_{true} defined on the space of observation paths and determined by $\Gamma_{nom}(u)$ and $\Gamma_{true}(u)$ respectively, under the controller K_{nom}^* . Before we look at the distance between probability distributions, we introduce a key concept in quantum information theory, which is that of “quantum entropy”. The entropy of a physical system (classical or quantum) provides a measure of uncertainty present in its states. It can be regarded as a measure of our uncertainty *before* we learn the value of the variables we are interested in or as a measure of the information gained *after* we learn the value of the variables. The distance between probability distributions is defined in terms of the “relative entropy” (see Chapter 11 of [102]):

$$\mathfrak{R}(\mathbf{P}_{true} \parallel \mathbf{P}_{nom}) \triangleq \mathbf{E}_{\mathbf{P}_{true}} \left[\log \frac{d\mathbf{P}_{true}}{d\mathbf{P}_{nom}} \right], \quad (22.4)$$

provided \mathbf{P}_{true} is absolutely continuous with respect to \mathbf{P}_{nom} . The relative entropy is a non-negative quantity and is equal to zero if and only if $\mathbf{P}_{true} = \mathbf{P}_{nom}$. From (20.6b), the distributions \mathbf{P}_{true} and \mathbf{P}_{nom} are given explicitly by

$$\mathbf{P}_{true}(y_1, \dots, y_M) = \prod_{k=0}^{M-1} p_{\Gamma_{true}}(y_{k+1} | u_k, \omega_k^{true}), \quad (22.5)$$

and

$$\mathbf{P}_{nom}(y_1, \dots, y_M) = \prod_{k=0}^{M-1} p_{\Gamma_{nom}}(y_{k+1} | u_k, \omega_k^{nom}), \quad (22.6)$$

where $p_\Gamma(\cdot)$ is defined by (20.3), u_k is determined by K_{nom}^* ,

$$\omega_{k+1}^{true} = \Lambda_{\Gamma_{true}}(u_k, y_{k+1})\omega_k^{true}, \quad (22.7)$$

and

$$\omega_{k+1}^{nom} = \Lambda_{\Gamma_{nom}}(u_k, y_{k+1})\omega_k^{nom}, \quad (22.8)$$

respectively under these distributions. We next introduce a lemma to compute the Radon-Nikodym derivative of these distributions.

Lemma 22.1 *Suppose \mathbf{P}_{true} is absolutely continuous with respect to \mathbf{P}_{nom} . Then the Radon-Nikodym derivative $\frac{d\mathbf{P}_{true}}{d\mathbf{P}_{nom}}$ can be written in the form*

$$\frac{d\mathbf{P}_{true}}{d\mathbf{P}_{nom}}(y_1, \dots, y_M) = \frac{\mathbf{P}_{true}(y_1, \dots, y_M)}{\mathbf{P}_{nom}(y_1, \dots, y_M)} = \prod_{k=0}^{M-1} f_{k+1}(y_{k+1}|y_1, \dots, y_k), \quad (22.9)$$

where

$$f_{k+1}(y_{k+1}|y_1, \dots, y_k) = \frac{p_{\Gamma_{true}}(y_{k+1}|u_k, \omega_k^{true})}{p_{\Gamma_{nom}}(y_{k+1}|u_k, \omega_k^{nom})} \geq 0, \quad (22.10)$$

and

$$\sum_{y_{k+1}} f_{k+1}(y_{k+1}|y_1, \dots, y_k) p_{\Gamma_{nom}}(y_{k+1}|u_k, \omega_k^{nom}) = 1. \quad (22.11)$$

Proof We have

$$\mathbf{P}_{true}(y_1, \dots, y_M) = \mathbf{P}_{true}(y_M|y_1, \dots, y_{M-1})\mathbf{P}_{true}(y_1, \dots, y_{M-1}),$$

and

$$\mathbf{P}_{nom}(y_1, \dots, y_M) = \mathbf{P}_{nom}(y_M|y_1, \dots, y_{M-1})\mathbf{P}_{nom}(y_1, \dots, y_{M-1}),$$

where

$$\begin{aligned} \mathbf{P}_{true}(y_M|y_1, \dots, y_{M-1}) &= p_{\Gamma_{true}}(y_M|u_{M-1}, \omega_{M-1}^{true}), \text{ from (20.6a),} \\ \text{and } \mathbf{P}_{nom}(y_M|y_1, \dots, y_{M-1}) &= p_{\Gamma_{nom}}(y_M|u_{M-1}, \omega_{M-1}^{nom}). \end{aligned}$$

Then

$$\frac{\mathbf{P}_{true}(y_1, \dots, y_M)}{\mathbf{P}_{nom}(y_1, \dots, y_M)} = f_M(y_M|y_1, \dots, y_{M-1}) \frac{\mathbf{P}_{true}(y_1, \dots, y_{M-1})}{\mathbf{P}_{nom}(y_1, \dots, y_{M-1})},$$

where

$$f_M(y_M|y_1, \dots, y_{M-1}) = \frac{\mathbf{P}_{true}(y_M|y_1, \dots, y_{M-1})}{\mathbf{P}_{nom}(y_M|y_1, \dots, y_{M-1})} = \frac{p_{\Gamma_{true}}(y_M|u_{M-1}, \omega_{M-1}^{true})}{p_{\Gamma_{nom}}(y_M|u_{M-1}, \omega_{M-1}^{nom})}. \quad (22.12)$$

Continuing in this way we obtain (22.9). The properties of $f_k(\cdot)$ follow from the fact that \mathbf{P}_{true} is a probability distribution. \blacksquare

We will consider a particular class of true models $\Gamma_{true}(u, y)$ motivated by the framework of Radon-Nikodym derivatives of quantum operations (see [108, 109]), and then demonstrate robustness with respect to this class. Specifically, we consider $\Gamma_{nom}(u, y)$ in the operator sum Kraus form (see [102]):

$$\Gamma_{nom}(u, y)\omega = \sum_{a \in \mathbf{A}} \gamma_{nom,a}(u, y)\omega\gamma_{nom,a}^\dagger(u, y), \quad (22.13)$$

for suitable operators $\gamma_{nom,a}(u, y)$, $a \in \mathbf{A}$ satisfying

$$\sum_{a \in \mathbf{A}, y \in \mathbf{Y}} \gamma_{nom,a}^\dagger(u, y)\gamma_{nom,a}(u, y) = I. \quad (22.14)$$

Here \mathbf{A} is a finite index set. The true model is assumed to be given by

$$\Gamma_{true}(u, y)\omega = \sum_{a \in \mathbf{A}} \lambda_a(u, y)\gamma_{nom,a}(u, y)\omega\gamma_{nom,a}^\dagger(u, y), \quad (22.15)$$

where $\lambda_a(u, y)$ are real numbers satisfying

$$0 \leq \lambda_a(u, y) \leq c(u, y), \quad (22.16)$$

for all a . Since $\Gamma_{true}(u, y)$ is required to be a normalized quantum operation, we also require

$$\sum_{a \in \mathbf{A}, y \in \mathbf{Y}} \lambda_a(u, y)\gamma_{nom,a}^\dagger(u, y)\gamma_{nom,a}(u, y) = I. \quad (22.17)$$

Thus we can think of the true model as a perturbation of the nominal model in the sense that the operator $\gamma_{nom,a}(u, y)$ is multiplicatively perturbed to $r_a(u, y)\gamma_{nom,a}(u, y)$, where the $r_a(u, y)$ are complex numbers such that $|r_a(u, y)|^2 = \lambda_a(u, y)$. In the terminology of [108] and [109], we say that $\Gamma_{true}(u, y)$ is “completely dominated” by $c(u, y)\Gamma_{nom}(u, y)$.

Lemma 22.2 *Let $\Gamma_{true}(u, y)$ be completely dominated by $c(u, y)\Gamma_{nom}(u, y)$ as described above. Then \mathbf{P}_{true} is absolutely continuous with respect to \mathbf{P}_{nom} . Moreover,*

$$f_{k+1}(y_{k+1}|y_1, \dots, y_k) = \frac{\sum_a \lambda_a(u_k, y_{k+1}) \langle \omega_k^{true}, \gamma_{nom}(u_k, y_{k+1}) \gamma_{nom}^\dagger(u_k, y_{k+1}) \rangle}{\sum_a \langle \omega_k^{nom}, \gamma_{nom}(u_k, y_{k+1}) \gamma_{nom}^\dagger(u_k, y_{k+1}) \rangle}. \quad (22.18)$$

Proof From (20.10), we have

$$\begin{aligned} \mathbf{P}_{true}(y_1, \dots, y_M) &= \langle \prod_{k=0}^{M-1, \leftarrow} \Gamma_{true}(u_k, y_{k+1}) \omega_0, I \rangle \\ &\leq \prod_{k=0}^{M-1} c(u_k, y_{k+1}) \langle \prod_{k=0}^{M-1, \leftarrow} \Gamma_{nom}(u_k, y_{k+1}) \omega_0, I \rangle, \\ &\hspace{15em} \text{from (22.15) and (22.16)} \\ &= \prod_{k=0}^{M-1} c(u_k, y_{k+1}) \mathbf{P}_{nom}(y_1, \dots, y_M). \end{aligned}$$

Hence, $\mathbf{P}_{nom}(y_1, \dots, y_M) = 0$ implies $\mathbf{P}_{true}(y_1, \dots, y_M) = 0$, as required. Also from (22.12), we have

$$f_{k+1}(y_{k+1}|y_1, \dots, y_k) = \frac{\mathbf{P}_{true}(y_{k+1}|y_1, \dots, y_k)}{\mathbf{P}_{nom}(y_{k+1}|y_1, \dots, y_k)}.$$

Now,

$$\begin{aligned} \mathbf{P}_{true}(y_{k+1}|y_1, \dots, y_k) &= \frac{\mathbf{P}_{true}(y_1, \dots, y_{k+1})}{\mathbf{P}_{true}(y_1, \dots, y_k)} \\ &= \frac{\prod_{i=0}^k p_\Gamma(y_{i+1}|u_i, \omega_i)}{\prod_{i=0}^{k-1} p_\Gamma(y_{i+1}|u_i, \omega_i)}, \quad \text{from (20.6a),} \\ &= \langle \Gamma(u_k, y_{k+1}) \omega_k^{true}, I \rangle, \quad \text{from (20.3),} \\ &= \langle \sum_{a \in \mathbf{A}} \lambda_a(u_k, y_{k+1}) \gamma_{nom,a}(u_k, y_{k+1}) \omega_k^{true} \gamma_{nom,a}^\dagger(u_k, y_{k+1}), I \rangle, \\ &\hspace{15em} \text{from (22.15),} \\ &= \sum_{a \in \mathbf{A}} \lambda_a(u_k, y_{k+1}) \langle \omega_k^{true}, \gamma_{nom}(u_k, y_{k+1}) \gamma_{nom}^\dagger(u_k, y_{k+1}) \rangle. \end{aligned}$$

Similarly,

$$\mathbf{P}_{nom}(y_{k+1}|y_1, \dots, y_k) = \sum_{a \in \mathbf{A}} \langle \omega_k^{nom}, \gamma_{nom}(u_k, y_{k+1}) \gamma_{nom}^\dagger(u_k, y_{k+1}) \rangle,$$

and the ratio of \mathbf{P}_{true} and \mathbf{P}_{nom} gives us (22.18). \blacksquare

We now consider the first risk-sensitive criterion (21.9). We will need the following general convex duality formula (see Chapter 1.4 of [110]):

$$\log \mathbf{E}_{\mathbf{P}}[e^f] = \sup_{\mathbf{Q}} \{ \mathbf{E}_{\mathbf{Q}}[f] - \mathfrak{R}(\mathbf{Q} \parallel \mathbf{P}) \}, \quad (22.19)$$

where \mathbf{P} and \mathbf{Q} are probability distributions, and where the relative entropy is given by

$$\mathfrak{R}(\mathbf{Q} \parallel \mathbf{P}) = \mathbf{E}_{\mathbf{Q}}[\log \frac{d\mathbf{Q}}{d\mathbf{P}}]. \quad (22.20)$$

The duality formula (22.19) implies that

$$\log \mathbf{E}_{\mathbf{P}}[e^f] \geq \mathbf{E}_{\mathbf{Q}}[f] - \mathfrak{R}(\mathbf{Q} \parallel \mathbf{P}), \quad (22.21)$$

for any probability distribution \mathbf{Q} which is absolutely continuous with respect to \mathbf{P} .

Theorem 22.1 *Suppose $\Gamma_{true}(u, y)$ is completely dominated by $c(u, y)\Gamma_{nom}(u, y)$ as described above. Consider the controller $K_{nom,1}^*$ determined by the nominal model for the risk-sensitive criteria (21.9). Then*

$$\mathbf{E}_{\omega,0}^{true} \left[\sum_{k=0}^{M-1} \langle \omega_k, L(u_k) \rangle + \langle \omega_M, N \rangle \right] \leq \frac{1}{\mu} \log J_{\omega,0}^{1,\mu}(K_{\hat{\omega}_0}^*) + \frac{1}{\mu} \mathfrak{R}(\mathbf{P}_{true} \parallel \mathbf{P}_{nom}), \quad (22.22)$$

where

$$\begin{aligned} \mathfrak{R}(\mathbf{P}_{true} \parallel \mathbf{P}_{nom}) &= \mathbf{E}_{\omega,0}^{true} \left[\log \prod_{k=0}^{M-1} f_{k+1}(y_{k+1}|y_1, \dots, y_k) \right] \\ &= \mathbf{E}_{\omega,0}^{true} \left[\sum_{k=0}^{M-1} \log f_{k+1}(y_{k+1}|y_1, \dots, y_k) \right], \end{aligned} \quad (22.23)$$

and $f_{k+1}(y_{k+1}|y_1, \dots, y_k)$ is given by (22.18).

Proof We apply the duality formula (22.21) where we set $\mathbf{P} = \mathbf{P}_{nom}$, $\mathbf{Q} = \mathbf{P}_{true}$, and

$$f = \sum_{k=0}^{M-1} \langle \omega_k, \mu L(u_k) \rangle + \langle \omega_M, \mu N \rangle.$$

Then,

$$\log \mathbf{E}_{\mathbf{P}}[e^f] = \log \mathbf{E}_{\omega,0}^{nom} \left[\exp \left(\sum_{k=0}^{M-1} \langle \omega_k, \mu L(u_k) \rangle + \langle \omega_M, \mu N \rangle \right) \right] = \log J_{\omega,0}^{1,\mu}(K),$$

from (21.9);

$$\mathbf{E}_{\mathbf{Q}}[f] = \mu \mathbf{E}_{\omega,0}^{true} \left[\sum_{k=0}^{M-1} \langle \omega_k, L(u_k) \rangle + \langle \omega_M, N \rangle \right];$$

and

$$\mathfrak{R}(\mathbf{Q} \parallel \mathbf{P}) = \mathbf{E}_{\mathbf{Q}} \left[\log \frac{d\mathbf{Q}}{d\mathbf{P}} \right] = \mathbf{E}_{\omega,0}^{true} \left[\log \prod_{k=0}^{M-1} f_{k+1}(y_{k+1} | y_1, \dots, y_k) \right], \text{ from (22.9),}$$

leading to (22.22). ■

We now turn to the second risk-sensitive criterion (21.10). Let X be a non-negative observable (e.g., $L(u)$ or N), and let $P_X(dx)$ denote the projection-valued measure corresponding to the observable X , so that

$$X = \int x P_X(dx), \quad e^{\mu X} = \int e^{\mu x} P_X(dx). \quad (22.24)$$

We next introduce a perturbation in the observable by including a new term $g(\cdot|X, \omega) \geq 0$, corresponding to the Radon-Nikodym derivative between the probability measure $\langle \omega, P_X(dx) \rangle$ associated with the nominal observable X and the probability measure $\langle \omega, P_{\tilde{X}}(dx) \rangle$ associated with the perturbed observable \tilde{X} . Then

$$\int g(x|X, \omega) \langle \omega, P_X(dx) \rangle = 1, \quad (22.25)$$

and we define the perturbed probability measure as

$$\langle \omega, P_{\tilde{X}}(dx) \rangle = g(x|X, \omega) \langle \omega, P_X(dx) \rangle. \quad (22.26)$$

For simplicity of notation, we shall write

$$\tilde{X} = Xg(X|X, \omega). \quad (22.27)$$

We introduce the following lemma to allow for perturbation in the cost function.

Lemma 22.3 *We have*

$$\log \langle \omega, e^{\mu X} \rangle = \sup_{g(\cdot|X, \omega)} \{ \mu \langle \omega, \tilde{X} \rangle - \mathfrak{C}(\tilde{X} \parallel X) \}, \quad (22.28)$$

where

$$\langle \omega, \tilde{X} \rangle = \int x g(x|X, \omega) \langle \omega, P_X(dx) \rangle, \quad (22.29)$$

$$\text{and } \mathfrak{C}(\tilde{X} \parallel X) = \int g(x|X, \omega) \log g(x|X, \omega) \langle \omega, P_X(dx) \rangle. \quad (22.30)$$

Proof We apply the duality formula (22.19) where we set

$$\begin{aligned} \mathbf{P}(dx) &= \langle \omega, P_X(dx) \rangle, \\ \mathbf{Q}(dx) &= g(x|X, \omega) \langle \omega, P_X(dx) \rangle, \\ \text{and } f(x) &= \mu x. \end{aligned}$$

From (22.20), we have

$$\begin{aligned} \mathfrak{R}(\mathbf{Q}(dx) \parallel \mathbf{P}(dx)) &= \mathbf{E}_{\mathbf{Q}(dx)} \left[\log \frac{d\mathbf{Q}(dx)}{d\mathbf{P}(dx)} \right] = \mathbf{E}_{\mathbf{Q}(dx)} [\log g(x|X, \omega)] \\ &= \int \log g(x|X, \omega) g(x|X, \omega) \langle \omega, P_X(dx) \rangle \\ &= \mathfrak{C}(\tilde{X} \parallel X). \end{aligned}$$

Also,

$$\begin{aligned} \log \mathbf{E}_{\mathbf{P}(dx)} [e^{\mu x}] &= \log \int e^{\mu x} \langle \omega, P_X(dx) \rangle = \log \langle \omega, e^{\mu X} \rangle, \text{ from (22.24);} \\ \mathbf{E}_{\mathbf{Q}(dx)} [\mu x] &= \mu \int x g(x|X, \omega) \langle \omega, P_X(dx) \rangle = \mu \langle \omega, \tilde{X} \rangle \text{ from (22.29).} \end{aligned} \quad (22.31)$$

■

Theorem 22.2 *Suppose $\Gamma_{true}(u, y)$ is completely dominated by $c(u, y)\Gamma_{nom}(u, y)$ as described above. Consider the controller $K_{nom,2}^*$ determined by the nominal*

model for the risk-sensitive criteria (21.10). Then

$$\begin{aligned} \mathbf{E}_{\omega,0}^{true} \left[\sum_{k=0}^{M-1} \langle \omega_k, \tilde{L}_k(u_k) \rangle + \langle \omega_M, \tilde{N}_M \rangle \right] &\leq \frac{1}{\mu} \log J_{\omega,0}^{2,\mu}(K_{\hat{\omega}_0}^{\hat{\mathbf{u}}^*,\mu}) + \frac{1}{\mu} \mathfrak{R}(\mathbf{P}_{true} \parallel \mathbf{P}_{nom}) \\ &\quad + \frac{1}{\mu} \mathfrak{C}(\tilde{L} \parallel L), \end{aligned} \quad (22.32)$$

where

$$\begin{aligned} \tilde{L}_k(u_k) &= L(u_k) g_k(L(u_k) | L(u_k), \omega_k), \\ \tilde{N}_M &= N g_M(N | N, \omega_M), \quad \text{from (22.29),} \end{aligned}$$

g_k and g_M are defined as in (22.25), $\mathfrak{R}(\mathbf{P}_{true} \parallel \mathbf{P}_{nom})$ is described by (22.23) and

$$\mathfrak{C}(\tilde{L} \parallel L) = \mathbf{E}_{\omega,0}^{true} \left[\sum_{k=0}^{M-1} \mathfrak{C}_{\omega_k}(\tilde{L}(u_k) \parallel L(u_k)) + \mathfrak{C}_{\omega_M}(\tilde{N} \parallel N) \right]. \quad (22.33)$$

Proof We apply the duality formula (22.21) where we set $\mathbf{P} = \mathbf{P}_{nom}$, $\mathbf{Q} = \mathbf{P}_{true}$, and

$$f = \sum_{k=0}^{M-1} \log \langle \omega_k, e^{\mu L(u_k)} \rangle + \log \langle \omega_M, e^{\mu N} \rangle.$$

We have

$$\begin{aligned} \log \mathbf{E}_{\mathbf{P}}[e^f] &= \log \mathbf{E}_{\mathbf{P}_{nom}} \left[e^{\sum_{k=0}^{M-1} \log \langle \omega_k, e^{\mu L(u_k)} \rangle + \log \langle \omega_M, e^{\mu N} \rangle} \right] \\ &= \log \mathbf{E}_{\mathbf{P}_{nom}} \left[\prod_{k=0}^{M-1} \langle \omega_k, e^{\mu L(u_k)} \rangle \cdot \langle \omega_M, e^{\mu N} \rangle \right] \\ &= \log J_{\omega,0}^{2,\mu}(K), \quad \text{from (21.10).} \end{aligned}$$

This gives

$$\log J_{\omega,0}^{2,\mu}(K_{\hat{\omega}_0}^{\hat{\mathbf{u}}^*}) \geq \mathbf{E}_{\omega,0}^{true} \left[\sum_{k=0}^{M-1} \log \langle \omega_k, e^{\mu L(u_k)} \rangle + \log \langle \omega_M, e^{\mu N} \rangle \right] - \mathfrak{R}(\mathbf{P}_{true} \parallel \mathbf{P}_{nom}). \quad (22.34)$$

Applying Lemma 22.3 to the first two terms on the right hand side of (22.34), we

obtain

$$\begin{aligned}\log\langle\omega_k, e^{\mu L(u_k)}\rangle &= \mu\langle\omega_k, \tilde{L}_k(u_k)\rangle - \mathfrak{C}(\tilde{L} \parallel L), \text{ and} \\ \log\langle\omega_M, e^{\mu N}\rangle &= \mu\langle\omega_M, \tilde{N}\rangle - \mathfrak{C}(\tilde{N} \parallel N).\end{aligned}$$

Therefore,

$$\begin{aligned}\mathbf{E}_{\omega,0}^{true} \left[\sum_{k=0}^{M-1} \log\langle\omega_k, e^{\mu L(u_k)}\rangle + \log\langle\omega_M, e^{\mu N}\rangle \right] \\ = \mu \mathbf{E}_{\omega,0}^{true} \left[\sum_{k=0}^{M-1} \langle\omega_k, \tilde{L}_k(u_k)\rangle + \langle\omega_M, \tilde{N}\rangle \right] \\ - \mathbf{E}_{\omega,0}^{true} \left[\sum_{k=0}^{M-1} \mathfrak{C}_{\omega_k}(\tilde{L}(u_k) \parallel L(u_k)) + \mathfrak{C}_{\omega_M}(\tilde{N} \parallel N) \right]. \quad (22.35)\end{aligned}$$

Substituting (22.35) in (22.34), we obtain (22.32). ■

Chapter 23

Two-level System Example

We consider an example from [1] of a two-level system on $\mathcal{H} = \mathbb{C}^2$ where it is desired to use feedback control to put the system into a given state. The problem can be visualised as follows. A particle beam is passed through a Stern-Gerlach¹ device resulting in two beams, one is in the spin up state and the other in the spin down state. The beam of particles in the spin up state is left untouched while the beam in the spin down state is subjected to a device (controller) which results in a change of the spin direction from down to up. The final outcome of this feedback arrangement is that all particles are in the up state. The pure states of the system are of the form

$$|\psi\rangle = c_{-1}|-1\rangle + c_1|1\rangle = c_{-1} \begin{pmatrix} 1 \\ 0 \end{pmatrix} + c_1 \begin{pmatrix} 0 \\ 1 \end{pmatrix} = \begin{pmatrix} c_{-1} \\ c_1 \end{pmatrix},$$

where $|-1\rangle$ and $|1\rangle$ denote the orthonormal basis of eigenvectors of the spin observable

$$A = \begin{pmatrix} -1 & 0 \\ 0 & 1 \end{pmatrix}, \quad (23.1)$$

corresponding to ideal measurement values $a = -1$ and $a = 1$ (spin down and spin up respectively). The actual measurement values $y \in \{-1, 1\}$ obtained are imperfect, being subject to an error probability $0 < \alpha < 1$. The imperfect (noisy) measurement can arise due to cross-contamination with a proportion of the other beam, interference and/or noise affected sensors.

¹Stern and Gerlach demonstrated the existence of systems with the properties of qubits in 1922; e.g. see Sec. 1.5 of [102].

The control actions available are to either do nothing, or to flip the state. Given an initial mixed state (density matrix)

$$\omega = \begin{pmatrix} \omega_{11} & \omega_{12} \\ \omega_{12}^* & \omega_{22} \end{pmatrix}, \quad (23.2)$$

it is desired to put the system into the up state

$$|1\rangle = \begin{pmatrix} 0 \\ 1 \end{pmatrix}, \text{ or } |1\rangle\langle 1| = \begin{pmatrix} 0 & 0 \\ 0 & 1 \end{pmatrix};$$

through a series of measurements and feedback control actions (say over a time horizon $M = 2$).

The controlled dynamics are determined by a controlled quantum operation, with nominal value

$$\Gamma_{nom}(u, y)\omega = q(y|-1)P_{-1}T^u\omega T^{u\dagger}P_{-1} + q(y|1)P_1T^u\omega T^{u\dagger}P_1, \quad (23.3)$$

where

$$T^u = \begin{cases} \begin{pmatrix} 1 & 0 \\ 0 & 1 \end{pmatrix} & \text{if } u = 0, \\ \begin{pmatrix} 0 & 1 \\ 1 & 0 \end{pmatrix} & \text{if } u = 1, \end{cases} \quad (23.4)$$

$$P_{-1} = \begin{pmatrix} 1 & 0 \\ 0 & 0 \end{pmatrix}, \quad P_1 = \begin{pmatrix} 0 & 0 \\ 0 & 1 \end{pmatrix}, \quad (23.5)$$

and

$$\begin{aligned} q(-1|-1) &= q(1|1) &= 1 - \alpha; \\ q(-1|1) &= q(1|-1) &= \alpha. \end{aligned}$$

Here, T^u represents the application of a unitary transformation. Based on the control value u , we decide either to do nothing leaving the states unchanged ($u = 0$) or to flip the states ($u = 1$). P_{-1} and P_1 are projection operators, corresponding to perfect measurements of the states while $q(\cdot|\cdot)$ introduces imperfection in the measurements with an error probability $0 < \alpha < 1$. The controlled quantum

operators can be determined explicitly as:

$$\Gamma(0, -1)\omega = \begin{pmatrix} (1 - \alpha)\omega_{11} & 0 \\ 0 & \alpha\omega_{22} \end{pmatrix}; \quad (23.6a)$$

$$\Gamma(0, 1)\omega = \begin{pmatrix} \alpha\omega_{11} & 0 \\ 0 & (1 - \alpha)\omega_{22} \end{pmatrix}; \quad (23.6b)$$

$$\Gamma(1, -1)\omega = \begin{pmatrix} (1 - \alpha)\omega_{22} & 0 \\ 0 & \alpha\omega_{11} \end{pmatrix}; \quad (23.6c)$$

$$\Gamma(1, 1)\omega = \begin{pmatrix} \alpha\omega_{22} & 0 \\ 0 & (1 - \alpha)\omega_{11} \end{pmatrix}. \quad (23.6d)$$

Let us consider a system with initial pure state

$$|\phi_0\rangle = \frac{1}{\sqrt{2}}|-1\rangle + \frac{1}{\sqrt{2}}|1\rangle \quad \text{or} \quad \omega_0 = \frac{1}{2} \begin{pmatrix} 1 & 1 \\ 1 & 1 \end{pmatrix}. \quad (23.7)$$

The initial state ω_0 and controller K are sufficient to define random sequences of $\omega_{0,M}$, inputs $u_{0,M-1}$, and outputs $y_{1,M}$ over a given time interval $0 \leq k \leq M$ iteratively as follows. The control value u_0 is determined by K_0 (no observations are involved yet), and it is applied to the quantum system, which responds by selecting y_1 at random according to the distribution $p(y_1|u_0, \omega_0)$. This then determines the next state ω_1 via (20.1). Next u_1 is given by $K_1(y_1)$ and applied to the system. This process is repeated until the final time.

For simplicity, we apply a feedback controller K to the quantum system over a short time-horizon of $M = 2$:

$$u_0 = K_0 = 0, \quad u_1 = K_1(y_1) = \begin{cases} 0 & : \text{ if } y_1 = 1, \\ 1 & : \text{ if } y_1 = -1. \end{cases} \quad (23.8)$$

We will use the following notation for the resulting conditional states,

$$\omega_1^{(u_0, y_1)} = \Lambda_\Gamma(u_0, y_1)\omega_0 = \frac{\Gamma(u_0, y_1)\omega_0}{p(y_1|u_0, \omega_0)}. \quad (23.9)$$

$\omega_1^{(u_0, y_1)}$ is the conditional state after a control signal u_0 is applied and a measure-

ment y_1 is performed. Similarly,

$$\omega_2^{(u_0, y_1), (u_1, y_2)} = \Lambda_\Gamma(u_1, y_2) \omega_1 = \frac{\Gamma(u_1, y_2) \omega_1}{p(y_2 | u_1, \omega_1)} \quad (23.10)$$

represents the conditional state of the quantum system after a control signal u_0 is applied and a measurement y_1 is obtained in the first stage, followed by a control signal u_1 and a measurement y_2 .

For the system with initial state described by (23.7), $p_1 = p(y_1 | u_0, \omega_0) = \frac{1}{2}$ can be easily derived using (20.3). We can therefore end up in one of the following two possible conditional states corresponding to $y_1 \in \{-1, 1\}$ (since u_0 is always zero):

$$\omega_1^{(0, -1)} = \begin{pmatrix} (1 - \alpha) & 0 \\ 0 & \alpha \end{pmatrix}, \quad \omega_1^{(0, 1)} = \begin{pmatrix} \alpha & 0 \\ 0 & (1 - \alpha) \end{pmatrix}. \quad (23.11)$$

Case 1. $y_1 = 1$

In this case, we do not need to flip the state to achieve the desired output $y_2 = 1$ and therefore $u_1 = 0$. The measurement y_2 however can still be 1 or -1. So we can end up in one of the two following conditional states ω_2 for the case when $y_1 = 1$.

$$\omega_2^{(0, 1), (0, 1)} \quad \text{or} \quad \omega_2^{(0, 1), (0, -1)}.$$

The associated probabilities $p_2 = p(y_2 | u_1, \omega_1)$ are given as follows

$$\begin{aligned} p(1 | 0, \omega_1^{(0, 1)}) &= \text{tr}[\Gamma(0, 1) \omega_1^{(0, 1)}] = \alpha^2 + (1 - \alpha)^2, \\ p(-1 | 0, \omega_1^{(0, 1)}) &= \text{tr}[\Gamma(0, -1) \omega_1^{(0, 1)}] = 2\alpha(1 - \alpha). \end{aligned}$$

The conditional state ω_2 can then be explicitly calculated as follows

$$\begin{aligned} \omega_2^{(0, 1), (0, 1)} &= \frac{1}{\alpha^2 + (1 - \alpha)^2} \begin{pmatrix} \alpha^2 & 0 \\ 0 & (1 - \alpha)^2 \end{pmatrix}, \\ \omega_2^{(0, 1), (0, -1)} &= \frac{1}{2} \begin{pmatrix} 1 & 0 \\ 0 & 1 \end{pmatrix}. \end{aligned}$$

Case 2. $y_1 = -1$

In this case, we need to apply $u_1 = 1$ to flip the state to achieve the desired output $y_2 = 1$. As before, the probabilities p_2 can be calculated to be

$$\begin{aligned} p(1|1, \omega_1^{(0,-1)}) &= \text{tr}[\Gamma(1, 1)\omega_1^{(0,-1)}] = \alpha^2 + (1 - \alpha)^2, \\ p(-1|1, \omega_1^{(0,-1)}) &= \text{tr}[\Gamma(1, -1)\omega_1^{(0,-1)}] = 2\alpha(1 - \alpha). \end{aligned}$$

and the conditional states ω_2 are given by

$$\begin{aligned} \omega_2^{(0,-1),(1,1)} &= \frac{1}{\alpha^2 + (1 - \alpha)^2} \begin{pmatrix} \alpha^2 & 0 \\ 0 & (1 - \alpha)^2 \end{pmatrix}, \\ \omega_2^{(0,-1),(1,-1)} &= \frac{1}{2} \begin{pmatrix} 1 & 0 \\ 0 & 1 \end{pmatrix}. \end{aligned}$$

The non-selective states $\rho_i (i = 0, 1, 2)$ which represent the average of the conditional state ω with respect to the measurement can also be determined as follows:

$$\rho_0 = \omega_0, \tag{23.12a}$$

$$\rho_1 = p(-1|0, \omega_0)\omega_1^{(0,-1)} + p(1|0, \omega_0)\omega_1^{(0,1)} = \frac{1}{2} \begin{pmatrix} 1 & 0 \\ 0 & 1 \end{pmatrix}, \tag{23.12b}$$

$$\begin{aligned} \rho_2 &= p(-1|0, \omega_0) \left[p(-1|1, \omega_1^{(0,-1)})\omega_2^{(0,-1),(1,-1)} + p(1|1, \omega_1^{(0,-1)})\omega_2^{(0,-1),(1,1)} \right] \\ &\quad + p(1|0, \omega_0) \left[p(-1|1, \omega_1^{(0,1)})\omega_2^{(0,1),(0,-1)} + p(1|1, \omega_1^{(0,1)})\omega_2^{(0,1),(0,1)} \right] \\ &= \begin{pmatrix} \alpha & 0 \\ 0 & (1 - \alpha) \end{pmatrix}. \end{aligned} \tag{23.12c}$$

It is clear from (23.12c) that the level of degradation in performance is dependent on the error probability parameter α , with the system terminating in the mixed state ρ_2 . In the case of perfect measurement, i.e., $\alpha = 0$, the system ends up in the desired pure state $\rho_2 = |1\rangle\langle 1|$.

For this system, we now consider a risk sensitive controller using criteria (21.10). We use our control objective of regulating the system to the desired pure state $|1\rangle$ to construct a corresponding cost function which is a non-negative observable $L(u)$. Indeed, for the cost function $L(u)$ to reflect our objective, we

define

$$C = \frac{1}{2}(A - I) = \begin{pmatrix} -1 & 0 \\ 0 & 0 \end{pmatrix}.$$

We choose C so that the expected value of C^2 is

$$\begin{aligned} \langle 1|C^2|1\rangle &= \text{tr}[C^2|1\rangle\langle 1|] = 0, \\ \langle -1|C^2|-1\rangle &= \text{tr}[C^2|-1\rangle\langle -1|] = 1. \end{aligned}$$

Note that C gives zero cost to the desired state and non-zero cost to the undesired state. We also include a cost of control action such that there is zero cost for doing nothing and a non-zero cost for the flip operation, as follows:

$$c(u) = \begin{cases} 0 & : u = 0, \\ p & : u = 1, \end{cases} \quad (23.13)$$

where $p > 0$. Thus we define the cost function to be

$$L(u) = C^2 + c(u) \quad (23.14)$$

We also define a cost for the final state as a non-negative observable N :

$$N = C^2. \quad (23.15)$$

It is worth mentioning that the optimal risk-sensitive controller depends on the nominal model parameters, as well as the cost parameters. Also, this dependence can be in the form of a threshold condition. From (23.3), the Kraus operators are

$$\gamma_{nom,a}(u, y) = \sqrt{q(y|a)}P_aT^u \quad (23.16)$$

where $a \in \{-1, 1\}$. We now suppose that the error probability α is not known exactly. Let $0 < \tilde{\alpha} < 1$ be the true value of this parameter and set

$$\begin{aligned} \tilde{q}(-1|-1) &= \tilde{q}(1|1) = 1 - \tilde{\alpha}, \\ \tilde{q}(-1|1) &= \tilde{q}(1|-1) = \tilde{\alpha}. \end{aligned}$$

Then the probability distribution $\tilde{q}(y|a)$ is absolutely continuous with respect to

$q(y|a)$, with Radon-Nikodym derivative

$$\lambda_a(u, y) = \frac{\tilde{q}(y|a)}{q(y|a)}. \quad (23.17)$$

Hence robustness can be considered relative to the class of “true” models with error parameter $\tilde{\alpha}$ described by

$$\Gamma_{true}(u, y)\omega = \tilde{q}(y| - 1)P_{-1}T^u\omega T^{u\dagger}P_{-1} + \tilde{q}(y|1)P_1T^u\omega T^{u\dagger}P_1. \quad (23.18)$$

Note that by construction $\Gamma_{true}(u, y)$ is normalized. This means that if the true error probability differs from the nominal value, the bounds (22.22) and (22.32) ensure a corresponding bound on the risk-neutral cost.

The cost observables $L(u)$ and N are both diagonal with respect to the basis $| - 1 \rangle, | 1 \rangle$. Thus we have the spectral formulas

$$L(u) = (1 + c(u))P_{-1} + c(u)P_1, \quad N = 1P_{-1} + 0P_1.$$

Let us consider the terminal cost observable N . Then

$$\langle \omega, N \rangle = \omega_{11},$$

and

$$\langle \omega, \tilde{N} \rangle = g_2(1|N, \omega)\omega_{11},$$

where $\tilde{N} = Ng_2(N|N, \omega)$ allows for perturbation in the final cost function using Lemma 22.3. If we let

$$g_2(1|N, \omega) = \tilde{n}_2, \text{ and choose } g_2(0|N, \omega) = \frac{1 - \tilde{n}_2\omega_{11}}{\omega_{22}},$$

for some $0 \leq \tilde{n}_2 \leq \frac{1}{\omega_{11}}$, then

$$g_2(1|N, \omega)\langle \omega, P_{-1} \rangle + g_2(0|N, \omega)\langle \omega, P_1 \rangle = 1$$

satisfying (22.25). Hence,

$$\langle \omega, \tilde{N} \rangle = \tilde{n}_2\omega_{11}.$$

Now consider the running cost observable $L(u)$. Since $L(0) = N$,

$$\langle \omega, L(0) \rangle = \omega_{11},$$

and

$$\langle \omega, \tilde{L}(0) \rangle = g_1(1|L(0), \omega) \omega_{11},$$

where

$$\tilde{L}(0) = L(0)g_1(1|L(0), \omega), \text{ as in Lemma 22.3.}$$

If we let

$$g_1(1|L(0), \omega) = \tilde{n}_1, \text{ and choose } g_1(0|L(0), \omega) = \frac{1 - \tilde{n}_1 \omega_{11}}{\omega_{22}},$$

for some $0 \leq \tilde{n}_1 \leq \frac{1}{\omega_{11}}$. Then

$$g_1(1|L(0), \omega) \langle \omega, P_{-1} \rangle + g_1(0|L(0), \omega) \langle \omega, P_1 \rangle = 1$$

and (22.25) must be satisfied. Hence,

$$\langle \omega, \tilde{L}(0) \rangle = \tilde{n}_1 \omega_{11}.$$

Now

$$\langle \omega, L(1) \rangle = (1 + p) \omega_{11} + p \omega_{22},$$

and

$$\tilde{L}(1) = L(1)g_1(L(1)|L(1), \omega).$$

If we let

$$g_1(1 + p|L(1), \omega) = \frac{1 + \tilde{p}}{1 + p},$$

and choose

$$g_1(p|L(1), \omega) = \frac{1 - \frac{1 + \tilde{p}}{1 + p} \omega_{11}}{\omega_{22}} \quad (23.19)$$

for some $0 \leq \tilde{p} \leq \frac{1 + p - \omega_{11}}{\omega_{11}}$, then (22.25) is satisfied, and

$$\begin{aligned} \langle \omega, \tilde{L}(1) \rangle &= g_1(1 + p|L(1), \omega) (1 + p) \omega_{11} + g_1(p|L(1), \omega) p \omega_{22} \\ &= (1 + \tilde{p}) \omega_{11} + p \left(1 - \frac{1 + \tilde{p}}{1 + p} \omega_{11} \right). \end{aligned}$$

where

$$\tilde{L}(1) = L(1)g_1(L(1)|L(1), \omega).$$

From the expressions (22.30) and (22.33), we can calculate $\mathfrak{C}(\tilde{L} \parallel L)$ as follows:

$$\begin{aligned} \mathfrak{C}_{\omega_0}(\tilde{L}(0) \parallel L(0)) &= \int g_1(L(0)|L(0), \omega) \log g_1(L(0)|L(0), \omega) \langle \omega, P_X(dx) \rangle \\ &= \int \tilde{n}_1 \log \tilde{n}_1 \langle \omega, P_X(dx) \rangle. \end{aligned} \quad (23.20)$$

Similarly,

$$\mathfrak{C}_{\omega_1}(\tilde{L}(1) \parallel L(1)) = \int g_1(L(1)|L(1), \omega) \log g_1(L(1)|L(1), \omega) \langle \omega, P_X(dx) \rangle.$$

Here, we need to consider the two non-zero possible values of $L(1)$ in the first argument of $g_1(\cdot|L(1), \omega)$, namely $(1+p)$ and p . From (23.19), we then have

$$\mathfrak{C}_{\omega_1}(\tilde{L}(1) \parallel L(1)) = \begin{cases} \int \left[\frac{1+\tilde{p}}{1+p} \log \left(\frac{1+\tilde{p}}{1+p} \right) \right] \langle \omega, P_X(dx) \rangle & : 1+p, \\ \int \left[\frac{1-\frac{1+\tilde{p}}{1+p}\omega_{11}}{\omega_{22}} \log \left(\frac{1-\frac{1+\tilde{p}}{1+p}\omega_{11}}{\omega_{22}} \right) \right] \langle \omega, P_X(dx) \rangle & : p. \end{cases} \quad (23.21)$$

Finally, for the terminal cost observable N , we have

$$\begin{aligned} \mathfrak{C}_{\omega_2}(\tilde{N} \parallel N) &= \int g_2(N|N, \omega) \log g_2(N|N, \omega) \langle \omega, P_X(dx) \rangle \\ &= \int \tilde{n}_2 \log \tilde{n}_2 \langle \omega, P_X(dx) \rangle. \end{aligned} \quad (23.22)$$

Hence, we have performance bounds for the given class of cost functions and given class of uncertainty.

23.1 Conclusion

A quantum system modelled using stochastic master equations has been described. Optimal control schemes were investigated for the system. In particular, the risk-neutral and risk-sensitive optimal control problems were formulated in terms of suitable observables, and were brought into a form that made them

amenable to be solved using dynamic programming. As quantum systems are subjected to varying degrees of uncertainty, a certain degree of robustness is usually necessary in the controller design and this is provided by the close connections of the risk-sensitive control approach to robust control. In this case, we sought an upper bound on the risk-neutral performance for a class of true quantum models given a nominal model. This bound was determined using a measure of the “distance” between the probability distributions associated with the nominal model and the true model and using the concept of “quantum entropy” within the framework of Radon-Nikodym derivatives. A series of theorems were derived and proved to show the robust properties of the risk-sensitive approach and we determined performance bounds for a class of uncertainty using a two-level example.

Conclusion and Future Research

In this thesis, we have considered the application of optimal and robust control approaches to quantum systems that are of current interest in the physics community. First, we investigated the frequency-locking problem of optical cavities and devised and implemented a systematic control solution to the linear problem using an integral LQG approach. This work was then extended to the general nonlinear problem and we presented a novel approach to the frequency locking problem. In particular, we used a singular perturbation approach to take advantage of the different time-scaling of the subsystems to model the nonlinearity present in the system. Instantaneous bounds were placed on the measurements, which in turn restricted the space of the estimated detuning variable to a convex set. The nonlinear problem was thus converted into one which was amenable to linear control design techniques and simulation results were generated to validate our controller design. Future work will involve implementing and validating this approach on a new experimental test-bed under construction in our control laboratory. On this note, it is also worthwhile mentioning that the proposed approach relies on a precise mathematical formulation of the model parameters and hence on an accurate identification of the system. In practice, many of those parameters may be hard to determine beyond a certain level of accuracy. A certain measure of sensitivity of the approach is thus warranted and if necessary, a degree of robustness with respect to parametric uncertainty can be included in the controller using appropriate control design techniques.

In the second part of the thesis, we considered the problem of optimising the level of squeezing observed in a given optical quadrature of light. A nonlinear model of an optical squeezer (OPO) was analysed to determine the steady-state conditions required for the generation of specific types of squeezed states of light. In particular, we derived a relationship between the phase angles of the input

fields required to achieve optimal squeezing. The linear behaviour of the system about some suitably chosen operating points, corresponding to pairs of phase angles, was then investigated. With the system excited with quantum noises only, we showed that classical controllers cannot improve the level of squeezing observed. Then, we introduced classical noises in the system, including fixed d.c. disturbances as would be the case in practice and designed corresponding controllers for the system. We showed through simulation that classical noises can (in theory) be completely suppressed to achieve noise level approaching that of the QNL. And finally, we considered the case where, in addition to the classical sources of noises, the detuning variable was also non-zero. A multivariable controller was designed and the simulation results obtained were very promising. The next natural stage of this work will be the implementation and validation of this controller on an experimental set-up. Furthermore, this work can also be extended by using suitable robust control design techniques such as the minimax LQG approach to cater for a wider operating range of the phase angles.

A theoretical problem in the field of quantum control is considered in the last part of the thesis. Building on the work of James and Petersen in [2], we formulated a risk-sensitive problem and determined an upper bound on the cost function of an associated risk-neutral problem for a class of true quantum systems which differed from a nominal model in the “observables”. We demonstrated our result using a two-level system. While such schemes may be difficult to implement in practice at this time, it is our view that robust control approaches will have a key role to play in the future of quantum control.

To conclude, we believe that it is still too early to make a call on the limits of quantum control. While for some applications, it is clear how modern control schemes can result in improved performance, the gap between some theoretical work performed in the area and the required technology seems to be here to stay for a while. However, there is hope. Recently, observations resulting from the interaction of a superconducting two-level system with a single photon, opened up new possibilities that could be exploited for quantum communication and quantum information processing; see, e.g., [111, 112]. Quantum entanglement which is one of the defining features of quantum mechanics and is absent in the classical world, has diverse potential applications including long distance transmission of data over optical fibres, biological and chemical sensing, and

spot-size laser read/write beams, among others; see [113]. Also, modern cavity quantum electrodynamics (QED) experiments performed in high quality cavity where the atom-photon system is shielded from decoherence (interactions with the environment), provide an ideal proving ground for principles of quantum control and will help identify research goals in the near future [114].

References

- [1] M. R. James. Risk-sensitive optimal control of quantum systems. *Phys. Rev. A*, 69(032108), 2004.
- [2] M. R. James and I. R. Petersen. Robustness properties of a class of optimal risk-sensitive controllers for quantum systems. In *Inter. Fed. Automatic Control World Congress*, pages 194–199, Prague, Czech Republic, 2005.
- [3] E. D. Black. An introduction to Pound-Drever-Hall laser frequency stabilization. *Am. J. Phys.*, 69(1):79–87, 2001.
- [4] Wiki. Pound-Drever-Hall technique. http://en.wikipedia.org/wiki/Pound-Drever-Hall_technique, Dec. 2009.
- [5] H. A. Bachor and T. C. Ralph. *A Guide to Experiments in Quantum Optics*. John Wiley, 2004.
- [6] A. E. Siegman. *Lasers*. University Science Books, 1986.
- [7] D. W. Allan. Time and Frequency (Time-Domain) Characterization, Estimation, and Prediction of Precision Clocks and Oscillators. *IEEE Trans. Ultrasonics, Ferroelectrics and Freq. cont.*, 34(6):647–654, Nov. 1987.
- [8] Chul-Ho. Shin and M. Ohtsu. Heterodyne Optical Phase-Locked Loop by Confocal Fabry-Perot Cavity Coupled AlGaAs Lasers. *IEEE Photonics Tech. Lett.*, 2(4):297–300, April 1990.
- [9] K. Kuboki and M. Ohtsu. The Allan Variance Real-time Processing System for Frequency Stability Measurement of Semiconductor Lasers. *IEEE Trans. Inst. Meas.*, 39(4):637–641, Aug. 1990.
- [10] K. B. MacAdam, A. Steinbach, and C. Wieman. A Narrow-band Tunable Diode Laser System with Grating Feedback, and a Saturated Absorption Spectrometer for Cs and Rb. *Am. J. Phys.*, 60(12):1098–1111, Dec. 1992.
- [11] R. L. Barger, M. S. Sorem, and J. L. Hall. Frequency Stabilization of a cw Dye Laser. *Applied Physics Letters*, 22(11):573–575, 1973.

- [12] M. Maric and A. Luiten. Power-Insensitive Side Locking for Laser Frequency Stabilization. *Optics Letters*, 30(10):101153, May 2005.
- [13] W. Weyerman, B. Neyenhius, J. Archibald, M. Washburn, D. Durfee, and S. Warnick. Identification and Control of a Grating-Stabilized External-Cavity Diode Laser. *IEEE Trans. Control Syst. Tech.*, 17(1):161–166, Jan. 2009.
- [14] S. Z. Sayed Hassen, E. Huntington, I. R. Petersen, and M. R. James. Frequency Locking of an Optical Cavity Using LQG Integral Control. In *Proceedings of the 17th IFAC World Congress*, pages 1821–1826, Seoul, South-Korea, July 2008.
- [15] S. Z. Sayed Hassen, M. Heurs, E. H. Huntington, I. R. Petersen, and M. R. James. Frequency Locking of an Optical Cavity using Linear-Quadratic Gaussian Integral Control. *J. Phys. B: At. Mol. Opt. Phys.*, 42(17):175501, Sept. 2009.
- [16] S. Z. Sayed Hassen and I. R. Petersen. A Time-Varying Kalman Filter Approach to Integral LQG Frequency Locking of an Optical Cavity. In *Proc. American Control Conf.*, pages 2736–2741, Baltimore, MD, USA, July 2010.
- [17] R. W. Boyd. *Nonlinear Optics*. Academic Press, Boston, 2008.
- [18] H. W. Wiseman and G. J. Milburn. *Quantum Measurement and Control*. Cambridge University Press, 2010.
- [19] E. Merzbacher. *Quantum Mechanics*. John Wiley & Sons Ltd., third edition, 1998.
- [20] E. F. Schubert. *Light-Emitting Diodes*. Cambridge University Press, New York, second edition, 2006.
- [21] H. Kogelnik and T. Li. Laser Beams and Resonators. *Applied Optics*, 5(10):1550–1567, 1966.
- [22] T. McKelvey, H. Akçay, and L. Ljung. Subspace-based Multivariable System Identification from Frequency Response Data. *IEEE Trans. Autom. Control*, 41(7):960–979, 1996.
- [23] D. A. Anderson. Alignment of Resonant Optical Cavities. *Applied Optics*, 23(17):2944–2949, Sept. 1984.
- [24] E. H. Huntington, M. R. James, and I. R. Petersen. Laser-cavity frequency locking using modern control. In *Proc. IEEE Conf. on Decision and Control*, pages 6346–6351, New Orleans, Dec. 2007.

- [25] C. W. Gardiner and P. Zoller. *Quantum Noise*. Springer, Berlin, 2000.
- [26] V. I. Arnold. *Mathematical Models of Classical Mechanics*. Graduate Texts in Mathematics. Springer, 1989.
- [27] P. van Overschee and B. De Moor. *Subspace Identification for Linear Systems*. Kluwer Academic Publishers, 1996.
- [28] B. Ho and R. Kalman. Effective Construction of Linear State-Variable Models from Input-Output Functions. *Regelungstechnik*, 14:545–548, 1966.
- [29] S. Y. Kung. A New Identification and Model Reduction Algorithm via Singular Value Decompositions. In *12th Asilomar Conference on Circuits, Systems and Computers*, pages 705–714, Pacific Grove, CA, 1978.
- [30] B. Gopinath. On the Identification of Linear Time-Invariant Systems from Input-Output Data. *Bell System Tech. J.*, 48(5):1101–1113, 1969.
- [31] B. De Moor, J. Vandewalle, L. Vandenbergh, and P. V. Miegheem. A Geometrical Strategy for the Identification of State Space models of Linear Multivariable Systems with Singular Value Decomposition. In *8th IFAC/IFORS Symp. Ident. and Syst. Parameter Estimation*, pages 700–704, Beijing, 1988.
- [32] K. Liu, R. N. Jacques, and D. W. Miller. Frequency Domain Structural System Identification by Observability Range Space Extraction. In *Proc. American Control Conf.*, pages 107–111, Baltimore, Maryland, June 1994.
- [33] K. Ogata. *Discrete-Time Control Systems*. Pearson Education, 2002.
- [34] T. Katayama. *Subspace Methods for System Identification*. Springer-Verlag London Ltd, 2005.
- [35] T. McKelvey. Subspace Methods for Frequency Domain Data. In *Proc. American Control Conf.*, pages 673–678, Boston, USA, 2004.
- [36] K. J. Åström and B. Wittenmark. *Computer Controlled Systems: Theory and Design*. Prentice-Hall, Inc., third edition, 1997.
- [37] R. E. Kalman. Contributions to the Theory of Optimal Control. *Boletín de la Sociedad Matemática Mexicana*, 5:102–119, 1960.
- [38] R. E. Kalman. A New Approach to Linear Filtering and Prediction Problems. *Transactions of the ASME—Journal of Basic Engineering*, 82(Series D):35–45, 1960.
- [39] R. E. Kalman and R. S. Bucy. New Results in Linear Filtering and Prediction Theory. *ASME Journal of Basic Engineering*, 83:95–108, 1961.

- [40] B. D. O. Anderson and J. B. Moore. *Linear Optimal Control*. Prentice-Hall, Englewood Cliffs, N. J., 1971.
- [41] H. Kwakernaak and R. Sivan. *Linear Optimal Control Systems*. John Wiley & Sons, Inc., 1972.
- [42] F. L. Lewis. *Optimal Estimation*. John Wiley & Sons, Inc., 1986.
- [43] K. Ogata. *Modern Control Engineering*. Prentice-Hall, 2002.
- [44] B. van Brunt. *The Calculus of Variations*. Springer, New York, 2004.
- [45] R. G. Brown. *Introduction to Random Signal Analysis and Kalman filtering*. John Wiley & Sons Ltd., 1983.
- [46] T. Başar and P. Bernhard. \mathcal{H}_∞ *Optimal Control and Related Minimax Design Problems: A Dynamic Game Approach*. Birkhäuser, Boston, 1995.
- [47] P. Whittle. Risk-sensitive linear/quadratic/gaussian control. *Adv. in App. Prob.*, 13:764–777, 1981.
- [48] M. J. Grimble. Design of optimal stochastic regulating systems including integral action. *Proc. IEE Control & Science*, 126(9):841–848, Sept. 1979.
- [49] Y-J. Cheng, P. L. Mussche, and A. E. Siegman. Measurement of Laser Quantum Frequency Fluctuations using a Pound-Drever Stabilization System. *IEEE Jour. Quantum Elect.*, 30(6):1498–1504, June 1994.
- [50] K. Zhou, J. C. Doyle, and K. Glover. *Robust and Optimal Control*. Prentice-Hall, 1996.
- [51] D. P. Bertsekas and I. B. Rhodes. Recursive State Estimation for a Set-Membership Description of Uncertainty. *IEEE Trans. Autom. Control*, 16(2):117–128, Apr. 1971.
- [52] P. Kokotović, H. K. Khalil, and J. O'Reilly. *Singular Perturbation Methods in Control: Analysis and Design*. Academic Press Inc., 1986.
- [53] T. W. Hansch and B. Couillaud. Laser Frequency Stabilization by Polarization Spectroscopy of a Reflecting Reference Cavity. *Optics Communications*, 35(3):441–444, Dec. 1980.
- [54] D. A. Shaddock, M. B. Gray, and D. E. McClelland. Frequency Locking a Laser to an Optical Cavity by use of Spatial Mode Interference. *Optics Letters*, 24(21):1499–1501, Nov. 1999.
- [55] D. M. Burton. *The History of Mathematics: An Introduction*. Allyn and Bacon, Boston, 1985.

- [56] O. Yaniv and M. Nagurka. Design of PID Controllers satisfying Gain margin and Sensitivity Constraints on a set of plants. *Automatica*, 40(1):111–116, Jan. 2004.
- [57] W. Pauli. *General Principles of Quantum Mechanics*. Springer, 1980.
- [58] C. M. Caves. Quantum-mechanical noise in an interferometer. *Phys. Rev. D*, 23(8):1693–1708, Apr 1981.
- [59] H. Vahlbruch, S. Chelkowski, B. Hage, A. Franzen, K. Danzmann, and R. Schnabel. Coherent Control of Vacuum Squeezing in the Gravitational-Wave Detection Band. *Phys. Rev. Lett.*, 97(1):011101, Jul 2006.
- [60] W. P. Bowen, N. Treps, B. C. Buchler, R. Schnabel, T. C. Ralph, H. Bachor, T. Symul, and P. K. Lam. Experimental investigation of continuous-variable quantum teleportation. *Phys. Rev. A*, 67(3):032302, Mar 2003.
- [61] A. Einstein, B. Podolsky, and N. Rosen. Can quantum-mechanical description of physical reality be considered complete? *Physical Review*, 47:777–780, 1935.
- [62] A. Aspect, P. Grangier, and G. Roger. Experimental Realization of Einstein-Podolsky-Rosen-Bohm Gedankenexperiment: A New Violation of Bell’s Inequalities. *Phys. Rev. Lett.*, 49(2):91–94, Jul 1982.
- [63] R. E. Slusher, L. W. Hollberg, B. Yurke, J. C. Mertz, and J. F. Valley. Observation of Squeezed States Generated by Four-Wave Mixing in an Optical Cavity. *Phys. Rev. Lett.*, 55(22):2409–2412, Nov 1985.
- [64] H. Vahlbruch, M. Mehmet, S. Chelkowski, B. Hage, A. Franzen, N. Lastzka, S. Gobler, K. Danzmann, and R. Schnabel. Observation of Squeezed Light with 10-dB Quantum-Noise Reduction. *Phys. Rev. Letters*, 100(033602), Jan. 2008.
- [65] A. Yariv. *Quantum Electronics*. John Wiley & Sons Ltd., 1989.
- [66] S. Z. Sayed Hassen, I. R. Petersen, E. H. Huntington, M. Heurs, and M. R. James. LQG control of an optical squeezer. In *Proc. American Control Conf.*, pages 2730–2735, Baltimore, MD, USA, July 2010.
- [67] S. Z. Sayed Hassen and I. R. Petersen. Optimal amplitude quadrature control of an optical squeezer using integral LQG approach. In *IEEE Multi-Conf. on Systems and Control*, Yokohama, Japan, Sept. 2010. Accepted.
- [68] S. Z. Sayed Hassen and I. R. Petersen. Optimal squeezing of an OPA using Multivariable Integral LQG Control. In *Proc. of the 18th IFAC World Congress*, Milan, Italy, August 2011. To be submitted.

- [69] M. Srednicki. *Quantum Field Theory*. Cambridge University Press, 2007.
- [70] M. J. Collett and C. W. Gardiner. Squeezing of intracavity and traveling-wave light fields produced in parametric amplification. *Phys. Rev. A*, 30(3):1386–1391, Sep 1984.
- [71] S. C. Edwards and V. P. Belavkin. Optimal quantum feedback control via quantum dynamic programming. arXiv:quant-ph/0506018, 2005.
- [72] K. Jacobs. Applications of feedback control in quantum systems. In *Proc. 6th Asian Cont. Conf.*, page 35, 2006. quant-ph/0605015.
- [73] A. C. Doherty and K. Jacobs. Feedback control of quantum systems using continuous state estimation. *Phys. Rev. A*, 60(2700), 1999.
- [74] A. J. Shaiju, I. R. Petersen, and M. R. James. Guaranteed cost LQG control of uncertain linear stochastic quantum systems. In *Proc. American Control Conf.*, pages 2118–2123, New York, July 2007.
- [75] M. J. D. Powell. *A Fortran Subroutine for Solving Systems of Nonlinear Algebraic Equations*. Numerical Methods for Nonlinear Algebraic Equations. Gordon and Breach, London, UK, 1970.
- [76] P. D. Drummond, K. J. McNeil, and D. F. Walls. Non-equilibrium transitions in sub/second harmonic generation. *Journal of Modern Optics*, 27(3):321–335, 1980.
- [77] P. J. Antsaklis and A. N. Michel. *A Linear Systems Primer*. Birkhäuser, 2007.
- [78] R. Eising. Between controllable and uncontrollable. *Systems and Control Letters*, 4(5):263–264, July 1984.
- [79] P. Gahinet and A. J. Laub. Algebraic Riccati equations and the distance to the nearest uncontrollable pair. *SIAM J. Control and Optimization*, 30(4):765–786, 1992.
- [80] M. Gu. New methods for estimating the distance to uncontrollability. *SIAM J. Matrix Anal. Appl.*, 21(3):989–1003, 2000.
- [81] M. Gu, E. Mengi, M. L. Overton, J. Xia, and J. Zhu. Fast methods of estimating the distance to uncontrollability. *SIAM J. Matrix Anal. Appl.*, 28(2):477–502, 2006.
- [82] H. Wiseman. *Quantum Trajectories and Feedback*. PhD thesis, University of Queensland, 1994.

- [83] H. Wiseman and G. J. Milburn. Squeezing via feedback. *Phys. Rev. A*, 49(1350), 1994.
- [84] A. C. Doherty, S. Habib, K. Jacobs, H. Mabuchi, and S. M. Tan. Quantum feedback control and classical control theory. *Phys. Rev. A*, 62(012105), 2000.
- [85] S. Habib, K. Jacobs, and H. Mabuchi. Quantum feedback control: How can we control quantum systems without disturbing them? *Los Alamos Science*, 27:126–135, 2002.
- [86] J. M. Geremia, J. K. Stockton, A. C. Doherty, and H. Mabuchi. Quantum kalman filtering and the heisenberg limit in atomic magnetometry. *Phys. Rev. Letters*, 91(25):250801, Dec. 2003.
- [87] R. Van Handel, J. K. Stockton, and H. Mabuchi. Feedback control of quantum state reduction. *IEEE Trans. Autom. Control*, 50(6):768–780, June 2005.
- [88] A. C. Doherty, K. Jacobs, and G. Jungman. Information, disturbance, and Hamiltonian quantum feedback control. *Phys. Rev. A*, 63(062306), 2001.
- [89] H. M. Wiseman. Adaptive phase measurements of optical modes: Going beyond the marginal Q distribution. *Phys. Rev. Lett.*, 75(25):4587–4590, Dec 1995.
- [90] M. A. Armen, J. K. Au, J. K. Stockton, A. C. Doherty, and H. Mabuchi. Adaptive homodyne measurement of optical phase. *Phys. Rev. Letters*, 89(13):133602, Sep 2002.
- [91] J. C. Doyle. Guaranteed margins for LQG regulators. *IEEE Trans. Autom. Control*, 23(4):756–757, August 1978.
- [92] J. C. Doyle, K. Glover, P. P. Khargonekar, and B. A. Francis. State-Space Solutions to Standard \mathcal{H}_2 and \mathcal{H}_∞ Control Problems. *IEEE Trans. Autom. Control*, 34(8):831–847, 1989.
- [93] M. R. James, J. S. Baras, and R. J. Elliott. Risk-sensitive control and dynamic games for partially observed discrete-time nonlinear systems. *IEEE Trans. Autom. Control*, 39(4):780–792, 1994.
- [94] R. K. Boel, M. R. James, and I. R. Petersen. Robustness and risk sensitive filtering. *IEEE Trans. Autom. Control*, 47(3):451–461, 2002.
- [95] I. R. Petersen, M. R. James, and P. Dupuis. Minimax optimal control of stochastic uncertain systems with relative entropy constraints. *IEEE Trans. Autom. Control*, 45(3):398–412, 2000.

- [96] P. Dupuis, M. R. James, and I. R. Petersen. Robust properties of risk-sensitive control. *Mathematics of Control, Signals, and Systems*, 13(4):318–332, 2000.
- [97] N. Yamamoto and L. Bouten. Quantum Risk-Sensitive Estimation and Robustness. *IEEE Trans. Autom. Control*, 54(1):92–107, Jan. 2009.
- [98] W. Rudin. *Real and Complex Analysis*. Mc Graw-Hill, 1987.
- [99] D. D’Alessandro. *Introduction to Quantum Control and Dynamics*. Chapman & Hall, 2008.
- [100] M. R. James, H. I. Nurdin, and I. R. Petersen. H^∞ control of linear quantum stochastic systems. *IEEE Trans. Autom. Control*, 53(8):1787–1803, Sep. 2008.
- [101] H. Mabuchi. Coherent feedback quantum control with a dynamic compensator. arXiv:0803.2007v1 [quant-ph], 2008.
- [102] M. A. Nielsen and I. L. Chuang. *Quantum Computation and Quantum Information*. Cambridge University Press, 2003.
- [103] A. Barchielli and V. P. Belavkin. Measurements continuous in time and a posteriori states in quantum. *Jour. Phys. A: Math. Gen.*, 24:1495–1514, 1991.
- [104] V.P. Belavkin. Theory of the control of observable quantum systems. *Automatica and Remote Control*, 44(2):178–188, 1983.
- [105] D. H. Jacobson. Optimal stochastic linear systems with exponential performance criteria and their relation to deterministic differential games. *IEEE Trans. Autom. Control*, 18(2):124–131, 1973.
- [106] A. Bensoussan and J. H. van Schuppen. Optimal control of partially observable stochastic systems with an exponential-of-integral performance index. *SIAM J. Control and Optimization*, 23:599–613, 1985.
- [107] R. E. Bellman. *Dynamic Programming*. Princeton University Press, 1957.
- [108] V. P. Belavkin and P. Staszewski. A radon-nikodym theorem for completely positive maps. *Reports on Mathematical Physics*, 24(1):49–55, August 1986.
- [109] M. Raginsky. Radon-nikodym derivatives of quantum operations. *J. of Math. Phys.*, 44(11):5003–5020, Nov. 2003.
- [110] P. Dupuis and R. S. Ellis. *A Weak Convergence Approach to the Theory of Large Deviations*. Wiley, New York, 1997.

-
- [111] A. Walraff, D. I. Schuster, A. Blais, L. Frunzio, R. S. Huang, J. Majer, S. Kumar, S. M. Girvin, and R. J. Schoelkopf. Strong coupling of a single photon to a superconducting qubit using circuit quantum electrodynamics. *Nature*, 431(7005):162–167, Sep. 2004.
 - [112] A. Blais, R. S. Huang, A. Wallraff, S. M. Girvin, and R. J. Schoelkopf. Cavity quantum electrodynamics for superconducting electrical circuits: An architecture for quantum computation. *Phys. Rev. A*, 69(6):062320, Jun 2004.
 - [113] K. J. Vahala. Optical microcavities. *Nature*, 424(6950):839–846, Aug. 2003.
 - [114] H. Mabuchi and A. C. Doherty. Cavity quantum electrodynamics: Coherence in context. *Science*, 298(5597):1372–1377, Nov. 2002.